

International Journal of Thermodynamics

Editor-in-Chief

L. Kuddusi

Honorary Editors

A. Bejan

M. J. Moran

J. Szargut

G. Tsatsaronis

A. Valero

M. R. von Spakovsky

Abstracting and Indexing:

Chemical Abstracts Services, Copernicus, DOAJ, EBSCO, Emerging Sources Citation Index, Engineering Index, Google Scholar, Scopus, and ULAKBIM



*International Centre for
Applied Thermodynamics*

Editor-in-Chief

Prof. Dr. Lütfullah KUDDUSİ

Associate Editor-in-Chief

Assoc. Prof. Dr. Patrice ESTELLÉ

Prof. Dr. Enrico SCIUBBA

Associate Editor

Prof. Dr. Ali KOSAR

Prof. Dr. Derya Burcu ÖZKAN

Prof. Dr. Mustafa ÖZDEMİR

Prof. Dr. Ahmet DURMAYAZ

Assoc. Prof. Dr. Onur TAYLAN

Prof. Dr. Mehmet ARİK

Prof. Dr. Ayşegül ABUŞOĞLU

Assoc. Prof. Dr. Ersin SAYAR

Prof. Dr. Hakan Fehmi ÖZTOP

Prof. Dr. G. Reza VAKİLİ-NEZHAAD

Prof. Dr. Bayram ŞAHİN

Editorial Board

Prof. Dr. Yasar DEMİREL

Prof. Dr. Lütfullah KUDDUSİ

Prof. Dr. Ahmet DURMAYAZ

Prof. Dr. Derya Burcu ÖZKAN

Prof. Dr. Mustafa ÖZDEMİR

Prof. Dr. Ali KOSAR

Assoc. Prof. Dr. Ersin SAYAR

Prof. Dr. Mehmet ARİK

Assoc. Prof. Dr. Abdussamet SUBASI

Daniel FAVRAT

Francois MARECHAL

Prof. Silvia Azucena NEBRA

Luis SERRA

Assoc. Prof. Dr. Onur TAYLAN

Prof. Dr. Ayşegül ABUŞOĞLU

Vittorio VERDA

Gian Paolo BERETTA

Abel HERNANDEZ-GUERRERO

Nilufer EGRİCAN

Dr. Sean WRIGHT

Prof. Dr. Hakan Fehmi ÖZTOP

Prof. Dr. Enrico SCIUBBA

Prof. Dr. G. Reza VAKİLİ-NEZHAAD

Prof. Dr. Bayram ŞAHİN

Publishing Editor

Assoc. Prof. Dr. Abdussamet SUBASI

Dr. Mustafa Yasin GÖKASLAN

Res. Assist. Ali Murat BİNARK

Language Editor

Assoc. Prof. Dr. Abdussamet SUBASI

Journal Contacts

Editor-in-Chief

Prof. Dr. Lütfullah Kuddusi

ISTANBUL TECHNICAL UNIVERSITY

kuddusi@itu.edu.tr

+902122931300/2452

Department of Mechanical Engineering

Istanbul Technical University

Gumussuyu, 34437 Istanbul Turkey

Volume: 26

Issue: 4

Web: <https://dergipark.org.tr/tr/pub/ijot>

International Journal of Thermodynamics (IJoT)




ISSN:1301-9724 / e-ISSN:2146-1511

CONTENTS

<u>Research Article</u>	
1. The Potential of Using the Incorporation of Concentrated Solar Power and Gas Turbines in the South of Libya	1-10
Sami Ehtiweh, Asya Gabbasa, Ismael A.S. Ehtiweh	
<u>Research Article</u>	
2. Phase Transition Thermodynamic Properties of 2-Methylquinoline, 2-Chloroquinoline and 2-Phenylquinoline	11-18
Rawand Samad Abdullah, Boris N. Solomonov	
<u>Research Article</u>	
3. New Thermodynamic Equation of State for Refrigerant HFO-1243zf	19-30
I. M. Astina, H. Ilham Alfishahri	
<u>Research Article</u>	
4. Experimental Investigations on Single-Phase Heat Transfer Enhancement in an Air-To-Water Heat Exchanger with Rectangular Perforated Flow Deflector Baffle Plate	31-39
Md A. Rahman	
<u>Research Article</u>	
5. High-Pressure Calibration TiN Equation of State	41-47
Sirwan K. Jalal, M. Mohammad Uonis, Raed H. Al-Saga	
<u>Research Article</u>	
6. Thermodynamic Properties of Selected Bicyclic Terpenes and Related Substances by Gas Chromatography and Group Contributions	48-56
L.A.A.P. Fonseca, Carlos E.L. Oliveira, Marco A. Cremasco	
<u>Research Article</u>	
7. Comparative Evaluation for Selected Gas Turbine Cycles	57-67
Mohamed Elwardany, Abd El-Moneim M. Nassib, Hany A. Mohamed	
<u>Research Article</u>	
8. Economic, Enviroeconomic Analysis of Active Solar Still Using Al ₂ O ₃ Nanoparticles	68-76
<u>Dharamveer Singh</u>	
<u>Research Article</u>	
9. Calculation of Complex Chemical Equilibrium Using Optimization Package Ipopt	77-83
Gleb V. Belov, Nina M. Aristova	

Research Article

The Potential of Using the Incorporation of Concentrated Solar Power and Gas Turbines in the South of Libya

¹ S. Ehtiwesh , ² A. Gabbasa , ^{3*} I. Ehtiwesh 

^{1,3} Sabratha University, Faculty of Engineering Sabratha, Department of Mechanical Engineering

² University of Zawia, Faculty of Oil & Gas and renewable energy Engineering

E-mail: ^{3*} ismael.ehtiwesh@sabu.edu.ly

Received 10 May 2023, Revised 19 August 2023, Accepted 30 August 2023

Abstract

In the southern part of Libya, there are a number of power plants and other large industrial developments using their power systems, such as petroleum fields. Gas turbines are frequently employed due to water scarcity in the region, such as the Asrir field power plant. However, fuel transportation is one of the main difficulties regarding cost and safety. The annual cost of fuel operation and transportation is admitted to be very high; therefore, this work aims to utilize solar energy potential to reduce fuel consumption. In this context, a power plant that is currently in operation in Libya, which is located close to the Sahara Desert in the southwestern region, was selected as a case study. The region was chosen because it offers extraordinary conditions for the establishment of concentrated power plants. Simulations studies were carried out at full load considering the nature of the solar flux that varies with the meteorological conditions and the thermodynamic calculations were made based on algebraic equations describing the power cycle and the solar field. In addition, the feasibility of fulfilling the power cycle's energy required using the CSPs system was also analyzed. The annual behavior of the solar field was determined using hourly data within the system advisor model (SAM) software. In order to examine the possibility of fuel reduction, the cost of fuel was linked with an exergy analysis from an economic perspective. The findings revealed that the plant efficiency could be increased and the fuel mass rate ratio could be reduced by preheating the air temperature entering the combustion chamber. The air/fuel ratio at the combustor was found 43, the design heat energy required to deliver to the combustion chamber is 414.4MW, and the energetic thermal efficiency of the power cycle is 32.6%. The thermal power design of the solar field is 532MW when average direct irradiation is equal to 1000kWh/m².

Keywords: Concentrated solar power; gas turbine; reduction of fuel consumptions; solar energy.

1. Introduction

The present study aims to address the potential of incorporating concentrated solar power systems (CSPs) as a sustainable alternative to clean energy generation within a gas turbine near a Sahara in Libya. CSPs transform radiant energy into thermal energy, and they cover a large array of different options, the most common ones are: parabolic trough, central receivers (power tower), parabolic dish and linear Fresnel [1]. The central receivers technology is selected due to gas power plants require a high temperature, it uses a large number of mirrors (heliostats) to concentrate the rays on a particular receiver that is placed at the top of a tower [1]. Their operation is expanding, particularly, in the US and Spain [2]; several commercial central receiver plants presently in operation use direct steam generation (DSG) technology; and some use molten salts as both the HTF and storage medium [3]. This technology achieves very high temperatures up to 800°C, thereby increasing the efficiency at which heat is converted into electricity in the power block and reducing the cost of thermal storage. An incorporated solar combined plant is modeled and simulated in the study [4] considering 20% solar, in the east of Algeria, where the region is near the location under study, therefore, the environmental conditions are similar.

The plant uses a gas turbine with exhaust heat recovery for steam generation and the overall efficiency is 49% at a nominal output. Experimental research [5] addressed the effects of forced convective cooling on the electrical and thermal performance of photovoltaic thermal collectors using two different angular-positioned finned heat sink attachments and a phase transition material (paraffin) with steel foam mixture. Air was forced to flow between the flat and angled fins with the use of a fan. Data from a reference photovoltaic module was used to determine solar radiation, temperature, electrical and thermal power, energy, and efficiency efficiencies. In comparison to the solar module, the inclined and flat-finned heat sink attached collectors were cooled by about 12% and 22%, respectively. Due to the given cooling, the electrical efficiency improvement with incline finned and flat finned heat sink application obtained roughly 5% and 6% compared to the solar module, which has a 4.4% electrical efficiency. Overall, the efficiencies were around 60% and 41%. The energy efficiency of photovoltaic modules is 4.7%; cooling with incline finned heat sink and a flat finned heat sink application increases it to 5.6% and 6.9%. Abdel Dayem et al. [6] investigated a numerical analysis considering an integrated solar combined cycle power plant taking in the

Makkah region. The result was compared with the data of the Kuraymat power plant. The capacity of the plant is 135MW, including 61MW that produced within the CSP system. The analysis presents that the model in Makkah is viable and it can be used by the electrical sector in Saudi Arabia. Poullikkas [7] carried out a feasibility analysis aiming to investigate whether the installation of CSPs in the Mediterranean region is economically feasible. The analysis included Cyprus's solar potential as well as all information available regarding the current RES policy of the Cyprus Government, including the applicable feed-in tariff of 0.26 cents per kWh. It is concluded that the implementation of CSPs in the region is profitable and economically feasible under appropriate conditions, namely, the plant size, the storage size, the initial and land cost. Furthermore, the investment can be increasingly attractive by increasing the plant size. The outcomes also showed that the additional benefit resulting from the 30€/t trading price for CO₂ emissions in all situations evaluated throughout the simulations was at 2.4€/kWh. The findings showed that land leasing price has a negative impact on final production costs, increasing the cost of electricity produced by the solar thermal power plant by 1.43€/kWh for every 1€/m² year rise in land leasing price. Studies [1, 8, 9, 10] follow the methodology proposed in [11], which is used to analyze the feasibility of installing CSPs along the Libyan coastline. The potential of solar resources and the appropriate factors for the use of CSPs in Tunisia was evaluated [12], the interconnection of electricity with Europe, and the opportunity for the development of renewable energy sources in North Africa by European support. The study indicates that the electricity generation exceeds the Andasol plant by 1793MWh. Experimental study [13] aimed at the energy and exergy analysis of Al₂O₃ Nano fluid circulation in two different flow patterns was done on PV/T collector cooling. The comparison module was a 20W polycrystalline PV module. The PV/T collectors were also built using the same PV modules. PV/T-A and PV/T-B collectors cooled PV modules by 29% and 48.5% more effectively when subjected to solar radiation of 793 W/m² (equal to 121W of solar power). Environmental economics were predicted to have a size of 0.094tCO₂/year, 0.12tCO₂/year carbon reduction, and corresponding carbon trade values of 1.4 and 1.8 dollars.

Natural gas power plants are available in two technologies, namely, simple cycle and combined cycle gas plants (CCGT) [14]. The integration of CSPs with natural gas plants can be directed to the steam cycle or to gas cycle. Therefore, solar energy produced by CSPs can be used to boil water in the heat recovery steam generator and inject it into the high-pressure turbine or to preheat the air before enters the combustor. The available hybrid-CSPs are mostly integrated with CCGT with the purpose of supplying additional saturated steam to the heat recovery steam generator via a high-pressure drum [3]. The incorporation of CSPs with natural gas can be employed by using several configurations at difference temperatures. Adding heat to gas turbines by CSPs technologies is a technical challenge as gas turbines operate at temperatures higher than steam turbines. On the other hand, the flexible operation of Brayton cycle where the fuel and air can be controlled, makes their combining with CSPs more valuable [15]. Therefore, CSPs adds heat to the power cycle to preheat the air before the combustion chamber, where the fuel rate control assures combustion can get the needed operation

temperature. Furthermore, there is another configuration of integration CSPs with a gas turbine where steam inject (STIG) into the combustor, by replacing or supplementing the steam generators. This technique can increase the generated power and increase the solar share [16, 17], and using this configuration does not need a high temperature from CSP. Moreover, depending on the compression ratio of the gas turbine, STIG can use simple and less expensive CSP technology such as parabolic trough, with saturation steam temperature in a range of 200–300°C. However, the STIG cycle needs water, and the water would be lost if not captured at the turbine exhaust. Solar energy is plentiful in sites where water is scarce and therefore the water consumption of the solar STIG cycle must be addressed. Therefore, preheating the air before in CSP straight to a Brayton cycle, which uses less water, is the proper option [18, 19, 20, 21].

Areas with high sun irradiation levels are most suited for solar thermal power facilities. These characteristics are prevalent in the majority of coastal and southern Saharan regions of Libya, and they are dominated by a large-scale Mediterranean climate with average annual levels of irradiation of (1600–1800kWh/m²) [22], which are quite suitable for practical applications. The Southern region of Libya has a high potential for CSP operation, namely, the Sunbelt region which offers excellent conditions for various commercial applications [8] within a direct normal irradiation (DNI) higher than 2000kWh/m² per year. There are several power plants in the south of Libya and large industrial projects such as petrol fields. Due to the water scarcity in the region, all currently operational power facilities employ gas turbines, such as the one in the Asrir field. However, in terms of cost and safety, fuel transportation is one of the major challenges. In addition to fuel cost, it is acknowledged that the annual cost of fuel transportation is also large; therefore, this work aims to study the incorporation of hybrid solar gas turbine in order to evaluate the potential of reducing the fuel consumptions. A power plant that is currently in operation, which is located close to the Sahara Desert, Ubari power plant was selected as a case study. The region offers outstanding conditions of CSPs rollout, namely: very high DNI, and a large amount of free flat land [23]. The Ubari power plant is located around 700 km from the Zawiya Refinery that feeds it the diesel, where the petroleum brings from the El-Sharara oil field. The Ubari power plant consists of four gas turbine units with a total capacity of 640 megawatts [24], the design power of each unit is 160MW. Figure 1 displays the monthly global horizontal and diffuse radiation for the region under study; the maximum radiation and minimum radiation correspond to July and December, respectively. Figure 2 shows the sunshine duration each month receives, June and July have the highest sunshine period, averaging more than 12 hours per day.

The concept behind the proposed system is to use concentrated solar power technology to harness solar radiation to heat up the air leaving the compressor before it enters the combustion chamber when the weather is sunny. As a result, the air itself is used as the working substance in the receiver instead of another working liquid. The operation temperature of the proposed technology (central receivers) is about 800 degrees Celsius, where the air goes through the tubes inside the receiver that heat up by a field of mirrors, which focus the rays of the Sun onto the receiver.

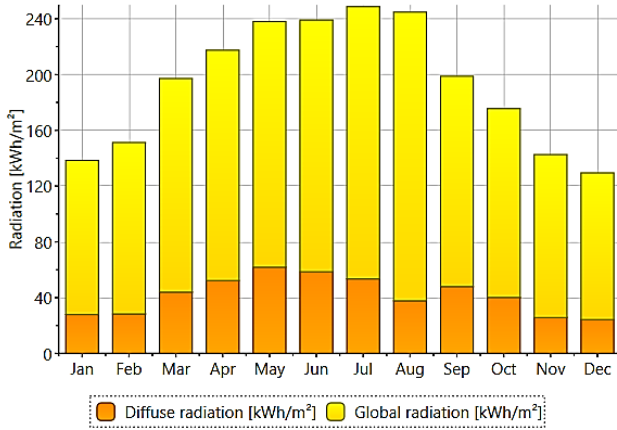


Figure 1. Daily global horizontal irradiation and normal direct irradiation of Ubari [25].

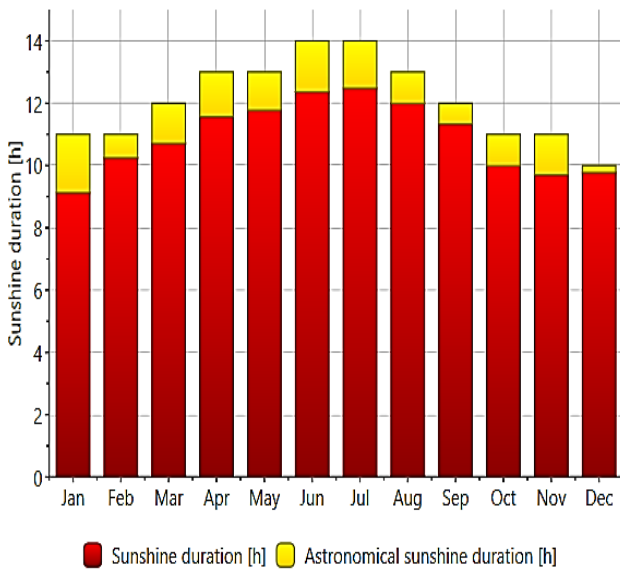


Figure 2. Average daily sunshine duration of Ubari region [25].

The variable nature of the solar flux means that the solar heat input to the gas-turbine is not constant, but varies with current meteorological conditions. In order to maintain a constant temperature at the entrance of the turbine, the fuel-flow to the combustion chamber is continuously controlled. An example of the operation of a hybrid solar gas-turbine is shown in Figure 3. The relative distribution of the heat input to the gas-turbine cycle depends upon the available solar flux. During daytime, heat from the solar sub-system can be harnessed by the gas-turbine, partly (or completely) replacing the heat input from fuel combustion and fuel flow to the combustion chamber decreases below the nominal value. Despite the drop in fuel flow, the combination of solar and fuel heat input provides the required nominal heat input to the gas-turbine, maintaining nominal electricity production. At night-time, the operation of the power plant continues in pure fossil-fuel mode. As such it is important to maintain high overall conversion efficiency for the power plant. If the power block efficiency is low, high carbon emissions during cloud passages and night-time operation can outweigh any savings achieved during solar operation. The present study aims to address the potential of incorporating concentrated solar power systems. The thermodynamic calculations of the selected power cycle were made using algebraic operations; and the feasibility of fulfilling the energy required in the combustion chamber

with the CSPs system was also analyzed. The System Advisor Model environment (SAM) [26], which has an embedded module of the TRNSYS environment, to examine the performance and economic viability of solar units can be utilized solely as a tool to estimate the thermal energy delivered to the solar receiver. However, SAM software is not equipped to handle a gas-cooled solar receiver and the associated power block (i.e., a Brayton Cycle). As such, any economic predictions are invalid, due to the many differences between gas and steam turbines and solar receivers. SAM will be used to calculate the optimal solar field layout, which can then be used to calculate the solar field size, thermal power and air temperature delivered to the power cycle on an hourly basis over the year.

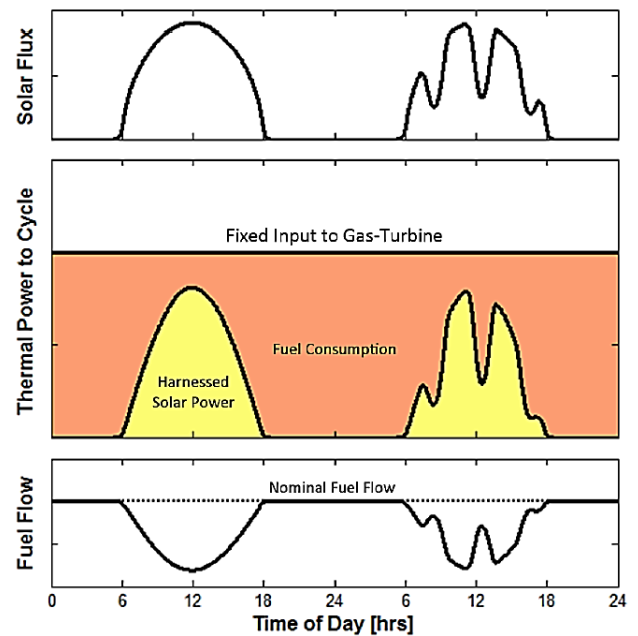


Figure 3. Operation of hybrid solar gas-turbine [27].

2. Mathematical model

For the electricity generation from the concentrated solar power systems, the thermal energy received at the solar field is required to be converted by an appropriate power cycle. The thermodynamic characterization was conducted along with the thermodynamic properties (P , T , v , h , s), which are determined for the operating state points of the cycle based on algebraic equations describing the power cycle and the solar field as depicted in Figure 4.

The ambient atmospheric temperature and pressure used for the compressor inlet are 25°C and 1atm , respectively, and the outlet pressure is calculated based on the design pressure ratio. The exergy balance at each state point is given as follows:

$$\dot{E}_x = \dot{m} * \left[(h_{out} - h_{in}) - T_0 \left(S_{out} - S_{in} - R \ln \left(\frac{P_{out}}{P_{in}} \right) \right) \right] \quad (1)$$

where h is the enthalpy, S is the entropy generation, which measures the irreversibilities generated during a process, \dot{E}_x is the exergy, and \dot{m} is mass flow, except at the chamber combustion, a mixture of air/fuel is considered.

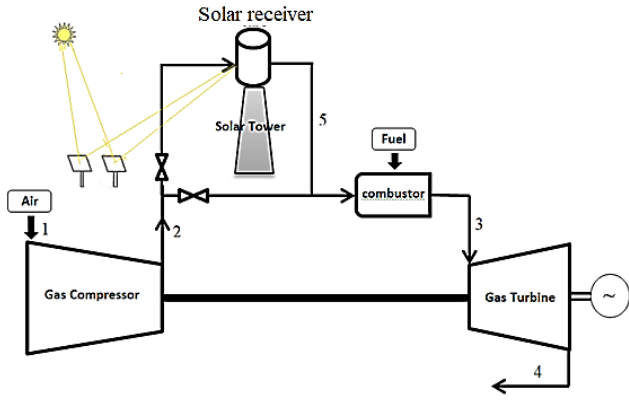


Figure 4. Sub-components of the hybrid solar gas-turbine unit.

It is possible to identify crucial information and understanding of subjects where significant advancements could be made by characterizing the utilization of energy resources in society in terms of exergy by the use of effective technologies, such as more effective energy resource conversions. In principle, the exergy matter can be determined by bringing it to the dead state by means of reversible processes. The thermodynamic analysis of the power cycle uses the net output thermal capacity as the objective function in the optimization process. The components associated with the cycle were analyzed under the assumption of steady-flow. The model is structured to define the properties at each state point of the cycle depicted in Figure 2 and then, sequentially, to determine energy, exergy, efficiency and irreversibility for each power cycle component. The energy and exergy balance are given as follows:

$$T_2 = \left(\frac{P_2}{P_1}\right)^{(k-1)/k} T_1 \quad (2)$$

$$\dot{W}_{comp} = \dot{m}_{air} * (h_1 - h_2) \quad (3)$$

$$\dot{E}_{x,1} = \dot{m}_{air} * \left[(h_1 - h_0) - T_0 \left(S_1 - S_0 - R \ln \left(\frac{P_1}{P_0} \right) \right) \right] \quad (4)$$

$$\dot{E}_{x,2} = \dot{m}_{air} * \left[(h_2 - h_0) - T_0 \left(S_2 - S_0 - R \ln \left(\frac{P_2}{P_0} \right) \right) \right] \quad (5)$$

$$\dot{E}_{xD,comp} = \dot{E}_{x,2} - \dot{E}_{x,1} - \dot{W}_{comp} \quad (6)$$

where \dot{E}_{xD} the exergy destruction.

$$\eta_{II,com} = \frac{\dot{E}_{x,2} - \dot{E}_{x,1}}{|\dot{W}_{comp}|} \quad (7)$$

$$\dot{W}_{Turbine} = \dot{m}_{gas} (h_3 - h_4) \quad (8)$$

$$\dot{E}_{x,3} = \dot{m}_{gas} * \left[(h_3 - h_0) - T_0 \left(S_3 - S_0 - R \ln \left(\frac{P_3}{P_0} \right) \right) \right] \quad (9)$$

$$\dot{E}_{x,4} = \dot{m}_{gas} * \left[(h_4 - h_0) - T_0 \left(S_4 - S_0 - R \ln \left(\frac{P_4}{P_0} \right) \right) \right] \quad (10)$$

$$\dot{E}_{xD,turbine} = \dot{E}_{x,3} - \dot{E}_{x,4} - \dot{W}_{Turbine} \quad (11)$$

$$\eta_{II,Turbine} = \frac{\dot{W}_{Actual,Turbine}}{\dot{E}_{x,3} - \dot{E}_{x,4}} \quad (12)$$

The thermal efficiency gauges the extent to which the energy input to the working fluid passing through the combustor is converted to mechanical output. Its determination is calculated as follows:

$$\dot{W}_{net} = \dot{W}_{Turbine} - \dot{W}_{com} \quad (13)$$

$$\dot{Q}_{in} = \dot{m}_{gas} (h_3 - h_5) \quad (14)$$

$$\eta_{I,Total} = \frac{\dot{W}_{net}}{\dot{Q}_{in}} \quad (15)$$

The quantity of heat gained by the combustion chamber \dot{Q}_{in} may come just from fuel combustion when the sun is not present, or it may come from both the burning of fuel and thermal energy from the solar field when sufficient solar radiation is available. The combustor operates at a steady state steady flow with no heat transfer with the surrounding. The specific exergy of the fuel at environmental conditions reduces to chemical exergy, which can be written as [28, 29]:

$$\varepsilon_{fuel} = \gamma_{fuel} H_{fuel} \quad (16)$$

where ε_{fuel} is the fuel specific exergy, γ_{fuel} the exergy grade function, and H_{fuel} the higher heating value of the fuel. Table 1 reported the higher heating value, chemical exergy, and fuel exergy grade function of different fuels, namely, natural gas and diesel [29].

Table 1. Ratio of fuel chemical exergy to lower heating value.

Fuel	H_{fuel} (kJ/kg)	ε_{fuel} (kJ/kg)	γ_{fuel}
Diesel	39500	42265	1.07
Natural Gas	55448	51702	0.93

All values of the exergy grade function are close to unity. Consequently, the common practice in such cases is to assume that the exergy of the fuel is approximately equal to the higher heating value [28]. The combustor operates at steady state steady flow with no heat transfer with the surrounding.

$$\dot{E}_{x,fuel} = \dot{m}_{fuel} \varepsilon_{fuel} \quad (17)$$

$$\dot{E}_{xD,combustion} = \dot{E}_{x,fuel} + \dot{E}_{x,2} - \dot{E}_{x,3} \quad (18)$$

$$\eta_{II,Total} = \frac{\dot{W}_{net}}{\dot{E}_{x,fuel} + \dot{E}_{x,5}} \quad (19)$$

The cost rate of exergy destruction of fuel \dot{C}_{fuel} (\$/h) is calculated based on the specific exergetic cost (SPECOC) method, as follows [30]:

$$\dot{C}_{fuel} = c_{fuel} \dot{E}_{x,fuel} \quad (20)$$

where c_{fuel} is the fuel cost rate per unit exergy (\$/kW-h). The objective of the steady-state combustion chamber model is to calculate the nominal mass flow of fuel required to drive the gas-turbine. The composition of the combustor

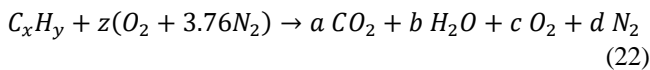
outlet gases must also be determined. The following assumptions have been used for the model of the combustor:

- Complete combustion occurs.
- No thermal losses from the combustion chamber.
- The water content of the combustion air is negligible.

The required mass flow of fuel can be determined by a simple energy balance in the combustion chamber. The energy released during the combustion of the fuel must be sufficient to heat the air by the solar field to reach the desired combustor outlet temperature. The mixture of air and fuel entering the combustor produces gas at a flow rate equal to the sum of the air and fuel, as determined by the following equation, with a fixed nominal pressure drop of 4% [27].

$$\dot{m}_{gas} = \dot{m}_{air} + \dot{m}_{fuel} \quad (21)$$

The combustion reaction with a hydrocarbon fuel and air is modeled using Eq. (22) [31], in which the fuel (typically natural gas) is considered a generic hydrocarbon. The minimum amount of air that supplies sufficient oxygen for the complete combustion of carbon, hydrogen, and any other elements in the fuel, which may oxidize is called theoretical air. When complete combustion is achieved with theoretical air, the products contain no oxygen. The assumption that air is 21% oxygen and 79% nitrogen by volume leads to the conclusion that for each mole of oxygen, $79/21 = 3.76$ moles of nitrogen are involved.



This amount of air is equal to 100% theoretical air ($c=0$) [31], in fact, complete combustion is not likely to be reached unless the amount of air supplied is somewhat bigger than the theoretical amount ($c>1$). With the coefficients to the substances called stoichiometric coefficients, the balance of atoms yields the theoretical air amount. Two important components frequently used to measure the ratio of fuel and air is the air/fuel ratio (AF) or the fuel/air ratio (FA) [32]. These ratios are usually expressed on a mass basis, and which can be on a mole basis. The quantities of fuel and air in a given combustion process are typically determined using these parameters. The amount of air in reaction to the amount of fuel is what is known as the air-fuel ratio.

$$AF_{mass} = \frac{m_{air}}{m_{fuel}} = AF_{mole} \frac{M_{air}}{M_{fuel}} \quad (23)$$

where m denotes mass and M denotes moles.

The total enthalpy and entropy of a product gas mixture at the combustion chamber are expressed as given [31]:

$$h = \sum n_i h_i \quad (24)$$

$$s = \sum n_i s_i - R \sum n_i \ln n_i \quad (25)$$

where n_i = moles of gas i . The model layout is representative of a utility-scale hybrid solar power plant, in which the large size of the power block requires the gas-turbine to remain at the base of the tower. Only radiation

losses are significant at high temperatures was assumed for the model of the solar receiver. The basic energy balance at a solar receiver was taken into consideration the solar heat input to the receiver, the useful thermal power extracted Q_{useful} , and the rate of heat loss. For the receiver energy balance can be expressed using Eq. (26) [27], where $Q_{received}$ is the thermal power collected by the solar receiver.

$$Q_{useful} = Q_{received} - Q_{loss} \quad (26)$$

$$Q_{loss} = A_r \epsilon_r \sigma \left(\left(\frac{T_2 + T_5}{2} \right)^4 - T_o^4 \right) \quad (27)$$

where, Q_{useful} is the thermal power delivering to the power cycle, σ is the Stefan-Boltzmann and $Q_{received}$ can be used to estimate the solar field size using the following equation:

$$Q_{received} = \eta_{opt} \alpha_r DNI . N_h . A_h \quad (28)$$

where A_r is receiver area, A_h is the heliostat area, N_h is the number of heliostats in the field, η_{opt} is the optical efficiency of the receiver, and the absorptivity and emissivity of the volumetric absorber, α_r and ϵ_r respectively. The optical efficiency of the receiver considers the effects of the quartz glass cover that maintains the pressure within the receiver. Higher operating pressures require thicker glass, which reduces the optical efficiency due to higher reflection and absorption at the glass window; this effect is considered in Eq. (29). The reference values for the operating pressure and optical efficiency are presented in [27], their values are 6.5 bar and 87%, respectively.

$$\log(\eta_{opt}) = \frac{P_2}{P_{ref}} \log(\eta_{opt}^{ref}) \quad (29)$$

The pressure losses with the receiver modules are estimated using Eq. (30) based on the mass flux Gr within the receiver, the operating pressure and the mean temperature within the receiver. Reference values are presented in [27], with a reference pressure drop of 40mbar, a reference mass flux G_{ref} of 1.063kg/m²s, and a reference mean temperature of 700°C [27].

$$\frac{\Delta p_{receiver}}{\Delta p_{ref}} = \frac{G_r^{ref} P_{ref}}{G_r P_2} \left(\frac{T_2 + T_5}{2 T_{mean}^{ref}} \right) \quad (30)$$

3. Results

The simulation was carried out at full load and the nominal design conditions are presented in Table 2. The variable nature of the solar flux means that the solar heat input to the gas turbine is not constant, but varies with current meteorological conditions. In order to maintain a constant temperature at the entrance of the turbine, the fuel flow to the combustion chamber is continuously controlled. The relative distribution of the heat input to the gas-turbine cycle depends upon the available solar flux. During the daytime, heat from the solar sub-system can be harnessed by the gas turbine, partly (or completely) replacing the heat input from fuel combustion and fuel flow to the combustion chamber decreases below the nominal value. Despite the drop in fuel flow, the combination of solar and fuel heat input provides the required nominal heat input to the gas turbine, maintaining nominal electricity production. At night-time, the operation of the power plant continues in pure fossil-fuel mode.

Table 2. Nominal design parameters.

Parameter	Amount
Design electric power	160 MW
Generator efficiency	85%
Turbine efficiency	90%
Air volume flow rate	427 m ³ /s
The reference state of air	25°C, 1.013bar
Compressor pressure ratio	10

The first simulation was carried out for a sample Brayton cycle without solar integration. Table 3 reports the stream state points' derived thermodynamics characteristics data, where the outcomes of the energetic and exergetic analysis are listed in Table 4, and Table 5 reported the flow rates of air, fuel and gas, which computed at the nominal parameters.

Table 3. Stream data for the power cycle.

S. ID	state	Temperature (C)	Pressure (kPa)	Enthalpy (kJ/kg)	Entropy (kJ/kg K)
1	Air	25	101.3	307.5	6.89
2	Air	249.4	1013	526.5	6.768
3	Fuel Gas	1000	1013	1364	6.587
4	Gases	588.9	102.8	890.8	6.796

Table 4. Energetics and exergetics of the power cycle components.

Components	Energetic MW	Exergetic input MW	Exergetic output MW
Compressor	105.85 (work)	64.8	218.8
Combustion	414.4 (heat)	690.2	683.7
Turbine	234.1 (work)	683.7	6.9

Table 5. Cycle parameters obtained at nominal conditions.

Variables	Amount	Units
\dot{W}	144	MW
\dot{m}_{air}	483.4	kg/s
\dot{m}_{fuel}	11.22	kg/s
\dot{m}_{gases}	494.7	kg/s
η_{cycle}	32.6	%

In conclusion, the average amount of energy needed to be delivered at the combustor is 414.4MW. The fuel mass flow rate is 11.22kg/s, the energetic thermal efficiency of the power cycle is 32.6% and the gross power output is 144MW, respectively. The second part aims to address the analysis of the solar systems; an accurate and comprehensive study of the performance and behavior of solar energy systems and their components; is required to conduct an hourly analysis on an annual basis. The reference of collected thermal power to be delivered by the solar receiver to the power block is considered based on the combustor energy presented in Table 4 (414MW_{th}).

The selection of the design thermal power is depended on two components, namely, optical solar field efficiency and solar multiple. The ratio of the thermal power generated by the solar field at the design point to the thermal power needed by the power cycle under nominal conditions is known as the solar multiple. High SM values without thermal storage function result in thermal energy overproduction that cannot be used to generate electricity. For solar-only systems like the present investigation, the SM is always bigger than one in order to maintain the power cycle's nominal conditions for a longer period of time than would be the case if the solar multiple were equal to one [33]. However, thermal energy overproduction can be useful only if a thermal energy storage system is used, otherwise, like the present study, economically no need to

employ a high value of SM that increases the size of the solar field, which raises costs and necessitates the need for larger land. As the solar multiple increases, the marginal cost of extending nominal receiver operation increases exponentially because the cost of the solar field is generally proportional to the solar multiple. Therefore, the design thermal power calculated for this analysis is 532MW_{th} based on solar multiple equal to 1.28 [33].

Then, SAM is utilized in this study solely as a tool to estimate the thermal power produced by the solar field. SAM can calculate the optimal heliostat field layout, which can then be used to calculate the total power delivered to the solar receiver on an hourly basis for the entire year. Table 6 reported the solar field geometrical and optical parameters and specifications used in the present investigation optimized by SAM environment, where SM, thermal power design and DNI are 1.28, 532MW_{th} and 1000 W/m², respectively. Figures 5 presented the daily average of air temperature collected by the receiver that leaves the solar field to the power cycle for each month. Figure 6 reported daily average of the received thermal power and useful thermal power delivered to the power cycle. The value of zero indicates that gas backup is now being used in place of solar heat flux. These results of the SAM simulation can be extracted into a data file for further calculations and analyses.

It can be noted that the solar share ranges between 6 hours in winter (December) to 12 hours in the summer (June) over the year. The useful thermal power that sends to power cycle varies between around 300MW_t on December and 415MW_t in July. Achieved temperature varies between around 650°C in the winter and 800°C in the summer.

Table 6. Geometrical and optical parameters for the solar field.

Solar Multiple	1.28
Design point DNI	1000 W/m ²
Thermal power design	532 MW _{th}
Heliostat width	12.2 m
Heliostat height	12.2 m
Tower height	187 m
Receiver material type	Stainless ASI316
Receiver tube outer diameter	40 mm
Receiver heat loss factor	1

Figure 7 demonstrated the hourly data based on an annual average profile of receiver optical and thermal efficiencies. Thermal efficiency is known as the ratio of received energy to useful energy, and its impact on the outcomes of Figure 6 is evidently proportional. Table 7 reported the first and second efficiencies for the model, fuel mass rate, The cost rate of exergy destruction of fuel, and exergy destruction rate, respectively, variation with the air temperature entering the combustor. As expected, the thermal energy efficiency is increased by raising the temperature of the air before it enters the combustion chamber, and the fuel rate is decreased, therefore, the air mass flow rate entering the combustion is decreased. The exergy destruction rate is decreased with the increase in the air temperature entering the combustor. The fuel cost per unit exergy is selected based on the Baghernejad et al. study [30], 0.012\$/MJ-h; the fuel cost rate decreased with the increase in the air temperature entering the combustion chamber.

For the solar sole scenario (no combustion), the range of the prediction air temperature produced by the solar system

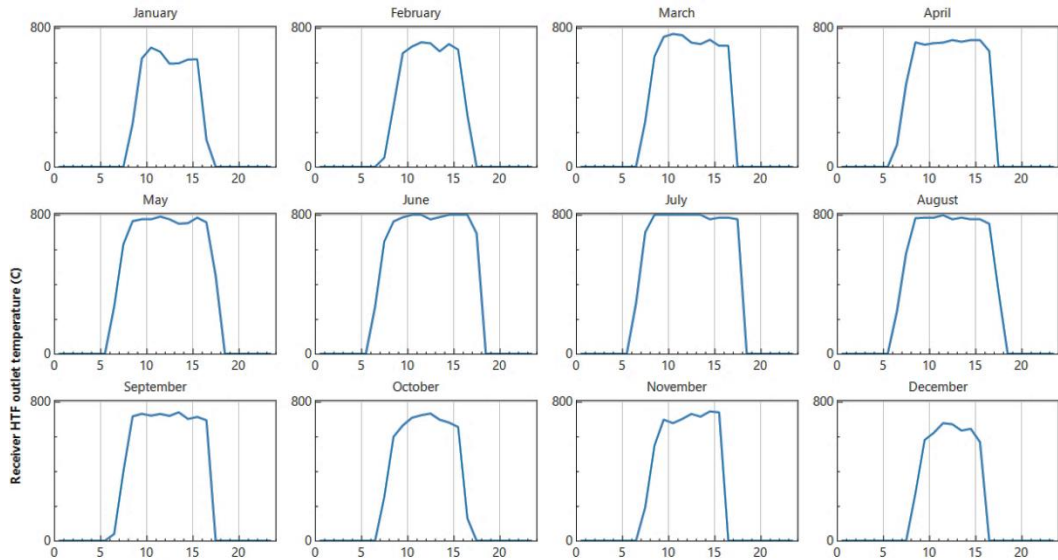


Figure 5. Solar field outlet temperature.

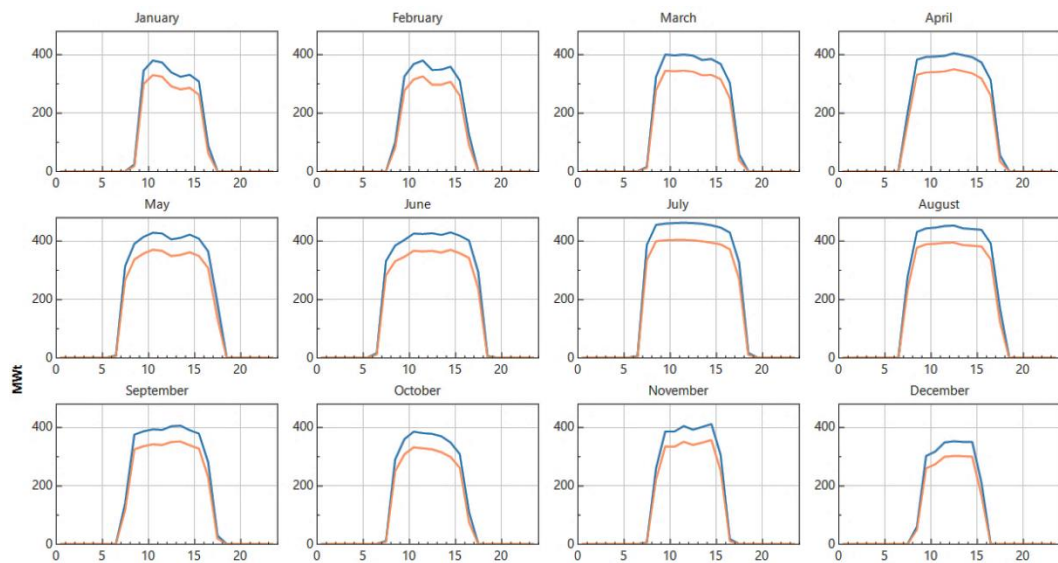


Figure 6. Solar field received (Blue) and useful thermal power (Orange).

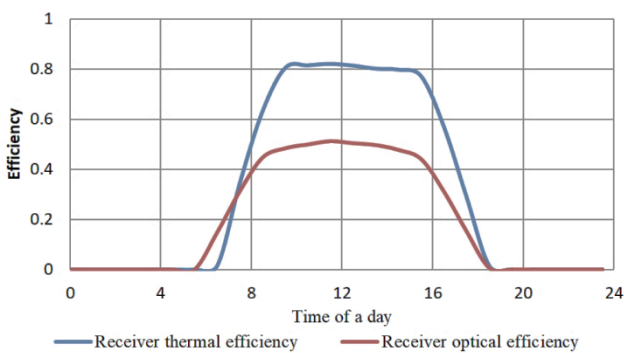


Figure 7. Annual average profile of the solar receiver's optical efficiency.

that enters the turbine is depending on the available solar flux, in particular produced air temperature. To generate 144MW (Design) at 750°C, the air flow rate is found equal to 430 kg/s. Therefore, for the solar sole scenario at varying air temperature that delivered by the solar field directly to the turbine, Figure 8 shows how the power cycle electricity output varies with air temperature inlet the turbine at different flow rates. The equilibrium between the air flow rate and solar heat flux is crucial for maintaining the air at

the highest temperature. It can be noted that when the air temperature produced by solar field is high (750°C) (solar only case study), the air mass flow (≈ 430 kg/s) is less than the design flow rate.

Table 7. Combustion temperature inlet variation with various results.

$T_{\text{comb, inlet}}$ °C	\dot{C}_{fuel} \$/h	$\dot{E}_{x, \text{comb}}$ MW	\dot{m}_{air} kg/s	\dot{m}_{Fuel} kg/s	η_I	η_{II}
250	20350	20.35	482	11.2	0.326	0.301
300	19082	19.08	452	10.5	0.334	0.308
350	17801	17.80	421	9.81	0.344	0.316
400	16506	16.51	391	9.10	0.354	0.325
450	15197	15.19	360	8.37	0.367	0.336
500	13874	13.87	328	7.64	0.382	0.349
550	12537	12.54	297	6.91	0.401	0.366
600	11186	11.19	265	6.16	0.424	0.387
650	9823	9.82	232	5.41	0.454	0.413
700	8447	6.17	200	4.65	0.494	0.449
750	7059	6.15	167	3.89	0.549	0.498

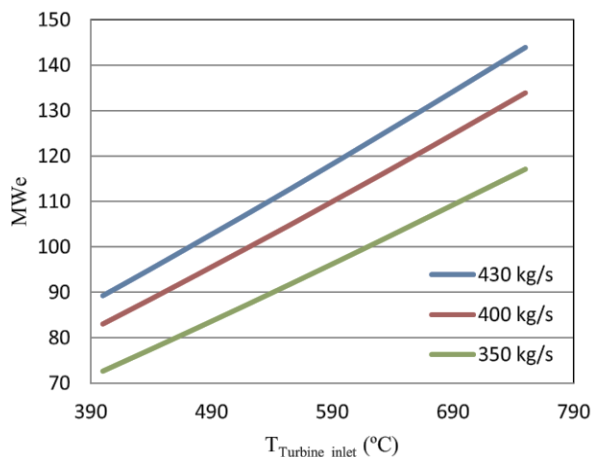


Figure 8. Variation in electricity production with turbine inlet air temperature for various air flows.

4. Conclusion

The potential of incorporating concentrated solar power systems with gas turbine was investigated considering the Ubari power plant. The main objective is to reduce the high operating and transportation costs for petroleum in the southern part of Libya, and therefore, to reduce the environmental harm that fuel causes. Analysis of the straightforward Brayton power cycle without solar function was carried out, and the conclusions were used as a design guide for the design and analysis of the solar field. The simulation was carried out at full load; the variable nature of the solar flux means that the solar heat energy delivered to the power cycle is not constant, and varies with current meteorological conditions. In order to maintain a constant temperature at the turbine inlet, the fuel flow to the combustion chamber is continuously controlled. The combustor heat energy required is 414.4MW and the air/fuel ratio is 43; the energetic thermal efficiency of the power cycle is 32.6% and the gross power output is 144MW. An hourly analysis based on an annual basis was simulated within the SAM environment. However, SAM software is not equipped to handle a gas-cooled solar receiver and the associated power cycle, therefore, SAM is utilized in this study solely as a tool to estimate the thermal energy collected by the solar receiver and the actual energy delivered to the power cycle. The designed system can deliver the required energy in about 6 hours in winter (December) and 12 hours in the summer (June). The fuel flow rate and fuel cost associated with exergy destruction are used to assess the economic approach. The analysis presented that by increasing the combustor inlet air temperature, the power cycle efficiency is increased and the fuel mass rate is decreased. The fuel cost rate can be minimized by increase combustor inlet air temperature. The use of sole solar energy requires a big storage system and a huge land, and it does not fulfill its goal during the winter. Therefore, the use of a hybrid solar gas turbine design to use less gas might be the most effective and cost-effective solution; where employing sole gas turbines requires the use and transportation of fuel, which is expensive and harmful to the environment.

Nomenclatures

A Area
 c The cost rate per unit exergy
 \dot{C} The cost rate of exergy destruction
 DNI Direct normal irradiation

\dot{E}_x Exergy
 \dot{E}_{xD} Exergy destruction
 G Mass flux
 h Enthalpy
 H The higher heating
 i Gas type
 M Moles
 m Mass
 \dot{m} Mass flow rate
 n Moles of gas
 N_h Number of Heliostats
 P Pressure
 Q Thermal energy
 s Entropy
 S Entropy generation
 T Temperature
 W Work

Greek symbols

α Absorptivity
 η Efficiency
 ε Emissivity
 ε The fuel specific exergy
 γ The exergy grade function
 σ The Stefan-Boltzmann

Abbreviations

h Heliostats
 o Atmosphere
 opt Optical
 r Receiver
 ref Reference
 SM Solar multiple

References:

- [1] I. A. S. Ehtiwesh, F. Neto Da Silva, and A. C. M. Sousa, "Deployment of parabolic trough concentrated solar power plants in North Africa – a case study for Libya," *Int. J. Green Energy*, Oct. 2018, doi:10.1080/15435075.2018.1533474.
- [2] I. A. S. Ehtiwesh, M. C. Coelho, and A. C. M. Sousa, "Exergetic and environmental life cycle assessment analysis of concentrated solar power plants," *Renew. Sustain. Energy Rev.*, vol. 56, pp. 145–155, 2016, doi:10.1016/j.rser.2015.11.066.
- [3] M. Muñoz and J. Muñoz-ant, "Comparison of Different Technologies for Integrated Solar Combined Cycles: Analysis of Concentrating Technology and Solar Integration," *MDPI, Energies*, 2018, doi:10.3390/en11051064.
- [4] H. Derbal, S. Bouaichaoui, N. El-Gharbi, M. Belhamei, and A. Benzaoui, "Modeling and numerical simulation of an integrated solar combined cycle system in Algeria," *Procedia Eng.*, vol. 33, pp. 199–208, Jan. 2012, doi.org/10.1016/j.proeng.2012.01.1194.
- [5] A. Al Hariri, S. Selimli, and H. Dumrul, "Effectiveness of heat sink fin position on photovoltaic thermal collector cooling supported by paraffin and steel foam: An experimental study," *Appl. Therm. Eng.*, vol. 213, no. June, p. 118784, 2022, doi:10.1016/j.applthermaleng.2022.118784.
- [6] A. Abdel Dayem, M. Metwally, A. Alghamdi, and E.

- Marzouk, "Numerical simulation and experimental validation of integrated solar combined power plant," *Energy Procedia*, vol. 50, pp. 290–305, 2014, doi.org/10.1016/j.egypro.2014.06.036.
- [7] A. Poullikkas, "Economic analysis of power generation from parabolic trough solar thermal plants for the Mediterranean region - A case study for the island of Cyprus," *Renew. Sustain. Energy Rev.*, vol. 13, no. 9, pp. 2474–2484, Dec. 2009, doi.org/10.1016/j.rser.2009.03.014.
- [8] M. Mashena and N. Alkishriwi, "Concentrated Solar Power Potential in Libya," *JASE*, vol. 11, no. 1, pp. 56–72, 2017.
- [9] B. Belgasim, Y. Aldali, M. J. R. Abdunnabi, G. Hashem, and K. Hossin, "The potential of concentrating solar power (CSP) for electricity generation in Libya," *Renew. Sustain. Energy Rev.*, vol. 90, no. March, pp. 1–15, 2018, doi:10.1016/j.rser.2018.03.045.
- [10] T. E. Boukelia, M. S. Mecibah, B. N. Kumar, and K. S. Reddy, "Optimization, selection and feasibility study of solar parabolic trough power plants for Algerian conditions," *Energy Convers. Manag.*, vol. 101, pp. 450–459, 2015, doi:10.1016/j.enconman.2015.05.067.
- [11] I. Ehtiwesh, F. Neto da Silva, and A. Sousa, "Performance and economic analysis of concentrated solar power plants in Libya," in *2nd International Conference on Energy and Environment: bringing together Engineering and Economics*, 2015, pp. 459–66.
- [12] M. Balghouthi, S. E. Trabelsi, M. Ben Amara, A. B. H. Ali, and A. Guizani, "Potential of concentrating solar power (CSP) technology in Tunisia and the possibility of interconnection with Europe," *Renew. Sustain. Energy Rev.*, vol. 56, pp. 1227–1248, 2016, doi:10.1016/j.rser.2015.12.052.
- [13] O. M. J. Jasim, S. Selimli, H. Dumrul, and S. Yilmaz, "Closed-loop aluminium oxide nanofluid cooled photovoltaic thermal collector energy and exergy analysis, an experimental study," *J. Energy Storage*, vol. 50, no. April, pp. 1–9, 2022, doi:10.1016/j.est.2022.104654
- [14] B. A. A. Yousef *et al.*, "Perspective on integration of concentrated solar power plants," no. April, pp. 1098–1125, 2021.
- [15] K. Kitzmiller, "Effect of Variable Guide Vanes and Natural Gas Hybridization for Accommodating Fluctuations in Solar Input to a Gas Turbine," vol. 134, no. November 2012, pp. 1–12, 2016, doi:10.1115/1.4006894.
- [16] M. Livshits and A. Kribus, "Solar hybrid steam injection gas turbine (STIG) cycle," *Sol. Energy*, vol. 86, no. 1, pp. 190–199, 2012, doi:10.1016/j.solener.2011.09.020.
- [17] G. Polonsky and A. Kribus, "Performance of the solar hybrid STIG cycle with latent heat storage," *Appl. Energy*, vol. 155, pp. 791–803, 2015, doi:10.1016/j.apenergy.2015.06.067.
- [18] F. Moreno-gamboa, A. Escudero-atehortua, and C. Nieto-londoño, "Performance evaluation of external fired hybrid solar gas-turbine power plant in Colombia using energy and exergy methods," *Therm. Sci. Eng. Prog.*, vol. 20, no. August, 2020, doi:10.1016/j.tsep.2020.100679.
- [19] K. Mohammadi, K. Ellingwood, and K. Powell, "Novel hybrid solar tower-gas turbine combined power cycles using supercritical carbon dioxide bottoming cycles," *Appl. Therm. Eng.*, p. 1-48, 2020, doi:10.1016/j.applthermaleng.2020.115588.
- [20] P. Schwarzbo, R. Buck, C. Sugarmen, A. Ring, P. Altwegg, and J. Enrile, "Solar gas turbine systems : Design , cost and perspectives," vol. 80, pp. 1231–1240, 2006, doi:10.1016/j.solener.2005.09.007.
- [21] B. Ssebabi, F. Dinter, J. Van Der Spuy, and M. Schatz, "Predicting the performance of a micro gas turbine under solar-hybrid operation," *Energy*, vol. 177, pp. 121–135, 2019, doi:10.1016/j.energy.2019.04.064
- [22] U. Desideri, F. Zepparelli, V. Morettini, and E. Garroni, "Comparative analysis of concentrating solar power and photovoltaic technologies: Technical and environmental evaluations," *Appl. Energy*, vol. 102, pp. 765–784, 2013, doi.org/10.1016/j.apenergy.2012.08.033
- [23] I. Ehtiwesh, "Exergetic , energetic , economic and environmental evaluation of concentrated solar power plants in Libya," PhD thesis, University of Aveiro, 2016, doi:http://ria.ua.pt/handle/10773/15882.
- [24] "GECOL to resume work at Ubari power plant project | The Libya Observer." [Online]. Available: <https://www.libyaobserver.ly/inbrief/gecol-resume-work-ubari-power-plant-project>.
- [25] M. Genossenschaft, "Meteonorm7 Software," *METEOTEST Genossenschaft*, <https://meteonorm.com>
- [26] National Renewable Energy Laboratory (NREL), "System Advisor Model (SAM 2022.12.2 r3 (SSC 280))." <https://sam.nrel.gov/download>.
- [27] J. Spelling, "Hybrid Solar Gas-Turbine Power Plants, A Thermo-economic Analysis," KTH Royal Institute of Technology - School of Industrial Engineering and Management, Doctoral Thesis, 2013.
- [28] I. Dincer, "Renewable energy and sustainable development: a crucial review," *Renew. Sustain. Energy Rev.*, vol. 4, no. 2, pp. 157–175, 2000.
- [29] A. Al-Ghandoor, I. Al-Hinti, B. Akash, and E. Abu-Nada, "Analysis of energy and exergy use in the Jordanian urban residential sector," *Int. J. Exergy*, vol. 5, no. 4, pp. 413–428, 2008, doi:10.1504/IJEX.2008.019113.
- [30] A. Baghernejad and A. Anvari-moghaddam, "Exergoeconomic and environmental analysis and multi-objective optimization of a new regenerative gas turbine combined cycle," *Appl. Sci.*, vol. 11, no. 23, 2021, doi:10.3390/app112311554.
- [31] M. Moran, H. Shapiro, D. Boettner, and M. Bailey, *Fundamentals of engineering thermodynamics*, Seven Edit. John Wiley & Sons, Inc., 2011.
- [32] C. Borgnakke and R. Sonntag, *Fundamentals of Thermodynamics*, Seventh. John Wiley & Sons, Inc., 2009.

[33] M. Montes, A. Abánades, J. Martínez-Val, and M. Valdés, “Solar multiple optimization for a solar-only thermal power plant, using oil as heat transfer fluid in

the parabolic trough collectors,” *Sol. Energy*, vol. 83, no. 12, pp. 2165–2176, Dec. 2009, doi.org/10.1016/j.solener.2009.08.010

Research Article

Phase Transition Thermodynamic Properties Of 2-Methylquinoline, 2-Chloroquinoline And 2-Phenylquinoline

^{1*} R. S. Abdullah , ²B. N. Solomonov 

^{1,2}Department of Physical Chemistry, Butlerov Institute of Chemistry, Kazan Federal University, Kremlevskaya str. 18, Kazan 420008, Russia

¹Department of Chemistry, College of Science, Salahaddin University-Erbil, Erbil, Kirkuk road, 44002, Iraq
E-mail: ^{1*}rawandabdullah34@gmail.com

Received 12 February 2023, Revised 13 April 2023, Accepted 1 July 2023

Abstract

Derivatives of quinoline are widely utilized in both industries and in healthcare. To understand the quinolines' quality and stability in usage, it is crucial to study their phase transition chemical thermodynamic characteristics. In this work, the phase transition thermodynamic characters of 2-methylquinoline (quinaldine), 2-chloroquinoline, and 2-phenylquinoline were investigated. Moreover, the sublimation/vaporization enthalpy of the compounds were determined the solution calorimetry-additivity scheme approach at 298.15 K. The solution calorimetry was applied to measure solution enthalpies of the compounds in benzene solvent at 298.15 K. While, the solvation enthalpy of the compounds were calculated additivity scheme approach. In addition, the transpiration method applied to estimate vapor pressure to temperature dependency to 2-Chloroquinoline. In consequence, the vapor pressure values with respect to temperature variation was determined to 2-Chloroquinoline compound for the first time. As a result, the phase transition chemical thermodynamic properties; enthalpy, entropy, and Gibbs energy for 2-methylquinoline, 2-chloroquinoline and 2-phenylquinoline were determined from crystalline/liquid to gas phase. Furthermore, in this work the thermochemical characteristics values of the studied compounds exhibited higher accuracy to those in literature data. Finally, the phase transition thermodynamically studied on 2-position of the quinoline compound, where it substituted to methyl, chloro and phenyl groups.

Keywords: *Quinoline derivatives; sublimation/vaporization enthalpy; solvation enthalpy; solution calorimetry; additive scheme approach; transpiration method; Gibbs energy; entropy.*

1. Introduction

Quinoline derivative compounds have many applications in both medicine and industry [1]. In medicine, due to their antibacterial properties, quinoline derivatives were utilized in the manufacturing of drugs for the treatment of influenza B-Mass virus [2]. Additionally, the quinolines have been used to treat diseases including cancer, malaria, and anti-inflammatory illnesses [3], [4], antidotes against poisoning, antidiabetic activities and antiviral HCV [5]. In the light of industry, the quinoline compounds have been applied in production electro-optical display devices [6] and researching studies to magnetic properties, [7] photochemistry, [8] materials science, solution studies, and homogeneous catalysis owing to the versatility of their steric and electronic properties [9].

Due to mentioned implementations quinoline derivative compounds, it is necessary to study phase transition thermochemistry to use the quinolines in right way. Therefore, phase transition thermodynamics quinolines studying is essential. Phase transition of the compounds means transfer in chemical phase and properties. By the way, it makes drugs and devices are unusable or poisoned, where they were made from the quinolines, in another word, it has been expired. Thus, the phase transition thermochemical

properties of the basic compounds (quinolines) in drugs and in devices are detected quality and stability drugs and manufacture devices.

The thermodynamic properties of phase transition presents energy transfer (enthalpy, entropy and Gibbs free energy (in this work)) of a chemical compound from its standard state (liquid or crystalline) to gas phase at constant temperature and 0.1 MPa pressure. The enthalpy of evaporation (sublimation/vaporization) of a chemical compound is a phase transition thermodynamics property was measured directly by calorimetric methods [10], [11] or indirectly from determination vapor pressure as a function to temperature [12], [13]. As consequence, the solution calorimetry was employed to determine the evaporation enthalpy of various compounds in specific solvents from solution enthalpy and solvation enthalpy values as estimated in previous works [14], [15], [16]–[20]. In this method, the solution enthalpy of the chemical compounds was measured solution calorimetry at standard temperature and solvation enthalpy the compounds in same solvent was established additivity scheme approach at 298.15 K [21]–[23]. Solution calorimetry technique was applied in obtaining enthalpy of sublimation/vaporization of the compounds as from following equation;

$$\Delta_{cr,liq}^g H_m^{Ai} = \Delta_{soln} H_m^{Ai/Bz} - \Delta_{solv} H_m^{Ai/Bz} \quad (1)$$

Where, $\Delta_{cr,liq}^g H_m^{Ai}$ is the sublimation/vaporization enthalpy of chemical compound Ai, $\Delta_{soln} H_m^{Ai/Bz}$ is the solution enthalpy of chemical compound Ai in benzene solvent and $\Delta_{solv} H_m^{Ai/Bz}$ is the solvation enthalpy of Ai compound in benzene solvent. The solvation enthalpy of the compounds were worked out additive scheme approach at 298.15 K (in detail described from section 3.2).

In addition, transpiration method as indirect method was applied to estimate sublimation/vaporization enthalpy to the chemical compounds. The transpiration method has been used in measuring vapor pressure to temperature dependency. From data, vapor pressure to temperature relation values of the studied compound will establish chemical thermodynamic properties, according to the following equation;

$$R \ln(P_t/P_0) = -\frac{\Delta_{cr,liq}^g G_m^0}{T_0} + \Delta_{cr,liq}^g H_m^0 \left(\frac{1}{T_0} - \frac{1}{T} \right) + \Delta_{cr,liq}^g C_{p,m}^0 \left(\frac{T_0}{T} - 1 + \ln \left(\frac{T}{T_0} \right) \right) \quad (2)$$

Where P_t saturated vapor pressure at T temperature, P_0 is the standard vapor pressure, T_0 is the standard temperature (298.15 K), $\Delta_{cr,liq}^g G_m^0$ Gibbs energy of evaporation, $\Delta_{cr,liq}^g C_{p,m}^0$ evaporation heat capacity. Then, the value of entropy of phase transition ($\Delta_{cr,liq}^g S$) of the compound could be measure as from following equation;

$$\Delta_{cr,liq}^g S = \Delta_{cr,liq}^g H/T \quad (3)$$

Consequently, the chemical thermodynamic characters were measured through equations used from vapor pressure to temperature correlation data from the transpiration method.

The phase transition of the chemical thermodynamic properties distinguish the stability and quality of drugs and devices were manufactured from chemical compounds. Especially, the phase transition thermodynamic properties; enthalpy, Gibbs energy and entropy. In this work, the thermochemical properties were estimated for the compounds 2-methylquinoline, 2-chloroquinoline and 2-phenylquinoline. As from figure (1) (chemical structure) the studied compounds are heterocyclic aromatic compounds where substituted at two-cite of the quinoline compound.

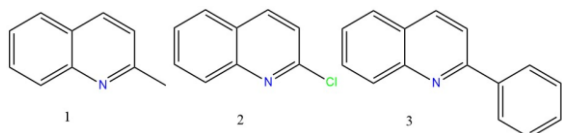


Figure 1. Chemical structure of the quinolines. 1) 2-methylquinoline, 2) 2-chloroquinoline, 3) 2-phenylquinoline.

Furthermore, the solution calorimetry-additive scheme approach and the transpiration method were applied in this work to determine the phase transition thermochemical properties of the studied compounds. The evaporation enthalpy was determined at 298.15 K to the three compounds solution calorimetry-additivity scheme approach. Besides, the thermochemical properties study of phase transition on

these compounds were also investigated from transpiration method.

2. Experimental Part

2.1 Materials

The quinoline derivatives are commercial origin materials. The quinoline solute compounds were in high mass fraction purity, the purity percent were more than 97% (table 1), in solution calorimetry the quinoline compounds were dissolved in benzene solvent. The benzene solvent was local commercial origin. Additionally, the benzene solvent was purified by standard methods [24], [15] through fraction distillation. Hence, the fraction mass purity of the solvent was raised to 99 %, gas chromatography GC Agilent 7820 A was tested.

Table 1. CAS number, origin and purity of the quinolines.

Compound	CAS	Origin	Purity %
2-Methylquinoline	91-63-4	Alfa Aesar	97+
2-Chloroquinoline	612-62-4	SIGMA-ALDRICH	99
2-Phenylquinoline	612-96-4	ACROS ORGANICS	99+

2.2 Solution Calorimetry

Enthalpy of solution quinoline compounds was measured with commercial TAM III solution calorimetry (TA Instruments, USA). First, small amount of a quinoline derivative compound (Quinaldine (2-methylquinoline), 2-Chloroquinoline or 2-phenylquinoline) was dissolved in the benzene solvent to get infinite dilution solution into the solution calorimetry glass cell. Furthermore, there are used two standard compounds with respect the state of the materials (crystalline and liquid) to measure solution enthalpy in solution calorimetry technique at 298.15 K. Moreover, the crystalline compound, first it was grinded to make like powder substance then weighted about 500 mg and it was dissolved into the glass cell, which it contained about 90 mL of the solvent. While, the liquid samples, small portions of the liquid compound between 50-300 μ L were injected electronically by operated syringe connected with long gold cannula immersed into the solvent [14][15].

First, the solution calorimetry was calibrated up on using standard crystalline and liquid compounds. The standard crystalline compound was potassium chloride. The KCl standard crystalline was dissolved in a purified water (distilled twice and deionized) into the calorimetry cell, its solution enthalpy at 298.15 was 17.475 ± 0.08 kJ.mol⁻¹, and in the literature, solution enthalpy of KCl was 17.205 kJ.mol⁻¹ at same temperature [25]. Identically, to the liquid compounds, the calorimetry was tested by propan-1-ol as standard liquid solute in the purified water and the value solution enthalpy was -10.16 ± 0.05 kJ.mol⁻¹ as well as the propanol-1 solution enthalpy value in the literature was -10.18 ± 0.03 kJ.mol⁻¹ [26]. Therefore, the values of solution enthalpies of our standards were well agree with the literature values.

2.3 Transpiration Method

Vapor pressure was measured over the liquefied compound of 2-chloroquinoline as a function to temperature through the transpiration method. First, about 0.5 g of the sample was mixed with glass beads and placed into the U-tube thermostatic at constant temperature ± 0.1 K. Then, the amount of the evaporated compound into the thermostat tube at a definite temperature carried out by Nitrogen gas flow stream with known rate and specific amount of time. After that, the sample condensed into the second cooling part tube.

The amount of condensed compound m_i was measured by the gas chromatography at each temperature with respect to an organic standard liquid compound. The nitrogen flow stream in a definite flow rate passed through the tube at selected temperature T_i . Definitely, the amount of saturated vapor pressure of the sample condensed in the cold trap was measured at definite time to know the volume V_{N_2} transported nitrogen gas at the specific rate according to general gas law, the procedure described elsewhere [12], [15], [27], [28] [29].

$$p_i = m_i \cdot R \cdot T_a / (V \cdot M_i) \quad (4)$$

Where; $V = V_{N_2} + V_i = (n_{N_2} + n_i) \cdot R \cdot T_a / P_a$

Where V is the volume of the gas phase consisting of the n_{N_2} moles of the carrier gas and n_i mole of gaseous compound under study at the atmospheric pressure P_a and the ambient temperature T_a . The volume of the carrier gas V_{N_2} was calculated through a digital flow rate microcontroller. The digital flow rate sensor was worked in an uncertainty at the level of 2.5 %. The flow rate of the nitrogen stream was also controlled by using soap bubble flow pipette and optimized in order to reach the saturation equilibrium of the transporting gas at each temperature under study. The volume of the carrier gas V_{N_2} read from the calibrated digital flow rate sensor.

3. Results and Discussion

Enthalpy of sublimation/vaporization (evaporation) is the enthalpy transfer of a compound from its standard state (crystalline or liquid) to gaseous phase at constant temperature and pressure 0.1 MPa. Solution calorimetry-additivity scheme approach and transpiration method were applied to measure the evaporation enthalpy to the three compounds substituted quinolines (2-methylquinoline, 2-chloroquinoline and 2-phenylquinoline) at 298.15 K. In addition, the other thermochemical properties of the compounds were estimated to the studied compounds. Accordingly, the chemical thermodynamic properties have been found to 2-chloroquinoline compound from transpiration method in this work and for the other compounds the properties were collected in the literature data. The quinoline derivative compounds chemical thermodynamic characters are established the stability and thermochemical energy of the compounds from standard state to gas phase as well as the impact of substituted groups at 2-position of the quinoline compound. Consequently, the stability and quality of the drugs and the devices, which made from the studied quinolines, could be known.

Hence, the evaporation enthalpy of the studied compounds was measured by the solution calorimetry-additive scheme approach and the transpiration methods at 298.15 K. Then, from solution calorimetry-additive scheme approach was determined the vaporization/sublimation enthalpy for quinoline derivatives according to equation (1).

While, the solution enthalpy was determined directly from the solution calorimetry at 298.15 K in benzene solvent and the solvation enthalpy was calculated by additivity scheme approach.

3.1 Solution Enthalpy

Solution enthalpy is the enthalpy of a compound in standard state (solid or liquid) to dissolve in solvent to make a solution infinite dilute solution at standard temperature and pressure 0.1 MPa. Solution enthalpy was determined directly from solution calorimetry at 298.15 K for the studied compounds. Moreover, according to the solution enthalpy values (table 2) indicate that all three compound exist the endothermic heat affect when dissolve in the benzene solvent. Furthermore, the low value solution enthalpy 2-methylquinoline due to the methyl group attached to the quinoline compound and the interaction with the benzene solvent as well as it is in liquid state. While, the solution enthalpy values 2-chloroquinoline and 2-phenylquinoline were close to each other because they are in crystalline state, the solution enthalpy values contain destroy crystalline lattice then process heat of solvation.

3.2 Solvation Enthalpy

Solvation enthalpy is the transfer enthalpy of a compound from gaseous state to a solvent to make a solution of infinite dilution at standard temperature and pressure 0.1 MPa. The solvation enthalpy is another phase transition chemical thermodynamic character indicates the solubility heat effect of compound. In this work, the solvation enthalpy was calculated to the three quinolines with respect to additivity scheme approach [15], [21], [22], [30]. According to the additive scheme approach, the solvation enthalpy was estimated.

Solvation enthalpy was calculated for the quinoline (as heterocyclic compound);

$$\Delta_{\text{solv}} H^{\text{ArXi}/S} = \Delta_{\text{solv}} H^{\text{ArH}/S} + \sum \Delta_{\text{solv}} H^{\text{Xi} \rightarrow \text{CH}/S} \quad (5)$$

Where $\Delta_{\text{solv}} H^{\text{ArXi}/S}$ is the solvation enthalpy of quinoline compound in solvent S , $\Delta_{\text{solv}} H^{\text{ArH}/S}$ is the solvation enthalpy of the naphthalene compound (removed nitrogen atom into the quinoline ring) in the solvent S and $\Delta_{\text{solv}} H^{\text{Xi} \rightarrow \text{CH}/S}$ is the solvation enthalpy of the substituted group with CH, it means azo group into the quinoline compound in solvent S . As notify, the solvents S must be same solvent to all components of a compound.

In addition, the solvation enthalpy of quinoline with attached group was measured as following equation;

$$\Delta_{\text{solv}} H^{\text{ArXi}/S} = \Delta_{\text{solv}} H^{\text{ArH}/S} + \Delta_{\text{solv}} H^{\text{Xi}/S} \quad (6)$$

Where $\Delta_{\text{solv}} H^{\text{ArXi}/S}$ is the solvation enthalpy of the substituted quinoline compounds ArXi in solvent S , $\Delta_{\text{solv}} H^{\text{ArH}/S}$ is solvation enthalpy of the compound without

Table 2. The values of solution enthalpy, solvation enthalpy and evaporation enthalpy in $\text{kJ} \cdot \text{mol}^{-1}$ at 298.15 K.

Compound	$-\Delta_{\text{solv}} H_m^{\text{Al/Bz}}^b$	$\Delta_{\text{soln}} H_m^{\text{Al/Bz}}^c$	$\Delta_{\text{liq,cr}}^g H_m^a$
2-Methylquinoline	63.8	1.45	65.25 ± 0.13
2-Chloroquinoline	66.4	21.21	87.61 ± 0.89
2-Phenylquinoline	82.68	19.92	108.0 ± 0.04

^a the values of standard uncertainty were calculated from standard deviation of repeating experiments of the solution calorimetry in this work. ^b the values were calculated from equations (5), (6) and (7). ^c the values were measured from solution calorimetry technique in this work.

any attached group (quinoline in this work) in solvent S , $\Delta_{solv}H^{Xi/S}$ is solvation enthalpy of the branched group (methyl, chloro and phenyl in this study) in the same solvent. Notably, the S solvent must be the same to all parts of the study compound [15].

Thereupon, solvation enthalpy was measured to 2-methylquinoline and 2-chloroquinoline. After that, the evaporation enthalpy for the two compounds was obtained. In another hand, the equation (7) was used in calculation enthalpy of solvation for 2-Phenyl quinoline compound, because the 2-phenyl quinoline compound didn't obey to the two above equations due to high deviation of the solvation enthalpy value. Therefore, the 2-phenyl quinoline compound has three aromatic rings and it was estimated as poly aromatic compound with respect to the additive scheme approach [19], as from following equation;

$$\Delta_{solv}H^{2PQ/Bz} = n. 1/6. \Delta_{solv}H^{Bz/Bz} + 1.08 . Y \quad (7)$$

Where $\Delta_{solv}H^{2PQ/Bz}$ is the solvation enthalpy of 2-phenylquinoline in benzene solvent, $\Delta_{solv}H^{Bz/Bz}$ is solvation enthalpy of benzene in benzene solvent, n is the number of carbon atoms and Y is the difference between carbon and hydrogen atoms. Consequently, the solvation enthalpy value for the 2-phenylquinoline compound was $-82.68 \text{ kJ.mol}^{-1}$ (table 2).

3.3 Evaporation Enthalpy

The sublimation/vaporization enthalpy was determined for 2-methyl quinoline, 2-chloro quinoline and 2-phenyl quinoline in applying the solution calorimetry-additivity scheme approach at standard temperature. Uniquely, the sublimation/vaporization enthalpy values in this work were in high accuracy observed the solution calorimetry at 298.15 K according to equations (mentioned above) with respect to standard uncertainty values. In addition, to establish values from solution calorimetry-additivity scheme approach of the 2-chloroquinoline and because it had only one literature value on its thermochemical properties (sublimation enthalpy), therefore, the thermochemical properties were determined through the transpiration method. In this method, the thermodynamic parameters were indirectly calculated in relation between temperature and saturated vapor pressure values of the studied compound.

First, determination of the heat capacity by vapor pressure to temperature dependency applying the Clausius-Clayperon equation, as shown below;

$$R \ln p_i = a + \frac{b}{T} + \Delta_{liq,cr}^g C_{p,m}^o \ln \left(\frac{T}{T_o} \right) \quad (8)$$

Where R is the general gas constant ($8.31447 \text{ J.mol}^{-1}.\text{K}^{-1}$), p_i is vapor pressure of compound i , a and b are adjustable constants, $\Delta_{liq,cr}^g C_{p,m}^o$ is molar heat capacity change of a compound from liquid or crystalline state to the gaseous phase at constant pressure and standard temperature, and T , T_o are selected temperature and reference temperature (298.15 K) respectively. Then, enthalpy of evaporation was measured, where, expressed below and adjusted to reference temperature 298.15 K ;

$$\Delta_{cr,liq}^g H^{Ai} = -b + \Delta_{liq,cr}^g C_{p,m}^o \times T \quad (9)$$

From equation (9), it is possible to determine the enthalpy of sublimation/vaporization of the studied compound, knowing the constant b and the change in heat capacity from the solid or liquid state to the gas phase at temperature T .

Moreover, the molar heat capacity phase transition the three compounds were calculated from Acree, Jr. and S. Chickos estimation equations for liquid and crystalline states respectively [31];

$$\Delta_{liq}^g C_{p,liq} = 10.58 + 0.26 C_{p,liq} \quad (10)$$

$$\Delta_{cr}^g C_{p,cr} = 0.75 + 0.15 C_{p,cr} \quad (11)$$

Therefore, from value molar heat capacity change and constant b at T temperature was measured the vaporization enthalpy for 2-chloroquinoline;

To confirm the sublimation enthalpy value of 2-chloroquinoline because only one value was found. Therefore, the vapor pressure to temperature dependency, vaporization/sublimation enthalpy, entropy change and Gibbs energy change values were determined by transpiration method in this work for the 2-chloroquinoline compound at the selected temperature and at suitable nitrogen flow rate to obtain the amount of evaporated vapor over the sample (table 3). Vapor pressure to temperature relation data over 2-chloroquinoline was measured for the first time and its thermochemical properties at reference temperature 298.15 K were determined temperature [29]. The uncertainties of vaporization/ sublimation enthalpies combined in literature values assessed. Additionally, the transpiration method uncertainties measurements were described in detail elsewhere [32].

Table 3. Vapor pressure of liquefied 2-Chloroquinoline from transpiration method.

$$\ln(p/p^\circ) = \frac{249.39}{R} - \frac{73847.58}{RT} - \frac{48.8}{R} \ln \frac{T}{298.15}$$

$$\Delta_{liq}^g H_{298.15 \text{ K}} = 66.76 \pm 0.55 \text{ kJ.mol}^{-1}$$

T_m , K	m , mg	$V(N_2)$, L	Gas-flow, $L.hr^{-1}$	P , Pa	$\Delta_{liq}^g H_{Tm \text{ K}}$ kJ.mol^{-1}	$\Delta_{liq}^g S_{Tm}$ $\text{J.K}^{-1}.\text{mol}^{-1}$
313.4	2.40	8.721	4.19	4.19	66.02	126.9
319.5	2.53	5.233	4.19	7.35	65.72	126.6
328.8	2.28	2.428	4.16	14.34	65.27	125.0
331.1	2.81	2.428	4.16	17.65	65.16	125.0
335.7	3.05	1.953	4.19	23.48	64.93	120.7
339.3	3.11	1.535	4.19	30.87	64.76	121.7
340.2	2.28	1.047	4.19	33.23	64.71	121.4
343.0	2.49	0.986	1.69	38.48	64.58	122.0
345.6	2.09	0.704	1.69	45.23	64.45	122.5
348.9	2.06	0.563	1.69	55.87	64.29	122.9
351.7	2.47	0.563	1.69	66.92	64.15	123.7
353.4	2.74	0.563	1.69	74.11	64.07	123.7
357.4	2.59	0.423	1.69	93.31	63.87	124.0

According to the vapor pressure to temperature values, the 2-Chloroquinoline enthalpy of vaporization value was $66.76 \pm 0.55 \text{ kJ.mol}^{-1}$ at reference temperature (298.15 K) because the compound has been liquefied then evaporated into the thermostat tube then it condensed after that the condensed state measured through gas chromatography method. Furthermore, with respect to the works [22], [33] the solution enthalpy (crystalline form, 2-Chloroquinoline) approximately equal to the fusion enthalpy $\Delta_{cr}^{liq} H^{Ai}$ at fusion temperature for the same compound. Consequently, sublimation enthalpy $\Delta_{cr}^g H_m^0$ for 2-Chloroquinoline was evaluated, following equations;

$$\Delta_{cr}^g H_m^0 = \Delta_{cr}^{liq} H^{Ai} + \Delta_{liq}^g H_m^0 \quad (12)$$

Where; $\Delta_{soln} H_{298.15 \text{ K}} \approx \Delta_{cr}^{liq} H^{Ai}$,

$$\text{Then, } \Delta_{cr}^g H_m^0 = \Delta_{soln} H_{298.15 \text{ K}} + \Delta_{liq}^g H_m^0 \quad (13)$$

Therefore, the sublimation enthalpy values 2-Chloroquinoline from solution calorimetry-additivity scheme approach and the transpiration method were $87.61 \pm 0.89 \text{ kJ.mol}^{-1}$ and $87.97 \pm 0.55 \text{ kJ.mol}^{-1}$ at 298.15 K respectively. While, the value of sublimation enthalpy for 2-Chloroquinoline by the microcalorimetry method was $84.3 \pm 2.6 \text{ kJ.mol}^{-1}$ [34] with higher uncertainty (standard deviation) than the values were obtained in this work (table 4). Hence, our values of sublimation enthalpy are higher accuracy (lower standard deviation). Besides, the sublimation enthalpy value of 2-Phenylquinoline was $108.0 \pm 0.04 \text{ kJ.mol}^{-1}$ in solution calorimetry-additivity scheme approach. In addition, it was compared with the literature average value was $104.8 \pm 2.2 \text{ kJ.mol}^{-1}$, when it was done by Knudsen mass-loss effusion method with higher uncertainty [27] than the value was observed in this work. The sublimation enthalpy difference between our method and the literature value where estimated by Knudson-mass loss effusion method was 3.57 kJ.mol^{-1} however, it agrees with

each other when compare uncertainty values. Likewise, vaporization enthalpy 2-methylquinoline in this work by solution calorimetry method was $65.25 \pm 0.13 \text{ kJ.mol}^{-1}$ at 298.15 K and vaporization enthalpy of same compound at 298 K in microcalorimetry method was $66.1 \pm 1.9 \text{ kJ.mol}^{-1}$ well agree with the value in this work. While, the other values of vaporization enthalpy didn't agree with our value due to they were measured in higher temperature like, in reference [35] the enthalpy was measured in temperature range 319-553 and applied Ebulliometry method, however, adjusted to reference temperature.

3.4 Gibbs Free Energy And Entropy of Phase Transition

Gibbs energy and entropy of the phase transition were estimated for the studied compounds at temperature 298.15 K (table 5). The Gibbs energy of the phase transition of the compounds from liquid or crystalline state to the gas phase were generally no favorably changed. Moreover, the highest value of the Gibbs energy was $44.3 \pm 0.04 \text{ kJ.mol}^{-1}$ for the 2-Phenylquinoline compound because it was in most stable crystalline state due to it has the maximum value of sublimation enthalpy. While, the minimum value of Gibbs energy was $13.36 \text{ kJ.mol}^{-1}$ was due to the chemical structure quinoline compound, where, it has not substituted group and it was in liquid state.

In another hand, the evaporation entropy values were obtained to quinoline and the substituted quinolines. The compounds of 2-Phenylquinoline and 2-Chloroquinoline were present maximum value of sublimation entropy because they were in crystalline state and they exist the highest values of sublimation enthalpy. Furthermore, the entropy of evaporation was determined at various temperature for 2-Chloroquinoline through the transpiration method. In consequence, the chemical thermodynamic parameters were evaluated and adjusted to the reference temperature 298.15 K.

In addition, the standard uncertainties values were combined in the transpiration method and in the solution calorimetry uncertainties where the vapor pressure and temperature uncertainties adjusted to the reference

Table 4. Various techniques to determine evaporation enthalpy.

Compound	M ^a	T/K	$\Delta_{liq,cr}^g C_{p,298 \text{ K}}^b$ J.K ⁻¹ .mol ⁻¹	$\Delta_{liq,cr}^g H_{298.15 \text{ K}}$ kJ.mol ⁻¹	$\Delta_{liq,cr}^g H_{T/K}^c$ kJ.mol ⁻¹	Ref.
Quinoline(liq) ^d	IPM,E	298–559			57.9 ± 0.1	[31]
	GS	298		58.1		[31]
	IPM,E	440			50.7 ± 0.1	[31]
	GC				53.3	[31]
	SC			63.59		This work
2-Methylquinoline(liq)	E	319–553			62.6 ± 0.1	[35]
	M	298		66.1 ± 1.9		[31]
	GS	281–313			61.2	[31]
	E	443–521			54.7	[31]
	SC	298.15		70.98	65.25 ± 0.13	This work
2-Chloroquinoline(cr)	CM	298.15			84.3 ± 2.6	[34]
	SC	298.15	26.64	87.61 ± 0.89		This work
	T	298.15		87.97 ± 0.55		This work
2-Phenylquinoline(cr)	KM	337–351			105.4 ± 0.9	[36]
	KM	337–351			103.1 ± 0.8	[36]
	KM	298.15		104.8 ± 2.2		[27]
	SC	298.15	36.81	108.0 ± 0.04		This work

^a methods, E= Ebulliometer, M=Microcalorimetric, V=vaporization method, GC= gas chromatography, GS =Gas saturation vaporization method, SC=Solution Calorimetry, CM= Calvet microcalorimetry, T= Transpiration method and KM=Knudsen mass-loss effusion. IPM= Inclined piston manometry. ^b the values were measured from estimation equation method (see text). ^c the values were calculated in literature data at mean temperature. ^d the quinoline compound was set just to comparison with the other compounds in this work.

Table 5. The thermodynamic properties of the quinolines.

Compound	$\Delta_{liq,cr}^g H_{298 K}^a$ kJ.mol ⁻¹	$\Delta_{liq,cr}^g G_{298 K}$ kJ.mol ⁻¹	$\Delta_{liq,cr}^g S$ J.K ⁻¹ .mol ⁻¹
Quinoline(liq)	58.1 ^e	13.36 ^g	150.05 ^f
2-Methylquinoline(liq)	65.25 ± 0.13	24.1 ± 0.03 ^d	126.8 ^d
2-Chloroquinoline(cr)	87.61 ± 0.89	28.1 ± 0.05 ^c	199.7 ± 1.9 ^c
2-Phenylquinoline(cr)	108.0 ± 0.04	44.3 ± 0.04 ^b	202.7 ± 2.7 ^b

^a values were measured by solution calorimetry-additive scheme method in this work (table 2). ^b values were determined from vapor pressure measurements [37]. ^c measured in this work by transpiration method. ^d according to Clark-Glaw equation from reference [38]. ^e from table 3. ^f the value was calculated from equation ($\Delta_{liq,cr}^g S_{298 K} = \Delta_{liq,cr}^g H_{298 K}/T_b$) T_b boiling point from reference [39]. ^g the value was calculated from equation: $\Delta_{liq,cr}^g G_{298 K} = \Delta_{liq,cr}^g H_{298 K} - (298.15 K) \cdot \Delta_{liq,cr}^g S_{298 K}$

In summing up, the evaporation enthalpy values studied compounds were determined from solution enthalpy values, which directly measured from solution calorimetry at 298.15 K. While, the solvation enthalpy values were calculated additivity scheme approach at standard temperature into the same solvent. Meanwhile, the evaporation enthalpy values were determined by solution calorimetry in high accuracy (lowest value of the standard deviation) for the three compounds of Quinaldine, 2-Chloroquinoline and 2-Phenylquinoline. In addition, the transpiration method was applied to determine vapor pressures to temperature dependency and the vaporization enthalpy of 2-Chloroquinoline was determined. Further, in the transpiration method calculated uncertainties of the thermochemical properties of vaporization enthalpy, free energy change and entropy change. By the way, the vaporization enthalpy of liquid 2-Chloroquinoline was modified to sublimation enthalpy without measuring fusion enthalpy instead used solution enthalpy of its solid state at temperature 298.15 K. The evaporation entropy from crystalline state to gas phase of 2-Chloroquinoline and 2-Phenylquinoline close to each other. However, the 2-Chloroquinoline and 2-Phenylquinoline considerably had high difference in their free energy change from solid state to gas phase due to the substituted groups of the chloro and phenyl.

4. Conclusion

Sublimation/vaporization enthalpy for the compounds Quinaldine (2-Methylquinoline), 2-Chloroquinoline, and 2-Phenylquinoline were determined using the solution calorimetry-additive scheme approach at 298.15 K. In addition, the chemical thermodynamic properties were established to studied compounds and the values were adjusted to the standard temperature. Accordingly, for the first time, vapor pressure over 2-Chloroquinoline to temperature dependence and other chemical thermodynamic properties were determined at various temperatures by the transpiration method. In the present study, the values evaporation enthalpies of the compounds were exist lower standard deviations in compare with those obtained in literature data. According to the three compounds were studied, comparatively the thermochemical properties were determined to 2-position substitution of quinolines in comparison to quinoline thermodynamic properties values where substituted to methyl, chloro and phenyl groups. Consequently, phase transition thermodynamic properties observed that the stability especially the energy require to evaporate the compounds as well as the amount of evaporation energy. In that case, the thermodynamic

characters indicate the quality and usable of the compounds in fields of medicine and industry.

Nomenclature

Bz	benzene solvent
C	heat capacity (is the amount of heat require to raise the temperature of a compound one degree)
cr	crystalline (standard state of the compound)
g	gas
G	Gibbs free energy in kJ
H	enthalpy in kJ
J	joule
k	kilo
K	kelvin
hr	hour unit
L	litter
liq	liquid
m	mass in mg
M	molecular mass
MPa	mega Pascal
P	pressure
R	general gas constant in (8.31447 kJ/(mol. K))
S	entropy in J
soln	solution
solv	solvation
T	temperature in K
V	volume
Δ	change or transfer state

References:

- [1] K. Li, T. Zou, Y. Chen, X. Guan, and C. Che, "Pincer-Type Platinum (II) Complexes Containing N-Heterocyclic Carbene (NHC) Ligand: Structures, Photophysical and Anion-Binding Properties, and Anticancer Activities," *Chem. Eur. J.*, vol. 21, no. 20, pp. 7441–7453, 2015, doi: 10.1002/chem.201406453.
- [2] M. Islamuddin, O. Afzal, W. H. Khan, M. Hisamuddin, A. S. A. Altamimi, I. Husain, K. Kato, M. A. Alamri, and S. Parveen, "Inhibition of Chikungunya Virus Infection by 4-Hydroxy-1-Methyl-3-(3-morpholinopropanoyl)quinoline-2(1 H)-one (QVIR) Targeting nsP2 and E2 Proteins," *ACS Omega*, vol. 6, no. 14, pp. 9791–9803, 2021, doi: 10.1021/acsomega.1c00447.
- [3] R. Pingaew, S. Prachayasittikul, and S. Ruchirawat, "Synthesis, Cytotoxic and Antimalarial Activities of Benzoyl Thiosemicarbazone Analogs of Isoquinoline and Related Compounds," *Molecules*, vol. 15, no. 2, 2010. doi: 10.3390/molecules15020988.
- [4] S. M. A. Hussaini, "Therapeutic significance of

- quinolines: a patent review (2013–2015),” *Expert Opin. Ther. Pat.*, vol. 26, no. 10, pp. 1201–1221, Oct. 2016, doi: 10.1080/13543776.2016.1216545.
- [5] A. A. Altaf, A. Shahzad, Z. Gul, N. Rasool, A. Badshah, B. Lal, and E. Khan, “A review on the medicinal importance of pyridine derivatives,” *J. Drug Des. Med. Chem.*, vol. 1, no. 1, pp. 1–11, 2015, [Online]. Available: doi: 10.11648/j.jddmc.20150101.11
- [6] G. Albrecht, C. Rössiger, J. M. Herr, H. Locke, H. Yanagi, R. Göttlich, and D. Schlettwein, “Optimization of the Substitution Pattern of 1, 3-Disubstituted Imidazo [1, 5-a] Pyridines and-Quinolines for Electro-Optical Applications,” *Phys. status solidi*, vol. 257, no. 5, p. 1900677, 2020, doi: 10.1002/pssb.201900677.
- [7] J. Qian, J. Hu, H. Yoshikawa, J. Zhang, K. Awaga, and C. Zhang, “External-Template-Assisted Formation of Octacyanometalate-Based MV–MnII (M= W, Mo) Bimetallic Coordination Polymers with Magnetic Properties,” *Eur. J. Inorg. Chem.*, vol. 2015, no. 12, pp. 2110–2119, 2015, doi: DOI: 10.1002/ejic.201403223.
- [8] A. Y. Tam, W. H. Lam, K. M. Wong, N. Zhu, and V. W. Yam, “Luminescent Alkynylplatinum (II) Complexes of 2, 6-Bis (N-alkylbenzimidazol-2'-yl) pyridine-Type Ligands with Ready Tunability of the Nature of the Emissive States by Solvent and Electronic Property Modulation,” *Chem. Eur. J.*, vol. 14, no. 15, pp. 4562–4576, 2008, doi: DOI: 10.1002/chem.200701914.
- [9] S. Günnaz, A. G. Gökçe, and H. Türkmen, “Synthesis of bimetallic complexes bridged by 2,6-bis(benzimidazol-2-yl) pyridine derivatives and their catalytic properties in transfer hydrogenation,” *Dalt. Trans.*, vol. 47, no. 48, pp. 17317–17328, 2018, doi: 10.1039/C8DT03178A.
- [10] L. M. P. F. Amaral and M. A. V. Ribeiro da Silva, “Calorimetric study of bromoacetophenone isomers,” *J. Chem. Thermodyn.*, vol. 78, pp. 254–259, 2014, doi: https://doi.org/10.1016/j.jct.2014.06.028.
- [11] A. L. R. Silva, Á. Cimas, and M. D. M. C. Ribeiro da Silva, “Energetic study of benzothiazole and two methylbenzothiazole derivatives: Calorimetric and computational approaches,” *J. Chem. Thermodyn.*, vol. 73, pp. 3–11, 2014, doi: https://doi.org/10.1016/j.jct.2013.06.021.
- [12] S. P. Verevkin and V. N. Emel’yanenko, “Transpiration method: Vapor pressures and enthalpies of vaporization of some low-boiling esters,” *Fluid Phase Equilib.*, vol. 266, no. 1, pp. 64–75, 2008, doi: https://doi.org/10.1016/j.fluid.2008.02.001.
- [13] A. Delle Site, “The vapor pressure of environmentally significant organic chemicals: a review of methods and data at ambient temperature,” *J. Phys. Chem. Ref. Data*, vol. 26, no. 1, pp. 157–193, 1997.
- [14] R. S. Abdullah, “Phase Transition Thermodynamics: Evaporation Enthalpy of 13 Naphthalene Derivatives,” *Russ. J. Phys. Chem. A*, vol. 97, no. 7, pp. 1361–1367, 2023, doi: 10.1134/S0036024423070245.
- [15] R. S. Abdullah and B. N. Solomonov, “Sublimation/vaporization and solvation enthalpies of monosubstituted pyridine derivatives,” *Chem. Thermodyn. Therm. Anal.*, vol. 8, p. 100087, Dec. 2022, doi: 10.1016/J.CTTA.2022.100087.
- [16] R. N. Nagrimanov, A. A. Samatov, T. M. Nasyrova, A. V. Buzyurov, T. A. Mukhametzyanov, C. Schick, B. N. Solomonov, and S. P. Verevkin, “Long-chain linear alcohols: Reconciliation of phase transition enthalpies,” *J. Chem. Thermodyn.*, vol. 146, p. 106103, 2020, doi: https://doi.org/10.1016/j.jct.2020.106103.
- [17] R. N. Nagrimanov, A. A. Samatov, A. V. Buzyurov, A. G. Kurshev, M. A. Ziganshin, D. H. Zaitsau, and B. N. Solomonov, “Thermochemical properties of mono- and di-cyano-aromatic compounds at 298.15 K,” *Thermochim. Acta*, vol. 668, pp. 152–158, 2018, doi: https://doi.org/10.1016/j.tca.2018.07.026.
- [18] B. N. Solomonov, M. A. Varfolomeev, R. N. Nagrimanov, T. A. Mukhametzyanov, and V. B. Novikov, “Enthalpies of solution, enthalpies of fusion and enthalpies of solvation of polyaromatic hydrocarbons: Instruments for determination of sublimation enthalpy at 298.15K,” *Thermochim. Acta*, vol. 622, pp. 107–112, 2015, doi: https://doi.org/10.1016/j.tca.2015.10.020.
- [19] B. N. Solomonov, R. N. Nagrimanov, and T. A. Mukhametzyanov, “Additive scheme for calculation of solvation enthalpies of heterocyclic aromatic compounds. Sublimation/vaporization enthalpy at 298.15K,” *Thermochim. Acta*, vol. 633, pp. 37–47, 2016, doi: https://doi.org/10.1016/j.tca.2016.03.031.
- [20] B. N. Solomonov, M. I. Yagofarov, and R. N. Nagrimanov, “Additivity of vaporization enthalpy: Group and molecular contributions exemplified by alkylaromatic compounds and their derivatives,” *J. Mol. Liq.*, vol. 342, p. 117472, 2021, doi: https://doi.org/10.1016/j.molliq.2021.117472.
- [21] B. N. Solomonov, M. A. Varfolomeev, R. N. Nagrimanov, V. B. Novikov, A. V. Buzyurov, Y. V. Fedorova, and T. A. Mukhametzyanov, “New method for determination of vaporization and sublimation enthalpy of aromatic compounds at 298.15 K using solution calorimetry technique and group-additivity scheme,” *Thermochim. Acta*, vol. 622, pp. 88–96, 2015, doi: 10.1016/j.tca.2015.09.022.
- [22] B. N. Solomonov, R. N. Nagrimanov, M. A. Varfolomeev, A. V. Buzyurov, and T. A. Mukhametzyanov, “Enthalpies of fusion and enthalpies of solvation of aromatic hydrocarbons derivatives: Estimation of sublimation enthalpies at 298.15K,” *Thermochim. Acta*, vol. 627–629, pp. 77–82, 2016, doi: https://doi.org/10.1016/j.tca.2016.02.001.
- [23] M. I. Yagofarov, R. N. Nagrimanov, and B. N. Solomonov, “Thermochemistry of phase transitions of aromatic amines: Estimation of the sublimation enthalpy at 298.15K through the fusion enthalpy,” *J. Chem. Thermodyn.*, vol. 113, pp. 301–307, 2017, doi: https://doi.org/10.1016/j.jct.2017.06.017.
- [24] W. L. F. Armarego and C. L. L. Chai, “Purification of organic chemicals,” *Purif. Lab. Chem.*, vol. 7, pp. 103–554, 2009.
- [25] H. Li, X. Chen, and F. Guo, “Enthalpy of solution for thiourea in triglycol and water,” *Russ. J. Phys. Chem. A*, vol. 84, no. 13, pp. 2259–2261, 2010, doi:

- 10.1134/S0036024410130091.
- [26] E. V Ivanov, V. K. Abrosimov, and V. I. Smirnov, "Enthalpies of solution of 1,1,3,3-tetramethylurea in normal and branched alkanols (C2–C4) at 298.15K," *J. Chem. Thermodyn.*, vol. 39, no. 12, pp. 1614–1619, 2007, doi: <https://doi.org/10.1016/j.jct.2007.04.008>.
- [27] S. P. Verevkin, S. P. Safronov, A. A. Samarov, and S. V. Vostrikov, "Hydrogen Storage: Thermodynamic Analysis of Alkyl-Quinolines and Alkyl-Pyridines as Potential Liquid Organic Hydrogen Carriers (LOHC)," *Appl. Sci.*, vol. 11, no. 24, 2021, doi: [10.3390/app112411758](https://doi.org/10.3390/app112411758).
- [28] A. A. Zhabina, R. N. Nagrimanov, V. N. Emel'yanenko, B. N. Solomonov, and S. P. Verevkin, "Nicotinamides: Evaluation of thermochemical experimental properties," *J. Chem. Thermodyn.*, vol. 103, pp. 69–75, 2016, doi: <https://doi.org/10.1016/j.jct.2016.08.002>.
- [29] R. N. Nagrimanov, D. H. Zaitsau, R. S. Abdullah, A. V. Blokhin, and B. N. Solomonov, "Thermochemistry of formation and phase transitions of substituted thiophenes at 298.15 K," *J. Chem. Thermodyn.*, vol. 186, p. 107123, 2023, doi: <https://doi.org/10.1016/j.jct.2023.107123>.
- [30] A. A. Samatov, R. N. Nagrimanov, E. A. Miroshnichenko, and B. N. Solomonov, "Vaporization/sublimation enthalpies of mono- and dimethyl-esters estimated by solution calorimetry method," *Thermochim. Acta*, vol. 685, p. 178529, 2020, doi: <https://doi.org/10.1016/j.tca.2020.178529>.
- [31] W. Acree Jr and J. S. Chickos, "Phase transition enthalpy measurements of organic and organometallic compounds. Sublimation, vaporization and fusion enthalpies from 1880 to 2015. Part 1. C1–C10," *J. Phys. Chem. Ref. Data*, vol. 45, no. 3, p. 33101, 2016, doi: [10.1063/1.4948363](https://doi.org/10.1063/1.4948363).
- [32] S. P. Verevkin, A. Y. Sazonova, V. N. Emel'yanenko, D. H. Zaitsau, M. A. Varfolomeev, B. N. Solomonov, and K. V. Zherikova, "Thermochemistry of halogen-substituted methylbenzenes," *J. Chem. Eng. Data*, vol. 60, no. 1, pp. 89–103, 2015, doi: doi.org/10.1021/je500784s.
- [33] B. N. Solomonov, M. A. Varfolomeev, R. N. Nagrimanov, T. A. Mukhametzyanov, and V. B. Novikov, "Enthalpies of solution, enthalpies of fusion and enthalpies of solvation of polyaromatic hydrocarbons: Instruments for determination of sublimation enthalpy at 298.15 K," *Thermochim. Acta*, vol. 622, pp. 107–112, 2015, doi: [10.1016/j.tca.2015.10.020](https://doi.org/10.1016/j.tca.2015.10.020).
- [34] M. A. V. R. da Silva, M. A. R. Matos, and L. M. P. F. Amaral, "Standard molar enthalpies of formation of 2-chloroquinoline, 4-chloroquinoline, 6-chloroquinoline and 4, 7-dichloroquinoline by rotating-bomb calorimetry," *J. Chem. Thermodyn.*, vol. 38, no. 1, pp. 49–55, 2006, doi: [10.1016/j.jct.2005.03.011](https://doi.org/10.1016/j.jct.2005.03.011).
- [35] R. D. Chirico and W. V. Steele, "Thermodynamic Properties of 2-Methylquinoline and 8-Methylquinoline," *J. Chem. Eng. Data*, vol. 50, no. 2, pp. 697–708, Mar. 2005, doi: [10.1021/je049595u](https://doi.org/10.1021/je049595u).
- [36] W. Acree Jr and J. S. Chickos, "Phase transition enthalpy measurements of organic and organometallic compounds and ionic liquids. Sublimation, vaporization, and fusion enthalpies from 1880 to 2015. Part 2. C11–C192," *J. Phys. Chem. Ref. Data*, vol. 46, no. 1, p. 13104, 2017, doi: [10.1063/1.4948363](https://doi.org/10.1063/1.4948363).
- [37] M. A. V. Ribeiro da Silva and M. A. R. Matos, "Recent work on the thermochemistry of some nitrogen heterocycles," *Pure Appl. Chem.*, vol. 69, p. 2305, 1997, doi: [10.1351/pac199769112295](https://doi.org/10.1351/pac199769112295).
- [38] S. P. Safronov, S. V. Vostrikov, A. A. Samarov, and S. P. Verevkin, "Reversible storage and release of hydrogen with LOHC: Evaluation of thermochemical data for methyl-quinolines with complementary experimental and computational methods," *Fuel*, vol. 317, Jun. 2022, doi: [10.1016/J.FUEL.2022.123501](https://doi.org/10.1016/J.FUEL.2022.123501).
- [39] R. M. Stephenson, *Handbook of the thermodynamics of organic compounds*. Springer Science & Business Media, 2012.

Research Article

New Thermodynamic Equation of State for Refrigerant HFO-1243zf

^{1*}I. M. Astina , ²H. I. Alfisahri 

^{1,2} Faculty of Mechanical and Aerospace Engineering, Institut Teknologi Bandung, West Java, Indonesia
E-mails: ^{1*}astina@itb.ac.id, ²hilmyilham67@gmail.com

Received 8 February 2023, Revised 26 April 2023, Accepted 20 May 2023

Abstract

R-1243zf is a new refrigerant that could replace R-134a. Its thermodynamic properties represented in the equation of state (EOS) play an essential role in analyzing and designing thermal systems. The EOS exists without including caloric property data due to unavailable data during the development time. New EOS was developed explicitly in Helmholtz free energy and optimized to represent the experimental data accurately and maintain thermodynamic consistency. The optimization process undergoes using a genetic algorithm and weighted-least squares regression. The experimental data used in the optimization have a range of 233–430 K and 0.106–34.6 MPa and were validated from the extrapolation and consistency to confirm the reliability. The average absolute deviation from the data is 0.48% for the ideal gas isobaric specific heat, 1.7% for the isochoric specific heat, 0.33% for the speed of sound, 0.22% for the liquid density in single-phase, 0.49% for the vapor density in single-phase, 0.96% for the vapor pressure, 2.2% for the saturated liquid density, and 3.2% for the saturated vapor density. The EOS has a reasonable extrapolation behavior from the triple point up to 700 K and 100 MPa.

Keywords: Modeling; thermodynamic properties; equation of state; HFO refrigerant; R-1243zf.

1. Introduction

The development of research in the refrigerant is still undergoing in response to the issues of ozone depletion and global warming, as well as the efforts to establish efficient thermal systems. The 2016 Kigali Amendment to the Montreal Protocol is an international agreement to phase down the consumption and production of hydrofluorocarbons (HFCs) [1]. Refrigerant tetrafluoroethane (R-134a) is widely spread and installed in refrigeration and air conditioning systems, but it has very high global warming effect. Therefore, it is necessary to look for solutions to replace these refrigerants in existing machines and develop new and environmentally friendly systems. Refrigerant 3,3,3-trifluoropropene (R-1243zf) has majorly similar properties to R-134a, so it is attractive as an alternative refrigerant and is the same potential substitution as R-1234yf and trans-1,3,3,3-tetrafluoropropene (R-1234ze(E)). Emissions of R-1243zf have no impact on ozone depletion but have a global warming potential (GWP) of less than one [2], as well as its mildly flammable in group A2L [3]. R-134a is widely and commonly used in organic Rankine, residential refrigeration, and vehicle cooling systems [4]. Recently, many publications regarding the experimental data and measurement of various thermodynamic properties of R-1243zf are available and described in more detail in Section 2. This fact indicates that the R-1243zf is widely still considered to be applied.

Thermodynamic properties, which play an essential role in the analysis and design of thermal systems, may be expressed in terms of Helmholtz free energy. The state-of-the-art equation of state (EOS) for R-1243zf was introduced by Akasaka [5] and Akasaka and Lemmon [6]. These

equations are multiparameter EOS used to represent a pure fluid or expanded to its mixture. Both EOS were developed without caloric data such as isochoric and isobaric specific heats, so inquiring about the accuracy of these properties. Subsequently, new caloric data such as isochoric specific heat, ideal gas isobaric specific heat, and speed of sound followed the existing EOSs. The new caloric data include data from Sheng et al. [7] and Chen et al. [8]. The accuracy of data on the caloric properties directly relates to enthalpy and entropy used in the analysis and design of thermal energy systems. The new EOS for R-1243zf needs the latest data fitted. Therefore, this article presents a new EOS, considering the latest data, thermodynamic consistency, and comprehensive assessment in modeling.

2. Survey and Available Data

Hydrofluoroolefin (HFO) is a fourth-generation refrigerant and alternative to HFCs [4]. The usage of HFCs reduces due to their high GWP effect. HFOs have a C=C double bond structure, free of chlorine, and have a short atmospheric lifetime. In addition, HFOs, which are environmentally friendly and much like HFCs, are expected to be suitable as substitutes. One of the HFOs with great potential is R-1243zf. This refrigerant, herewith the R-1234yf and R-1234ze(E), has similar thermodynamic properties to HFC-134a. R-1243zf is a good choice for the substitute because it has the most similar characteristics to R-134a compared to the others and has a better coefficient of performance in several models.

A critical pressure and temperature were taken from Higashi and Sakoda [9]. The critical density and the triple point temperature derived from the EOS of Akasaka and

Lemmon [6] were due to unavailable experimental data. The critical temperature and density function as reduction parameters for temperature and density, respectively. The critical temperature (T_c) and pressure (p_c) are 376.93 K and 3.518 MPa [9], respectively. The critical density (ρ_c) is 413.02 kg·m⁻³ [6], and triple point temperature (T_{tp}) is 220 K [6]. Additionally, the universal gas constant (\bar{R}) used is 8.314462618 J·mol⁻¹·K⁻¹ [10], and the molecular mass (M) is 96.05113 kg·kmol⁻¹ [7].

The PVT data, either at saturation or in a single phase, are required to develop the EOS. The saturation data from the triple point to the critical point are essential input data on the development. The PVT data in the single phase covers the liquid and gas phases, including the supercritical region. Additionally, caloric properties significantly improve the accuracy of EOS to represent specific heat, enthalpy, and entropy. The data required are in a wide range for the development of the EOS. Furthermore, the collected data are available in Table 1.

Table 1. Available experimental data for R-1243zf.

No	Prop.	Source	Points	Range	
				MPa	K
1	p_s	Raabe and Marginn [11]	10	-	263–353
2	p_s	Brown et al. [12]	83	-	233–372
3	p_s	Higashi et al. [13]	20	-	310–376
4	p_s	Yin et al. [14]	26	-	253–376
5	p_s	Yang et al. [15]	17	-	273–353
6	ρ'	Raabe and Marginn [11]	10	-	263–353
7	ρ'	Higashi and Sakoda [9]	6	-	366–376
8	ρ''	Raabe and Marginn [11]	10	-	263–353
9	ρ''	Higashi and Sakoda [9]	7	-	366–376
10	PVT	Di Nicola et al. [16]	410	1.11–26.9	278–368
11	PVT	Higashi and Sakoda [9]	75	0.235–32.5	328–430
12	PVT	Yin et al. [14]	128	0.106–2.88	253–368
13	c_v	Sheng et al. [7]	64	1.58–10.21	299–351
14	c_p^o	Chen et al. [8]	11	-	313–363
15	w	Chen et al. [8]	92	0.170–1.98	313–363

The data at the saturation condition are used to develop ancillary equations and the residual part of the EOS. For vapor pressure, data from Higashi et al. [13], Raabe and Marginn [11], and Brown et al. [17] is also used in the equations of Akasaka and Lemmon [6]. Yin et al. [14] and Yang et al. [12] data are the most recent data. For density, no new data is available yet. The distribution of PVT experimental data is shown in Figure 1. The newly published data set is that of Yin et al. [14]. The data of Nicola et al. [16] has a broader range than the data of Higashi and Sakoda [9].

The caloric property data are not as abundant as other data. There are two resources, one for isochoric-specific heat and the other for speed of sound. This data distribution is shown in Figure 2. Sheng et al. [7] reported the data set for isochoric specific heat. As same as the specific-heat data, the

speed-of-sound data was reported by Chen et al. [8]. Both data are newer than the existing EOS of Akasaka and Lemmon [6]. These data are inputted into the optimization process of the residual part. This data set plays an essential role in the development and assessment and is closely related to energy analysis. The distribution of the data is shown in Figure 2. These data are less than the PVT data, and the temperature and pressure ranges are still narrow.

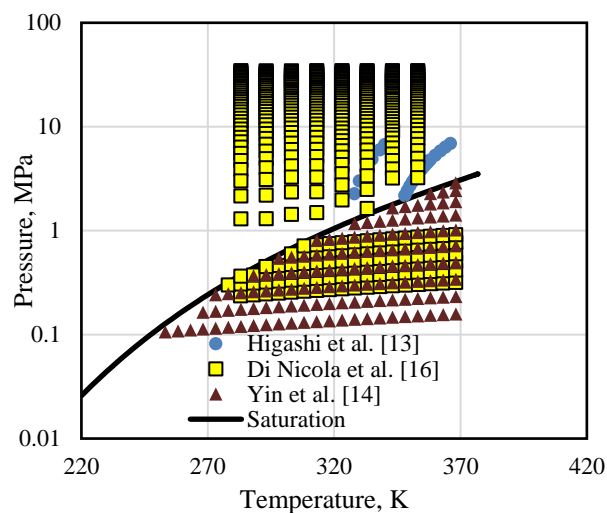


Figure 1. Data distribution of PVT properties.

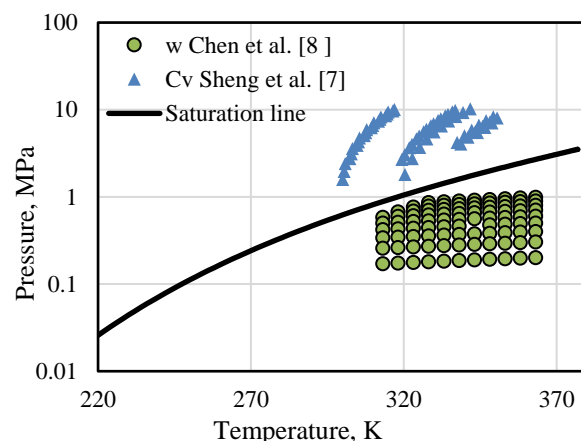


Figure 2. Data distribution of caloric properties.

The ideal gas isobaric heat data is analytical data derived from experimental data for the speed of sound. This data is used in the process of optimizing the ideal part of EOS. When the Akasaka and Lemmon equations [6] were developed, data for the isobaric-specific heat of an ideal gas were not yet available, so the data from analytical modeling based on the molecule's shape using the Joback-Reid method [17] was used. Now available data from the experimental results can be used, namely data from Chen et al. [8]. The amount of data generated is very limited, but its role is essential to verify and improve the quality of the previous equation.

The second and third virial coefficient data are involved in the equational optimization process of the residual part of EOS. Publication of experimental data on pressure, temperature, and density usually includes the second and third virial coefficient equations modeled from the experimental data, for example, the publication of Yin et al. [14]. Chen et al. [8] reported eleven data points for the second and third virial coefficients. Data from Yin et al. [14]

are valid in the range of 253–368 K because the measurement is in that range.

3. Modeling and Formulation

Mathematical modeling of thermodynamic properties is very complex because the relationship between one property and another is interrelated for a state. This complexity arises when one wishes to construct EOS in which one mathematical model can account for all the thermodynamic properties at a known state. Modeling for this case in the field of thermodynamic properties is referred to as multi-property modeling. The explanation of this multiparameter EOS modeling was given in detail by Span [18]. In mathematical thermodynamics, the relationship between fluid properties with the help of thermodynamic laws and definitions can be processed to obtain the relationship between these properties. Table 2 represents thermodynamic property relation respect to EOS with basis of Helmholtz free energy. EOS is fitted to input data as regression process to get an accurate one.

Optimization of the equation's structure is a part of the process of finding accurate and reliable equations. One step of the optimization procedure in this work uses a genetic algorithm. Genetic algorithms find the functional form of the equation, which is usually a power or exponential number that is hard to regress. The genetic algorithm optimization method combines random solutions and evolutionary processes. Optimization using the random solution method could always produce the best solution but requires an evaluation process for all combinations that could take very long time for complex cases such as the modeling of thermodynamic equations. Genetic algorithms imitate evolution based on natural selection, especially on chromosomes or genetics. Through this approach, the optimization process becomes focused on a convergent value approaching the best solution with fewer evaluation processes than the random solution method so that the optimization process becomes much faster. Fitness is the sum of the least squares objective function with its weighting factor. For multi-property optimization, the resulting fitness is the sum of the regression results of all the properties included in the optimization.

The process of developing for the thermodynamic model uses a genetic algorithm to find non-linear terms and uses least squares linear regression to obtain linear coefficients. The developed models consist of EOS and ancillary equations for vapor pressure, saturated liquid, and saturated vapor densities. Adhering to the concept of the different properties between ideal gas and real-fluid properties, the EOS is divided into two parts: ideal and residual parts. The regression model presented in Eq. (1) includes the mathematical relation in Table 2. Variable W in the equation is the weighting factor, y_{data} is the measured data (property input), and y_{cal} is the property calculated based on density and temperature input for a case of developing EOS and based on temperature for case developing the ancillary equations. The y_{data} is filled with values from the left side; the y_{cal} is from the right side in the mathematical equations.

$$\chi = \sum_{i=1}^n W_i (y_{data} - y_{cal})^2 \quad (1)$$

The properties included in modeling depend on available input data. However, pressure-volume-density and caloric property data must be included, aside from Maxwell's relation of vapor pressure and virial coefficients. The sum of

least square (χ) is minimized in regression processes to get accurate models.

Table 2. Thermodynamic relations respect to EOS.

Properties	Mathematical relations
Helmholtz free energy	$\alpha = \frac{A}{RT} = \alpha^o + \alpha^r$
Ideal gas isobaric specific heat	$\frac{c_p^o}{R} = 1 - \tau^2 \alpha_{\tau\tau}^o = 1 + \frac{c_p^o(\tau)}{R}$
Pressure	$\frac{p(\delta, \tau)}{\rho RT} = 1 + \delta \alpha_{\delta}^r$
Vapor pressure	$\frac{p_s(\delta', \delta'', \tau_s)}{RT_s} = \frac{\rho' \rho''}{\rho' - \rho''} \left(\ln \left(\frac{\delta'}{\delta''} \right) + \alpha^{r'} - \alpha^{r''} \right)$
Isobaric specific heat	$\frac{c_p(\delta, \tau)}{R} = \frac{c_p(\delta, \tau)}{R} + \frac{(1 + \delta \alpha_{\delta}^r - \delta \tau \alpha_{\delta\tau}^r)^2}{(1 + 2\delta \alpha_{\delta}^r + \delta^2 \alpha_{\delta\delta}^r)}$
Isochoric specific heat	$c_v(\delta, \tau)/R = -\tau^2 (\alpha_{\tau\tau}^o + \alpha_{\tau\tau}^r)$
Saturated liquid specific heat	$\frac{c_s'(\delta', \delta'', \tau_s)}{R} = \frac{c_v(\delta', \tau_s)}{R} + \frac{(1 + \delta' \alpha_{\delta}^{r'} - \delta' \tau_s \alpha_{\delta\tau}^{r'})}{(1 + 2\delta' \alpha_{\delta}^{r'} + \delta'^2 \alpha_{\delta\delta}^{r'})} \times \left\{ 1 + \delta' \alpha_{\delta}^{r'} - \delta' \tau_s \alpha_{\delta\tau}^{r'} - \frac{1}{R \rho_c \delta'} \frac{dp_s(\delta', \delta'', \tau_s)}{dT} \right\}$
Saturated vapor specific heat	$\frac{c_s''(\delta', \delta'', \tau_s)}{R} = \frac{c_v(\delta'', \tau_s)}{R} + \frac{(1 + \delta'' \alpha_{\delta}^{r''} - \delta'' \tau_s \alpha_{\delta\tau}^{r''})}{(1 + 2\delta'' \alpha_{\delta}^{r''} + \delta''^2 \alpha_{\delta\delta}^{r''})} \times \left\{ 1 + \delta'' \alpha_{\delta}^{r''} - \delta'' \tau_s \alpha_{\delta\tau}^{r''} - \frac{1}{R \rho_c \delta''} \frac{dp_s(\delta', \delta'', \tau_s)}{dT} \right\}$
Speed of Sound	$\frac{w^2(\delta, \tau)M}{RT} = 1 + 2\delta \alpha_{\delta}^r + \delta^2 \alpha_{\delta\delta}^r + \frac{(1 + \delta \alpha_{\delta}^r - \delta \tau \alpha_{\delta\tau}^r)^2}{c_v(\delta, \tau)/R}$
Enthalpy	$\frac{h(\delta, \tau)}{RT} = \tau (\alpha_{\tau}^o + \alpha_{\tau}^r) + 1 + \delta \alpha_{\delta}^r$
Entropy	$\frac{s(\delta, \tau)}{R} = \tau (\alpha_{\tau}^o + \alpha_{\tau}^r) - (\alpha^o + \alpha^r)$
Internal energy	$\frac{u(\delta, \tau)}{RT} = \tau (\alpha_{\tau}^o + \alpha_{\tau}^r)$
Third virial coefficient	$B(\tau) \rho_c = \lim_{\delta \rightarrow 0} \alpha_{\delta}^r$
Second virial coefficient	$C(\tau) \rho_c^2 = \lim_{\delta \rightarrow 0} \alpha_{\delta\delta}^r$
$\delta = \frac{\rho}{\rho_c}, \tau = \frac{T_c}{T}, R = \frac{\bar{R}}{M}, A = u - Ts, \alpha_{\delta} = \left(\frac{\partial \alpha}{\partial \delta} \right)_{\tau}, \alpha_{\tau} = \left(\frac{\partial \alpha}{\partial \tau} \right)_{\delta}, \alpha_{\delta\delta} = \left(\frac{\partial^2 \alpha}{\partial \delta^2} \right)_{\tau}, \alpha_{\tau\tau} = \left(\frac{\partial^2 \alpha}{\partial \tau^2} \right)_{\delta}, \alpha_{\delta\tau} = \left(\frac{\partial^2 \alpha}{\partial \delta \partial \tau} \right)$	

Both ancillary equations and EOS must be able to provide accurate calculation results. The ancillary equations play an essential role in preparing input data for developing

the EOS and initial guess for the iteration process conducted in calculating thermodynamic properties when one or more unknown properties are the independent variables.

The most complex EOS formulation today is the IAPWS 1995 equation for ordinary water by Wagner and Pruß [19]. For EOS based on the Helmholtz free energy, regardless of the complexity of the formulation given, derivation of the other thermodynamic properties from the Helmholtz free energy still has the same fundamental mathematical relationship so that the previous mathematical relation can be applied to calculate the properties. The modeling procedure and program code used in this study were used for refrigerants of HFC, hydrocarbon, HFO, and hydrochlorofluoroolefin (HCFO). Our recent article reported their implementation for HFO [20] dan HCFO [21]. More detailed optimization procedures used can be found in previous work [22].

4. Thermodynamic Property Model

The thermodynamic property models as results of this study consist of ancillary equations for vapor pressure, saturated liquid density, and saturated vapor density as well as the EOS.

4.1 Ancillary Equation

The optimization process of ancillary equations uses a genetic algorithm. The ancillary equation for the density of saturated vapor is expressed on a logarithmic basis, while the equation for the saturated liquid density has a linear basis. The saturated vapor pressure correlates with the temperature (T) with four terms as given in Eq. (2). Critical pressure (p_c) and critical temperature (T_c) are inside for getting dimensionless relation. The exponents of the equation terms on the right side are the results of optimization with a genetic algorithm. Variable E is the coefficients obtained from the optimization process, which are $E_1 = -7.3416$, $E_2 = -3.1588$, $E_3 = -3.1012$, and $E_4 = -4.1381$. The sum of the terms used in this equation equals the ancillary equation used by Akasaka and Lemmon [6]. The term number is sufficient to represent the properties properly and is small enough to run a quick calculation process.

$$\ln\left(\frac{p}{p_c}\right) = \frac{T_c}{T} \left(E_1 \left[1 - \frac{T_c}{T}\right] + E_2 \left[1 - \frac{T_c}{T}\right]^{1.6} + E_3 \left[1 - \frac{T_c}{T}\right]^2 + E_4 \left[1 - \frac{T_c}{T}\right]^5 \right) \quad (2)$$

The next two ancillary equations for saturated liquid density (ρ') and saturated vapor density (ρ''), respectively, are written in Eqs. (3) and (4). Both equations are represented in dimensionless with dividing with critical density (ρ_c) and critical temperature. The equations have four terms. Variables F and G are coefficients as optimization processes in their development. The coefficients obtained are $F_1 = 0.018161$, $F_2 = -0.53941$, $F_3 = 2.5054$, $F_4 = 0.75331$, $G_1 = 0.89105$, $G_2 = -3.3802$, $G_3 = -7.8192$, and $G_4 = -31.145$.

$$\frac{\rho'}{\rho_c} = 1 + F_1 \left[1 - \frac{T}{T_c}\right]^{0.1} + F_2 \left[1 - \frac{T}{T_c}\right]^{0.2} + F_3 \left[1 - \frac{T}{T_c}\right]^{0.3} + F_4 \left[1 - \frac{T}{T_c}\right]^{0.9} \quad (3)$$

$$\ln\left(\frac{\rho''}{\rho_c} - 1\right) = G_1 \left[1 - \frac{T}{T_c}\right]^{0.2} + G_2 \left[1 - \frac{T}{T_c}\right]^{0.3} + G_3 \left[1 - \frac{T}{T_c}\right]^{1.2} + G_4 \left[1 - \frac{T}{T_c}\right]^{3.8} \quad (4)$$

The terms used are less than the term from the ancillary equations used by Akasaka and Lemmon [6]. The use of fewer terms makes the calculation process faster without sacrificing the accuracy of the equation. The ancillary equations for the densities of saturated liquid and saturated vapor to assist the optimization process of the EOS and as the initial iteration value in root calculation to find thermodynamic properties either in single-phase or two-phase for the case of known properties excluding temperature or density.

4.2 New Helmholtz Equation of State

The new EOS (α) consists of two parts: the ideal part (α^o) and the residual part (α^r) and the relation is $\alpha = \alpha^o + \alpha^r$. The ideal part is obtained by integrating the ideal-gas isobaric specific heat equation at a reference state. The ideal gas isobaric heat equation should be obtained first as the final result in Eq. (5). The equation has just two terms of the Einstein-Planck functional form. In this short relation, the equation can represent satisfied accuracy. The residual part must be prepared prior to complete the ideal part with its two integral constant values because of the reference state selected for the EOS is not in the ideal gas state. Finally, the new EOS is fitted to a reference state of the International Institute of Refrigeration. The final result of the ideal part is written in Eq. (6) with the numerical coefficients and constants in Table 3.

$$\frac{c_p^o(\tau)}{R} = \sum_{i=1}^2 N_i^o \tau^2 b_i^2 \frac{\exp(-b_i \tau)}{(1 - \exp(-b_i \tau))^2} \quad (5)$$

$$\alpha^o(\delta, \tau) = \ln \frac{\delta}{\tau} + \sum_{i=1}^2 N_i^o \ln(1 - \exp(-b_i \tau)) + \sum_{i=3}^4 N_i^o \tau^{b_i} \quad (6)$$

Table 3. Numerical coefficients of the ideal gas.

i	b_i	N_i^o
1	1.5050	1.3863×10^1
2	5.5650	9.6280×10^0
3	0	-1.1263×10^1
4	1	9.4400×10^0

The residual part obtained from this work appears in Eq. (7). Table 4 represents the numerical coefficients and constants of the equation. The polynomial terms of the equation usually represent the thermodynamic properties of the vapor phase, while the exponential terms of the equation represent the properties of the liquid phase [23]. The terms for the density variable must be integer, while the terms for the temperature variable must be real numbers. The value of the t term of the temperature variable functions for modeling the critical region [23]. Outside the critical region, the term τ^{t_i} can cause very high fluctuations so that it must be damped with the others, namely δ^{d_i} in the vapor phase and $\exp[-\delta^{\theta_i}]$ in the liquid phase.

$$\alpha^r(\delta, \tau) = \sum_{i=1}^6 N_i \delta^{d_i} \tau^{t_i} + \sum_{i=7}^{20} N_i \delta^{d_i} \tau^{t_i} \exp[-\delta^{\theta_i}] \quad (7)$$

The combination of genetic algorithms and weighted least square regression is applied in the optimization program to obtain EOS and ancillary equations. EOS results from this study of a general structure to accommodate polynomials, exponentials, and Gaussian-Bell terms. The nonlinear correlations for caloric properties are compensated via a

limited iterative regression in the process of the optimal residual structure to represent the input data in the modeling.

Table 4. Numerical coefficients of the residual part.

i	d_i	t_i	θ_i	N_i
1	1	0.425	-	1.2694572×10^0
2	4	0.45	-	2.9865027×10^{-2}
3	2	1.3	-	$-8.5288450 \times 10^{-2}$
4	1	1.325	-	-2.5317951×10^0
5	3	1.9	-	$-6.0204735 \times 10^{-2}$
6	4	2	-	1.6375506×10^{-2}
7	2	3.525	1	$-4.7744050 \times 10^{-1}$
8	2	2.125	1	6.0054790×10^{-1}
9	3	2.235	1	8.6505374×10^{-1}
10	2	4.625	1	2.6476831×10^1
11	2	7	1	$-2.9446209 \times 10^{-2}$
12	1	7.125	1	-1.0141306×10^0
13	1	7.25	1	9.3621188×10^{-1}
14	5	2	2	$-8.5592024 \times 10^{-2}$
15	4	4	2	$-6.3548921 \times 10^{-2}$
16	6	5.875	2	3.5316930×10^{-2}
17	7	5.75	2	$-1.7172415 \times 10^{-2}$
18	1	0	3	$-3.6957644 \times 10^{-2}$
19	7	4.5	3	$-1.1731380 \times 10^{-2}$
20	2	6.5	3	$-8.7493600 \times 10^{-2}$

Compared with Akasaka and Lemmon, the combination of stepwise linear regression and nonlinear least-square regression to obtain the final EOS. Even though there are differences in the process, there are similarities in modeling: optimization of the equation structure and linear coefficient of the equation, and all constraints cannot be included directly in the optimization process but evaluated after getting the best model. The method used in this study, even though it operates with many equation structure predictions, the optimization process can still be faster. The developed EOS consists of polynomial and exponential terms simpler than the EOS of Akasaka and Lemmon [6].

5. Assessments

The evaluation for properties in single-phase is divided into two parts: gas phase and liquid phase. It is divided due to significantly different characteristics of the data in the gas phase and liquid phase, so the evaluation needs to be done separately. Experimental data of thermodynamic properties of pressure, temperature, and density used in the optimization process consist of 335 data points from temperature 283–386 K and pressure 1.30–34.6 MPa. Meanwhile, the available caloric data has a narrower range, namely temperature in range of 300 K to 350 K and pressure in range of 0.1 MPa to 10 MPa.

5.1 Visualization and Evaluation

The data uncertainty of Chen et al. [8] at 0.5% requires the minimum target deviation from this equation at 0.5%. The distribution of the ideal gas isobaric specific heat deviation concerning the Akasaka and Lemmon equation [6]

and experimental data over the entire range appears in Figure 3. The difference in value from both EOS is less than 0.5%.

Deviation of the data from Akasaka and Lemmon [6] increases in the temperature range of 300 K because this range of the data from Chen et al. [8] was optimized using more weighting factor values. Figure 4 shows that the comparison concerning the data of Chen et al. [8] results in an average absolute deviation (AAD) of 0.48%, a standard deviation (STD) of 0.25%, and a maximum absolute deviation (MAX) of 0.94%. This result is already in the range of experimental data uncertainty.

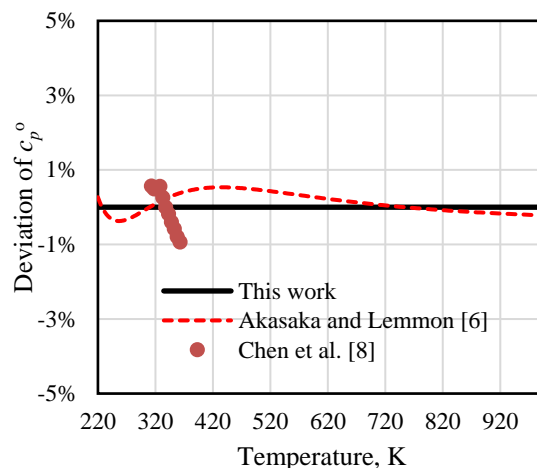


Figure 3. Deviation of the ideal gas specific heat.

There are five sources of experimental data used with temperature range of 233–376 K. The deviation of the vapor pressure from the new EOS to experimental data and artificial models can be seen in Figure 4.

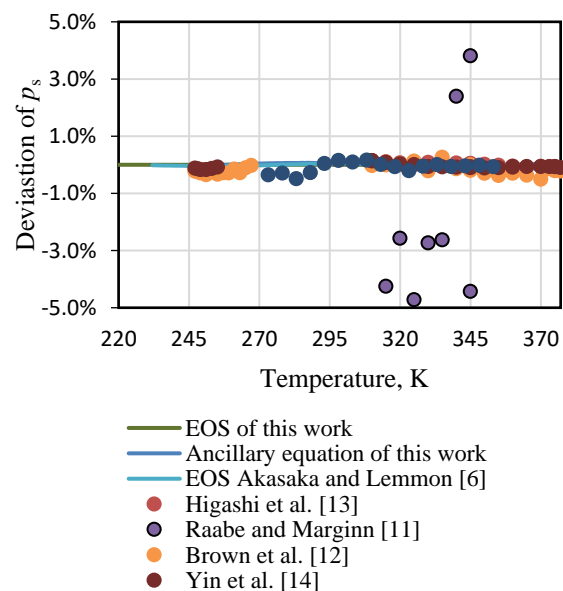


Figure 4. Deviation of the vapor pressures.

In the temperature range of 310–376 K, there are data set from Higashi et al. [13], which has an AAD of 0.070%, a MAX of 0.15%, and an STD of 0.033%. At a temperature range of 233–372 K, data sets from Brown et al. [12] were used, which have an AAD of 0.14%, a MAX of 0.85%, and an STD of 0.17%. At a temperature range of 263–353 K, data sets from Raabe and Marginn [11] were used. These data sets have an AAD of 4.4%, a MAX of 8.7%, and an STD of 2.1%.

Two recent data sets were obtained from Yin et al. [18], which have a temperature range from 253 to 376 K and have an AAD of 0.091%, a MAX of 0.17%, and an STD of 0.040%, and the data set of Yang et al. [15], which has a temperature range from 273 to 353 K and has an AAD of 0.14%, a MAX of 0.49%, and an STD of 0.14%.

Two data sets from Higashi and Sakoda [9] and Raabe and Marginn [11] fitted are the density at saturated liquid and vapor states. The amount of data available for saturated density is very scarce. Density deviations from the new EOS for the saturated-liquid and vapor states concerning experimental and derived property data are shown in Figures 5 and 6, respectively. For saturated liquid density data of Higashi and Sakoda [9], it results in an AAD of 0.56% with an STD of 0.23% and a MAX of 1.0%. Similar to the data for saturated steam, the data from Raabe and Marginn [16] yield a much higher deviation because the data are resulted from molecular modeling. These data produce an AAD of 3.1% with an STD of 1.1% and a MAX of 4.4%.

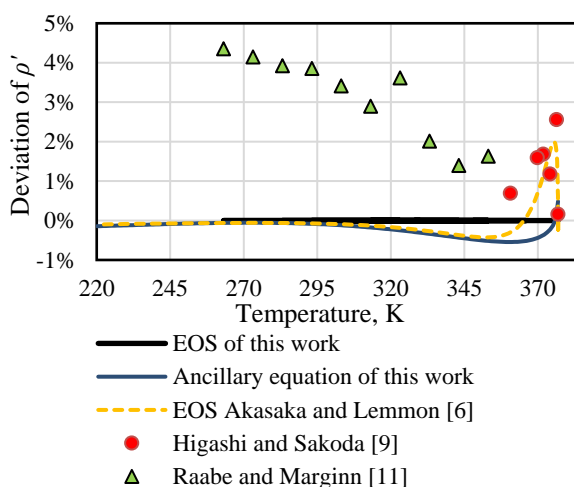


Figure 5. Deviation of saturated liquid density.

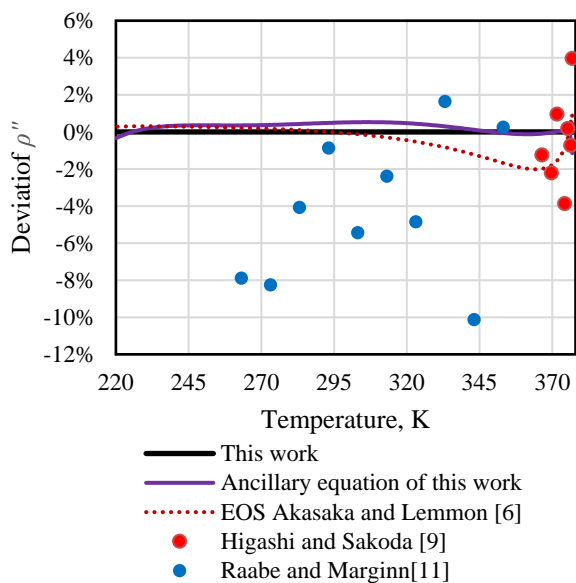


Figure 6. Deviation of the saturated vapor density.

For the saturated vapor density, data from Higashi and Sakoda [9] recorded an AAD of 1.3% with an STD of 0.97% and a MAX of 3.0%. Meanwhile, the data owned by Raabe and Marginn [11] performed AAD of 4.3% with an STD of 2.8% and a MAX of 8.7%.

In the temperature range of 328–386 K, there are data from Higashi et al. [13] having an AAD of 0.41%, a MAX of 1.1%, and an STD of 0.33%. On the other hand, at temperatures of 283–386 K, data from Brown et al. [12] have an AAD of 0.027%, a MAX of 0.35%, and an STD of 0.045%.

Figures 7 and 8 show the density deviation from the EOS concerning temperature and pressure, respectively. Experimental data on thermodynamic properties of pressure, temperature, and liquid density used in the optimization process consist of 269 data points from a temperature of 253–430 K and pressure of 0.110–6.86 MPa.

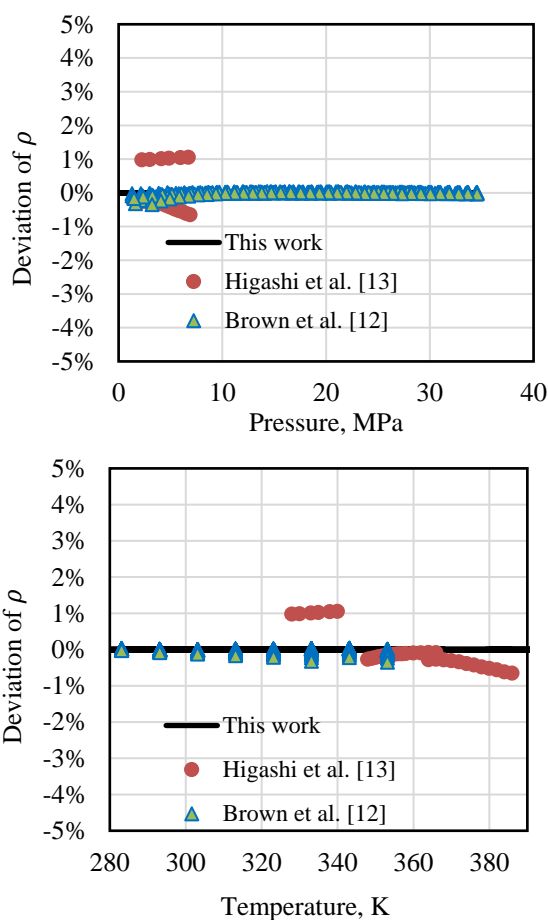


Figure 7. Deviation of the liquid density.

In the temperature range of 330 K to 430 K, the data from Higashi et al. [15] has an AAD of 0.55%, a MAX of 1.3%, and an STD of 0.35%. Meanwhile, data set from Brown et al. [17] for a temperature of 278–368 K has an AAD of 0.67%, a MAX of 2.8%, and an STD of 0.51%. The latest and most recent data set taken from Yin et al. [14] has a temperature range from 253 to 368 K and has an AAD of 0.25%, a MAX of 0.85%, and an STD of 0.21%.

The process of fitting the caloric properties of the fluid in the development of EOS is essential to get a good result of other properties such as internal energy, enthalpy, and entropy. Since the refrigerant of this study is relatively new, it is not widely applied. Only a set of experimental data is available. It is the isochoric heat data set reported by Sheng et al. [7]. and has 64 data points with a temperature range of 299–351 K. All these data are in the liquid phase. After comparing with the data calculated from the EOS of this work, it performs an AAD is 1.7% with an STD of 0.79% and a MAX of 3.3%. The deviation distribution appears in Figure 9.

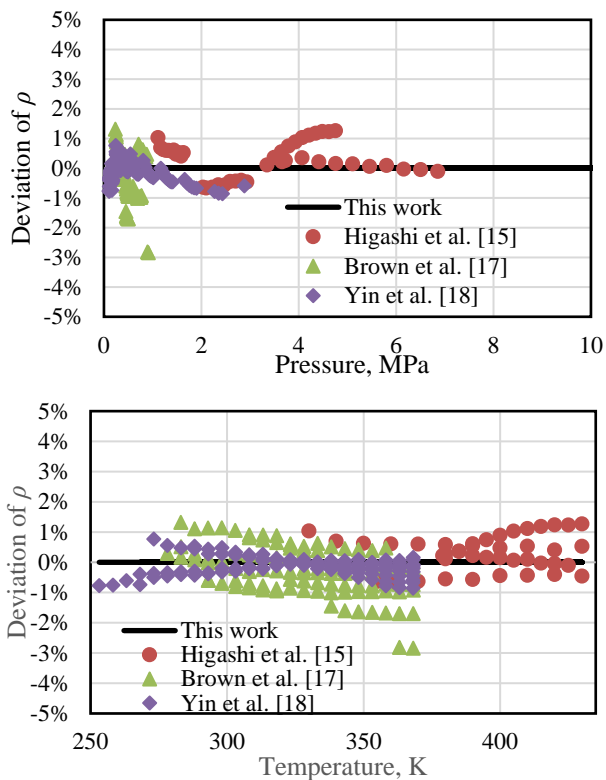


Figure 8. Deviation of the vapor density in the single phase.

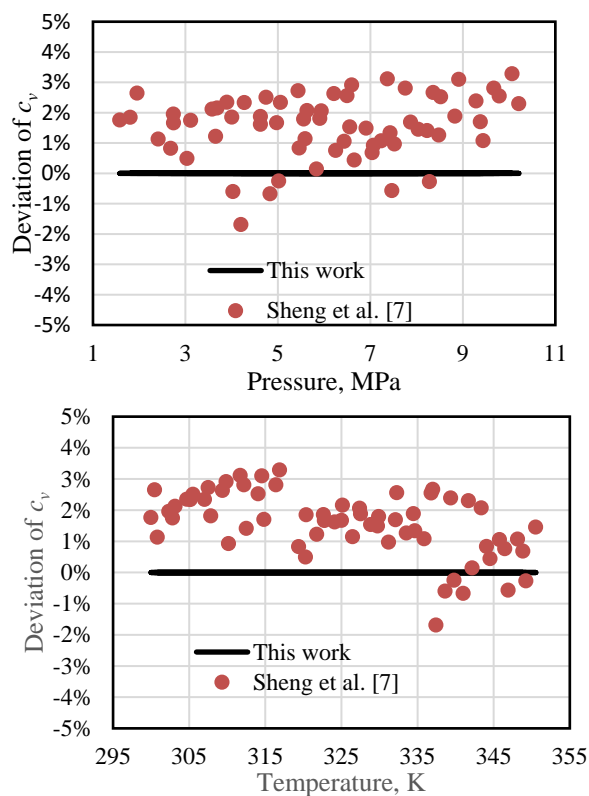


Figure 9. Deviation of the isochoric specific heat in the single phase.

The speed of sound data set available in the gas phase consists of 92 data points in the temperature range 313–363 K, which were reported by Chen et al. [8]. Compared to other property data, the speed of sound data has the highest accuracy. Chen et al. [8] claimed that the experimental data have an uncertainty of up to 0.018%. Because of its accuracy, higher weighting factors were given to the speed of sound data. The deviation of the experimental data concerning the

data calculated from this work can be seen in Figure 10. This data set can be represented by the EOS with an AAD of 0.33%, an STD of 0.23%, and a MAX of 0.97%.

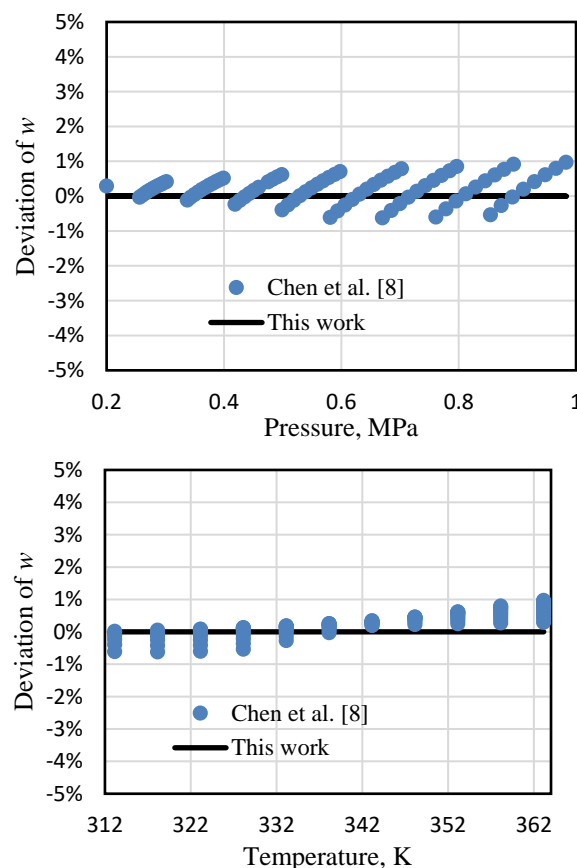


Figure 10. Deviation of the speed of sound in the single phase.

5.2 Thermodynamic Consistencies

It is not sufficient just to evaluate the performance of the equation by comparing experimental data and calculated data, especially if the experimental data available is limited. The extrapolation behavior of the equations in this study was assessed from the plot of pressure and specific volume curves on isothermal lines, plots of caloric properties curves (isochoric specific heat, isobaric specific heat, and speed of sound) on isobaric lines, ideal curves (inverse Joule-Thomson curve, Boyle curve, and Joule inverse curve), and the second and third virial coefficients.

Extrapolation curves for pressure, specific volume, and temperature can be seen in Figure 11. The curves were plotted within a temperature range of 220–1000 K and a pressure range of 0.025–1000 MPa. In single-phase, the resulting curve has a reasonable shape without any intersecting isotherm line from low to high temperatures. In the saturation state, the saturated lines have a proper shape; the lines rise at the saturated-liquid state and flatten out at the critical point and two-phase, then decrease at the saturated vapor condition. Under two-phase conditions, all isothermal lines are at the same pressure.

Next, the extrapolation curve for the caloric properties is evaluated. The extrapolation curve for caloric properties was plotted within the temperature range of 220–750 K and the pressure range of 0.025–100 MPa. The first caloric property to be discussed is isochoric specific heat. The isochoric-specific heat curve requires special observations because the shape of this curve is very sensitive to the changes in the

equation term, and because only experimental data available for specific heat is isochoric-specific heat data. The isochoric-specific heat extrapolation curve can be seen in Figure 12. In general, isochoric-specific heat curves have a reasonable shape. In the liquid state, the isobaric lines have an upward trend as the temperature increases, then increases drastically near the critical point then decreases, and then rises again at very high temperatures. In the liquid phase at low temperatures, there are few waves on the curve and the isobaric lines appear to coincide. The curve in this low-temperature range can be seen in Figure 13. Even so, the trend line remains upward on all the isobaric lines. There is no line intersecting each other.

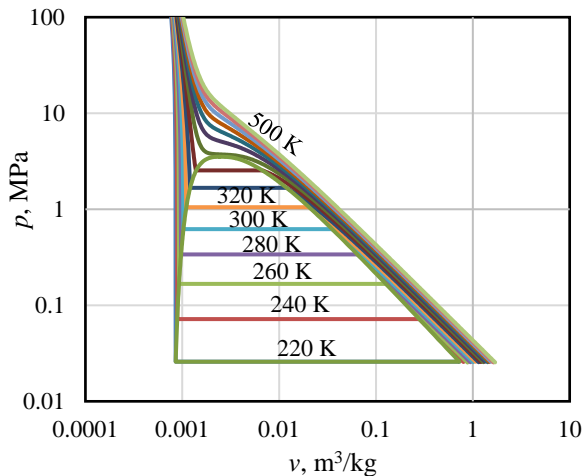


Figure 11. PVT Extrapolation of the new EOS.

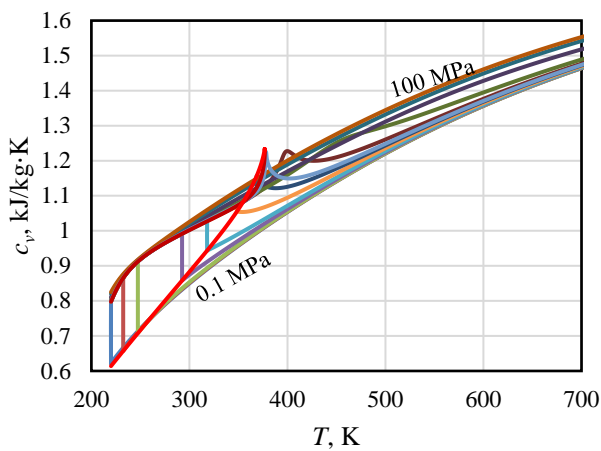


Figure 12. Isochoric heat extrapolation of the new EOS.

The experimental data available for isochoric heat are only within the temperature range of 299–351 K and pressure range of 1.50–10.2 MPa. Therefore, a new set of data in the temperature and pressure ranges as shown in Figure 13 is needed to ensure that the shape of the extrapolation curve is closer to the actual conditions.

Figures 13 and 14 show extrapolation curves for isobaric-specific heat and speed of sound, respectively. The extrapolation curves for these two thermodynamic properties already have a reasonable shape within the temperature and pressure range. In an isobaric heat curve, the trend is like that in an isochoric-specific heat curve. As the isobaric line approaches the critical point, the curve will rise sharply, decrease rapidly to a specific value, and then ramp up with increasing temperature. As for the speed-of-sound curves, isobaric lines in the critical region follow a different trend,

decreasing with increasing temperature in the liquid phase and rising with increasing temperature in the gas phase. The minimum value occurs at the critical point.

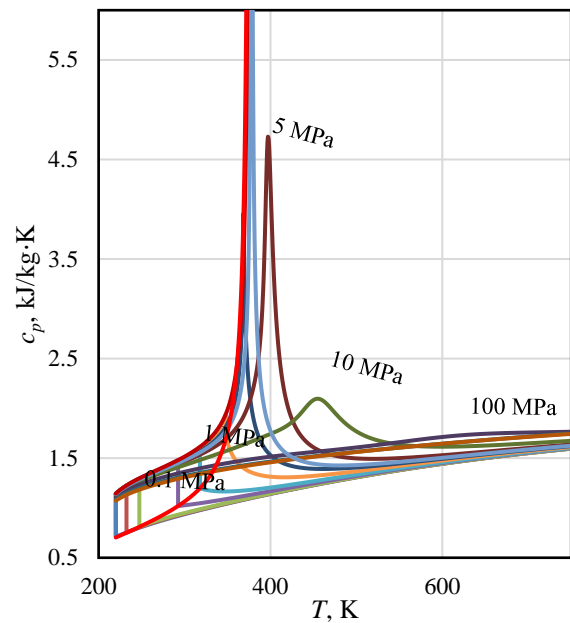


Figure 13. Isobaric heat extrapolation of the new EOS.

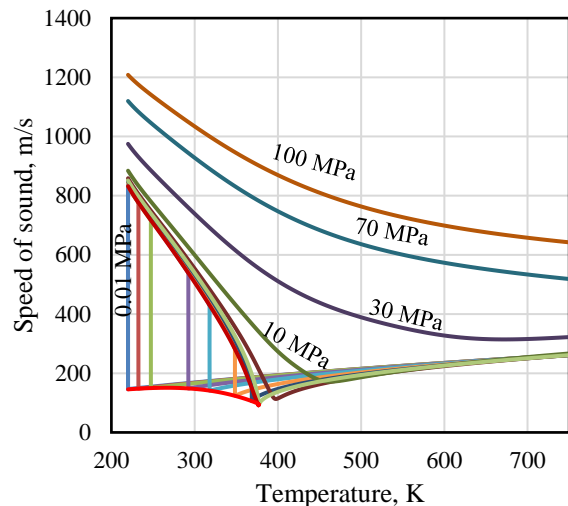


Figure 14. Speed of sound extrapolation of the new EOS.

Ideal curves do not provide numerical information, but rational behaviors can represent a good extrapolation ability of the equation. Figure 15 shows the curve comparison from the EOS of this work and Akasaka and Lemmon [6]. In general, the four curves have the same trend, large values at low temperatures, and then their value drops drastically at high temperatures by turning downwards to form an asymptote line. For the ideal curves of the Akasaka and Lemmon EOS, don't follow this trend at high temperatures. On the other hand, the Boyle curve, the Joule inversion curve, and the Joule-Thomson curve have good agreement between the EOS of this study and Akasaka and Lemmon.

The last parameter that needs to be evaluated to determine the extrapolation ability of the equation is the second and third virial coefficients. The appropriate shape of virial coefficient curves can represent a good equation extrapolation ability. In general, the shape of a good virial coefficient curve is going upward drastically at low temperatures, then form asymptotes towards zero pressure at

very high temperatures. The second and third virial coefficient curves calculated respectively are shown in Figures 16 and 17. In the second virial coefficient graph, the curve obtained from the EOS in this work coincides with the curve from the experimental data (Yin et al. [14] and Chen et al. [8]) as well as the curves obtained from Akasaka and Lemmon [8]. The third virial coefficients obtained from this work do not coincide with the data compared (Yin et al. [14], and Akasaka and Lemmon [6]), but they have the same trend.

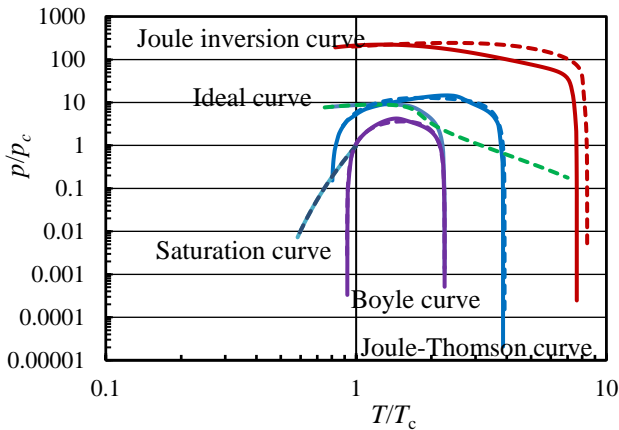


Figure 15. Ideal curves of the new EOS with solid curves of this work, dashed curves of Akasaka and Lemmon EOS.

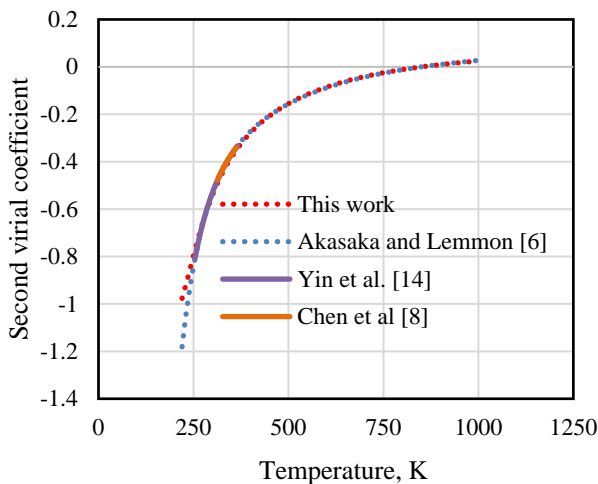


Figure 16. Behavior of second virial coefficients from the new EOS.

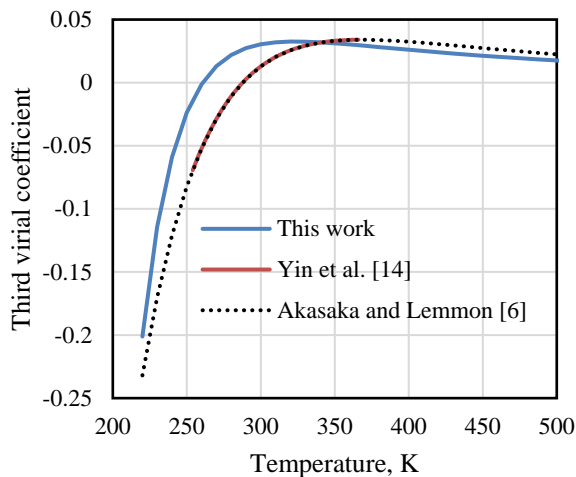


Figure 17. Behavior of third virial coefficients from the new EOS.

5.3 Statistical Comparison

To further assess the quality of the new EOS from this work, a detailed statistical evaluation between EOS of this work and other existing EOS is given. Better statistics mean having smaller values for each parameter (AAD, STD, and MAX), although in this evaluation, the STD results are not used much because the results of the AAD and the MAX are sufficient for comparison. The new EOS compared to is the Akasaka and Lemmon EOS [6], because it is the latest existing EOS.

The first evaluation that will be carried out is density in single phase. A comparison of statistics can be seen in Table 5. In the liquid phase, the EOS in this study has a better AAD than the data of Di Nicola et al. [16] but worse than Higashi and Sakoda [9]. The opposite condition applies to the MAX data. This result happens because in both data sets, there are data points that are near saturation conditions, so that in these areas, it is difficult to get a good deviation. In the gas phase, the deviation is generally better on Higashi and Sakoda [14] and Yin et al. [14], but worse on Di Nicola et al. [16]. This happens because the fitting process is intended to be closer to the data of Yin et al. [14], which used fluid with higher purity for the experiment.

Comparison of the liquid and saturated density can be seen in Tables 5 and 6, respectively. In general, these two properties have the same statistical comparison. The statistics for Raabe and Marginn data [11] are better than the Akasaka and Lemmon [6] but worse for Higashi and Sakoda [9]. It happened because the data of Higashi and Sakoda [9] are very close to the critical point causing difficulty in the fitting process. This difficulty is due to the structural form of the equation excluding the Gaussian-Bell form. However, the resulting deviation is quite close compared to the equation of Akasaka and Lemmon [6].

Statistical comparison for caloric and ideal properties can be seen in 7. All data on caloric and ideal properties from the equations in this study have better statistics than the Akasaka and Lemmon [6].

6. Conclusion

The new EOS of R-1243zf has the functional form of Helmholtz-free energy. The optimization was conducted using a genetic algorithm and weighted-least squares regression. The EOS can provide accurate results of the thermodynamic properties when compared to the experimental data. In general, the accuracy of the proposed EOS is better than the Akasaka and Lemmon EOS, except for the saturation states. Evaluation for the extrapolation ability consists of thermodynamic properties at temperatures outside the experimental data, ideal curves, and the second and third virial coefficients. Based on the evaluation, this equation has a good extrapolation ability judged by the shape of the curves under the theories of thermodynamics. Further evaluation is needed for the isochoric-specific heat curve due to the lack of available experimental data.

The proposed EOS consists of two parts: the ideal and residual parts. Ancillary equations for properties on saturated condition were also developed to assist the optimization process and to calculate the thermodynamic properties from the EOS. The ideal part was developed with the ideal isobaric specific heat data. The properties derived from ideal part compared to the experimental data yielded an AAD of 0.48%, an STD of 0.25%, and a MAX of 0.94%. The residual part was developed with multi-property input data. In saturation state, there are three properties used, saturated

Table 5. Statistical comparison results of EOS.

Prop.	Data Source	EOS*	Points	Phase	AAD (%)	STD (%)	MAX (%)
PVT	Di Nicola et al. [16]	New	302	Liquid	0.0270	0.0450	0.350
		Exist			0.0330	0.0240	0.0910
PVT	Higashi & Sakoda [9]	New	33	Liquid	0.411	0.340	1.06
		Exist			0.253	0.390	1.12
PVT	Di Nicola et al. [16]	New	99	Gas	0.667	0.510	2.77
		Exist			0.592	0.480	2.35
PVT	Higashi & Sakoda [9]	New	42	Gas	0.548	0.350	1.28
		Exist			0.731	0.520	1.78
PVT	Yin et al. [14]	New	128	Gas	0.245	0.211	0.850
		Exist			0.347	0.195	1.01
p_s	Raabe & Marginn [11]	New	10	-	4.38	2.05	8.69
		Exist			4.40	2.04	8.70
p_s	Brown et al. [12]	New	83	-	0.138	0.168	0.851
		Exist			0.150	0.167	0.834
p_s	Higashi et al. [13]	New	20	-	0.0700	0.0330	0.147
		Exist			0.0260	0.0210	0.0860
p_s	Yin et al. [14]	New	26	-	0.0910	0.0400	0.170
		Exist			0.108	0.0370	0.165
p_s	Yang et al. [15]	New	17	-	0.141	0.135	0.490
		Exist			0.155	0.138	0.504
ρ'	Raabe & Marginn [11]	New	10	-	3.12	1.03	4.35
		Exist			3.29	0.910	4.41
ρ'	Higashi & Sakoda [9]	New	6	-	1.31	0.760	2.56
		Exist			0.790	0.210	0.980
ρ''	Raabe & Marginn [11]	New	10	-	4.58	3.20	10.1
		Exist			4.65	2.79	8.80
ρ''	Higashi & Sakoda [9]	New	7	-	1.88	1.41	3.97
		Exist			1.32	0.960	3.03
c_p^0	Chen et al. [8]	New	11	Gas	0.478	0.252	0.936
		Exist			0.597	0.369	1.32
c_v	Sheng et al. [7]	New	64	Liquid	1.71	0.792	3.29
		Exist			2.35	0.719	3.82
w	Chen et al. [8]	New	92	Gas	0.330	0.234	0.969
		Exist			0.441	0.307	1.29

*Exist is the EOS developed by Akasaka and Lemmon [6]; New is the EOS from this study.

pressure, which has an AAD of 0.96%, an STD of 0.49%, and a MAX of 2.1%; saturated liquid density which has an AAD of 2.2%, an STD of 0.89%, and a MAX of 3.5%; and the saturated vapor density which has an AAD of 3.2%, an STD of 2.3%, and a MAX of 7.1%. In single-phase, for the liquid density data, this equation has an AAD of 0.22%, an STD of 0.19%, and a MAX of 0.71%. For gas density data, this equation has an AAD of 0.49%, an STD of 0.36%, and a MAX of 1.6%. The final data is from the caloric properties, which consist of isochoric specific heat, which has an AAD of 1.7%, an STD of 0.79%, and a MAX of 3.3%; and the speed of sound data which has an AAD of 0.33%, an STD of 0.23%, and a MAX of 0.97%.

Ancillary equations were developed for saturated pressure, saturated liquid density and saturated vapor density. For saturated pressure, the developed ancillary equation has an AAD of 0.96%, an STD of 0.47%, and a MAX of 2.1%. For the saturated liquid density, the ancillary equation in this work has an AAD of 1.9%, an STD of 0.65%, and a MAX of 2.7%; and the saturated vapor density which has an AAD of 2.8%, an STD of 1.9%, and a MAX of 5.8%.

Nomenclature

Symbols

A	Helmholtz free energy [kJ·kg ⁻¹]
AAD	Average absolute deviation
B	Second virial coefficient [dm ³ ·mol ⁻¹]
b	Numerical coefficient
C	Third virial coefficient [dm ⁶ ·mol ⁻²]
c	Specific heat capacity [kJ·kg ⁻¹ ·K ⁻¹]
d	Numerical constant
E	Numerical coefficient
F	Numerical coefficient
G	Numerical coefficient
M	Molar mass [kg·kmol ⁻¹]
MAX	Maximum deviation
N	Numerical Coefficient
R	Gas constant [kJ·kg ⁻¹ ·K ⁻¹]
\bar{R}	Universal gas constant [J·mol ⁻¹ ·K ⁻¹]
s	Specific entropy [kJ·kg ⁻¹ ·K ⁻¹]
STD	Standard deviation
T	Temperature [K]
t	numerical constant
u	Internal energy [kJ·kg ⁻¹]
p	Pressure [MPa]
PVT	Pressure Volume Temperature

W	Weighting factor
w	Speed of sound [$\text{m}\cdot\text{s}^{-1}$]
χ	Sum of weighted least square
<i>Greek Letters</i>	
α	Reduced Helmholtz free energy, A/RT
δ	Reduced density, ρ/ρ_c
θ	Numerical constant
ρ	Density [$\text{kg}\cdot\text{m}^{-3}$]
τ	Inverse reduced temperature, T_c/T
<i>Subscript</i>	
c	Critical parameter
cal	Calculated value
$data$	Input data value
i	Serial number of term
p	Process at constant pressure
s	Saturation
tp	Triple point
v	Process at constant volume
<i>Superscripts</i>	
o	Ideal part
r	Residual part
'	Saturated-liquid state
“	Saturated-vapor state

References:


- [1] UN, *Amendment to the Montreal Protocol on Substances that Deplete the Ozone Layer*, New York: United Nations, 2016.
- [2] B. Gil, J. J. Kasperski, "Efficiency Evaluation of the Ejector Cooling Cycle using a New Generation of HFO/HCFO Refrigerant as a R134a Replacement," *Energies*, 11(8), 2136, 2018, doi: 10.3390/en11082136.
- [3] JSRAE, "Risk Assessment of Mildly Flammable," JSRAE, Tokyo, 2015.
- [4] N. A. Lai, "Thermodynamic Properties of HFO-1243zf and Their Application in Study on a Refrigeration Cycle," *Applied Thermal Engineering*, 70(1), 1–6, 2014, doi: 10.1016/j.applthermaleng.2014.04.042.
- [5] R. Akasaka, "Recent Trends in the Development of Helmholtz Energy Equations of State and Their Application to 3,3,3-Trifluoroprop-1-ene (R-1243zf)," *Science and Technology for the Built Environment*, 22(8), 1136–1144, 2016, doi: 10.1080/23744731.2016.1208000.
- [6] R. Akasaka, E. W. Lemmon, "Fundamental Equations of State for cis-1,3,3,3-Tetrafluoro propene [R-1234ze(Z)] and 3,3,3-Trifluoropropene (R-1243zf)," *Journal of Chemical and Engineering Data*, 64(11), 4679–4691, 2019, doi: 10.1021/acs.jced.9b00007.
- [7] B. Sheng, Z. Li, W. Liu, X. Chen, Y. Zhao, X. Dong, H. Yan, J. Shen, M. M. Gong, "The Isochoric Special Heat Capacity for 3,3,3-Trifluoroprop-1-ene (R1243zf) at Temperatures from (299 to 351) K and Pressures up to 11 MPa," *The Journal of Chemical Thermodynamics*, 153, 106319–106324, 2021, doi: 10.1016/j.jct.2020.106319.
- [8] H. Chen, K. Zhang, Z. Yang, Y. Y. Duan, "Experimental Speed of Sound for 3,3,3-Trifluoropropene (R-1243zf) in Gaseous Phase Measured with Cylindrical Resonator," *Journal of Chemical and Engineering Data*, 66(5), 2256–2263, 2021, doi: 10.1021/acs.jced.1c00098.
- [9] Y. Higashi, N. Sakoda, "Measurements of PvT Properties, Saturated Densities, and Critical Parameters for 3,3,3-Trifluoropropene (HFO1243zf)," *Journal of Chemical and Engineering Data*, 63(10), 3818–3822, 2018, doi: 10.1021/acs.jced.8b00452.
- [10] E. Tiesinga, P. J. Mohr, D. B. Newell, B. N. Taylor, "CODATA Recommended Values of the Fundamental Physical Constants: 2018," *Journal of Physical and Chemical Reference Data*, 50(3), 033105, 2021, doi: 10.1063/5.0064853.
- [11] G. Raabe, E. J. Maginn, "A Force Field for 3,3,3-Fluoro-1-propenes, Including HFO-1234yf," *The Journal of Physical Chemistry B*, 114(31), 10133–10142, 2010, doi: 10.1021/jp102534z.
- [12] J. S. Brown, G. di Nicola, L. Fedele, S. Bobbo, C. Zilio, "Saturated Pressure Measurements of 3,3,3-Trifluoroprop-1-ene (R1243zf) for Reduced Temperatures Ranging from 0.62 to 0.98," *Fluid Phase Equilibria*, 351, 48–52, 2013, doi: 10.1016/j.fluid.2012.09.036.
- [13] Y. Higashi, N. Sakoda, M. A. Islam, Y. Takata, S. Koyama, R. Akasaka, "Measurements of Saturation Pressures for Trifluoroethene (R1123) and 3,3,3-Trifluoropropene (R1243zf)," *Journal of Chemical and Engineering Data*, 63(2), 417–421, 2018, doi: 10.1021/acs.jced.7b00818.
- [14] J. Yin, J. Ke, G. Zhao, S. Ma, "Saturated Vapor Pressure and Gaseous pvT Property Measurements for 3,3,3-Trifluoroprop-1-ene (R1243zf)," *Int. J. of Refrigeration*, 117, 175–180, 2020, doi: 10.1016/j.ijrefrig.2020.04.021.
- [15] Z. Yang, A. Valtz, C. Coquelet, J. Wu, J. Lu, "Experimental Measurement and Modelling of Vapor-Liquid Equilibrium for 3,3,3-Trifluoro propene (R1243zf) and trans-1,3,3,3-Tetrafluoro propene (R1234ze(E)) Binary System," *Int. J. of Refrigeration*, 120, 137–149, 2020, doi: 10.1016/j.ijrefrig.2020.08.016.
- [16] G. di Nicola, J. S. Brown, L. Fedele, M. Securo, S. Bobbo, C. Zilio, "Subcooled Liquid Density Measurements and PvT Measurements in the Vapor phase for 3,3,3-Trifluoroprop-1-ene (R1243zf)," *Int. J. of Refrigeration*, 36(8), 2209–2215, 2013, doi: 10.1016/j.ijrefrig.2013.08.004.
- [17] K. G. Joback, R. C. Reid, "Estimation of Pure-Component Properties from Group-Contributions," *Chemical Engineering Communications*, 57(1–6), 233–243, 1987, doi: 10.1080/00986448708960487.
- [18] R. Span, Multiparameter Equations of State: An Accurate Source of Thermodynamic Property Data,

Berlin: Springer, 2000, doi: 10.1007/978-3-662-04092-8.

- [19] W. Wagner, A. Pruß, "The IAPWS Formulation 1995 for the Thermodynamic Properties of Ordinary Water Substance for General and Scientific Use," *Journal of Physical and Chemical Reference Data*, 31(2), 387–535, 2022, doi: 10.1063 /1.1461829.
- [20] I. M. Astina, G. Budiarmo, R. Harrison, "New Helmholtz Equation of State for HFO-1234ze(E) with Comprehensive Assessment," *Fluid Phase Equilibria*, 531, 112921, 2021, doi: 10.1016/j.fluid .2020.112921.
- [23] E. W. Lemmon, R. T. Jacobsen, "A New Functional Form and New Fitting Techniques for Equations of State with Application to Pentafluoroethane (HFC-125)," *Journal of Physical and Chemical Reference Data*, 34(1), 69–108, 2004, doi: 10.1063/1.179 7813.
- [21] G. Budiarmo, I. M. Astina, "Development of Helmholtz Equation of State for Thermodynamic Properties of R-1233zd(E)," *Int. Journal of Scientific Research in Science and Technology*, 9(3), 765–776, 2022, doi: 10.32628/IJSRST2293 148.
- [22] I. M. Astina, H. Sato, "A Rapid Genetic Optimization Technique for Rational Thermodynamic Modeling Having Reliable Third Virial Coefficient," in *15th Symposium on Thermophysical Properties*, Boulder, 2003.

Research Article

Experimental Investigations on Single-Phase Heat Transfer Enhancement in an Air-To-Water Heat Exchanger with Rectangular Perforated Flow Deflector Baffle Plate

¹*Md A. Rahman 

¹ Department of Mechanical Engineering, Birla Institute of Technology, Mesra, Ranchi, India
E-mail: ¹*rahman.md4u@gmail.com

Received 18 April 2023, Revised 13 August 2023, Accepted 28 August 2023

Abstract

Experimental analysis was conducted to investigate the turbulent heat transfer behaviors within a tubular heat exchanger, incorporating a novel baffle plate design. The new design includes a perforated circular baffle plate with a rectangular flow deflector that can be adjusted to different inclination angles. The baffle plate is strategically positioned at the entrance of the heat exchanger, resulting in a swirling flow downstream. To assess the impact of the baffle plate design, three baffle plates were placed longitudinally along the flow, with varying pitch ratios (l/D). The effects of pitch ratio (ranging from 0.6 to 1.2), deflector inclination angle (ranging between 30° to 50°), and Reynolds numbers (ranging between 16000 to 29000) were examined. The outcomes highlighted the substantial impact of pitch ratio and inclination angle on the thermal enhancement factor. In particular, compared to single segmental baffle plates working under similar operating conditions. The result indicates that an inclination angle of 30° and a pitch ratio of 1 exhibited an average 41.49% augmentation in thermal-fluidic performance compared with an exchanger with a segmental baffle plate.

Keywords: Thermal enhancement factor; flow resistance; inclination angle; swirl flow, re-circulation; rectangular deflector.

1. Introduction

Recent population boom and urbanization have led researchers to focus on efficient energy consumption and utilization. To reduce energy consumption, efficient and compact thermal system designs are adopted. HX (heat exchangers) are standard thermal exchange devices widely used in commercials, industrial and domestic sectors. Some typical applications are cooling in power plants, automobiles, domestic, solar dryers, boilers/steam generators, the chemical processing industry, and waste heat recovery. Thus the demand for energy-efficient HX has led to the development of various heat augmentation techniques [1]. Different strategies of heat transfer enhancement, namely active, passive, and compound methods, are suggested [2, 3] with the mutual objective of plummeting thermal boundary layer thickness to achieve an improved surface heat transfer coefficient.

No outside source of heat transfer is needed for the passive approach. This approach involves altering or extending the surfaces to generate turbulence in the flow field. This turbulence can modify the thermal boundary layer and change the flow pattern. Artificial roughness is the most basic turbulence promoter in this form of passive enhancement. Other turbulence promoters associated with this approach include extended surfaces, swirl devices, and vortex generators.

The presence of artificial roughness breaks up the laminar layer located near the wall and causes turbulence to

form between the ridges. This turbulence is created when the flow separates and attaches itself to the wall again, leaving the main flow pattern unaffected. Geometric constraints of surface roughness like channel aspect ratio (AR), rib angle of attack (α), relative rib pitch (p/e), relative rib height ratio (e/D) along with the rib shape and type (solid, perforated, and slit rib, etc.) have a direct influence on heat transfer coefficients. Prasad and Saini [4, 5] studied transverse ribs on the absorber plate of a solar air heater duct. A maximum increment of 2.38 in the relative Nu and a 4.25 increment in relative f when contrasted to smooth duct, with a relative roughness pitch (p/e) of 10 and relative roughness (e/D) of 0.033. Similar work carried out by Prasad et al. [6]. Lu and Jiang [7] investigated the influence of ribs with an inclination angle of 20° and 60° on the thermo-hydraulic performance and heat transfer rate. The research results revealed that the maximum performance and heat transfer rate was achieved at these two angles. Liu et al. [8] experimented to study the consequence of different constraints on a rectangular channel with opposite walls having grooves of different relative pitch (p/e), aspect ratio (W/H), angle of attack (α), and blockage ratio (e/D). The parameters used for the experiment ranged from 0.25 to 1 for p/e , 45 to 60 degrees for angle of attack, and 0.047 to 0.078 for blockage ratio. An attack angle of 45 degrees shows Nu rise by 15-25%.

Another effective technique is to increase the effective heat transfer area and add turbulence to the flow. This method includes extended surfaces as fin/baffles, negatively

impacting pressure drop and requiring higher pumping power. Experimental examination on heat transfer and friction loss by Sriromreum et al. [9] on a zigzag Z-baffle (45°) with relative height and relative pitch range of baffles were of 0.1–0.3 and 1.5–3, respectively. Nu and f were improved significantly for in-phase 45° Z-baffles rather than its counterpart (out-phase 45°). Kwankaomeng et al. [10] numerically studied angled inclined baffles with an attack angle of 30° under a laminar flow regime. The BR and PR variations of (0.1–0.5) and (1–2) revealed an enhancement in Nu and f of 9.23 and 45.31, respectively, for PR of 1.5 and BR of 0.3.

Priyam et al. [11]. Studied the effect of fin pitch and mass flow rate of transverse wavy fins. The results showed an enhancement in thermal efficiency of 62.53, and an effective temperature rise of 63.41%, respectively. Gawande et al. [12] experimental and numerical investigation on an absorber plate with L-shape ribs, with relative roughness, pitch relative rib height range of 7.14–17.86. Results indicated maximum enhancement in Nu and f of 2.827 and 3.424 at a relative pitch of 7.14.

A more recent and promising heat transfer enhancement technique is swirl flow devices. The technique augments heat transfer by applying a twisted tape in the flow stream that can generate swirls by trimming the boundary layer by generating a secondary flow in vortices along an existing axial flow. Recently various swirl devices have been tested, such as conical rings, helical wire, and twisted tapes.

Ard et al. [13] evaluated the effects of wing position (h/e) of square-wing perforated slanting baffles on the heat transfer rate and Δp characteristics in a rectangular channel with air as working fluid drawn in using 3 HP blower and base plate ($L \times W$) heated using 1.0 KW heater. The baffle pitch ratio (p/e) was constant at 5.0, with testing done at different Re values 6000, 9000, 12,000, 15,000, 18,000, 21,000, and 24,000 with four different wings location (h/e) 0.92, 0.83, 0.75, and 0.67. Results showed that the highest heat transfer rates accomplished in channels at the four locations were 148%, 157%, 166%, and 180% compared to smooth channels, while the pressure losses increased 9.51–10.99 times, respectively. Additionally, SW-PBs caused lower Δp than solid transverse baffles and higher thermal performance.

Sanchouli et al. [14] explored the prospective to enhance the heat transfer capabilities of phase change material (PCM) in an HX with a double-tube design by incorporating innovative ring-shaped fins with a lattice structure. These lattice ring-shaped fins, which consisted of straight and circular strip modules, were located on the inner tube. To compare the thermal efficiency of the lattice ring-shaped fins with traditional ring-shaped fins, they ensured that an equal amount of fins was used for the comparison. They also examined how the spacing between the fins (longitudinal pitch) affected the duration of the melting process and the PCM's energy storage capacity. They compared the findings between the lattice and conventional ring-shaped fins.

The domino effect showed that converting the ring-shaped fins to lattice fins reduced the melting time by 27%, 37.5%, 53.5%, and 69.5% for longitudinal pitches of 125 mm, 62.5 mm, 31.25 mm, and 15.625 mm, respectively. Among the different longitudinal pitches, the lattice fins with a spacing of 31.25 mm exhibited the highest thermal performance. The study also emphasized the significance of the arrangement of the lattice ring-shaped fin components in achieving optimal thermal performance. The total melting

time of the PCM was improved by 40% compared to the case with a longitudinal pitch of 125 mm, demonstrating the advantages of the 31.25 mm spacing. The study also considered a non-uniform distribution of lattice components for the ring-shaped fins and observed a 16% enhancement in the full melting time matched to the best ring-shaped fins with a uniform lattice distribution.

Rahman and Dhiman [15, 16] examined the effect of a novel trapezoidal perforated baffle plate on PEC used in air-water HX. The baffle plate was equipped with a trapezoidal flow deflector with its larger end attached to the baffle plate at different α . The effect of PR, α , and flow orientation (parallel and counter flow) on the TEF was studied. The result showed that the TEF is a noteworthy function of PR and α . Specifically, in the range of Re from 16000 to 28000, the duct with perforated flow deflector baffle plates achieved an average of 3.75 times higher performance with a deflector with α of 50° and PR of 1.4. Additionally, when the flow orientation changed from parallel to counter flow, there was an average 7.4% improvement in PEC when the deflector with α was set to 30° , with the highest HX effectiveness observed at lower α and high PR values.

Alam et al. [17] experimentally studied twisted tape inserts of various twist and pitch ratios as heat transfer enhancement devices. The result was an 18–70% increase in heat transfer rate and an 87–132% increase in pressure drop with Re range of 4000 to 10000. Guo et al. [18] numerically investigated the center-cleared twisted tape for heat transfer enhancement, showing an improvement of 7–20% in thermal performance compared to conventional twisted tape

Thianpong et al. [19] studied the combined effect of twisted tape inserted inside a dimpled tube under a turbulent flow regime. Three different twist ratios (3, 5, and 7) and PR (0.7–1) were tested. The result showed that the combined effect of twisted tape and dimples is more prominent on heat transfer and friction factor than dimple or plain tube acting alone. Esmaeilzadeh et al. [20] experimental investigation of heat transfer and pressure drop in a circular tube equipped with a twisted tape of varying thicknesses (0.5–2 mm) revealed that thick tapes are more effective. Bhuiya et al. [21] investigated double counter twisted tapes with varying twist ratios (1.95 to 7.75). A maximum of 240% increase in the heat transfer rate and a 286% increase in friction factor were reported.

The above literature examined various turbulator designs to enhance heat transfer. Emphasis was placed on devices that create swirls to manipulate the flow path, resulting in increased fluid mixing and turbulence. This ultimately leads to enhanced heat transfer within the flow regime. Further, it can also be concluded that turbulators with lower α and baffles with lower PR and lower perforation ratio show the highest Nu compared to smooth duct flow with a parallel rise in Δp . The swirl flow brings along a toroidal recirculation zone. It generates secondary flow, and additional vortices formation, which constantly washes the heat transfer surface area, reducing the thermal boundary layer and increasing hm .

A novel swirler is fabricated and tested in this current hooping for a better TEF index. The swirler is a flat circular perforated baffle plate with a rectangular flow deflector. The flow deflector is attached at different α (angle made by deflector with baffle plate surface). The baffle plate is placed at the entry of the test section to produce a decaying swirl flow, which increases the duct fluid residual time and generates near-wall turbulence [22]. Increasing the number of baffle plates in the longitudinal direction leads to flow

reversal/recirculation, further enhancing turbulence. The Pitch ratio (PR) term defines the distance between the baffle plates. The research was conducted in a circular duct to investigate the impact of changing the PR and α on heat transfer and f . Various PR, ranging from 0.6 to 1.2, and four α (30° , 40° , and 50°) were tested under identical inlet conditions. The Re, estimated using D_h , ranged from 16000 to 28000. The superiority of different configurations was determined by comparing the results of ducts equipped with deflector baffle plates (DBP) to ducts with SBP having the same BR, PR, and Re.

2. Methodology

2.1 Experimental Setup

The experimental setup shown in Figure 1 consists of an axial flow fan, a mixing device, a straightener, a heat exchanger (HX), thermocouple probes, an orifice plate, pressure transducers, and a data acquisition system. The fan sucks atmospheric air from the environment and runs it through the air duct. The air flows through the mixing device and straightener before entering the HX. Temperature probes are installed at the inlet ($T_{a, in}$) and outlet ($T_{a, out}$) portions of the HX as ASHRAE standard recommended [23], and calibrated T-type copper-constantan thermocouples probes are used to measure the air temperature. Orifice plates are operated according to the ISO5801 standard to measure the airflow rate. Pressure ports are also generated, located at 120° angle to the center of the baffle plate, with 3 on the inlet and 3 on the exit side. A VDAS DAQ card, with a differential transducer of 0-1 psi, is used to measure the pressure drop and the LabVIEW program records the data. The water is heated to a constant temperature of 60°C by 8 kW electrical heating elements controlled by a thermostat. The airflow rate is calculated using Eq. (4) and (5), using data from the orifice plate.

Consistency of liquid characteristics (density and temperature) inside the bathtub is ensured using mechanical mixers. A 0.25 hp feed pump, a flow regulating valve, and a flow-measuring device are being used to manage the quantity of hot liquid, which is available continuously at 4 LPM with the help of the flow-measuring device into a header from which it is evenly spread to a heat exchanger tube network. The tubes have been mounted in the HX on baffles that are spaced out at regular intervals. Details of the baffles and the position of the tubes can be found in the following paragraph. RTDs of the PT100 type have been employed to measure the temperature of the hot water-carrying piping at various points in the testing arrangement. A constant LPM of hot water at a set inlet temperature is provided throughout the trial while adjusting the flow rate of air circulation. Before recording data, the system was let to reach a steady state. The

temperatures of the air entering and exiting the HX and the surface temperature of the copper tubing were recorded after the HX had been stabilized, and the repeatability of the experimental outcome was verified thrice and an average standard deviation of 1.46. The root mean square was utilized to evaluate the precision of the immediate measuring device, and Table 1 displays the conditions under which the heat exchangers were tested. Coleman and Steele [24] gave two tables (2 and 3) illustrating the uncertainties involved.

Table 1. Testing conditions used in experiments.

Air-intake temperature	$32.5 \pm 0.5^\circ\text{C}$
Air-intake velocity	7- 10 m/s
Water-intake temperature	$60 - 65^\circ\text{C}$
Mass flow rate of water,	0.06 kg/s

Table 2. Precision with measurements.

Variable	Accurateness
Temperature of air-intake, $^\circ\text{C}$	± 0.5
Δp , Pa	± 0.1
Temperature of water-intake, $^\circ\text{C}$	± 0.5
Flow rate of water, kg/s	± 0.006

Table 3. Uncertainties in the experimental data.

Variables	Max skepticism (%)
Re	± 3.25
Nu_m	± 3.45
v	± 5
f	± 5.34
Q	± 5

2.2 Test Section Details

The part of the system shown in Figure 2 consists of Plexiglas with $kp=0.2$. It has a length of 60 cm, an internal diameter (ID) of 19 cm, and a thickness of 0.5 cm. Running parallel to this Plexiglas is a channel in which DHP Copper tubes, C12200, of $k_r=300$ with ID 8mm and thickness 1mm have been installed. The warm liquid or gas is transported through copper pipes, while the air from the environment is directed through the duct. Two series of thermocouples are employed to determine the temperature of the copper pipes, with each set composed of five thermocouples for each pipe.

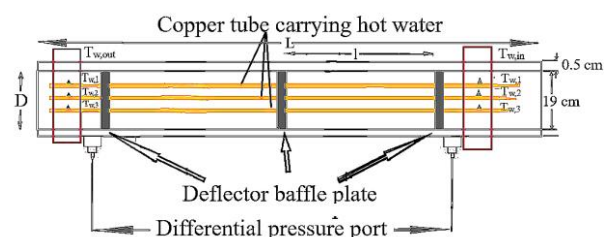


Figure 2. Test section.

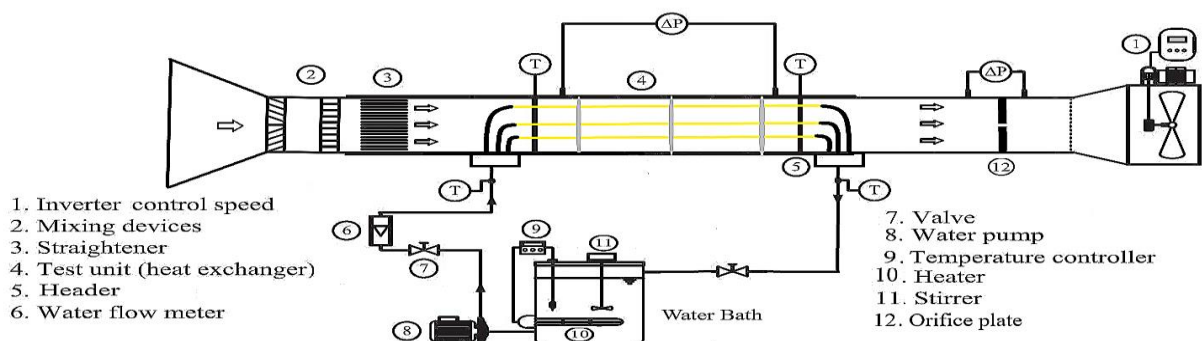


Figure 1 The experimental setup's schematic. [15].

These thermocouples, labeled T_{w1} - T_{w5} , are used to record the temperature of the copper pipe inlets and outlets. To further analyze the air temperatures at the inlet and exit of the test section, $T_{a, in}$, and $T_{a, out}$ thermocouples, are added.

2.3 Baffle Plate with Tube Arrangement

Figure 3(a) and (b) show the novel DBP and SBP, respectively, with one tube at the center and four arranged in a circular array 4cm away from the center of the baffle plate. The dimensions of the rectangular perforation seen in Figure (a) are estimated by equating the BR for DBP and SBP estimated using Equation .2. The novel baffle plate shown in

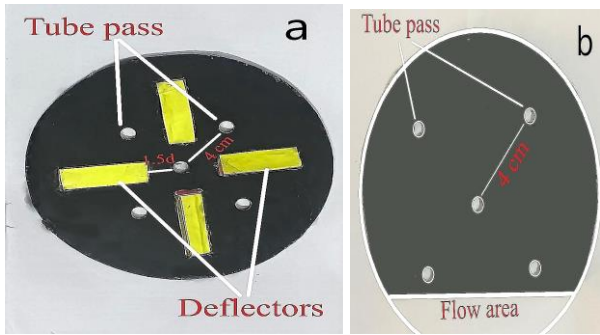


Figure.3(a). DBP five tube configurations, (b). SBP.

Figure 4 (a) with a pictorial view in Figure 4(c) is made of a 5mm Plexiglas sheet cut into circular cross-sections of 19mm diameter using a CNC glass-cutting machine. Later four rectangular holes of (5d x 1.5d) and a center distance of 1.5d are punched in the Baffle plate at an angle of 90 °with each other, which allows air inflow in the test section. Four deflectors of the identical dimension as the rectangular opening (made of 3mm Plexiglas) have been fixed at the preferred inclination angle (α) to the baffle plate, as seen in Figure 4 (b). The inclination of the deflectors thus generates a passage for air, called a flow area of constant height (h). This configuration aids in transitioning the airflow from an axial to a swirling flow. As a result of the deflector, the flow between the baffle plates becomes circular, and the airflow morphs into a smooth swirling pattern as it passes through the tube bundles. When " α " is present, the axial flow intensifies and transforms into a plug flow. The spinning motion increases pressure and enhances a significant portion of the heat transfer between the baffle plates. The distance between the baffle plates dictates the turbulence and circulation within the channel, making the baffle plate's pitch ratio, (PR) important. Values of 0.6, 0.8, 1, and 1.2 were investigated to examine the influence of PR. Consequently,

the rotational air structures bring forth turbulence and foster the formation and movement of vortices within the duct. This leads to continuously washing the tube wall and manipulating the thermal boundary layer. The study encompasses three α angles, namely 30°, 40°, and 50°. This configuration creates an opening that allows air to circulate, effectively functioning as a flow area.

2.4 Design Constraint under Investigation

PR [19, 20] is estimated as

$$PR = \frac{l}{D} \quad (1)$$

BR [25] is estimated as

$$BR = \frac{K}{A} \quad (2)$$

Where, K=cross-sectional area of baffle plate - (4 times the cross-sectional area of the rectangular opening) and, A=cross-sectional area of the baffle plate.

This study assessed the flow of DBP in a round conduit with a constant BR of 0.70 for a longitudinal flow at distinct Re with samples at three different angular inclinations (30°, 40°, and 50°). A further experiment was conducted with a duct without SBP of the same BR at comparable Re ranges. The outcomes of the examination were then examined to determine the impact of PR and α on the TEF of the HX.

2.5 Data Reduction

Cao's [26] technique is employed to assess h_m . These governing parameters are listed below.

$$Re = \frac{\rho v D_h}{\mu} \quad (3)$$

The average bulk temperature of the air-side intake and outlet is utilized to assess the thermal properties of air, such as ρ and μ (viscosity).

$$v = \sqrt{\frac{2\Delta P_0}{\rho}} \quad (4)$$

$$Q_{air} = C_f A_0 \sqrt{\frac{2\Delta P}{\rho}} \quad (5)$$

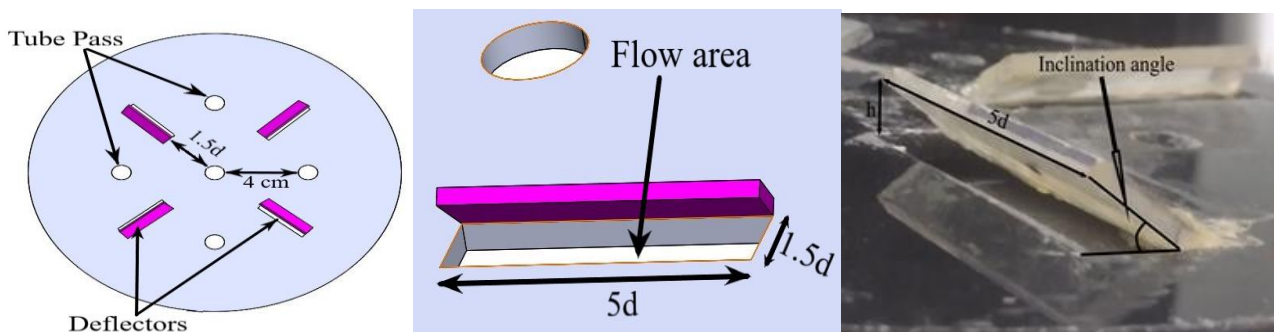


Figure 4 (a). DBP has five tube arrangements, (b).Flow area details, (c) Inclination angle.

$$h_m = \frac{Q}{A_p \Delta t_{lm}} \quad (6)$$

$$Q = C_p \rho v A_c (T_{a,out} - T_{a,in}) \quad (7)$$

The air temperature entering the test section is labeled as $T_{a,in}$, while the temperature of the air as it exits is referred to as $T_{a,out}$, Δt_{lm} is calculated as

$$\Delta t_{lm} = \frac{(t_{w,in} - t_{a,in}) - (t_{w,out} - t_{a,out})}{\ln \left(\frac{t_{w,in} - t_{a,in}}{t_{w,out} - t_{a,out}} \right)} \quad (8)$$

The average copper tube wall is calculated by finding the average inlet temperature ($t_{w,in}$) and the outlet temperature ($t_{w,out}$).

$$t_{w,in} = \left[\frac{\sum_1^5 T_{w,i} A_i}{A_p} \right]_{in}, t_{w,out} = \left[\frac{\sum_1^5 T_{w,i} A_i}{A_p} \right]_{out} \quad (9)$$

For each of the sections specified by subscript i , where i is 1-5, the heat transfer area, A_i , is associated with the location of a thermocouple on the tube carrying hot water in the test section at the inlet and outlet concerning the direction of airflow.

Average Nu , f , and j describe the thermal and flow characteristics.

$$Nu = \frac{h_m D_m}{\lambda} \quad (10)$$

$$j = \frac{Nu}{Re Pr^{1/3}} \quad (11)$$

$$f = \frac{2 \Delta p D}{\rho v^2 L} \quad (12)$$

From Equations 5 and 6

$$h_{c,m} = \frac{C_p \rho v A_c (T_{a,out} - T_{a,in})}{A_p \Delta t_{lm}} \quad (13)$$

Dimensionless factors like (j/j_0) , (f/f_0) , and $[TEF = (j/j_0)/(f/f_0)^{1/3}]$ respectively were used. Using the measured values of f_0 and j_0 of a duct without baffles as benchmarks, compare the corresponding values (f and j) of the duct installed with DBP [15,16].

3. Result and Discussion

3.1 Authentication of the Experimental Outcome

The Nu_m and f obtained from the experiment are compared with correlation Eq. (10) and (12) for precise measurement.

Nu correlations:

a) Dittus and Boelter correlation [27]

$$Nu_s = 0.023 Re^{4/5} Pr^{0.4} \quad \text{For } Re \geq 1 \times 10^4 \quad (14)$$

b) Gnielinski

$$Nu_s = \frac{\left(\frac{f}{8} \right) (Re - 1000) Pr}{\left[1 + 12.7 \left(\frac{f}{8} \right)^{1/2} (Pr^{2/3} - 1) \right]} \quad (15)$$

The correlation is valid for $0.5 \leq Pr \leq 2000$ and $3000 \leq Re \leq 5 \times 10^6$

Friction factor correlation:

a) Colebrook-White correlation [28]:

$$\frac{1}{\sqrt{f}} = 1.8 \log \left(\frac{Re}{6.9} \right) \quad \text{For } 4000 \leq Re \leq 10^8 \quad (16)$$

b) Blasius

$$f = 0.316 Re^{-0.25} \quad \text{for } 3000 \leq Re \leq 5 \times 10^6 \quad (17)$$

The deviation between experimental results and the outcomes obtained using correlation, as shown in Figure 5, confirms the accuracy of the experimental findings. The absolute deviation between these results is indicated in Table 4.

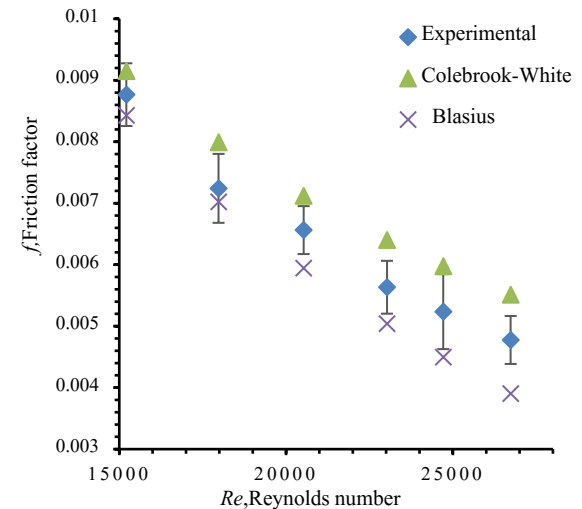
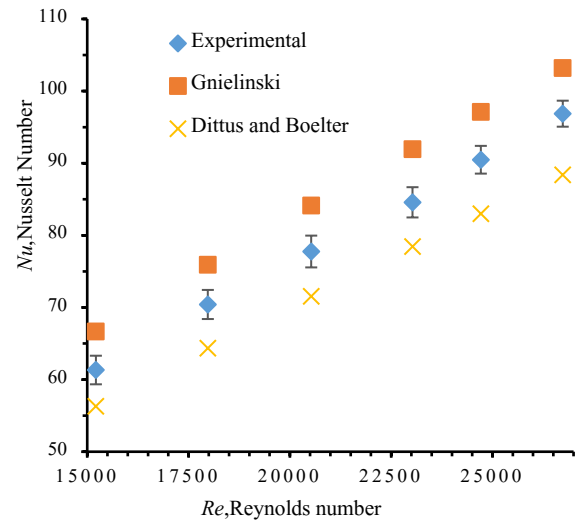


Figure 5. Contrast of Nu and f for duct without baffle plate (Nu_s vs. ;(b) f vs. Re).

Table 4. Average Deviance from Empirical Correlation.

	Nu		f
Correlation used↓	Avg. Deviation i n %	Correlatio n used↓	Avg. deviation i n %)
Dittus and B oelter	-8.180	Colobroo k	+11.066
Gnielinski	+9.054	Blasius	-9.88

3.2 Heat Transfer Augmentation

The presence of a deflector baffle contributes to a significant boost in heat transfer rate over the specified Re range due to the development of powerful reverse flow and the destruction of the thermal boundary layer. Figure 6 shows the fluctuation in relative j/j_0 with Re . The j/j_0 values for DBP rise with a rise in Re to attain a maximum value beyond which it decreases. This fashion in j/j_0 is analogous to all the inclination angles of DBP. DBP with a smaller inclination angle ($\alpha=30^\circ$) shows the highest relative values compared to others α . In turbulent motion, the energy associated with the random fluid motions, known as eddy energy, is transferred throughout the fluid. This random motion creates many small convective cells, allowing heat transfer to occur faster than in a laminar flow because these cells can transport a considerable amount of energy through a large area. Additionally, eddies increase the effective surface area for

near the tube and duct wall. Thus, it is unavoidable that a higher pressure loss will be incurred to increase the heat transfer rate. As revealed in Figure 6, due to the sudden decline in flow passage area for baffles with smaller α , the duct side fluid velocity increases, which results in a jet effect and destruction to the boundary layer formation over the tube and wall, also the fluid revolution washes the tube bundles. The spiral motion produces good mixing, directly leading to improved heat transfer. Moreover, a higher flow velocity enhances the duct-side fluid flushing ability.

As Re further increases, the flow velocity also increases. This higher velocity can cause a reduction in the residence time of the fluid near the heat transfer surface. As a result, there may be insufficient time for effective heat exchange to occur, leading to lower heat transfer rates. Furthermore, the flow may exhibit a more fully developed turbulent profile at higher Re , resulting in a thicker inertial sublayer near the surface, which acts as a thermal resistance, impeding heat transfer. An increase in Re can lead to the forming of flow separation or recirculation zones. These stagnant regions can restrict heat flow and reduce heat transfer efficiency. While it is generally expected that higher Re would correspond to higher heat transfer rates, in current cases, the above factors can lead to a decrease in heat transfer with the rise in Re , and the optimum Re and PR values for efficient heat transfer are shown in Table 5. The study by Wang et al. [29] showed the importance of PR , indicating that downstream vortex flow increases with decreasing the down-wash spacing. However, if the spacing is too small, the interaction between the vortex flows will be strong, causing vortex break-up and decreasing heat transfer enhancement. In contrast, larger spacing's will result in too rapid separation of vortex flow from the boundary layer, consequently leading to high-pressure losses. Thus, it is essential to have an appropriate down-wash baffle plate (PR) spacing to maximize heat transfer. To understand the effect of PR , averaged values of relative j/j_0 shows that max relative j/j_0 is obtained at a lower α value and were plotted against PR for different α values. Figure.8 PR value, which explains Wang's claim regarding the secondary flow, vortex formation, and flow reattachment. As depicted in Figure. 7, fluctuating average (j/j_0) occurs with the PR change. The turbulence intensity between the baffle plates changes with PR ; hence heat transfer rate will fluctuate.

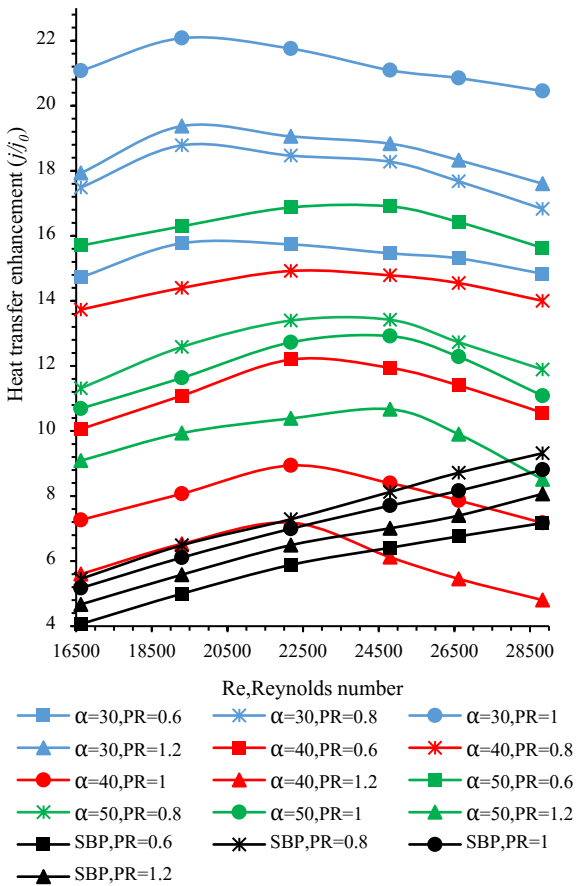


Figure 6. Effect on j/j_0 , with the change in Re .

heat to be conducted from one particle to another, thus accelerating the diffusion process. The circulation of eddies also creates regions of low and high pressure, replenishing the depleted energy necessary for the convection process

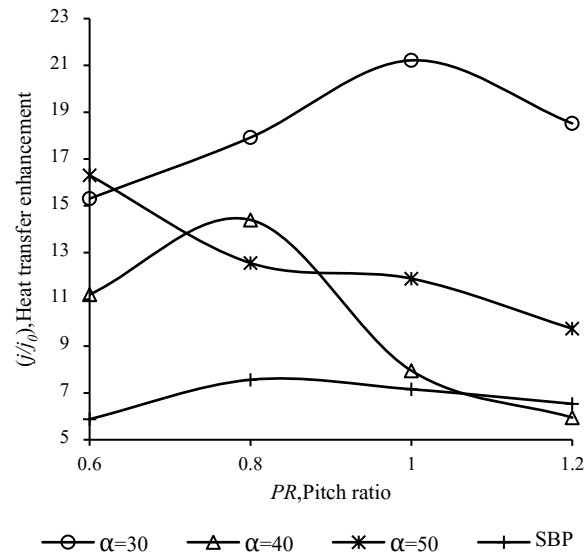


Figure 7. Effect of Averaged (j/j_0) on PR .

Averaged relative j/j_0 is higher for smaller α values and attains a maximum of 21.21 at PR=1 for $\alpha=30^\circ$.

Table 5. Maximum (j/j_0) values.

α	PR	(j/j_0)	Re	% rise compared to SBP
30	1	21.21	18500	62.88
40	0.8	14.39	22100	31.30
50	0.6	16.30	24700	46.25

At a smaller α value, the maximum average (j/j_0) value is noted at a larger PR value and reduces with a surge in α value. An extreme of 21.21 with a percentage rise of 62.88 % in relative Colburn factor is noted when PR=1 and $\alpha=30^\circ$, shown in Table.5, compared to SBP.

3.2 Flow Resistance and TEF

The coefficient of friction was derived from Eq. (12). As shown in Figure 8, the relative friction value (f/f_0) is compared to the Re. In the corresponding range of Re, the Conduit installed with DBP can be expected to present greater flow resistance due to the obstruction in the stream direction. All DBP samples exhibited a similar pattern, exhibiting lower values when the Re was low, gradually increasing with a rise in Re. it is envisioned that the magnitude of the pressure will be in a descending fashion ($\alpha=30^\circ, 40^\circ, 50^\circ$) due to the augmented airflow restriction and vigorous turbulence associated with increased inclination

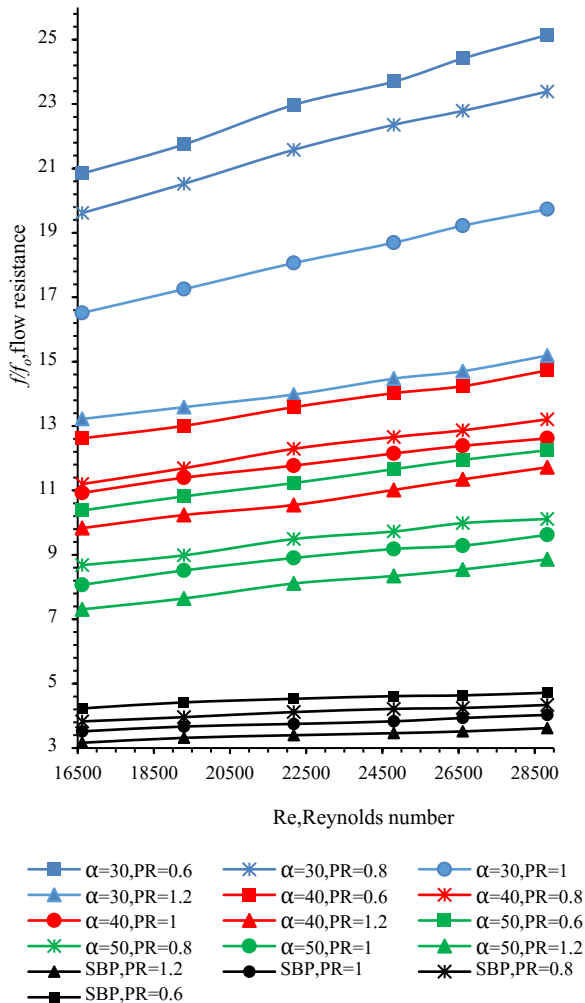


Figure 8. Effect of f/f_0 on Re.

angles resulting in augmented thermal exchange yet intensified friction loss noted when $\alpha=30$. Consequently, noteworthy pressure drops are revealed as velocities expand, turbulence intensifies, and further connections between the fluid and boundary occur, as seen in Figure 8.

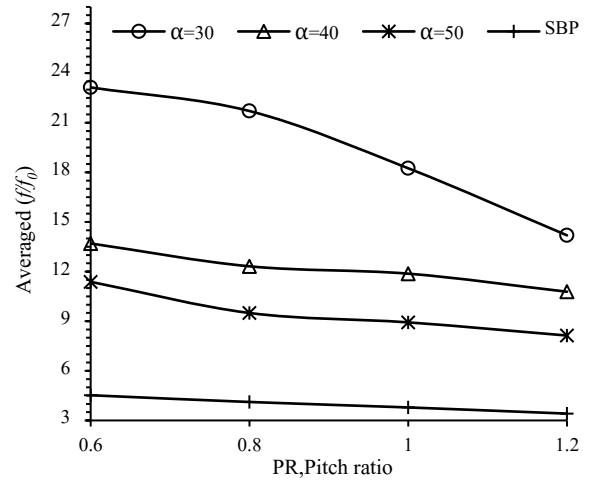


Figure 9. Consequence of α on Average f/f_0 Vs. PR.

Figure 9 demonstrates that the averaged f/f_0 increases as the value of PR and α decreases, reaching a maximum of 23.136 when PR is 0.6, and α is 30° . This can be attributed to a deflector acting as a fluid obstruder, which means that the flow of kinetic energy is lost, resulting in a pressure drop. The minimum value of α provides a powerful swirling flow, increasing the contact between the secondary flow and the duct wall, producing more turbulence and swirl. Due to the vortex formation from several baffles, the flow resistance increases, leading to a significant pressure drop.

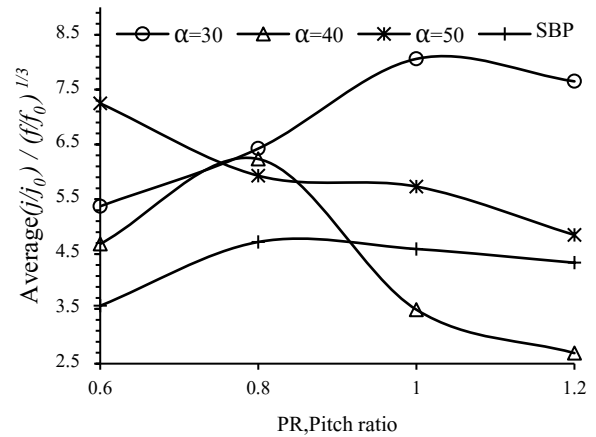


Figure 10. Effect of α on Reynolds average $(j/j_0)/(f/f_0)^{1/3}$ Vs. P_R .

It is observed from Figure 10 that an average increase of 37.43% in TEF value is observed for $\alpha=30$ when compared to SBP. It can also be concluded that lower α and larger PR values are fruitful for a given Re range. The average rise in TEF compared to SBP is shown in Table 6.

4. Conclusion

Upon comparing DBP samples, it is noted that:

The incline angle of the duct showed a considerable impact on the flow velocity; with a tilt of $30^\circ, 40^\circ$, and 50° ,

Table 6. Averages TEF values.

α	PR	value	% rise compared to SBP
30	1	8.05	41.49
40	0.8	6.23	24.39
50	0.6	7.28	35.30
SBP	0.8	4.71	-----

the velocity was discovered to have increased by 28.07%, 18.57%, and 1.23%, respectively, when compared to the duct with SBP.

The maximum relative j/j_o is at lower Re and lower α for the given Re range. Current HX works best with lower α and higher PR values.

Flow Resistance reduces with an increase in α . The average flow resistance usually reduces with increased PR value but is maximum at PR=0.6.

The average TEF increases with an increase in α and is maximum at $\alpha=30^\circ$ with a value of 8.05 at PR=1

The effect of Pr is negligible due to the working fluid air and the temperature range. Further study needs to be done to explore the user of other liquids such as water, oil, or slurry to explore the possibility of this novel design in shell and tube heat exchangers, exhaust gas heat recovery, gas turbines, and other process industries.

Acknowledgements:

The authors express their gratitude for the facility, help, and support from the Department of Mechanical Engineering, BIT-Mesra, India.

Nomenclature

HX	Heat exchanger
Nu	Nusselt number
TEF	Thermal Performance Factor
R	Thermo-fluid performance
Re	Reynolds number
PR	Pith ratio
f	Friction factor
BR	Blockage ratio
DBP	Deflector baffle plate
SBP	Segmental baffle plate
D	Duct inner diameter
d	Tube outer diameter
v	Average axial velocity (m/s)
D_h	Hydraulic diameter
ΔP	Pressure drop is the test section's (Pa)
Q	Heat transfer rate for air (Watts)
A_p	Heat transfer surface area (m ²)
ΔP_o	Pressure drop in orifice plate in (Pa)
Δt_{lm}	LMTD (Duct and tube wall)
α	Inclination angle
l	Distance between baffle plate(m)
A_c	Flow area (m ²)
D_e	Equivalent diameter (m)
k_p	Thermal conductivity of Plexiglass (W/mK)
k_t	Thermal conductivity of Copper tube (W/mK)
λ	Thermal conductivity of air
ρ	Density of air (kg/m ³)
Pr	Prandtl number of air
h_m	Avg convective heat transfer coefficient (W/m ² .K)
μ	Coefficient of dynamic viscosity (kg/m.s)
Q_{air}	Air discharge

References:

- [1] R.I.Webb, *Principles of Enhanced heat transfer, 1st Ed.* New York: John Wiley-Interscience, 1994.
- [2] A.E. Bergles, "Heat transfer enhancement – the encouragement and accommodation of high heat fluxes," *J. Heat transfer.*, 119, 8–19, 1997, <https://doi.org/10.1115/1.2824105>
- [3] M.Sheikholeslami, M.Gorji-Bandpy, D.D.Ganji, "Review of heat transfer enhancement methods: Focus on passive methods using swirl flow devices," *Renew. Sustain. Energy Rev*, 49, 444–469, 2015, <https://doi.org/10.1016/j.rser.2015.04.113>
- [4] B.N.Prasad, J.S.Saini, "Effect of artificial roughness on heat transfer and friction factor in a solar air heater," *Sol Energy.*, 41,555–60, 1988, [https://doi.org/10.1016/0038-092X\(88\)90058-8](https://doi.org/10.1016/0038-092X(88)90058-8)
- [5] B.N.Prasad, J.S.Saini, "Optimal thermohydraulic performance of artificially roughened solar air heaters," *Solar.*, 47, 91–6, 1991, [https://doi.org/10.1016/0038-092X\(91\)90039-Y](https://doi.org/10.1016/0038-092X(91)90039-Y)
- [6] B.N.Prasad, A.Kumar, K.D.P.Singh, "Optimization of thermo hydraulic performance in three sides artificially roughened solar air heaters," *Sol Energy.*, 111,313–9, 2015, <https://doi.org/10.1016/j.solener.2014.10.030>
- [7] B.Lu, P.X.Jiang, "Experimental and numerical investigation of convection heat transfer in a rectangular channel with angled ribs," *Exp Therm Fluid Sci.*, 30,513–21, 2006, <https://doi.org/10.1016/j.expthermflusci.2005.09.007>
- [8] J.Liu, J.Gao, T.Gao, X.Shi, "Heat transfer characteristics in steam-cooled rectangular channels with two opposite rib-roughened walls," *Appl Therm Eng.*,50,104–11, 2013, <https://doi.org/10.1016/j.applthermaleng.2012.05.003>
- [9] P.Sriromreun, C.Thianpong, P.Promvonge, "Experimental and numerical study on heat transfer enhancement in a channel with Z-shaped baffles," *Int Commun Heat Mass Transf.*, 39,945–52, 2012, <https://doi.org/10.1016/j.icheatmasstransfer.2012.05.016>
- [10] S.Kwankaomeng, P.Promvonge, "Numerical prediction on laminar heat transfer in square duct with 30° angled baffle on one wall," *Int Commun Heat Mass Transf.*, 37, 857–66, 2010, <https://doi.org/10.1016/j.icheatmasstransfer.2010.05.005>
- [11] A.Priyam, P.Chand, "Thermal and thermohydraulic performance of wavy finned absorber solar air heater," *Sol Energy.*, 130,250–9, 2016, <https://doi.org/10.1016/j.solener.2016.02.030>
- [12] V.B.Gawande, A.S.Dhoble, D.B.Zodpe, S.Chamoli, "Experimental and CFD investigation of convection heat transfer in solar air heater with reverse L-shaped ribs," *Sol Energy.*,131,275–95, 2016, <https://doi.org/10.1016/j.solener.2016.02.040>
- [13] S.Eiamsa-Ard, A.Phila, M.Pimsarn, "Heat transfer mechanism and thermal performance of a channel with square-wing perforated transverse baffles installed: effect of square-wing location," *J Therm Anal Calorim.*, 2023, <https://doi.org/10.1007/s10973-022-11937-w>

- [14] M. Sanchouli, S. Payan, A. Payan, S.A.Nada, "Investigation of the enhancing thermal performance of phase change material in a double-tube heat exchanger using grid annular fins," *Case Stud. Therm. Eng.*, 34, 101986, 2022, <https://doi.org/10.1016/j.csite.2022.101986>
- [15] M.A.Rahman, S.K.Dhiman, "Performance evaluation of turbulent circular heat exchanger with a novel flow deflector-type baffle plate," *J Eng Res.*, 100105, 2023, <https://doi.org/10.1016/j.jer.2023.100105>
- [16] M. A. Rahman, S.K.Dhiman, "Investigations of the turbulent thermo-fluid performance in a circular heat exchanger with a novel flow deflector-type baffle plate," *Bull. Pol. Acad. Sci.: Tech.*, 2023, doi: 10.24425/bpasts.2023.145939
- [17] T.Alam, M.Kim, "Numerical study on thermal hydraulic performance improvement in solar air heater duct with semi ellipse shaped obstacles," *Energy.*, 112,588–98, 2016, <http://dx.doi.org/10.1016/j.energy.2016.06.105>
- [18] J. Guo, A.W. Fan, X.Y. Zhang, W. Liu, "A numerical study on heat transfer and friction factor characteristics of laminar flow in a circular tube fitted with center-cleared twisted tape," *Int. J. Therm Sci.*, 50, 1263–1270, 2011, <https://doi.org/10.1016/j.ijthermalsci.2011.02.010>
- [19] C.Thianpong, P.Eiamsa-ard, K.Wongcharee, S.Eiamsa-ard, "Compound heat transfer enhancement of a dimpled tube with a twisted tape swirl generator," *Int Commun Heat Mass Transf.*,36,698–704, 2009,<https://doi.org/10.1016/j.icheatmasstransfer.2009.03.026>
- [20] E.Esmaeilzadeh, H.Almohammadi, A.Nokhosteen, A.Motezaker, A.N.Omrani, "Study on heat transfer and friction factor characteristics of Al₂O₃ water through circular tube with twisted tape inserts with different thicknesses," *Int J Therm Sci.*, 82, 72–83, 2014, <https://doi.org/10.1016/j.ijthermalsci.2014.03.005>
- [21] M.M.K.Bhuiya, A.S.M.Sayem, M.Islam, M.S.U.Chowdhury, M.Shahabuddin, "Performance assessment in a heat exchanger tube fitted with double counter twisted tape inserts," *Int Commun Heat Mass Transf.*,50,25–33,2014, <https://doi.org/10.1016/j.icheatmasstransfer.2013.11.005>
- [22] A.Durmus, M.Esen, "Investigation of heat transfer and pressure drop in a concentric heat exchanger with snail entrance," *Appl Therm Eng.*, 22(3), 321–32, 2002, [https://doi.org/10.1016/S1359-4311\(01\)00078-3](https://doi.org/10.1016/S1359-4311(01)00078-3)
- [23] ASHRAE Handbook-Fundamental, *Principles of Heating, Ventilation and Air-conditioning Engineers*, 8th Ed. Atlanta: American Society of Heating, Refrigerating and Air-Conditioning Engineers, Inc., chap. 13, 14–15, 1993.
- [24] H.W.Coleman,W.G. Steele, *Experimentation, validation, and uncertainty analysis for engineers*, 4th Ed. New York: John Wiley & Sons, 2018.
- [25] J.D.Holmes, *Wind Loading of Structures*, 2nd Ed. New York: Taylor & Francis, 168-169, 2007.
- [26] Y.Z.Cao, *Experimental Heat Transfer*, 1st Ed. Beijing: National Defense Industry Press, 120-125, 1998.
- [27] F.W.Dittus, L.M.K.Boelter,*Heat Transfer in Automobile Radiators of the Tubular Type*, Berkley: University of California Press, 2, 443, 1930.
- [28] F.W.White, *Fluid mechanics*, 3rd Ed. New York: McGraw-Hill, 2003.
- [29] J.L.Wang, Z.S.Zhang, X.Zeng, "Effect of longitudinal vortices on the turbulent structure in near-wall region," *Acta Mechanica Sinica.*, 26(5), 1994, 625e629 (in Chinese).

Research Article

High-Pressure Calibration TiN Equation of State

^{1*} S.K. Jalal , ² M.M. Uonis , ³ R.H. Al-Saqa 

¹ Al Qalam university college, Kirkuk, Iraq

Shex Raza High School, Directorate of Education of Chamchamal

² Dept. New and Renewable Energy, College of Science, University of Mosul, Iraq

Directorate General of Education/ Nineveh, Iraq

E-mail: ^{1*} sirwan.kareemj@gmail.com

Received 1 September 2022, Revised 30 November 2022, Accepted 7 December 2022

Abstract

High pressure is becoming an interesting area of research for originating vital properties in crystalline solids. In the present study, the pressure equation of the state of TiN was investigated by employing various equations of state (EoS) presented in the literature, such as Dodson EoS, Barden EOS, Birch-Murnaghan (B-M) EoS. The EoSs were processed to find the high-pressure effects on the characterizations of TiN such as volume compression ratio, bulk modulus B , Grüneisen parameter, and phonon frequency spectrum. It was shown that a gigantic pressure results in a significant reduction in the volume of the TiN material, and the volume compression ratio reduction, is almost the same for the existing equations of state and the comparative literature results up to a pressure of 80 GPa. The maximum pressure difference is observed to be 4.85 GPa. over the entire pressure of 120 GPa. Increasing the bulk modulus with high pressure was expected by the present EoSs, and up to the pressure of about 60 GPa, all curves of bulk modulus are matched with each other. Eventually, a fair comparison has been made between the present results and the first principle approximation along with the generalized gradient approximation method in which a perfect agreement was observed. Finally, the feasibility of TiN EoS as a standard pressure calibration was demonstrated.

Keywords: Equation of state EOS; volume compression ratio V_p/V_0 ; Bulk modulus B ; Grüneisen parameter; phonon density of state

1. Introduction

High microhardness, chemical and thermal stability, and refractoriness are all characteristics of titanium nitride. TiN is used in many different ways, including as a component in specialized refractories and cermets, as a material for metal crucibles during anoxic casting, and as a precursor for wear-resistant and aesthetically pleasing "gold-like" coatings. Studies on the combustion of compacted titanium powder samples in nitrogen revealed that one of the main factors influencing the combustion is the nitrogen filtration velocity within the titanium. A common, less expensive, and purer source of titanium than titanium powders is titanium sponge [1]. Despite its contribution to a wide variety of advanced industries, Titanium nitride has the great benefit of being electro-conductive and chemically stable, making it possible to mill it using the electro-discharge machining (EDM) method [2].

Under atmospheric pressure, TiN has a crystalline structure of NaCl (B1) and it can undergo a phase transition from B1 structure to CsCl (B2) structure at 320 GPa [3]. Hence, extra high pressure can be applied to this crystal while maintaining its phase and without occurring structural transition. To determine the effect of high pressure on the TiN structure, numerous efforts have been made. Using generalized gradient approximation [1] high-pressure effects on lattice volume, Bulk modulus, and phonon density of state have been studied up to the pressure of 50 GPa. Using

diamond anvil cell and X-ray diffraction method the EoS and stability of this compound have been measured up to the pressure of nearly 70 GPa and temperature of 2700 K [4] and up to pressure of 94 GPa [5]. Based on the first principle approximation, the elastic constants, Debye temperature, and bulk modulus of this material, were investigated at high temperatures as well as high pressures [6]. In theoretical modeling, thermodynamic properties such as the relative compression volume, and bulk modulus of TiN are studied at moderate pressures up to (0–6 GPa) and high temperatures up to 2000 K [7].

High-pressure effects have attracted the scientific community to use equations of state as a time and cost-effective method to determine various characterizations of solid crystalline under high pressures. Different equations of state have been employed to describe pressure effects on various properties of Nano-TiO₂ [8]. Using three different equations of state, high pressure inducing useful characterization in Monoclinic Sulfur (S β) for the treatment of scabies in dermatology has been studied in [9]. Various equations of state were used to calculate, the bulk modulus and spinodal pressure of C₆₀ under strong compression [10]. The impacts of high pressure on the structural stability and melting point of Mo₅SiB₂ were investigated by using the first-principles calculations.

In this study, the effects of high pressure on the titanium nitrite are presented. The calculations of some properties

such as compressibility (V_p/V_0), bulk modulus (B), Grüneisen parameter, and phonon density of state are included, by employing Dodson EOS, Bardeen EOS, and modified Birch-Murnaghan EoS. The purpose of using different EOSs is to compare their results with each other along with the results in the relevant published scientific research. Moreover, owing to the high value of the bulk modulus of TiN, the pressure - V_p/V_0 relationship employment as a standard calibration for measuring high pressure is investigated. The presented results are compared with peer-reviewed up-to-date publications using the first principle and generalized gradient approximation.

2. Equation of State (EoS) for Solid Materials

Equations of the state are the relationships between the thermodynamic variable, such as pressure, temperature, and volume. When the temperature is kept constant, the pressure-volume relations are termed the isothermal equation of state. Equations of state offer, a time and cost-effective method to determine various characterizations of solid crystalline under high pressures [8]. This study tests the validity of three different EoS to be applied to TiN material in determining various thermodynamic and thermo-elastic properties under strong compression. EOSs are classified as follows:

1- Dodson EOS

Based on two simple parameters (Dodson, 1987) [11] derived an empirical EOS that fits all metals, metal alloys, ionic crystals, as well as semiconductors. The equation is given by:

$$P_{Do} = \frac{27}{8} B_0 B_0'{}^2 \left[\begin{array}{l} \left(\eta \right)^{-2/3} - 1 + 4 \left(1 - \frac{2}{3B_0'} \right) \\ \times \left\{ 1 - \left(\eta \right)^{-1/3} - \frac{1}{6} \left(1 - \frac{2}{3B_0'} \right) \ln \eta \right\} \end{array} \right] \quad (1)$$

where P_{Do} refers to the pressure due to the Dodson EOS, B_0 is bulk modulus at ambient pressure, B_0' indicates the first pressure derivative of bulk modulus, and $\eta = \frac{V_p}{V_0}$, is the volume compression ratio.

2- Birch-Murnaghan (B-M) EOS

B-M is a well-known equation of state for describing the thermodynamic behavior of the solid phase under high pressures, which is derived based on the internal potential energy in the solid and the pressure derivative of this internal potential energy. The B-M EOS [9, 12] is expressed by:

$$P_{B-M} = \frac{3B_0}{2} \left[\eta^{-7/3} - \eta^{-5/3} \right] \left[1 + \frac{3}{4} (B_0' - 4) (\eta^{-2/3} - 1) \right] \quad (2)$$

where P_{B-M} refers to the pressure required to introduce the compression ratio η .

3- Bardeen EOS [13].

Has settlement from the interatomic potential function (E_r):

$$E_r = \frac{a}{r^3} + \frac{b}{r^2} + \frac{c}{r} \quad (3)$$

where, (a , b , c) are constant values, and (r) is the position function. Hence, the Bardeen equation can be given as:

$$P_{Ba} = 3B_0 \left(\eta^{-5/3} - \eta^{-4/3} \right) \left[1 + \frac{3}{2} (B_0' - 3) \left(\eta^{-1/3} - 1 \right) \right] \quad (4)$$

where, $P_{Bard.}$ is pressure according to the Bardeen EoS. An advantage of studying equations of state appears from its correlation with bulk modulus (B), which allows deriving the pressure dependence of bulk modulus. The bulk modulus of a substance is the pressure applied on the substance to introduce a relative change or reduction in the volume of the material, which is mathematically defined by: $B = -\Delta P / (\Delta V / V)$. This equation is rearranged to get the form of eq.5:

$$B = -V \frac{\partial P}{\partial V} \quad (5)$$

Eq.5 is represented as a bulk modulus dependent on pressure. This indicates that the bulk modulus increases with increasing pressure or reduction in the volume of the unit cell of solid material. At a given temperature, experiments have shown that the bulk modulus depends on the compression produced in the material (Birch, 1986). When the lattice spacing is decreased as a result of high pressure leads to introduce a significant repulsive interatomic force against the external agent. Hence, the bulk modulus equivalent to each equation of state is derived with Eq. (5). To derive the bulk modulus under high pressure by using Dodson EOS and B-M EOS, eq.1 and eq.2 are derivatives with respect to volume to obtain eq.6 and eq.7 as in the following steps:

$$\frac{dP_{Do}}{dV} = \frac{27}{8} B_0 B_0'{}^2 \left[\begin{array}{l} \frac{-2}{3} \frac{V^{-2/3}}{V_0^{2/3}} + 4 \left(1 - \frac{2}{3B_0'} \right) \times \\ \left\{ \frac{1}{3} \frac{V^{-1/3}}{V_0^{-1/3}} - \frac{1}{6} \left(1 - \frac{2}{3B_0'} \right) \frac{1}{V} \right\} \end{array} \right] \quad (6)$$

then becomes

$$\frac{dP_{Do}}{dV} = \frac{27}{8} B_0 B_0'{}^2 \left[\begin{array}{l} \frac{-2}{3} \frac{V^{-2/3}}{V_0^{2/3}} + 4 \left(1 - \frac{2}{3B_0'} \right) \times \\ \left\{ \frac{1}{3} \frac{V^{-1/3}}{V_0^{-1/3}} - \frac{1}{6} \left(1 - \frac{2}{3B_0'} \right) \frac{1}{V} \right\} \end{array} \right] \quad (7)$$

Differentiation of Eq. 2:

$$\frac{dP_{B-M}}{dV} = \frac{3}{2} B_0 \left[\left(\frac{V_p}{V_0} \right)^{-7} - (\eta)^{-5/3} \right] \left[\frac{3}{4} (B_0' - 4) \left[\frac{-2}{3} \frac{V_p^{-5/3}}{V_0^{-2/3}} \right] \right] + \frac{3}{2} B_0 \left[\frac{-7}{3} \frac{V_p^{-10/3}}{V_0^{-7/3}} + \frac{5}{3} \frac{V_p^{-8/3}}{V_0^{-5/3}} \right] \left[1 + \frac{3}{4} (B_0' - 4) \left[\left(\frac{V_p}{V_0} \right)^{-2} - 1 \right] \right] \quad (8)$$

where $\frac{dP_{Do}}{dV}$ and are pressure derivatives of Dodson and B-M, EoS respectively. Then, substituting Eqs. (7 & 8) into the bulk modulus definition in Eq. 5, one can find the Dodson EoS and EoS in terms of isothermal bulk modulus, as shown in Eq. 9 and Eq. 10:

$$B_{Do} = \frac{27}{8} B_o B_o'^2 \left[\frac{2}{3} (\eta)^{\frac{-2}{3}} - 4 \left(1 - \frac{2}{3B_o'} \right) \times \left\{ \frac{1}{3} (\eta)^{\frac{-1}{3}} - \frac{1}{6} \left(1 - \frac{2}{3B_o'} \right) \right\} \right] \quad (9)$$

$$B_{B-M} = \frac{B_o}{2} \left[7\eta^{\frac{-7}{3}} - 5\eta^{\frac{-5}{3}} \right] + \frac{3}{8} B_o (B_o' - 4) \times \left(9\eta^{\frac{-9}{3}} - 14\eta^{\frac{-7}{3}} + 5\eta^{\frac{-5}{3}} \right) \quad (10)$$

where B_{B-M} denotes the bulk modulus as a function of relative volume/pressure, in terms of Dodson EoS and B-M EoS respectively.

By the same method, expressions for the bulk modulus under high pressure according to Bardeen can expressed:

$$B_{Ba} = 3B_o \left(\frac{5}{3} \eta^{\frac{-5}{3}} - \frac{4}{3} \eta^{\frac{-4}{3}} - (B_o' - 3) \times \left(5\eta^{\frac{-5}{3}} - 3\eta^{\frac{-4}{3}} - 2\eta^{\frac{-4}{3}} \right) \right) \quad (11)$$

Where, B_{Ba} , is the bulk modulus according to Bardeen EoS.

3. Phonon Lattice Vibration

Einstein presented a model for atomic harmonic motions of the crystalline solids, in which all atoms are vibrating independently to each other with the same frequency. On the other hand, the idea of the single frequency dominant is no longer valid after Debye modifies solid lattice vibration. In Debye's model, instead of a specific frequency, a wide range of atomic frequencies are possible, in such a way that the number of frequencies is equal to the total degree of the freedom of the solid. The particles do not oscillate independently, but the vibrational motion of an atom does interact with its neighbors, and so on. Hence there is a band (spectrum) of frequency ranging from w to $w + dw$. The quanta of lattice vibration are referred to as phonons or modes of vibration, in which the number of active modes in the spectrum is termed as the density of state $g(w)$. In the Grüneisen theory [14, 15], the vibrational frequency of modes varies with the volume V of the unit cell, via Eq. 12 :

$$\gamma_i = - \frac{\partial \ln \omega_i}{\partial \ln V} \quad (12)$$

where denotes the Grüneisen parameter, ω_i is the frequency of the i^{th} mode of vibration, which is dependent on the lattice volume that is altered when high pressure is applied to the crystalline solid. Hence, the characteristics of the phonons

are dependent on the volume of the atomic unit cell because of the lattice an- harmonic behavior of the crystal. High pressure transforms the phonon energy into higher energy levels, as well as reduces the number of modes that acquire those high energy levels [16]. Consequently, the pressure dependence of both phonon frequency spectrum and density of the states are described by [12, 17]:

$$\omega = \omega_0 \eta^{-\gamma} \quad (13)$$

$$D(\omega, V_p) = D(\omega_0, V_0) \eta^\gamma \quad (14)$$

where, ω_0 and ω are the lattice frequency at atmospheric pressure and high-pressure P respectively. $D(\omega_0, V_0)$ and are respectively representing the density of states (modes) at zero pressure and high pressure. However, γ varies very slowly, and it is considered to be pressure-dependent. According to the following equation.

$$\gamma = \gamma_o \eta \quad (15)$$

Where, γ_o and γ stands for the Grüneisen parameter at zero pressure and high pressure respectively. The pressure dependence γ is due to the lattice an-harmonic behavior of crystalline [18]. Various methods were proposed for calculating the Grüneisen parameter at ambient conditions for various metals and alloys. For instance, the Grüneisen parameter can be calculated from the first pressure derivative of bulk modulus by the following relationships [19]:

$$\gamma = \frac{1}{2} \frac{dB}{dP} - 0.9 \quad (16)$$

4. Result and Discussion

In the present work, the high-pressure effect on the various properties of TiN such as unit cell volume V_p , Bulk modulus B , vibrational Grüneisen parameter γ , and phonon frequency spectrum is considered to be studied by employing three equations of state EoSs. The constant parameters used in this study are ($B_o = 281$ GPa, $B_o' = 4.46$) [20]. Figure 1 illustrates the variation of volume compression ratio from 1 to 0.78 at various high pressures for TiN, by using Dodson, Barden, and B-M EoS. It is clear that up to pressure, 80 GPa no real differentiation between the results of the three EoSs is observed. A comparable result with very little slope is seen at the lowest data of V_p/V_o which is 0.78. The present result of V_p/V_o attained with the EOSs is motivated to be compared with peer publication [1, 6], in which the first principle approximation method was used to estimate V_p/V_o of TiN up to pressure around 50 GPa and 60 GPa. It is shown that simulated results in [1, 6] are in very good agreement with the presented results obtained by the three considered EoSs. The marginal difference between the results of EoSs along with the presented findings in the literature, is due to the presence of a high bulk modulus of TiN, which is measured at 1281.6 GPa and its first pressure derivative of 4.46.

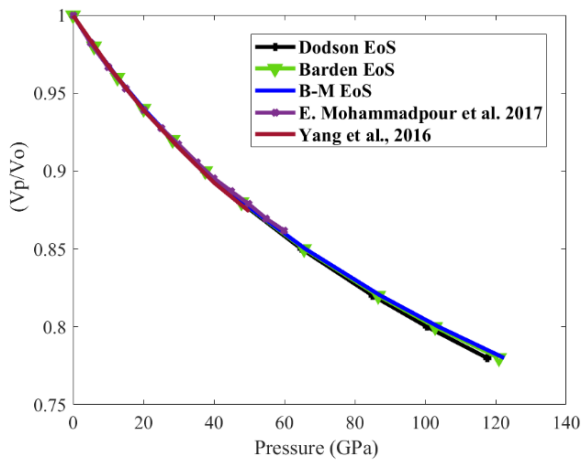


Figure 1. Compatibility of TiN, obtained with the present EoS, in comparison with Yang et al., 2016 [1] and E. Mohammadpour et al., 2017 [6].

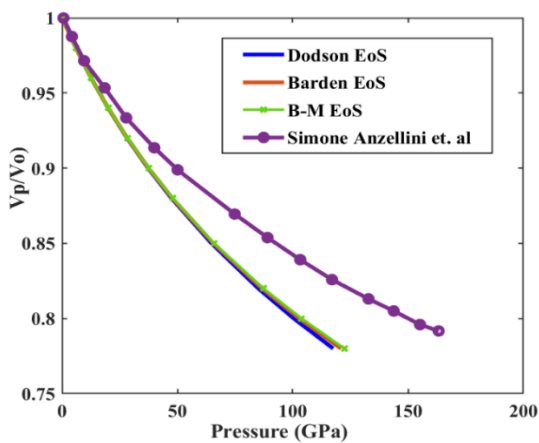


Figure 2. Comparison of the compressibility of TiN with Rhenium as measured by Simone et al., [21].

Furthermore, Figure 2 shows the comparison between the EoS of TiN and the EoS of Rhenium. It can be seen that Rhenium exhibits a lower compressibility than that of TiN under the same pressure. The low compressibility of Rhenium is due to its large ambient bulk modulus value. The bulk modulus of solid materials tends to increase under the application of high pressure. The lattice contraction resulting from the high pressure leads to the enhancement of the electrical repulsive force between neighboring particles which consequently increases the crystal resistance against the external pressure. Thus the increment in the bulk modulus has been proved in experimental as well as theoretical studies [6]. A remarkable outcome of the EoSs is the deduction of the pressure dependence of the bulk modulus which was given in Eqs. 7-9. The proposed EoSs give bulk modulus formulas that increase with increasing pressure and fit the experimental and theoretical observations. The variation in the value of bulk modulus with high pressure for TiN, calculated with the proposed EoSs along with peer publication investigation is depicted in Figure 3. The bulk modulus rose with increasing pressure from 280 GPa at ambient conditions, to up to 770 GPa at high pressure of 130 GPa with maintaining the relative volume of 0.78. However, all the results give a roughly equal value of B up to the pressure of 50 GPa, beyond this pressure limit the bulk modulus of Dodson EoS starts to diverge from the other results, demonstrating a difference of 70 GPa at the highest pressure of about 130 GPa. Table 1 represents a

statistical description of the results given in Figure 1 and Figure 3. Three volume compression ratio data (0.861, 0.84, and 0.80) are taken, and the pressure corresponding to each data is computed by the existing EoSs along with literature data. The averages of the pressures obtained by the three EoSs are found to be (58.61 GPa, 72.0239 GPa, 102.356 GPa). The standard deviation of the result of each EOS from the mean as well as the literature deviation from the mean are tabulated. It is shown that the standard deviation of the EoSs is increased with pressure (0.44, 0.614 and 2.95) GPa. Moreover, the bulk modulus at a high pressure of 59 GPa was calculated with each EoS, and the literature data are presented. The mean bulk modulus and the standard deviation are 493.9 GPa and 45.64 GPa respectively. The literature deviation from the mean bulk modulus of the EoSs is 41.85 GPa, which accounts for 8.47%.

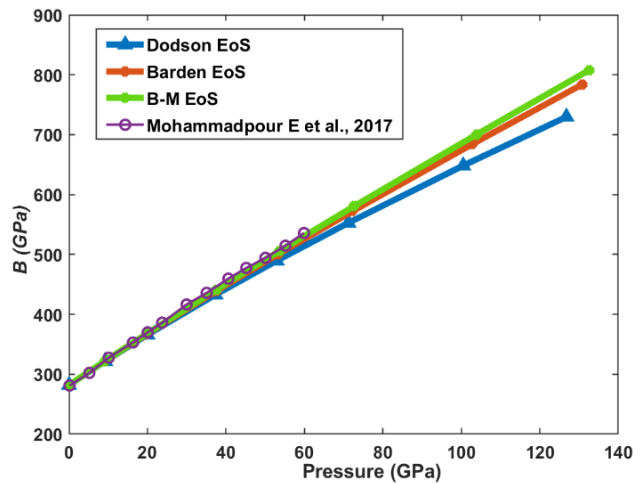


Figure 3. Bulk modulus as a function of pressure, calculated in the present study and compared with Mohammadpour E et al., [6].

The effect of high pressure on the Grüneisen parameter γ is of great importance due to its high relevance to the phonon frequency spectrum and density of states.

In the current contribution the γ at ambient state is found by substituting the first pressure derivatives of bulk modulus ($B'_0 = 4.46$) [6, 20] into Eq. 15, to get γ at zero pressure which equals 1.33. Then by combining the computed Vp/Vo data in Figure 1 into Eq.14, the Grüneisen parameter at various pressures is computed and shown in Figure 4. It can be seen that a very slight reduction in the Grüneisen parameter from 1.33 at ambient pressure to around 1.006 at a high pressure of 130 Gpa is recorded by the three EoSs, with a negligible difference between the three data predicted. This result confirms the high lattice harmonicity of the TiN crystal up to a high-pressure range. The calculation of TiN, at zero pressure and its pressure dependence is considered as an initiative study.

The phonon frequency spectrum and density of states of TiN at atmospheric pressure were measured by [1] and the same phonon density of state was also investigated under high pressure of 50 GPa. In the current contribution, by combining the equations 12-14 with Vp/Vo data in Figure 1 and γ data in Figure 4, the phonon frequency spectrum and density of states under 50 GPa, by the three EoSs are displaced in Figure 4, and a comparative literature data is presented [1]. Due to the high bulk modulus of TiN, the curves of the proposed EoSs are matched to each other,

Table 1. Shows the statistic of deviation of the results obtained with the different equations of state and the comparative literature [6]

V_p/V_o	EoS	Pressure (Gpa)	Mean Pressure of the EoSs	Statistics		
				literature deviation from the mean	Standard deviation from the mean	
0.861	- Dodson	58.12	58.61 GPa	P mean=1.28 GPa	0.44 GPa	
	- Barden	58.72				
	- B-M	58.98				
	- Literature	59.89				
0.84	- Dodson	71.2134	72.023 9 GPa		0.614 GPa	
	- Barden	72.2084				
	- B-M	72.6501				
0.80	- Dodson	100.4744	102.356 GPa		2.95 GPa	
	- Barden	102.7867				
	- B-M	103.8077				
B		Pressure	B of EoS	Mean	Literature deviation	Standard deviation
	Dodson EoS	59 GPa	514 GPa	493.9 GPa	41.85 GPa	45.64 GPa
	Barden EoS		525.7 GPa			
	B-M EoS		442 GPa			
	Literature		535.75 GPa			

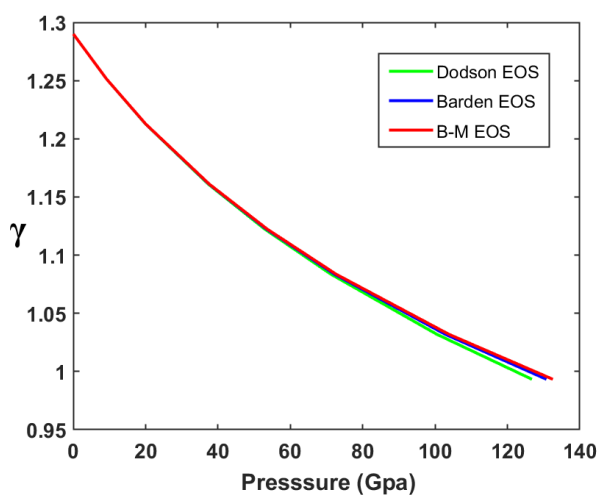


Figure 4. Variation of Grüneisen parameter with high pressure.

consequently, no substantial difference is observed. The phonon frequency spectrum shown in Figure 5 is comprised of two main bands of energy, the lower energy band is an acoustical mode and the higher energy band is the optical mode of the spectrum. Under the effect of high pressure, the optical spectrum is shifted towards higher energy. It is worth mentioning, that the high-pressure effect of the phonon

frequency spectrum measured in [1] by the first principle approximation, is in agreement with the present result by the above EOSs. Eventually, the comparative literature data along with the results of the existing EoSs, predict the same fact of the effects of high pressure on phonon density of state.

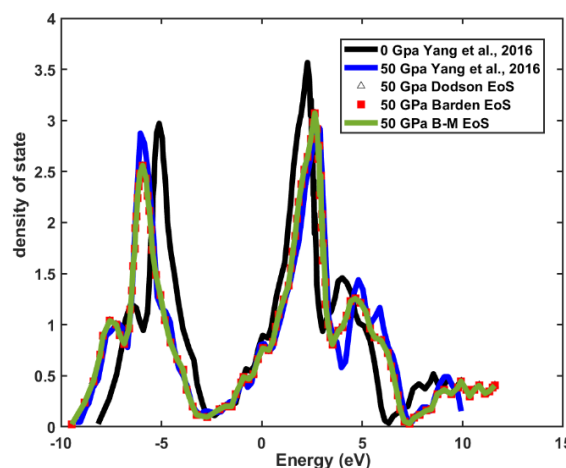


Figure 5. Phonon frequency spectrum and density of state of TiN, at zero pressure, and under 50 GPa calculated in the present study in comparison with [1].

It is worth mentioning, that the high-pressure effect of the phonon frequency spectrum measured in [1] by the first principle approximation, is in agreement with the present result by the above EOSs. Eventually, the comparative literature data along with the results of the existing EoSs, predict the same fact of the effects of high pressure on phonon density of state. The increase in the energy of the active modes in the present study completely fits the obtained result by [1], but there is a small discrepancy between the density of states at a pressure of 50 GPa. From the peak of the optical branch the density of state of the current study is greater by 0.152 from the presented literature data [1]. In contrast, from the acoustical band, the density of state calculated from the EoSs is lower than that recorded in [1] by 0.3157. At the ambient pressure, the total density of state $d(\omega)$ of the optical spectrum is 3.5, and the proposed EoSs predicted the reduction in this $d(\omega)$ by 14%, while in [1] the $d(\omega)$ is reduced by 0.6465 which equals 18% of the total density of state. To illustrate a higher transformation in energy and density of states, Figure 6 reflects the same fact, by measuring the phonon frequency spectrum and the density of states at 100 GPa by using Dodson EoS only. in comparison with the previous results. Under 100 GPa, a clear discrepancy between the results of the different curves is observed.

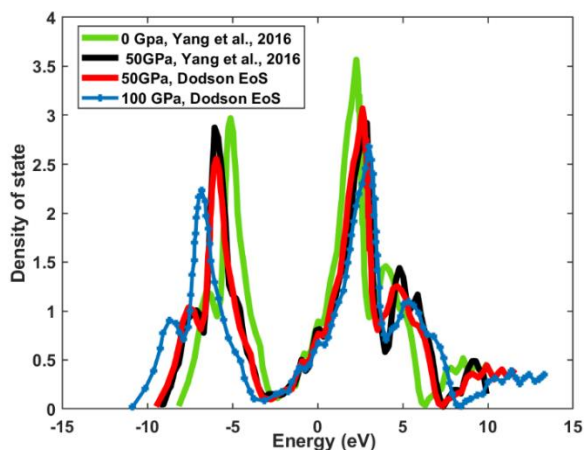


Figure 6. Phonon frequency spectrum and density of state of TiN, at zero pressure, and under 50GPa and 100GPa, calculated in the present study in comparison with, Yang et al. [1].

5. Conclusion

In the present three EoSs are proposed to determine the effect of high pressure on thermodynamic properties of TiN. The calculations included relative volume, Bulk modulus, Grüneisen parameter, and phonon density of state. However, these thermodynamic properties of TiN have already been determined by using first principle and generalized gradient approximation, this study was an initiative to test the feasibility of the EoSs to give results comparable with the peer publications. Due to the high compatibility (bulk modulus) of TiN, V_P/V_0 , B , and γ , all the EOSs gave roughly the same results up to 80 GPa. This indicates that the EoS of TiN using any of the considered EoS can be used as a fair pressure calibration method for other materials. According to our knowledge, the calculations of the Grüneisen parameter at ambient conditions, and its variation under high pressure can be a new contribution in the high-pressure research that can attract the scientific community. Eventually, the present results achieved with the considered EoSs demonstrated the same variation trend of the phonon

energy and density of states, as were predicted by the first principle approximation and the generalized gradient approximation in the literature results.

Nomenclature

TiN	Titanium nitride
GPa	Giga Pascal
K	Kelvin
η	Eta
V	Volume (cm ³)
P	Pressure (Gpa)
V_P/V_0	Volume compression ration
V_P	Volume under high pressure (cm ³)
V_0	Volume at ambient condition (cm ³)
γ	Grüneisen parameter

References:

- [1] R. Yang, C. Zhu, Q. Wei, and Z. Du, "Investigations on structural, elastic, thermodynamic and electronic properties of TiN, Ti₂N, and Ti₃N₂ under high pressure by first-principles," *Journal of Physics and Chemistry of Solids*, 98, 10-19, 2016.
- [2] J. Russias, S. Cardinal, J. Fontaine, G. Fantozzi, C. Esnouf, and K. Bienvenu, "Bulk titanium nitride material obtained from SHS starting powder: densification, mechanical characterization, and tribological approach," *International Journal of Refractory Metals and Hard Materials*, 23, no. 4-6, 344-349, 2005.
- [3] T.i Li, T. Liu, H. Wei, S.Hussain, B. Miao, W. Zeng, "Atomic and electronic structure of the TiN/MgO interface from first principles," *Computational Materials Science*, 105, 83-89, 2015.
- [4] K. Daviau, R. A. Fischer, M. C. Brennan, Junjie Dong, T. Suer, S. Couper, Y. Meng, V. B. Prakapenka., "Equation of state of TiN at high pressures and temperatures: A possible host for nitrogen in planetary mantles," *Journal of Geophysical Research: Solid Earth*, vol. 126, no. 2, p. e2020JB020074, 2021.
- [5] A. Dewaele, P. Loubeyre, and M. Mezouar, "Equations of state of six metals above 94 GPa," *Physical Review B*, 70, no. 9, 094112, 2004.
- [6] E. Mohammadpour, M. Altarawneh, J. Al-Nu'airat, Z.-T. Jiang, N. Mondinos, and B. Z. Dlugogorski, "Thermo-mechanical properties of cubic titanium nitride," *Molecular Simulation*, 44, 5, 415-423, 2018.
- [7] C. Dong, C. Jingdong, Z. Yinglu, Y. Benhai, W. Chunlei, and S. Deheng, "Theoretical study of the elastic properties of titanium nitride," *Acta Metallurgica Sinica (English Letters)*, 22, no. 2, 146-152, 2009.
- [8] A. I. Ghazal and A. M. Al-sheikh, "Thermo Elastic Properties of Nano-TiO₂ Under High Pressure Using Different Equations of State," in *Journal of Physics: Conference Series*, 1999, n1: IOP Publishing, 012075. 2021
- [9] R. ALSAQA and N. S. SULTAN, "Study of Thermodynamic Properties of Monoclinic Sulfur (β) Under High Pressure Using Three Different Equations of State for the Treatment Scabies in Dermatology," *International Journal of Thermodynamics*, 1-6. 2020.

- [10] A. Al-sheikh, S. Jalal, and R. Al-saqa, "Equation of state and thermo dynamic behaviour of C60 under high pressure, " *Universal Journal of Mechanical Engineering*, 8, , 59, 2020.
- [11] B. W. Dodson, "Universal scaling relations in compressibility of solids, " *Physical Review B*, 35, 6, p. 2619, 1987.
- [12] M. M. Tbeen, "Size Dependent Thermo Elastic Properties of Nano Lead Sulfide (PbS) under High Pressure, " *Rafidain Journal of Science*, 30, 12-20, 2021.
- [13] J. Bardeen, "Compressibilities of the alkali metals, " *The Journal of Chemical Physics*, 6, 372-378, 1938.
- [14] S. J. Al-Faris and S. K. Jalal, "Grüneisen Parameter Variation Consideration in Theoretical High-Pressure Studies for C60, " *Iranian Journal of Science and Technology, Transactions A: Science*, 46, 689-695, 2022.
- [15] R. H. Al-Saqa and S. J. Al-Taie, "Theoretical Study of Mechanical, Elastic and Phonon Frequency Spectrum Properties for GaAs at High Pressure, " *Журнал Сибирского федерального университета. Математика и физика*, 12, 371-378, 2019.
- [16] S. K. Jalal, A. M. Al-Sheikh, and R. H. Al-Saqa, "High pressure effects on the phonon frequency spectrum of silicon nanoparticle," *Iranian Journal of Science and Technology, Transactions A: Science*, 45, 391-396, 2021.
- [17] S. J. AL-FARÍS, R. H. Al-Saqa, H. M. MOHHAMED, and S. KAREEM, "High pressure effects on the structural properties of GaN compound using equations of state, " *International Journal of thermodynamics*, 25, 79-84, 2022.
- [18] A. ALSHEKH, S. KAREEM, and S. MAWLLOD, "Theoretical high-pressure study of phonon density of state and Debye temperature of solid C60: Grüneisen approximation approach, " *International Journal of Thermodynamics*, 25, 10-15, 2022.
- [19] N. Vočadlo and G. D. Price, "The Grüneisen parameter—computer calculations via lattice dynamics, " *Physics of the earth and planetary interiors*, 82, 261-270, 1994.
- [20] K. Prasert, P. Thanomngam, and K. Sarasamak, "First-Principles Investigation on Elastic Constants of TiN under High Pressure, " in *Advanced Materials Research*, 2013, 802: Trans Tech Publ, 109-113.
- [21] S. Anzellini, A. Dewaele, F. Occelli, P. Loubeyre, and M. Mezouar, "Equation of state of rhenium and application for ultra high-pressure calibration, " *Journal of Applied Physics*, 115, 043511, 2014.

Research Article

Thermodynamic Properties of Selected Bicyclic Terpenes and Related Substances by Gas Chromatography and Group Contributions

^{1*}L.A.A.P. Fonseca , ²C.E.L. Oliveira , ³M.A. Cremasco 

^{1,3} University of Campinas (UNICAMP)
² Federal University of Maranhão (UFMA)
E-mail: ^{1*}lucianapreviato2014@gmail.com

Received 27 January 2023, Revised 21 July 2023, Accepted 19 August 2023

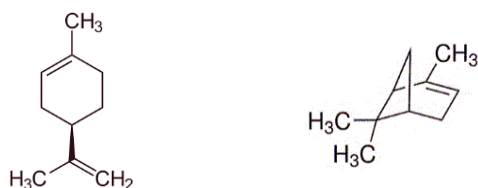
Abstract

Terpene compounds in the lower layer of the atmosphere can contribute to environmental problems through the formation of particulate material known as secondary organic aerosol (SOA). A clear understanding of the formation and composition of these particles hinges on reliable thermodynamic data. Quick estimation of these physical properties is highly desired. While experimental methods require significant resources and time, the prediction of pure-component properties through group contributions is easily applicable and straightforward. The present study compares the experimental enthalpies of vaporization at 298.15 K for bicyclic terpenes and related substances derived from the gas chromatography technique with estimated values provided by three group contribution methods. A new group contribution model specifically designed for terpene compounds is introduced. Furthermore, this study reveals previously unreported values in the literature for the enthalpy of vaporization at 298.15 K and the normal boiling temperature of Thymol methyl ether, Fenchyl alcohol, and Bicyclo [4.1.0] heptane-7-carboxylic acid.

Keywords: Group contribution; gas chromatography; enthalpy of vaporization; bicyclic compounds.

1. Introduction

Terpene compounds are naturally produced through secondary metabolism in a wide range of plants. These compounds are simple hydrocarbons that differ in the number of isoprene units. Hemiterpenes are formed by one isoprene unit (C₅), monoterpenes by two (C₁₀), sesquiterpenes by three (C₁₅), diterpenes by four (C₂₀), triterpenes by six (C₃₀), and tetraterpenes by eight (C₄₀). Additionally, terpenoids are defined as a modified class of terpenes with different functional groups. Terpenes can be further classified based on the degree of cyclization in the molecule, including acyclic (open chain), monocyclic, or bicyclic structures (refer to Figure 1) [1]. Compounds from this group have various applications in the chemical, pharmaceutical, and food industries, and they are also emitted into the environment in significant quantities, contributing to the diverse array of organic species found in the atmosphere [2,3].



Monocyclic: (+)-Limonene Bicyclic: α -Pinene
Figure 1. Terpene compounds molecular structures.

The significant presence of terpenes in the lower layer of the atmosphere poses environmental challenges due to their

tendency to react with ozone, hydroxyl radicals, and nitrate radicals. These reactions result in the formation of particulate matter known as secondary organic aerosols (SOA) [4]. SOA can alter the radiative balance of the atmosphere by either absorbing or scattering solar radiation [5,6,7], thereby impacting air quality [8].

A comprehensive understanding of the formation and composition of these particles depends on reliable thermodynamic data for the compounds responsible for the generation of SOA. For instance, many algorithms used to predict emission rates of terpene compounds are based on physical evaporation and diffusion data [9,10,11].

The lack of such data in the existing literature emphasizes the necessity to explore robust tools capable of determining properties like vapor pressure (P_{vap}), normal boiling temperature (T_{nb}), and enthalpy of vaporization ($\Delta_{\text{vap}}H$). Typically, these thermodynamic quantities are obtained through conventional experimental techniques such as isoteniscope, Knudsen effusion, gas saturation, and gas chromatography [12,13,14], or alternative techniques like thermogravimetry [15]. Gas chromatography, among these methods, provides an accurate means of determining the thermodynamic properties of organic compounds. Its widespread use is attributed to its high purity, small sample size requirement, and reproducibility [14,16,17].

Many experimental techniques require a substantial amount of measured data, chemically pure compounds, and high-performance equipment, which can be expensive. As the sophistication of chemicals and processes increases, along with greater societal demands for sustainability, health, safety, and economy, there is a growing need to

accurately estimate thermodynamic properties and implement property models [18]. Group contribution models are simple and accessible techniques based on molecular structural information. These models are valuable tools when measured data is unavailable and provide a diverse range of property estimates [19]. In recent work, Mann et al. [20] evaluated the prospects of group contribution models and emphasized that combining Artificial Intelligence (AI), data analysis, and models based on fundamental principles, such as classical group contribution models, with the availability of measured data holds promise in this context.

The objective of this study is to determine the enthalpies of vaporization at 298.15 K and normal boiling temperatures for eight terpene compounds using gas chromatography correlation. In addition, unpublished thermodynamic data for thymol methyl ether, alcohol fenchyl, and bicyclo [4.1.0] heptane-7-carboxylic acid are provided. Three group contribution methods are employed to estimate the enthalpies of vaporization at 298.15 K for the selected terpene compounds: Chickos et al. [21] present a method that considers the molecular structure of organic compounds and includes intramolecular interactions; Joback and Reid's model [22] is a general approach that incorporates additional contributions; and a new group contribution model specifically designed for terpene compounds is introduced, addressing the gaps left by some models in the literature, with a particular focus on bicyclic terpene compounds.

2. Experimental

2.1 Chemicals

A description of the chemicals used in this work is given in Table 1. The purity of the terpene compounds analyzed by gas chromatography (> 95%) was sufficient to determine their retention times. All chemicals, including the n-alkanes standards (C₅-C₁₆), were provided by Sigma Aldrich (Holzminden, Germany).

Table 1. Sample descriptions.

Chemical name	Formula	Purity, %	<i>M</i> (g.mol ⁻¹)	CAS RN
(+)-Limonene	C ₁₀ H ₁₆	97.0	136.23	5989-27-5
Thymol methyl ⁽¹⁾	C ₁₁ H ₁₆ O	≥ 99.0	164.24	1076-56-8
(+)- α -Pinene	C ₁₀ H ₁₆	≥ 99.0	136.23	7785-70-8
(+)- β -Pinene	C ₁₀ H ₁₆	≥ 99.0	136.23	19902-08-0
5-Vinyl ⁽²⁾	C ₉ H ₁₂	95.0	120.19	3048-64-4
5-Ethylidene ⁽³⁾	C ₉ H ₁₂	99.0	120.19	16219-75-3
Fenchyl alcohol	C ₁₀ H ₁₈ O	≥96.0	154.25	1632-73-1
Bicyclo [4.1.0] ⁽⁴⁾	C ₈ H ₁₂ O ₂	95.0	140.18	41894-76-2

⁽¹⁾ Thymol methyl ether; ⁽²⁾ 5-Vinyl-2-norbornene; ⁽³⁾ 5-Ethylidene-2-norbornene;

⁽⁴⁾ Bicyclo [4.1.0] heptane-7-carboxylic acid.

2.2 Gas Chromatography

The compounds' retention times were determined using a Perkin Elmer (Autosystem XL GC) gas chromatograph equipped with a flame ionization detector (FID). A NST 05 capillary column (60 m x 0.25 mm i.d. x 0.25 μ m film thickness) was used for compound separation under isothermal conditions of column temperature (40 °C to 200 °C), injector temperature of 230 °C, a detector at 250 °C, and an injection volume of 1.0 μ L. The carrier gas (He) flow rate was set to 1.0 mL/min. The compounds were dissolved in methanol at a concentration of 20 mg/mL. The n-alkanes (C₅ to C₁₆) were used as reference compounds. Both the studied compounds and the n-alkanes mixture were injected under the same chromatography conditions. The Kováts retention indices (I_X) were calculated using the n-alkanes with retention times encompassing each studied compound. The

analyses were performed in triplicate and followed Hoskovec et al. [14] methodology. Table 2 provides the Kováts retention indices for the studied compounds at different temperature ranges.

2.3 Kováts Retention Indices

Isothermal Kováts retention indices (I_X) are defined as Eq. (1).

$$I_X = 100z + 100 \left(\frac{\ln t_{R,X} - \ln t_{R,z}}{\ln t_{R,z+1} - \ln t_{R,z}} \right) = 100z + 100 \frac{\ln(\gamma_z^\infty P_z / \gamma_X^\infty P_X)}{\ln(\gamma_z^\infty P_z / \gamma_{z+1}^\infty P_{z+1})} \quad (1)$$

In Eq. (1), $t_{R,X}$, $\text{son}P_X$, and γ_X^∞ represent the retention time, vapor pressure, and infinite dilution activity coefficient, respectively, of solute X in the stationary phase. The subscripts z and z+1 identify the reference n-alkanes with z and z+1 carbon atoms, whose retention times encompass that of solute X.

2.4 Thermodynamic Properties

With the requisite collection of the Kováts retention indices assembled by Eq. (1), the vapor pressures were determined from Eq. (2).

$$\ln P_x = \ln P_z + [(100z - I_x) \ln(P_z/P_{z+1})/100] \quad (2)$$

The vapor pressures of reference C₅ to C₁₆ n-alkanes at different temperatures used in this work were calculated using the Cox Equation, Eq. (3).

$$\ln \left(\frac{P}{P_0} \right) = \left(1 - \frac{T_0}{T} \right) \exp(A_0 + A_1 T + A_2 T^2) \quad (3)$$

In Eq. (3) the coefficients derived for temperatures between the triple and boiling points were taken from a critical compilation of n-alkanes data [23].

Published P values of the compounds studied at 298.15 K were obtained from literature and web-available databases [24, 25]. The same sources along with the commercial Sigma Aldrich catalogue served as a literature source for normal boiling point (T_{nb}) data.

The Antoine Equation Eq. (4) parameters A, B, and C, were determined using non-linear regression techniques and are presented in Table 3.

$$\ln(P_{vap}/Pa) = A - \frac{B}{T(K) + C} \quad (4)$$

For processing the P_{vap} versus T data, the Kirchhoff-Rankin-type Eq. (5) was used. The parameters of Eq. (5) are presented in Table 4.

$$\ln(P_{vap}/Pa) = \frac{1}{R} b_0 + \frac{1}{RT} b_1 + \frac{1}{R} b_2 \ln(T/T_0) \quad (5)$$

In Eq. (5) T₀ is arbitrarily equaled to 298.15 K and R=8.3145 J.K⁻¹.mol⁻¹. The enthalpy of vaporization at temperature T may be calculated from Eq. (6).

$$\Delta_{vap}H = -b_1 + b_2 T \quad (6)$$

Table 2. Experimental data. Kováts retention indices of studied compounds at different T ranges.

Kováts Retention Indices (I _K)								
T (K)	Monocyclic Terpenes		Bicyclic Terpenes					
	Limonene	Thymol methyl ether	(+)- α -Pinene	(+)- β -Pinene	5-vinyl ⁽¹⁾	5-Ethylidene ⁽²⁾	Fenchyl alcohol	Bicyclo [4.1.0] ⁽³⁾
313.15	-	-	926.35	965.20	-	-	-	-
323.15	1021.19	-	929.58	969.20	-	-	-	-
333.15	1023.72	-	932.52	972.80	878.20	909.84	-	-
343.15	1027.83	1228.54	936.44	978.02	880.76	911.97	-	-
353.15	1030.81	1230.54	939.51	982.15	883.20	913.99	-	-
363.17	1033.93	1233.65	943.49	986.63	885.24	915.47	-	-
373.15	1038.35	1233.11	947.91	992.24	886.95	917.07	1114.62	246.58
383.15	1039.34	1234.87	951.31	994.56	891.24	918.93	1113.78	256.62
393.15	1041.91	1238.14	954.41	998.16	891.70	918.52	1116.50	266.54
403.15	1045.54	1239.03	958.69	1002.91	893.70	920.52	1121.49	276.52
413.15	1049.26	1241.75	963.81	1007.63	894.45	921.01	1126.04	286.63
423.15	1052.04	1243.69	-	-	-	-	1131.15	296.58
433.15	-	1245.59	-	-	-	-	1134.05	246.50
443.15	-	1247.27	-	-	-	-	1136.75	-
453.15	-	-	-	-	-	-	1142.42	-
463.15	-	-	-	-	-	-	1148.00	-
473.15	-	-	-	-	-	-	1155.00	-

⁽¹⁾5-Vinyl-2-norbornene; ⁽²⁾5-Ethylidene-2-norbornene; ⁽³⁾Bicyclo [4.1.0] heptane-7-carboxylic acid.

Table 3. Vapor Pressure: Antoine Equation Parameters.

Compound	A	B	C	r ^{2(a)}
(+)-Limonene	20.92 ± 0.14	3741.14 ± 84.79	-62.53 ± 3.44	0.99998
Thymol methyl ether	20.87 ± 0.16	3866.04 ± 99.65	-86.93 ± 3.99	0.99997
(+)- α -Pinene	20.12 ± 0.10	3185.64 ± 56.06	-70.82 ± 2.51	0.99999
(+)- β -Pinene	20.64 ± 0.14	3597.34 ± 81.82	-57.67 ± 3.39	0.99998
5-Vinyl-2-norbornene	21.19 ± 0.24	3648.92 ± 153.90	-45.65 ± 6.82	0.99996
5-Ethylidene-2-norbornene	21.45 ± 0.19	3667.36 ± 125.39	-34.8 ± 5.71	0.99998
Fenchyl alcohol	19.33 ± 0.27	2869.94 ± 168.46	-113.19 ± 8.91	0.99985
Bicyclo [4.1.0] heptane-7-carboxylic acid	18.80 ± 0.29	2528.18 ± 144.33	-162.43 ± 6.97	0.99997

^(a): correlation coefficients (r², %).

Table 4. Parameters of Eq. (5).

Compound	b ₀	b ₁	b ₂	r ^{2(a)}
(+)-Limonene	256.2 ± 3.9	-63822 ± 1168	-50.5 ± 3.2	0.99998
Thymol methyl ether	298.1 ± 5.5	-82189 ± 1705	-73.9 ± 4.3	0.99997
(+)- α -Pinene	257.5 ± 3.1	-61608 ± 922	-56.8 ± 2.6	0.99998
(+)- β -Pinene	244.7 ± 4.0	-58834 ± 1205	-45.4 ± 3.4	0.99997
5-Vinyl-2-norbornene	225.4 ± 6.4	-50452 ± 1954	-29.6 ± 5.3	0.99996
5-Ethylidene-2-norbornene	229.5 ± 4.6	-52642 ± 1398	-30.2 ± 3.8	0.99998
Fenchyl alcohol	295.40 ± 12.0	-77914 ± 3736	-78.6 ± 8.9	0.99984
Bicyclo [4.1.0] heptane-7-carboxylic acid	464.10 ± 17.4	-136073 ± 5412	-190.9 ± 13.3	0.99997

^(a): correlation coefficients (r², %).

Eqs. (5) and (6) were implemented to predict $\Delta_{\text{vap}}H$ values at 298.15 K for the studied compounds. In addition, since it is known that the normal boiling temperature T_{nb} of a substance in the liquid phase is the temperature at which its vapor pressure equals atmospheric pressure (1 atm), it is possible to define P in Eq. (5) as 1 atm to obtain the T_{nb} data. Table 5 summarizes the enthalpy of vaporization ($\Delta_{\text{vap}}H$) at

298.15 K and the normal boiling temperature (T_{nb}) of studied terpene compounds.

3. Group Contribution Methods

The group contribution methods are based on the principle that a function of structurally dependent parameters defines the property values. These values are determined by.

Table 5. $\Delta_{vap}H$ and T_{nb} : Literature and Experimental data obtained in this work at 298.15 K and 101.325 kPa.

Compound	$T_{nb}^{lit(a)}$ (K)	$T_{nb}^{exp(b)}$ (K)	RD ^(c) %	$\Delta_{vap}H^{lit(a)}$ (kJ mol ⁻¹)	Method ^(d)	$\Delta_{vap}H^{exp(b)}$ (kJ mol ⁻¹)	RD ^(c) %
(+)-Limonene	451.15 ^(e)	461.44	2.28	49.60 ^(g)	GC	48.77	1.67
Thymol methyl ether	-	501.77	-	-	GC	60.16	-
(+)- α -Pinene	429.35 ^(e)	442.44	3.05	44.84 ^(g)	GC	44.67	0.40
(+)- β -Pinene	439.15 ^(e)	453.01	3.16	46.19 ^(g)	GC	45.30	1.93
5-Vinyl-2-norbornene	414.2 ^(f)	423.12	2.15	42.29 ^(h)		41.64	1.33
5-Ethylidene-2-norbornene	419.2 ^(f)	429.15	2.37	44.30 ⁽ⁱ⁾	EB	43.63	1.51
Fenchyl alcohol	-	481.30	-	-	GC	54.47	-
Bicyclo [4.1.0] heptane-7-carboxylic acid	-	516.95	-	-	GC	79.15	-

^(a) T_{nb}^{lit} and $\Delta_{vap}H^{lit}$: literature normal boiling temperature and enthalpy of vaporization at 298.15 K.

^(b) T_{nb}^{exp} and $\Delta_{vap}H^{exp}$: experimental normal boiling temperature and enthalpy of vaporization at 298.15 K obtained in this work.

^(c) RD: absolute relative deviation.

^(d) Gas Chromatography (GC), Ebulliometry (EB).

^(e)[24]. ^(f)[25]. ^(g)[14]. ^(h)[26]. ⁽ⁱ⁾[27].

summing the frequency of each group occurring in the molecule multiplied by its contribution. These methods provide quick estimates without requiring substantial computational resources. The representation of molecular structures through functional groups provides these methods with a predictive quality regarding the range of molecular structures that can be handled. Methods based on the group contribution approach has been developed for a wide range of properties and are routinely used when measured data for properties are not available [19].

To ensure consistency in the results, terpene compounds with available enthalpies of vaporization in the literature [14,26,27] were selected. Enthalpies of vaporization at 298.15 K were predicted using the methods proposed by Chickos et al. [21], Joback and Reid [22], and a new group contribution method was introduced in this work. Each of these methods employs specific fragmentation schemes and interactions between groups

3.1 Proposed Model

This newly developed group contribution method is designed to estimate the enthalpy of vaporization of pure organic compounds. It introduces a specific fragmentation scheme adapted for essential oil compounds, which primarily consist of monoterpene hydrocarbons, sesquiterpene hydrocarbons, and oxygenated derivatives. The selection of compounds for the database followed specific criteria, including saturated and unsaturated hydrocarbons with open-chain and branched structures ranging from C₇ to C₁₅ carbon atoms. It also encompassed bicyclic hydrocarbons and oxygenated derivatives. Due to their low occurrence in essential oils, compounds containing sulfur, nitrogen, and alkynes hydrocarbons were excluded from the database. The proposed method is based on first-order groups. The fragmentation scheme considers molecular characteristics, such as distinguishing between open-chain, cyclic, aromatic groups, and bicyclic structures. A total of 26 groups were defined. Table 6 presents all the groups utilized in the regression and their respective contributions to the prediction of enthalpy of vaporization.

The proposed model comprises a dataset of 1,719 different organic substances, with a total of 3,591 data points for enthalpy of vaporization. Considering that some terpenes in the dataset have multiple values for enthalpy of vaporization, the division was based on the number of compounds. The cross-validation technique was chosen for parameter selection as it enhances the model's generalization

capacity [28]. The training and validation phases utilized 80% of the database, while the remaining 20% was allocated for testing. Parameter optimization was performed using gradient descent, which is widely used in training machine learning models, such as linear regression. It provides an efficient way to find optimal parameter values that minimize the cost function, allowing the models to better fit the training data and make accurate predictions on new, unseen data.

Regarding the contribution values, some considerations are necessary. Groups containing carbonyl (C=O) and hydroxyl (-OH) exhibit the highest contributions, which aligns with their polar nature and strong intermolecular dipole-dipole forces. Additionally, groups containing hydroxyl, such as alcohols, phenols, and carboxylic acids, also demonstrate significant contributions due to hydrogen bonding. Descriptors for bicyclic compounds and cis-trans isomerism display negative values, reflecting the stereoisomeric positions in these compound types. Moreover, groups associated with aliphatic compounds or segments of molecules, such as -CH₃ and -CH₂-, show lower contributions, likely attributed to the branching that diminishes intermolecular attraction and influences thermodynamic properties such as normal boiling temperature and enthalpy of vaporization.

The Eq. 7 performs the prediction by the proposed model.

$$\Delta_{vap}H = 19.55 + \sum_i N_i C_i \quad (7)$$

In Eq. (7), N_i represents the occurrence of each group in the structure, and C_i denotes the contribution to the enthalpy of vaporization from each group. The application of this method is shown in Table 7.

The relative deviation (RD) for each method is defined in Eq. (8).

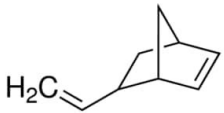
$$RD\% = 100 \cdot abs \left[\frac{\Delta_{vap}H^{exp} - \Delta_{vap}H^{est}}{\Delta_{vap}H^{exp}} \right] \quad (8)$$

In Eq. (8), $\Delta_{vap}H^{exp}$ and $\Delta_{vap}H^{est}$ represent the experimental and estimated enthalpies of vaporization, respectively.

Table 6. Proposed model group contribution fragments.

N°	Group	Contribution
0	h_0	19.548
1	-CH ₃	0.475
2	-CH ₂ -	3.900
3	>CH-	4.172
4	>C<	4.380
5	=CH ₂	-1.196
6	=CH-	4.525
7	=C<	5.008
8	-CH ₂ - (cyclic)	2.793
9	>CH- (cyclic)	3.197
10	>C< (cyclic)	4.535
11	=CH- (cyclic)	3.048
12	=C< (cyclic)	4.862
13	=CH (aromatic)	2.808
14	=C< (aromatic)	5.610
15	OH (alcohol)	17.421
16	-O-	2.255
17	O-C=O	12.162
18	C=O	6.301
19	OH (phenol)	7.979
20	-O- (cyclic)	4.307
21	C=O (cyclic)	10.589
22	bicyclic (correction)	-2.053
23	HC=O	8.912
24	OHC=O	30.201
25	cis correction	0.983
26	trans correction	1.338

Table 7. Estimated enthalpy of vaporization ($\Delta_{vap}H^{est}$) of 5-Vinyl-2-norbornene using this work proposed model at constant temperature (298.15 K). Experimental literature data [26]: $\Delta_{vap}H^{exp}$ (298.15 K) = 42.29 kJ/mol.

Compound	Proposed model	
	Group Contribution	
 5-Vinyl-2-norbornene	h_0	19.548
	-CH ₂ - (ring)	2.792
	=CH- (ring)	3.048
	>CH- (ring)	3.197
	=CH-	4.525
	=CH ₂	-1.196
	Bicyclic correction	-2.053
	$\Delta_{vap}H^{est}$ (kJ.mol ⁻¹)	42.10
	$\Delta_{vap}H^{exp}$ (kJ.mol ⁻¹) ^(a)	42.29
	RD (%)	0.45

^(a)[26].

3.2 Chickos et al. (1998)

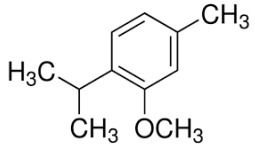
In this method [21], the evaluation of the nature and location of functional groups is performed. The steric environment of the functional groups is identified using characteristics such as hybridization and substitution.

Estimation is further enhanced by accounting for intramolecular hydrogen bonding.

$$\Delta_{vap}H = 4.69(N_C - N_Q) + 1.3N_Q + 3.0 + \sum_i n_i F_i b_i + C \quad (9)$$

Eq. (9) defines the parameters N_C and N_Q as the total number of carbons and the total number of quaternary sp^3 hybridized carbon atoms, respectively. The product $F_i b_i$ depends on the nature (b) and location (F) of the functional group, while C represents a correction parameter associated with intramolecular interactions. The application of this method is presented in Table 8.

Table 8. Estimated enthalpy of vaporization ($\Delta_{vap}H^{est}$) of Thymol methyl ether at 298.15 K using the method proposed by Chickos et al. [21]. Experimental data from this study: $\Delta_{vap}H^{exp}$ (298.15 K) = 60.16 kJ/mol.

Compound	Chickos et al.'s [21]	
 Thymol methyl ether	Group contribution	
	N_C	11
	N_Q	0
	Functional group class	b_i
	> O	5.0
	Substitution Factor	F_i
	Single substitution on a primary sp^3 atom	1.62
	Single substitution on a quaternary sp^2 atom	0.85
	Correction	C
	Ortho and vicinal alkyl branching cyclic sulfides on sp^2 and sp^3 carbons on 5 and 6-membered rings	-2
$\Delta_{vap}H^{est}$ (kJ.mol ⁻¹)	62.69	
$\Delta_{vap}H^{exp}$ (kJ.mol ⁻¹) ^(a)	60.16	
RD (%)	4.21	

^(a)Experimental enthalpy of vaporization at 298.15 K obtained in this work.

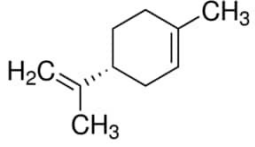
3.3 Joback and Reid (1987)

The method proposed by Joback and Reid [22] predicts eleven important and commonly thermodynamic properties of pure components from molecular structure only. This method assumes that there are no interactions between the groups and therefore only uses additive contributions.

$$\Delta_{vap}H = 15.30 + \sum_i N_i h_{v,i} \quad (10)$$

In Eq. (10), N_i represents the occurrence of each group in the structure, and $h_{v,i}$ denotes the contribution to the enthalpy of vaporization from each group. The application of this method is summarized in Table 9.

Table 9. Estimated enthalpy of vaporization ($\Delta_{vap}H^{est}$) of (+)-Limonene at 298.15 K using the method proposed by Joback and Reid [22]. Experimental literature data [14]: $\Delta_{vap}H^{exp}$ (298.15 K) = 49.60 kJ/mol.

Compound	Joback and Reid's method [22]	
 (+)-Limonene	Group Contribution	
	h_0	15.30
	CH ₃	2.373
	=CH ₂	1.724
	=C<	2.138
	CH _(ring)	1.942
	=CH _(ring)	2.544
	=C< _(ring)	3.059
	CH ₂ (ring)	2.398
	$\Delta_{vap}H^{est}$ (kJ.mol ⁻¹)	38.55
$\Delta_{vap}H^{exp}$ (kJ.mol ⁻¹) ^(a)	49.60	
RD (%)	22.28	

^(a)[14].

4. Results and Discussion

New experimental data were obtained for terpene compounds, including (+)-Limonene, Thymol methyl ether, (+)- α -Pinene, (+)- β -Pinene, 5-Vinyl-2-norbornene, 5-Ethylidene-2-norbornene, Fenchyl alcohol and Bicyclo [4.1.0] heptane-7-carboxylic acid at 298.15 K using gas chromatography correlation.

Table 2 presents the Kováts retention index values for the monocyclic and bicyclic terpenes evaluated in this study. From the I_x data of each compound within their respective temperature range, the dependence of vapor pressure on temperature was evaluated using Eq. (2). The resulting vapor pressure curves for the analyzed bicyclic and monocyclic terpenes are displayed in Figure 2 and Figure 3, respectively.

^(a) 5-Vinyl-2-norbornene; ^(b) 5-Ethylidene-2-norbornene; ^(c) Bicyclo [4.1.0] heptane-7-carboxylic acid.

Figure 2. Temperature dependence of the vapor pressure for the bicyclic terpenes studied in this work.

By analyzing the temperature-dependent vapor pressure, the constants of the Antoine equation Eq. (3) were determined. As shown in Table 3, all the compounds exhibited correlation coefficients (r^2) above 0.999, indicating a strong fit to the model.

Figure 3. Temperature dependence of the vapor pressure for the monocyclic terpenes studied in this work.

The enthalpy of vaporization, which is directly related to vapor pressure, was calculated using Eq. (5) based on the obtained vapor pressure curves (Figures 2 and 3). The parameter values for Eq. (5) were obtained through nonlinear regression analysis performed using Origin 8.1 (Origin Lab, Northampton, Massachusetts, USA), and are presented in Table 4. The normal boiling temperature (T_{nb}) was calculated by extrapolating the data to 101.325 kPa using an iteration procedure in Excel. The calculated values for $\Delta_{vap}H$ in this work were compared with literature data, and the absolute relative deviation demonstrated agreement with results

reported in the literature, as shown in Table 5. Furthermore, a comparison of our boiling point temperatures with literature values revealed a low relative deviation in predicting T_{nb}^{exp} , indicating that gas chromatography using n-alkanes as standards can be a reliable method for obtaining these thermodynamic properties experimentally.

The absolute relative deviation (RD) is defined as Eq. (11).

$$RD\% = 100 \cdot abs(TP^{lit} - TP^{exp} / TP^{lit}) \quad (11)$$

In Eq. (11), TP^{lit} and TP^{exp} referred to the thermodynamic properties of the literature and that obtained experimentally in this work. The TP parameter is substituted by the enthalpy of vaporization or normal boiling temperature depending on the analyzed property.

Experimental data for enthalpy of vaporization from the literature and determined in this work were compared with data provided from estimation methods at constant temperature (298.15 K) developed by Chickos et al. [21], Joback and Reid [22] and a new group contribution method proposed in this work. The performance of the studied methods was examined and discussed. The results are presented in Table 10.

The mean relative deviation (MRD) for each method is defined in Equation (12):

$$MRD (\%) = \frac{100}{n} abs \left[\frac{\Delta_{vap}H^{exp,i} - \Delta_{vap}H^{est,i}}{\Delta_{vap}H^{exp,i}} \right] \quad (12)$$

In Eq. (12), n is the number of compounds, and i represents each compound.

The method proposed by Chickos et al. [21] demonstrates reasonable estimates for most of the studied monocyclic and bicyclic terpenes, with a mean relative deviation of 9.51%. Although this model incorporates contributions for functional groups, types of carbon bonding and hybridization, as well as correction terms for intramolecular interactions, its database is limited in terms of the number of compounds representing each functional group and molecular structure. Moreover, it does not distinguish the contributions of isomers, as observed in the cases of (+)- α -Pinene and (+)- β -Pinene, as well as 5-Vinyl-2-norbornene and 5-Ethylidene-2-norbornene, respectively.

Joback and Reid [22] proposed a classical group contribution method that utilizes additive contributions and does not consider intramolecular interactions. However, it demonstrated the highest mean relative deviation of 20.00% among the examined models. This method assumes no interactions between groups and relies solely on additive contributions. Additionally, it does not differentiate between aromatic and non-aromatic rings, which significantly impacts the performance of this group contribution method.

The proposed model encompasses terpene compounds and integrates group contributions for bicyclic compounds. In this method, the most significant deviation of 11.69% was observed for (+)-Limonene and Thymol methyl ether, while the smallest deviation was found for bicyclic compounds. This model includes groups that describe the studied molecules, specifically terpene compounds, with the addition of bicyclic structures and isomers. However, it lacks a correction for interactions between carbons in cyclic or aromatic structures, resulting in a mean relative deviation of 8.00%

Table 10. The enthalpy of vaporization at 298.15 K: experimental ($\Delta_{\text{vap}}H^{\text{exp}}$) and estimated ($\Delta_{\text{vap}}H^{\text{est}}$) data.

Compounds	$\Delta_{\text{vap}}H^{\text{exp}}$ (kJ.mol ⁻¹)	Estimated enthalpy of vaporization (kJ.mol ⁻¹)					
		Chickos et al.'s method [21]		Proposed model		Joback and Reid's method [22]	
		$\Delta_{\text{vap}}H^{\text{est}}$	RD%	$\Delta_{\text{vap}}H^{\text{est}}$	RD%	$\Delta_{\text{vap}}H^{\text{est}}$	RD%
Monocyclic terpene							
(+)-Limonene	49.60 ^(a)	49.90	0.60	43.80	11.69	38.55	22.28
Thymol methyl ether	60.16 ^(b)	62.69	4.21	53.13	11.69	45.72	24.00
Bicyclic terpene							
(+)- α -Pinene	44.84 ^(a)	46.51	3.72	43.35	3.32	37.36	16.68
(+)- β -Pinene	46.19 ^(a)	46.51	0.69	41.42	10.33	36.56	20.85
5-Vinyl-2-norbornene	42.29 ^(c)	45.21	6.90	42.10	0.45	34.95	17.36
5-Ethylidene-2-norbornene	44.30 ^(d)	45.21	2.05	45.43	2.55	36.72	17.11
Fenchyl alcohol	54.47 ^(b)	83.75	53.75	60.18	10.48	51.63	5.21
Bicyclo [4.1.0] ^e	79.15 ^(b)	82.42	4.13	68.46	13.51	50.26	36.50
MRD (%)			9.51		8.00		20.00

^e Bicyclo [4.1.0] heptane-7-carboxylic acid.
 Experimental data from literature: ^(a)[14], ^(c)[26], ^(d)[27].
^(b) Experimental data obtained in this work.

Figure 4 illustrates the distribution of the three group contributions to estimated vaporization enthalpies in relation to the experimental data.

Pinene, (+)- β -Pinene, 5-Vinyl-2-norbornene, 5-Ethylidene -2-norbornene, Thymol methyl ether, Fenchyl alcohol, and Bicyclo [4.1.0] heptane-7-carboxylic acid were determined by gas chromatography technique using n-alkanes as standards, yielding good results. The referenced thermodynamic parameters of the last three compounds were previously unpublished in the literature and are being presented for the first time in this study.

The comparison of the three studied group contributions highlights that a reliable database and the fragmentation scheme are crucial for an accurate group contribution method. Among the studied models, the proposed model demonstrated better performance for the analyzed compounds ($r^2 = 0.8398$). It is a first-order group model. The accuracy of the group contribution-simple (based on first-order groups) is qualitatively acceptable, but a more precise prediction is obtained through the addition of second and third-order group contributions [29]. The proposed model fills a gap in predictive methods specific to the physical properties of terpene compounds and can be further enhanced by incorporating second and third-order contributions.

Figure 4. Enthalpies of vaporization distribution: estimated ($\Delta_{\text{vap}}H^{\text{est}}$) and experimental ($\Delta_{\text{vap}}H^{\text{exp}}$) data.

Comparing the results obtained by the studied models and analyzing Figure 4, it can be observed that the proposed model achieved a correlation coefficient (r^2) value of 0.8398, indicating a high level of accuracy in fitting the utilized data. In contrast, Chickos et al. [21] and Joback and Reid [22] proposed models had r^2 values of 0.6693 and 0.6666, respectively, suggesting a comparatively less precise fit. Consequently, the proposed model demonstrated superior performance when compared to the other evaluated models.

5. Conclusion

This paper compares three group contribution methods, including a new model specifically designed for terpene compounds, with different fragmentation schemes. These methods were evaluated against experimental enthalpies of vaporization obtained through gas chromatography correlation. Reliable experimental thermodynamic data are crucial for understanding chemical processes like secondary organic aerosol (SOA) formation and for building the database used in the development of group contribution models. However, experimental techniques often require significant effort. Group contribution methods are valuable in this regard as they only require knowledge of the chemical structure to estimate physical properties.

The enthalpy of vaporization ($\Delta_{\text{vap}}H$) at 298.15 K and the normal boiling temperature (T_{nb}) of (+)-Limonene, (+)- α -

Nomenclature

$\Delta_{\text{vap}}H$	Enthalpy of vaporization (kJ.mol ⁻¹)
exp	The superscript symbol "exp" means experimental
est	The superscript symbol "est" means estimated
lit	The superscript symbol "lit" means literature
GC	Gas chromatography
I_x	Kováts retention index
MRD	Mean relative deviation
P_{vap}	Vapor pressure (Pa)
RD	Relative deviation
R	universal gas constant (J.K ⁻¹ .mol ⁻¹)
r^2	Correlation coefficient
T	Temperature (K)
T_0	Reference temperature (K)
T_{nb}	Normal boiling temperature (K)
TP	Thermodynamic property
t_r	Retention time (s)
X	Solute, analyzed compound
γ^∞	Infinite dilution activity coefficient
z	Carbon number

References




- [1] P.M. Dewick, "The biosynthesis of C5-C25 terpenoid compounds," *Nat. Prod. Rep.*, 19, 181-222, 2002.

- [2] F. Fehsenfeld, J. Calvert, R. Fall, P. Goldan, A.B. Guenther, C.N. Hewitt, B. Lamb, S. Liu, M. Trainer, H. Westbert, P. Zimmerman, "Emissions of volatile organic compounds from vegetation and the implications for atmospheric chemistry," *Glob. Biogeochem. Cycles*, 6, 389-430, 1992.
- [3] A.H. Goldstein, I.E. Galbally, "Known and Unexplored Organic Constituents in the Earth's Atmosphere," *Environ. Sci. Technol.*, 41, 1514-1521, 2007.
- [4] Y. Yokouchi, Y. Ambe, "Aerosols formed from the chemical reaction of monoterpenes and ozone," *Atmos. Environ.*, 19, 1271-1276, 1985.
- [5] S.N. Pandis, A.S. Wexler, J.H. Seinfeld. "Secondary organic aerosol formation and transport — II. Predicting the ambient secondary organic aerosol size distribution," *Atmos. Environ.*, 15, 2403-2416, 1993.
- [6] M. Keller, M. Lerda, "Isoprene emission from tropical forest canopy leaves," *Glob. Biogeochem. Cycles*, 13, 19-29, 1999.
- [7] M. Kanakidou, J.H. Seinfeld, S.N. Pandis, I. Barnes, F.J. Dentener, M.C. Facchini, R. Van Dingenen, B. Ervens, A. Nenes, C.J. Nielsen, E. Swietlicki, J.P. Putaud, Y. Balkanski, S. Fuzzi, J. Horth, G.K. Moortgat, R. Winterhalter, C.E.L. Myhre, K. Tsigaridis, E. Vignati, E.G. Stephanou, J. Wilson, "Organic aerosol and global climate modelling: a review," *Atmospheric Chem. Phys.*, 5, 1053-1123, 2005.
- [8] D.W. Dockery, C.A. Pope, X.P. Xu, J.D. Spengler, J.H. Ware, M.E. Fay, B.G. Ferris, F.E. Speizer, "An association between air pollution and mortality in six U.S. cities," *N. Engl. J. Med.*, 329, 1753-1759, 1993.
- [9] D. T. Tingey, M. Manning, L.C. Grothaus, W.F. Burns, "Influence of light and temperature on monoterpene emission rates from slash pine," *Plant Physiol.*, 65, 797-801, 1980.
- [10] A.B. Guenther, R.K. Monson, R. Fall, "Isoprene and monoterpene emission rate variability: observations with Eucalyptus and emission rate algorithm development," *J. Geophys. Res.*, 96, 10799-10808, 1991.
- [11] Ü. Niinemets, R. K. Monson, A. Arneth, P. Ciccioli, J. Kesselmeier, U. Kuhn, S.M. Noe, J. Peñuelas, M. Staudt, "The leaf-level emission factor of volatile isoprenoids: caveats, model algorithms, response shapes and scaling," *Biogeosciences*, 7, 1809-1832, 2010.
- [12] V. Stejfa, M. Fulem, K. Ruzicka, C. Cervinka, M.A.A. Rocha, L.M.N.B.F. Santos, B. Schröder, "Thermodynamic study of selected monoterpenes," *J. Chem. Thermodyn.*, 60, 117-125, 2013.
- [13] V. Majer, M. Svoboda, J. Pick. *Heats of Vaporizations of Fluids*, New York: Elsevier, 1989.
- [14] M. Hoskovec, D. Grygarová, J. Cvačka, L. Streinz, J. Zima, S.P. Verevkin, B. Koutek, "Determining the vapour pressures of plant volatiles from gas chromatographic retention," *J. Chromatogr. A*, 1083, 161-172, 2005.
- [15] C.E.L. Oliveira, M.A. Cremasco, "Determination of the vapor pressure of *Lippia gracilis* Schum essential oil by thermogravimetric analysis," *Thermochim. Acta*, 577, 1-4, 2014.
- [16] S.F. Donovan, "New method for estimating vapor pressure by the use of gas chromatography," *J. Chromatogr. A*, 749, 123-129, 1996.
- [17] B. Koutek, M. Hoskovec, P. Vrkočová, L. Feltl, "Gas chromatographic determination of vapour pressures of pheromone-like compounds IV. Acetates, a reinvestigation," *J. Chromatogr. A*, 759, 93-109, 1997.
- [18] J.P. O'Connell, R. Gani, P.M. Mathias, G. Maurer, J.D. Olson, P.A. Crafts, "Thermodynamic Property Modeling for Chemical Process and Product Engineering: Some Perspectives," *Ind. Eng. Chem. Res.*, 48, 4619-4637, 2009.
- [19] R. Gani, "Group contribution-based property estimation methods: advances and perspectives," *Curr. Opin. Chem. Eng.*, 23, 184-196, 2019.
- [20] V. Mann, R. Gani, V. Venkatasubramanian, "Group contribution-based property modeling for chemical product design: A perspective in the AI era," *Fluid Ph. Equilib.*, 568, 113734, 2023.
- [21] J.S. Chickos, W.E. Acree, J.F. Liebman, "Estimating phase change and entropies in Computational Thermochemistry: Prediction Estimation of Molecular Thermodynamics," in K. Irikura, D. Frurip (Eds.), *ACS Symposium Series n. 677*, American Chemistry Society, Washington DC, 63-91, 1998.
- [22] K. G. Joback, R. C. Reid, "Estimation of Pure-Component Properties From Group-Contributions," *Chem. Eng. Commun.*, 57, 233-243, 1987.
- [23] K. Růžička, V. Majer, "Simultaneous treatment of vapor pressures and related thermal data between the triple and normal boiling temperatures for n -alkanes C₅ – C₂₀," *J. Phys. Chem. Ref. Data*, 23, 1-39, 1994.
- [24] D.R. Lide. *CRC Handbook of Chemistry and Physics*, 84 ed., CRC Press, 2004.
- [25] National Institute of Standards and Technology. Chemistry Web Book. NIST Standard Reference Database Number 69. 2011.[Online]. Available: <https://webbook.nist.gov/chemistry/name-ser/>. (accessed Jan. 20, 2023).
- [26] W. V. Steele, R. D. Chirico, S. E. Knipmeyer, A. Nguyen, N. K. Smith, "Thermodynamic Properties and Ideal-Gas Enthalpies of Formation for Butyl Vinyl Ether, 1,2-Dimethoxyethane, Methyl Glycolate, Bicyclo [2.2.1]hept-2-ene, 5-Vinylbicyclo[2.2.1]hept-2-ene, trans-Azobenzene, Butyl Acrylate, Di-tert-butyl Ether, and Hexane-1,6-diol," *J. Chem. Eng. Data*, 41, 1285-1302, 1996.
- [27] W. Acree Jr., J.S. Chickos, "Phase Transition Enthalpy Measurements of Organic and Organometallic Compounds. Sublimation, Vaporization and Fusion Enthalpies From 1880 to 2015. Part 1. C₁ – C₁₀," *J. Phys. Chem. Ref. Data*. 45, 2016.
- [28] N.J. Nilsson, "Introduction to machine learning: an early draft of a proposed textbook," Robotics Laboratory, Department of Computer Science. Stanford, 2005.

- [29] A.S. Hukkerikar, B. Sarup, A. Ten Kate, J. Abildskov, G. Sin, R. Gani, "Group-contribution (GC) based estimation of properties of pure components: improved property estimation and uncertainty analysis," *Fluid Phase Equilib.*, 321, 25–43, 2012.

Research Article

Comparative Evaluation for Selected Gas Turbine Cycles

^{1*}Mohamed Elwardany , ²Abd El-Moneim M. Nassib , ³Hany A. Mohamed 

^{1,2,3} Department of Mechanical Power Engineering, Faculty of Engineering, Assiut University, Assiut 71516, Egypt

³ Manufacturing Department, Modern Academy for Engineering and Technology, Cairo 11571, Egypt

E-mail: ^{1*} M.Wardany@anu.edu.eg

Received 21 March 2023, Revised 25 August 2023, Accepted 11 September 2023

Abstract

The energy and exergy evaluation of simple gas turbine (SGT), gas turbine with air bottoming cycle (GT-ABC), and partial oxidation gas turbine (POGT) are studied. The governing equations for each cycle are solved using energy equation Solver (EES) software. The characteristics performance for selected cycles are discussed and verified with that obtained for available practical cycles (SGT, GT-ABC, POGT). The present results show a good agreement with the practical one. The effects of significant operational parameters, turbine inlet temperature (TIT), compression ratio (CR), and compressor inlet temperature (CIT), on the specific fuel consumption, energy and exergy efficiencies are discussed. According to the findings, a reduction in CIT and a rise in TIT and CR led to enhance energy and exergy efficiency for each configuration with different ranges. Results revealed that the GT-ABC and POGT cycles are more efficient than those of SGT at the same operational parameters. The energy and exergy efficiencies are 38.4%, 36.2% for SGT, 40%, 37.8 % for GT-ABC, and 41.6%, 39.3% for POGT. The POGT cycle has a better energy and exergy performance at a lower pressure ratio than the SGT and GT-ABC.

Keywords: Gas turbine; thermal analysis; energy; exergy; efficiency.

1. Introduction

Energy consumption is a critical development metric, driven by factors such as population growth, urbanization, industrialization, and technological advancements. This surge in energy demand, primarily met by fossil fuels accounting for 80% of electricity generation, has led to environmental issues, including pollution and the greenhouse effect [1]. Global electricity demand is rising at an annual rate of approximately 6% [2], with fossil fuels, particularly natural gas (NG), contributing significantly to CO₂ emissions [3]. NG presently constitutes 22% of global primary energy production and is projected to increase its share in electricity generation by 2040, reaching 28% from 22% in 2012 [4]. The concept of "analysis of thermal power plants" encompasses the effective utilization of energy resources. Prior to 1940, the energy efficiency of power plants was assessed using the first law of thermodynamics, while exergy analysis, based on the second law, has since offered insights into energy losses, aiding in the design, evaluation, optimization, and enhancement of thermal power plants [5]–[8].

Exergy analysis stands out as an effective technique for optimizing energy systems by offering an intricate understanding of a system's thermodynamic performance. This analytical approach proves invaluable in pinpointing areas ripe for enhancement and fine-tuning the operation and design of energy systems, leading to heightened efficiency, reduced energy consumption, and a diminished environmental footprint. A standout advantage of exergy assessment lies in its ability to provide a comprehensive overview

of energy flows and losses within a system. By discerning the exergy destruction within each component of a system, engineers gain the insights necessary to identify energy losses and develop strategies to curtail them. This, in turn, paves the way for significant strides in energy efficiency and cost reduction. Exergy analysis also facilitates the optimization of energy systems under various operational conditions [9]–[12].

Significant energy losses to the ecosystem arise from incomplete combustion processes and the rapid expansion of high-temperature, high-pressure exhaust gases, resulting in environmental pollution and contributing to global warming [10],[11]. A study by Ibrahim et al.[15] studied simplified gas turbine model through energy and exergy assessments found that the combustion chamber was the primary locus of exergy destruction. The air compressor exhibited energy and exergy efficiencies of 92% and 94.9%, respectively. In comparison, the combustion chamber demonstrated energy and exergy efficiencies of 61.8% and 67.5%, in contrast to the 82% and 92% efficiencies of gas turbines. The combined energetic and exergetic efficiencies were calculated at 34.3% and 32.4%, respectively. Kurt et al. [16] investigated various operational parameters of gas turbine power plants and determined that the highest overall power output occurred at TIT=1600K, CIT=288.15 K, and PR=22 when analyzed for turbine inlet temperature (TIT), compressor inlet temperature (CIT), and pressure ratio (PR). Conversely, it peaked at CIT=273.15K, TIT=1423.15 K, and PR=18 when considering compressor inlet temperature. Sa et al. [17] proposed an empirical relationship regarding a gas turbine's capacity to generate electricity under ambient air conditions

differing from ISO standards. Their findings, derived from over 8,000 data readings across approximately 280 days of gas turbine operation, indicated that for each degree increase in ambient temperature beyond ISO conditions, the gas turbine experienced a 1.47 MW power output reduction and a 0.1% decline in thermal efficiency.

Abou Al-Sood et al. [18] provided insights into the operational performance of a gas turbine employing an irreversible intercooler, regenerative, and reheat gas cycle. Optimization studies unveiled that the lowest temperature ranged from 302 K to 315 K, while the highest temperature fluctuated between 1320 K and 1360 K. To maximize performance parameters, the cycle's highest pressure was found to be optimal within the range of 1449 kPa to 2830 kPa. On a related study, Aydin [19] introduced exergy sustainability indicators for the assessment of gas turbine power plant operations, considering two distinct configurations. In Case A, based on LM6000 GT technology, the power plant generated 43.3 MW of electricity at full capacity, while Case B, incorporating steam turbine cycles, produced 54.3 MW. The addition of the steam cycle led to a 10% reduction in the waste-exergy ratio. In both cases, the power plants exhibited recoverable exergy ratios of approximately 22% and 13.1%, respectively. Notably, the environmental impact factor improved by about 50% in the scenario of the steam cycle power plant (Case B). Ultimately, the exergetic sustainability indices for Case A and Case B power plant configurations were calculated at 0.651 and 0.978, respectively, reflecting their sustainability and efficiency.

In the late 1980s, an Air Bottoming Cycle (ABC) emerged as a viable alternative to the conventional steam bottoming cycle, which utilizes hot combustion products for heat in the bottoming cycle [20]. Carcasci et al. [20] conducted an investigation into an ABC system integrated with an industrial medium-power gas turbine. The results revealed that this gas turbine, when coupled with the ABC, exhibited enhanced power output and higher thermal efficiency compared to a standalone gas turbine. Notably, the primary GE10 turbine's thermal efficiency experienced a notable increase of 7.6%, while its output power surged by 22.3%. Ghazikhani et al. [21] further delved into the exergy aspects of a simple gas turbine versus a GT-ABC configuration. Their findings indicated that exhaust exergy recovery in the GT-ABC ranged from 8.6% to 14.1% of the fuel exergy, depending on operating conditions, while only 4.7% to 7.4% of the fuel exergy was lost due to the added components in the ABC. The specific fuel consumption (SFC) of the GT-ABC was generally 13.3% lower, and the specific work was 15.4% higher compared to the simple gas turbine. Alklaibi et al. [14] conducted a comparative analysis of the GT-ABC against simple and modified gas turbines, examining the influence of bottoming and topping cycle pressure ratios on work output and thermal efficiency. They found that at peak efficiency, the simple gas turbine cycle with ABC improved efficiency by 4.78%. An exergy analysis revealed that a gas turbine bottoming cycle reduced overall exergy destruction by 6%. Notably, the loss of exergy in the exhaust gas of a conventional gas turbine accounted for 47% of the overall exergy destruction, a figure reduced to 31% when implementing a GT-ABC system. Graziani et al. [22] explored the impact of ambient temperature on the exergy destruction of a GT-ABC, observing a 6% average improvement in second-law efficiency when adding a heat exchanger to a basic gas turbine to recover exhaust exergy

despite maintaining identical inlet air temperatures in both cycles.

Gas turbines have been the subject of cycle enhancements because the traditional Brayton cycle has inherent limitations in terms of efficiency and emissions improvement. To address these challenges, various enhancements such as recuperation, intercooling, reheat, and water/steam injection have been incorporated into cycle performance studies. These modifications aim to facilitate more complete fuel combustion. One innovative approach is the use of Partial Oxidation Gas Turbines (POGT), which employ a partial oxidation reactor instead of a conventional combustor, requiring stoichiometric air-fuel ratios. POGT benefits from a higher specific heat compared to complete combustion [23], [24]. This technology results in a remarkable 10% increase in system efficiency compared to a standard gas turbine bottoming cycle. These efficiency gains can be attributed to several factors, including nearly isothermal expansion, reduced density of partial oxidation products, increased volumetric gas flow in the turbine (15-20%), and significantly lower airflow requirements, typically 65% less than those of a conventional expansion turbine [23].

In their study, Diyoke et al. [25] conducted a comprehensive evaluation of a hybrid gas turbine and biomass power system with the aim of promoting sustainable multi-generation practices in Nigeria. They introduced two distinct configurations of this hybrid system, which coupled a Gas Turbine Combined Cycle (GTC) with a Biomass Power System (BPS) integrated with an Absorption Refrigeration System (ARS) to facilitate Combined Cooling, Heating, and Power (CCHP) generation. Configuration 1 and Configuration 2 exhibited overall exergy efficiencies estimated at approximately 17% and 19%, respectively. Notably, among the various system components, the biomass gasifier contributed the most to exergy destruction (87%), followed by the combustion chamber (5.5%) and the syngas engine generator (3%). Their emission analysis revealed that these hybrid systems emitted roughly 30% less CO₂ in comparison to a standard recuperated GTC of equivalent capacity.

Additionally, the Levelized Cost of Electricity (LCOE) for the first and second proposed systems was calculated at 0.1373 and 0.1328 \$/kWh, respectively, highlighting their potential advantages in terms of multiple output capabilities and CO₂ emission reduction. This innovative approach combines biomass and natural gas resources for enhanced sustainability. In a separate study, Fan et al. [26] conducted a comparative investigation into the design and performance of innovative cascade CO₂ combined cycles for harnessing waste heat from gas turbine (GT) exhaust. They introduced a novel two-stage cascaded supercritical CO₂ and transcritical CO₂ (sCO₂-tCO₂) power cycle for waste heat recovery (WHR) from GT exhaust. Simulation results demonstrated that the SSBC-tCO₂ cycle outperformed the RSBC-tCO₂ cycle in its suitability as a bottoming cycle for GT, owing to its ability to generate higher power with a simpler configuration. Compared to traditional GT-RSBC and GT-SSBC setups, the optimal GT-CCO₂ cycle (GT-SSBC-tCO₂) exhibited significant improvements of 5.32% and 4.32% in thermal efficiency, showcasing its potential for enhancing energy efficiency and waste heat utilization in gas turbine systems.

Ryu et al. [27] conducted a comparative assessment of integrated solid oxide fuel cell-gas turbine (SOFC-GT)

systems for marine vessels, using ammonia and hydrogen as fuels. They used Aspen HYSYS V.12.1 for system design and modeling, analyzing it based on the first and second laws of thermodynamics. Direct ammonia and hydrogen SOFCs achieved energy efficiencies of 60.96% and 64.46%, respectively. Combining the systems increased energy efficiencies by 12.37% and 13.97% when using ammonia and hydrogen, compared to single SOFC systems. The study also examined exergy destruction in primary system components and determined the most suitable fuel utilization factor. This analysis highlights ammonia as a hydrogen carrier and emphasizes waste heat recovery for enhancing SOFC system performance.

In this study, we evaluated the energy and exergy performance of selected gas cycles (SGT, GT-ABC, POGT) under the same operation and design parameters. We used EES to simulate data and assess the impact of environmental conditions and other factors on cycle performance. Data were based on prior literature for each model.

2. Modelling and Analysis

2.1 Energy Analysis

The energy evaluations of the gas turbine cycle are related to the Brayton cycle. The computation will include evaluating the input and output energy of the system. The primary components of the gas turbine cycle include air compressors, combustion chamber, and gas turbine. Following are the equations required for analyzing each component of the gas turbine cycle [7].

Compressor:

$$T_2 = T_1 \left(1 + \frac{1}{\eta_{AC}} \left(r_{AC}^{\frac{k-1}{k}} - 1 \right) \right) \quad (1)$$

$$\dot{W}_{AC} = \dot{m}_a c_{pa} (T_2 - T_1) \quad (2)$$

$$c_{pa}(T) = 1.048 - \left(\frac{1.83T}{10^4} \right) + \left(\frac{9.45T^2}{10^7} \right) - \left(\frac{5.49T^3}{10^{10}} \right) + \left(\frac{7.92T^4}{10^{14}} \right) \quad (3)$$

In equation. (1), T_1 and T_2 represent the air temperature at the compressor input and discharge sections, k is the specific heat ratio, and r is the compression ratio. The power consumption of the compressor is calculated using equation (2). Equation (3) provides the air specific heat depending on the varying temperatures.

Combustion chamber:

$$\dot{m}_a h_2 + \dot{m}_f \text{LHV} = \dot{m}_g h_3 + (1 - \eta_{cc}) \dot{m}_f \text{LHV} \quad (4)$$

$$\dot{m}_g = \dot{m}_f + \dot{m}_a \quad (5)$$

$$f = \frac{\dot{m}_f}{\dot{m}_a} \quad (6)$$

Fuel air ratio is illustrated in equation (6). Lower heating value (LHV) differs based on the characteristics of the fuel used. This analysis employs natural gas (NG) in the combustion chamber. Chemically, NG is mostly methane (CH₄), about 75% to 99% of the gas; however, small quantities of other hydrocarbons can also be found in natural gas, along with carbon dioxide, hydrogen, nitrogen, carbon monoxide, and hydrogen sulfide [28].

Gas turbine:

$$T_4 = T_3 \left(1 - \eta_{GT} \left(1 - \left(\frac{P_3}{P_4} \right)^{\frac{k-1}{k}} \right) \right) \quad (7)$$

$$\dot{W}_{GT} = \dot{m}_g c_{p,g} (T_{A_3} - T_{A_4}) \quad (8)$$

$$c_{p,g}(T) = 0.991 + \left(\frac{6.997T}{10^5} \right) + \left(\frac{2.712T^2}{10^7} \right) - \left(\frac{1.2244T^3}{10^{10}} \right) \quad (9)$$

In equation. (7), T_3 and T_4 represent the turbine input and output combustion gas temperatures, respectively.

Power output from the turbine is calculated using equation (8). Equation (3) evaluates the specific heat of air based on varying temperature.

2.2 Exergy Analysis

Exergy is the maximum useful work achieved as a system reaches equilibrium with its surroundings. Utilizing the second law of thermodynamics, mass and energy balances, exergy analysis is an effective technique for evaluating the performance of energy systems. Exergy includes four components: chemical, physical, kinetic, and potential exergies. Only chemical and physical exergies are accounted for in the analyses, while kinetic and potential exergy are ignored. Physical exergy shows the maximum work capacity of a system. In contrast, chemical exergy is related to a system's chemical composition variation from equilibrium conditions [29]. General exergy analysis equations are shown below:

$$\dot{E}_{x, \text{heat}} + \sum_i \dot{m}_i e_{x,i} = \sum_e \dot{m}_e e_{x,e} + \dot{E}_{x,w} + \dot{I}_{\text{dest}} \quad (10)$$

$$\dot{E}_{x,w} = \dot{W} \quad (11)$$

$$\dot{E}_{x, \text{heat}} = \left(1 - \frac{T_o}{T_i} \right) \dot{Q}_i \quad (12)$$

$$\dot{E}_x = \dot{E}_{x, \text{phy}} + \dot{E}_{x, \text{che}} \quad (13)$$

Using equation. (10), the exergy flow rate for each system component can be determined [30]. Equation. (11) demonstrates the work performed by the system from exergy flow [30]. The rate of exergy generation with heat is shown in equation (12) [30]. The physical and chemical exergies of the component are shown in equation (13) [30].

The physical exergy is produced due to the system deviation from its dead state condition in terms of pressure and temperature [15]. Use the following equations to calculate the system physical exergy [46].

$$e_x = e_{x, \text{phy}} + e_{x, \text{che}} \quad (14)$$

$$e_{x, \text{phy}} = e_x^T + e_x^P \quad (15)$$

$$e_x^T = c_p \left((T - T_o) - T_o \ln \frac{T}{T_o} \right) \quad (16)$$

$$e_x^p = RT_o \ln \frac{P}{P_o} \quad (17)$$

The physical exergy calculation is shown in equation (15). Equations (16) and (17) determine physical exergy based on temperature and pressure. P_o and T_o represent the surrounding pressure and temperature, whereas C_p and R denote the specific heat at constant pressure and gas constant, respectively [30].

Chemical exergy is caused when the chemical composition of the system deviates from the surrounding dead-state condition [15]. The following equation can be used to determine the exergy flow of the fuel.

$$\xi = \frac{e_{x, \text{fuel}}}{LHV_{\text{fuel}}} \quad (18)$$

According to equation (18), ξ represents the ratio of exergy flow to the LHV of the fuel. ($LHV_{\text{fuel}} = 48,806 \text{ KJ/kg}$) Usually, the value for ξ is 1.06 for NG [15]. Thus, the value of fuel exergy can be calculated using the ratio of exergy and the LHV. The following equation can be used to determine the exergy of the combustion products [15].

$$e_{x, \text{cg}} = \frac{[\sum_{i=1}^n x_i e_{x, \text{che}, i} + RT_o \sum_{x=1}^n x_i \ln(x_i)]}{\sum(x_i)} \quad (19)$$

The subscripts I in equation (19) identify the type of air fraction, x is the molar fraction of air, and $e_{x, \text{che}}$ is the standard chemical exergy of each component of air fraction. Table 1 contains the Standard chemical exergy and molar fraction of each gas. The following equations can achieve a more accurate result [31].

$$\lambda = \frac{0.058 \dot{m}_{\text{air}}}{\dot{m}_{\text{fuel}}} \quad (20)$$

$$x_{N_2} = \frac{(7.524)\lambda}{1 + (9.6254)\lambda} \quad (21)$$

$$x_{O_2} = \frac{2(\lambda - 1)}{1 + (9.6254)\lambda} \quad (22)$$

$$x_{CO_2} = \frac{1 + (0.0028)\lambda}{1 + (9.6254)\lambda} \quad (23)$$

$$x_{H_2O} = \frac{2 + (0.0972)}{1 + (9.6254)\lambda} \quad (24)$$

Equations (20 – 24) can compute the molar fraction of each element of the combustion products; the equations are only useful when NG is used as the fuel. Subscript k represents the fuel-air ratio [31].

Table 1. Standard exergy and molar fraction [31].

Element	$e_{x, \text{che}}$ (KJ/mol)	Molar fraction (%)
N_2	0.72	75.67
O_2	3.97	20.34
CO_2	19.87	0.03
H_2O	9.49	3.03

2.3 Exergy Destruction

The product calculations for the exergy flow rate for each part were utilized to determine the exergy destruction. After

each process, the exergy flow will practically decrease. Usually, exergy destruction can be calculated by equation (25) [30].

$$\dot{E}_{x, \text{in}} - \dot{E}_{x, \text{out}} = \dot{E}_{x, D} \quad (25)$$

Air Compressor

$$\dot{E}_{x, D, AC} = \dot{E}_{x_1} - \dot{E}_{x_2} + \dot{W}_{AC} \quad (26)$$

Combustion chamber

$$\dot{E}_{x, D, CC} = \dot{E}_{x_2} + \dot{E}_{x_5} - \dot{E}_{x_3} \quad (27)$$

Gas turbine

$$\dot{E}_{x, D, GT} = \dot{E}_{x_3} - \dot{E}_{x_4} - \dot{W}_{GT} \quad (28)$$

2.4 Component Efficiency

Every component undergoes energy and exergy assessment to identify which has the lowest and highest efficiency. The exergy efficiency can be calculated by the following equation [29].

Air Compressor

$$\eta_{x, AC} = \frac{\dot{E}_{x_2} - \dot{E}_{x_1}}{\dot{W}_{AC}} \quad (29)$$

Combustion chamber

$$\eta_{x, CC} = \frac{\dot{E}_{x_3}}{\dot{E}_{x_3} - \dot{E}_{x_1}} \quad (30)$$

Gas turbine

$$\eta_{x, GT} = \frac{\dot{W}_{GT}}{\dot{E}_{x_3} - \dot{E}_{x_4}} \quad (31)$$

Equation (29) is used to determine the efficiency of the air compressor. Work output and exergy destruction significantly contribute to assessing the efficiency of the air compressor, while the same is true for equation (31), in which the exergy destruction and work output of a gas turbine determine the efficiency. In equation (30), the exergy rate and the exergy destruction for fuel affect the efficiency of the combustion chamber [31]. The equations below can determine the simple gas turbine cycle's overall exergy and energy efficiencies [30].

$$\dot{W}_{\text{net}} = \dot{W}_{GT} - \dot{W}_{AC} \quad (32)$$

$$\text{SFC} = 3600 \frac{\dot{m}_{\text{fuel}}}{\dot{W}_{\text{net}}} \quad (33)$$

$$\eta_I = \frac{\dot{W}_{\text{net}}}{\dot{m}_{\text{fuel}} LHV} \quad (34)$$

$$\eta_{II} = \frac{\dot{W}_{\text{net}, GT}}{\dot{E}_{x, f}} \quad (35)$$

Equation (33) shows the specific fuel consumption for the gas turbine. Equation (35) shows the overall exergy efficiency. Subscript $\dot{E}_{x, f}$ Denotes the fuel exergy

flow rate, while equation (34) shows the overall energy efficiency of the cycle [30].

2.5 Simple Gas Turbine (SGT)

As illustrated in Figure 1. Air is compressed by the compressor before being combined with fuel and fired in the combustion chamber. The hot combustion exhausts expand through the turbine and generate mechanical work. The exhaust gases are then released from the turbine. The energy produced can be used to generate electricity and operate various industrial machinery.

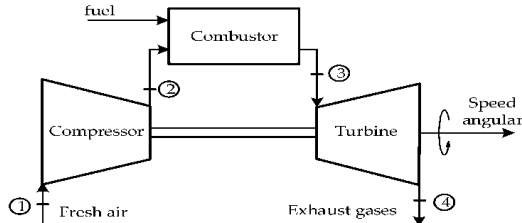


Figure 1. Simple gas turbine (SGT)[32].

The specific fuel consumption, work output, overall energy, and exergy efficiencies for a simple gas turbine cycle can be determined using the equations below [30].

$$\dot{W}_{Net,SGT} = \dot{W}_{GT} - \dot{W}_{AC} \quad (36)$$

$$SFC = 3600 \frac{\dot{m}_{fuel}}{\dot{W}_{net,SGT}} \quad (37)$$

$$\eta_{I,SGT} = \frac{\dot{W}_{net,SGT}}{\dot{m}_{fuel}LHV} \quad (38)$$

$$\eta_{II,SGT} = \frac{\dot{W}_{net,GT}}{\dot{E}_{x,f}} \quad (39)$$

2.6 Gas Turbine with Air Bottoming Cycle (GT-ABC)

A gas turbine with air air-bottoming cycle (GT-ABC) (Figure 2) is a combined cycle that primarily generates electricity from a gas turbine. The gas turbine generates power, while the air bottoming cycle captures and converts exhaust gases into a useful form. Combining a gas turbine with an air-bottoming cycle results in improved efficiency and power production than a single gas turbine. A heat-recovery heat exchanger is the combustion chamber for the bottoming cycle [14].

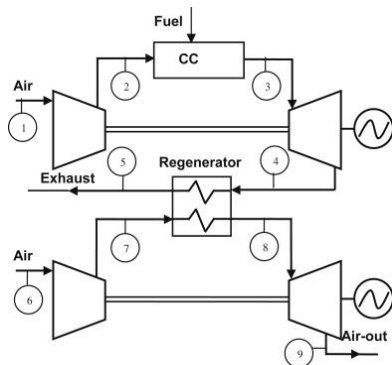


Figure 2. Gas turbine with air bottoming cycle (GT-ABC) [33].

The gas turbine topping cycle was first analyzed based on the details cycle components models described in the

previous section. GT-ABC forms the gas turbine cycle by coupling the air-bottoming with the topping cycle.

The specific fuel consumption, work output, overall energy, and exergy efficiencies for a gas turbine with an air bottoming cycle can be determined using the equations below [30].

$$\dot{W}_{Net,GT-ABC} = \dot{W}_{GT_1} + \dot{W}_{GT_2} - \dot{W}_{AC_1} - \dot{W}_{AC_2} \quad (40)$$

$$SFC = 3600 \frac{\dot{m}_{fuel}}{\dot{W}_{net,GT-ABC}} \quad (41)$$

$$\eta_{I,GT-ABC} = \frac{\dot{W}_{net,GT-ABC}}{\dot{m}_f LHV} \quad (42)$$

$$\eta_{II,GT-ABC} = \frac{\dot{W}_{net,GT-ABC}}{\dot{E}_{x,f}} \quad (43)$$

2.7 Partial Oxidation Gas Turbine (POGT)

A partial oxidation gas turbine (POGT) illustrates in Figure 3, is a specific type of gas turbine that generates electricity using a partial oxidation process. A fuel, such as NG, is burned in a combustion chamber with a restricted quantity of oxygen. This produces a carbon monoxide and hydrogen mixture, subsequently powering the turbine. A gas produced by this cycle has a greater specific heat than a gas produced by complete combustion.

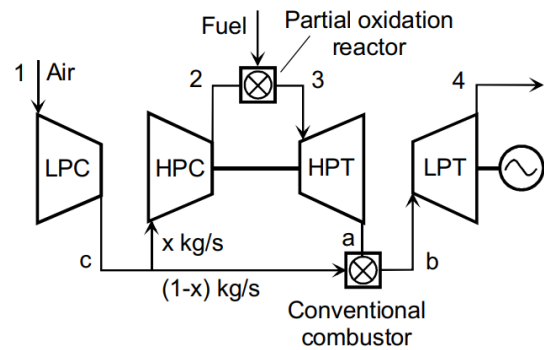


Figure 3. Partial oxidation gas turbine (POGT) [34].

Typically, a Partial oxidation reactor (POR) runs in fuel-rich conditions with equivalency ratios of 2.5. The typical POR exit temperature is between 1093 and 1316°C., in line with turbine inlet requirements [23]. The required turbine inlet temperature T_3 determines fraction x in the PO reaction. For temperatures ranging from 1200 to 1400 °C, x has a value between 0.15 and 0.22. [35].

The following equations can determine the work output, specific fuel consumption, and overall energy and exergy efficiencies for a partial oxidation gas turbine (POGT) [30].

$$\dot{W}_{Net,POGT} = \dot{W}_{HPT} + \dot{W}_{LPT} - \dot{W}_{HPC} - \dot{W}_{LPC} \quad (44)$$

$$SFC = 3600 \frac{\dot{m}_{fuel}}{\dot{W}_{net,POGT}} \quad (45)$$

$$\eta_{I,POGT} = \frac{\dot{W}_{net,POGT}}{\dot{m}_f LHV} \quad (46)$$

$$\eta_{II,POGT} = \frac{\dot{W}_{net,POGT}}{\dot{E}_{x,f}} \quad (47)$$

3. Models Validation

3.1 Simple Gas Turbine (SGT)

Based on the above analysis, a simulation program was developed using EES software [34] for the SGT, GT-ABC, and POGT cycles. The obtained solution for SGT is validated with the results of [15]. Table 3 shows the Operating parameters for the validation process. The comparison between the reference and present models is shown in Table 2, and the model shows a good agreement.

Table 2. Comparison between the Exergy efficiency for all components of simple gas cycle in the present model with [15].

Components	Exergy efficiency (%) present study	Exergy efficiency (%) [15]	Relative error
Air Compressor	88.2	94.9	7.1
Combustion Chamber	73.7	75.3	7.9
Gas Turbine	93.9	94.6	2.5
Power Cycle	29.7	32.3	8.3

3.2 Gas Turbine with Air Bottoming Cycle (GT-ABC)

The findings are compared to the results data taken from [30] and [32] to validate the GT-ABC model. Figure 4 shows the operating parameters used in the validation process for the SFC against turbine inlet temperature for (GT-ABC). As TIT is increased, the SFC decreases. The findings from the developed models showed a good agreement with the published data [30], and [32]. Once the SGT, GT-ABC, and POGT cycle model was developed and validated in EES software, we conducted a comparative parametric analysis.

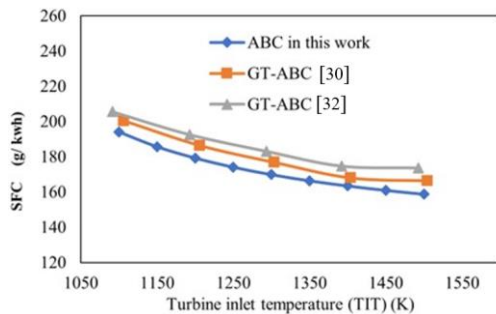


Figure 4. Difference between the results of the gas turbine with air bottoming cycle (GT-ABC) model and those of [33], [36].

4. Results and Discussion

In this study, a comparative analysis of selected gas turbine cycles has been conducted. The conventional energy and exergy analysis for SGT, GT-ABC, and POGT cycles is applied to evaluate the performance of these cycles. The input data for the thermal performance analysis are presented below (Table 3).

Table 4 compares the model findings for overall energy and exergy efficiency and SFC for different cycles. For all systems, the TIT was 1400 °C, and the ambient temperature was 25 °C. The pressure ratio of the topping cycles was 20. The pressure ratio was assumed to be 2 for the bottoming cycles. In POGT, the mass fraction was assumed to be 0.2. The table shows that the GT-ABC and POGT cycles are more efficient than the SGT. Under these conditions, the energy and exergy efficiency are 38.4%, 36.2% for SGT, 40%, 37.8 % for GT-ABC, and 41.6%, 39.3% for POGT. In

addition, the SFC for SGT, GT-ABC, and POGT cycles are 149.5, 136.3, and 177 (g/kwh), respectively.

Table 3. Input data for thermodynamic analysis of SGT, GT-ABC, and POGT [21], [33], [35], [36].

Parameters	Value
Dead state conditions	$P_o = 1.01 \text{ bar}$, $T_o = 293.15 \text{ K}$
Isentropic efficiency of the compressor	85%
Isentropic efficiency of the turbine	87%
Combustion efficiency	98 %
Heat exchanger effectiveness	0.85
Air Mass flow rate, topping cycle	1 kg/s
Air Mass flow rate, bottoming cycle	1 kg/s
Air mass fraction for POGT	0.2
Turbine inlet temperature	900 °C, 1200 °C, 1400 °C
Topping cycle pressure ratio	8, 12, 20
Ambient temperature	5 °C, 25 °C, 35 °C
Compressor inlet pressure	94 kPa
Gasses specific heat	1.14 kJ/kg K
Air Specific heat	1.005 kJ/kg K
Ratio of specific heat for gasses	1.33
Ratio of specific heat for air	1.4
Bottoming cycle pressure ratio	2
Fuel type	NG
Low heating value of NG	48806 kJ/kg

Table 4. The overall energy and exergy efficiencies and SFC for different cycles (TIT = 1400 °C, $T_o = 25 \text{ °C}$, $R_c = 20$, $x = 0.2$ and $rc = 2$).

Cycle type	Energy efficiency (%)	Exergy efficiency (%)	SFC (g/kwh)
SGT	38.4	36.23	149.5
GT-ABC	40.07	37.8	136.3
POGT	41.67	39.31	177

4.1 Effect of Operating Conditions

This section presents the simulation findings of the impact of operating conditions on the performance of the selected gas turbine cycles. The effects of operating parameters on SFC, energy, and exergy efficiencies are conducted using a computer model developed on EES software. The performance of the cycles was assessed under the same operational conditions. The results found are presented in Figure 5 to 11 based on the theoretical relationships earlier mentioned. The plots of the simulations for the SGT, GT-ABC and POGT cycles are presented and analyzed here.

4.1.1 Effect of Turbine Inlet Temperature on Energy and Exergy Efficiencies

The turbine inlet temperature (TIT) has a considerable impact on gas turbine performance. Increasing TIT requires higher SFC, which increases costs and greenhouse gas emissions [37], [38]. The effect of the TIT on the energy and exergy efficiency of each cycle was studied for TIT values ranging from (900 °C to 1400 °C). The findings show that the thermal efficiency increase as the TIT increases, as shown in Figure 5. The graph trend, which seems to align with the available literature data, provides further evidence that the model can determine the actual cycle performance within a reasonable range. Results show that when turbine intake temperatures increase, both exergy and energy efficiencies increase proportionally for all cycles. With varying the TIT,

the energy and exergy efficiencies of GT-ABC are higher than SGT and POGT.

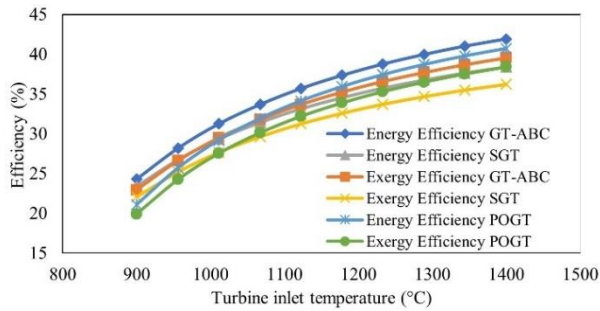


Figure 5. Energy and exergy efficiencies variation against turbine inlet temperature ($R_c = 20$, $T_o = 25^\circ\text{C}$, $x = 0.2$ and $r_c = 2$).

4.1.2 Effect of Turbine Inlet Temperature on Specific Fuel Consumption

Specific fuel consumption (SFC) indicates the quantity of fuel needed for power production. The SFC is an excellent indicator of the optimal cycle and can be used to compare SGT, GT-ABC, and POGT. As a result, the cycle with the lowest SFC is more valuable than the others. Plotting the TIT against the SFC (Figure 6) at the same operational data revealed that the SFC of each cycle decreases with increased TIT reach about stable conditions at certain TIT., which may be attributed to the significant gain in thermal efficiency with TIT. According to the variation of TIT, The SFC of GT-ABC is higher than that for SGT and POGT. There is a significant difference, specifically in the low range of TIT. There is a minor difference between The SFC of SGT and GT-ABC.

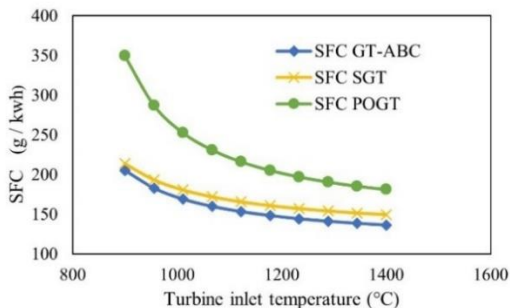


Figure 6. Specific fuel consumption (SFC) variation against turbine inlet temperature ($R_c = 20$, $T_o = 25^\circ\text{C}$, $x = 0.2$ and $r_c = 2$).

4.1.3 Effect of Compression Ratio on Energy and Exergy Efficiencies

The pressure ratio was changed between 2 and 35; increasing the compression ratio in gas turbine cycles increases the energy and exergy efficiencies. Similar trends were observed for SGT, GT-ABC, and POGT, as seen from the presented data in Figure 7. The findings show that the energy and exergy efficiencies will decrease for each cycle at low and high-pressure ratios (below or above the design condition). The optimum pressure ratio for SGT is 24, corresponding to 42.2%, 39.8% energy, and exergy efficiencies, respectively. In contrast, the optimum pressure ratio for GT-ABC is 30, corresponding to 39.7% and 36.8% energy and exergy efficiency, respectively. In addition, the optimum pressure ratio for POGT is 13, corresponding to energy and exergy efficiencies of 42.5% and 40.7 %,

respectively. The energy and exergy efficiencies of SGT increase between 20% and 40% sharply in the low compression ratio range between 2 and 13. Then, the efficiencies grow gradually in the higher range of compression ratio between 13 and 30. While in the low compression ratio range of 2 to 10, the energy and exergy efficiencies of GT-ABC improved sharply between 15% and 30%. The efficiencies gradually rise in the higher compression ratio range of 10 to 30. In contrast, the energy and exergy efficiencies of POGT increase significantly between 30% and 42% in the low compression ratio range of 2 to 13. The efficiencies gradually decrease in the higher compression ratio range of 13 to 30.

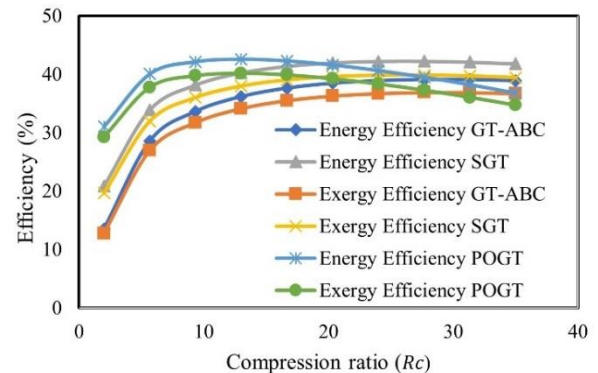


Figure 7. Energy and exergy efficiencies variation with compression ratio ($TIT = 1400^\circ\text{C}$, $T_o = 25^\circ\text{C}$, $x = 0.2$ and $r_c = 2$).

4.1.4 Effect of Compression Ratio on Specific Fuel Consumption

Figure 8 illustrates the effect of compression ratio on SFC for SGT, GT-ABC, and POGT cycles. The general trend is similar for each cycle. The SFC reduces significantly in the compression ratio range between 2 and 6, then stabilizes in the compression ratio range between 6 and 35. For the low range of compression ratio, the SFC for POGT is lower than other cycles, while at the high range of compression ratio, the SFC for SGT is lower than different cycles, reaching around 130 g/kwh.

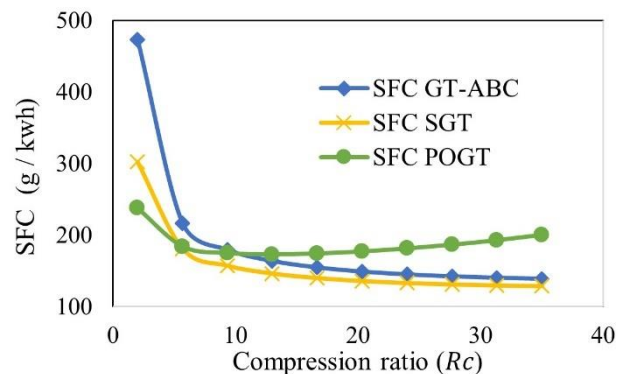


Figure 8. Specific fuel consumption (SFC) variation against compression ratio ($TIT = 1400^\circ\text{C}$, $T_o = 25^\circ\text{C}$, $x = 0.2$ and $r_c = 2$).

4.1.5 Effect of Ambient Air Temperature on Energy and Exergy Efficiencies

To investigate the impact of environmental conditions on the operation of each cycle., the ambient temperature varied from 5 °C to 35 °C. Figure 9 illustrates how the energy and exergy efficiencies change as a function of ambient

temperature for the SGT, GT-ABC, and POGT. Increased ambient temperature decreases energy and exergy efficiencies for all cycles. It is revealed that the POGT has higher energy and exergy efficiencies than the other cycle. Moreover, it declines because of a rise in ambient temperature. For example, at $T_o = 5\text{ }^\circ\text{C}$, the energy efficiency of SGT, GT-ABC, and POGT was 39.6%, 41.4, and 41.3 %, respectively, while the exergy efficiency was 37.3%, 39.1%, and 40.9%. In contrast, at $T_o = 35\text{ }^\circ\text{C}$, the energy efficiency of SGT, GT-ABC, and POGT were 37.7%, 39.2%, and 40.7%, respectively, while the exergy efficiencies were 35.5%, 37 %, and 38.4%. As shown in Figure 9 even while the POGT has higher overall efficiency than the SGT, GT-ABC, the rate at which efficiency decreases with ambient temperature in the basic cycle is lower.

4.1.6 Effect of Ambient Air Temperature on Specific Fuel Consumption

The specific fuel consumption SFC shows the quantity of fuel required to produce a certain level of power. The work that the gas turbine reduces as the ambient temperature increases. As a result, the SFC of the gas turbine increases. For all cycles, the SFC of the gas turbine cycle increases with the ambient air temperature. Significant variation was revealed for the POGT, as shown in Figure 10. It proves that at a fixed compression ratio, a rise in intake air temperature leads to a rise in fuel consumption. This can be interpreted as follows; as the ambient temperature declines, the air mass flow rate at the compressor input rises, resulting in a reduction in SFC.

A comprehensive quantitative comparison of the SGT, GT-ABC, and POGT is given in Table 5 .The values of overall energy and exergy efficiencies and SFC according to an extensive range of operating conditions are shown. The

table shows that under all low-pressure ratio values (8 to 20), the POGT cycle has higher energy and exergy performance than the SGT, GT-ABC, and GT-ABC cycles.

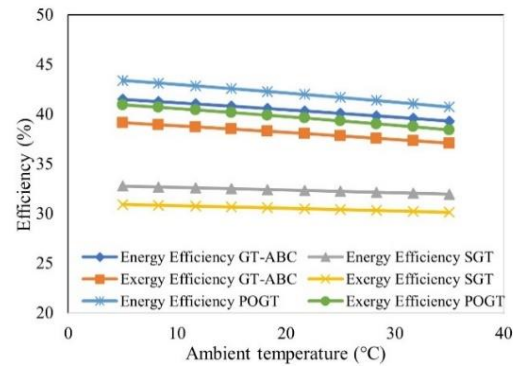


Figure 9. Variation of energy and exergy efficiency with the ambient condition ($TIT = 1400\text{ }^\circ\text{C}$, $R_c = 20$, $x = 0.2$ and $rc = 2$).

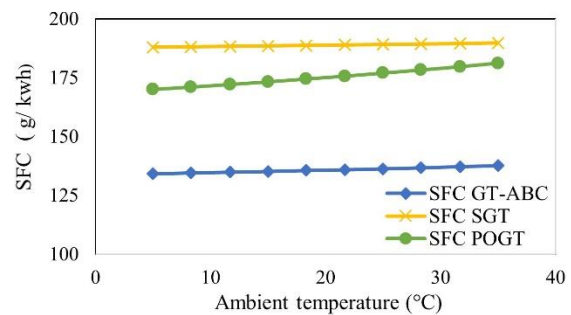


Figure 10. Specific fuel consumption (SFC) variation against ambient temperature ($TIT = 1400\text{ }^\circ\text{C}$, $R_c = 20$, $x = 0.2$ and $rc = 2$).

Table 5. Overall efficiency and Specific fuel consumption (SFC) for different values of TIT , T_o , and R_c associated with the SGT, GT-ABC, and POGT cycles. (The pressure ratio of the bottoming cycle for GT-ABC is $rc = 2$, and the mass fraction for POGT is $x = 0.2$).

$TIT\text{ (}^\circ\text{C)}$	$T_o\text{ (}^\circ\text{C)}$	R_c	Simple-GT			GT-ABC			POGT		
			Energy efficiency (%)	Exergy efficiency (%)	SFC (g/kwh)	Energy efficiency (%)	Exergy efficiency (%)	SFC (g/kwh)	Energy efficiency (%)	Exergy efficiency (%)	SFC (g/kwh)
900	5	8	27.77	26.2	215.5	30.12	28.41	191.9	40.54	38.24	182
		20	27.71	26.14	190.7	28.12	26.53	179.5	30.35	28.63	243.1
		30	21.82	20.58	215.6	21.25	20.05	207.9	15.8	14.91	215.6
	25	8	26.44	24.94	221.7	28.35	26.75	199.3	39.81	37.56	185.3
		20	23.38	22.06	213.8	23.08	21.77	205.2	24.65	23.25	299.3
		30	13.18	12.44	324.7	11.54	10.88	333.7	2.115	1.995	324.7
	35	8	25.69	24.24	225.6	27.37	25.82	203.8	39.38	37.15	187.3
		20	20.75	19.57	233.2	20.01	18.88	227.4	21.1	19.9	349.6
		30	7.426	7.006	570.3	5.066	4.779	686.6	7.366	6.949	570.3
1200	5	8	31.47	29.69	194.4	34.71	32.74	169.3	41.7	39.34	176.9
		20	36.83	34.74	155.3	38.43	36.25	142.4	40.37	38.09	182.7
		30	36.82	34.74	148	37.8	35.66	137.4	36.22	34.17	203.7
	25	8	30.75	29.01	196.4	33.77	31.85	171.7	41.25	38.91	178.8
		20	35.04	33.06	159.2	36.35	34.3	146.5	37.95	35.8	194.4
		30	34	32.08	154.5	34.63	32.67	144	31.82	30.02	231.8
	35	8	30.37	28.65	197.6	33.26	31.37	173.1	40.98	38.66	180
		20	34.04	32.11	161.7	35.19	33.2	149.1	36.56	34.49	201.8
		30	32.36	30.52	159	32.79	30.93	148.5	29.2	27.55	252.6
1400	5	8	32.75	30.9	187.9	36.25	34.2	162.3	42.04	39.66	175.5
		20	39.62	37.38	147.4	41.48	39.13	134.2	43.37	40.92	170.1
		30	40.9	38.59	138	42.17	39.78	127.3	41.55	39.19	177.5
	25	8	32.22	30.39	189.1	35.55	33.54	163.7	41.66	39.3	177
		20	38.4	36.23	149.5	40.07	37.8	136.3	41.67	39.31	177
		30	39.1	36.88	141	40.15	37.88	130.2	38.7	36.51	190.6
	35	8	31.93	30.12	189.8	35.17	33.18	164.5	41.45	39.1	178
		20	37.73	35.59	150.7	39.29	37.07	137.6	40.71	38.41	181.2
		30	38.08	35.92	142.8	39.01	36.8	132.1	37.06	34.96	199

5. Conclusion:

In this article, a comparative study was conducted based on energy and exergy analysis for SGT, GT-ABC, and POGT cycles to determine the most effective system, along with the developed model and EES software that has been used to evaluate the effect of critical operational parameters. The main results observed from the study are summarized below:

- The parametric analysis showed that the ambient temperature, turbine inlet temperature, and compression ratio significantly affected the energy and exergy efficiencies of SGT, GT-ABC, and POGT cycles.
- As the compression ratio grows, the energy and exergy efficiencies of the SGT, GT-ABC, and POGT cycles also increase.
- The energy and exergy efficiencies of each cycle will degrade at low- and high-pressure ratios (below or above the design condition). The optimum pressure ratio for SGT is 24, corresponding to 42.2%, 39.8% energy, and exergy efficiencies, respectively. In contrast, the optimum pressure ratio for GT-ABC is 30, related to 39.7% and 36.8% energy and exergy efficiency, respectively. In addition, the optimum pressure ratio for POGT is 13, corresponding to 42.5% and 40.7 % energy and exergy efficiencies, respectively.
- There is an optimum TIT at which each cycle's energy and exergy efficiencies are at their highest values for all pressure ratios.
- Comprehensive modelling shows that the POGT cycle can achieve higher efficiency at the same turbine inlet temperature and pressure ratio. The model findings indicate that when the ambient temperature rises, the total efficiency of all cycles decreases.
- For all cycles, at (TIT = 1400 °C, T_o = 25 °C, R_c = 20, x=0.2 and r_c = 2), the GT-ABC and POGT cycles are more efficient than that SGT. Under these conditions, the energy and exergy efficiency are 38.4%, 36.2% for SGT, 40%, 37.8 % for GT-ABC, and 41.6%, 39.3% for POGT. In addition, the SFC for SGT, GT-ABC, and POGT cycles is 149.5, 136.3, and 177 (g/kwh), respectively.
- Finally, in all low-pressure ratio conditions (8 to 20), the POGT cycle has a higher energy and exergy performance than the SGT, GT-ABC.

Nomenclature

Symbols

C_p	Specific heat (kJ/kg.)
h	Specific enthalpy (J/kg)
\dot{m}	Mass flow rate (kg/s)
P	Pressure (kPa)
q	Heat supplied (W)
R_c	Pressure ratio in topping cycle
r_c	Pressure ratio in bottoming cycle
s	Specific entropy (J/kg. K)
T	Temperature (K)
W	Work (W)

Abbreviation

AF	Air-to-fuel ratio
CIT	Compressor inlet temperature
GT-ABC	Gas turbine with air bottoming cycle
LHV	Fuel lower heating value (kJ/kg)
NG	Natural gas
SGT	Simple gas turbine
SFC	Specific fuel consumption (g/wh)
TIT	Turbine inlet temperature (k)
POGT	Partial oxidation gas turbine

Subscripts

a	Air
B	Bottoming cycle
c	Compressor
cc	Combustion chamber
GT	Gas turbine
net	Net
o	Outlet
p	Pump
T	Topping cycle

Greek Symbols

η	Thermal efficiency
ϵ	Effectiveness of HE
γ	Ratio of specific heat

References:

- [1] J. A. M. da Silva, S. Ávila Filho, and M. Carvalho, "Assessment of energy and exergy efficiencies in steam generators," *Journal of the Brazilian Society of Mechanical Sciences and Engineering*, vol. 39, no. 8, pp. 3217–3226, 2017, doi: 10.1007/s40430-016-0704-6.
- [2] M. N. Ibrahim, T. K., Mohammed, M. K., Awad, O. I., Abdalla, A. N., Basrawi, F., Mohammed, "A comprehensive review on the exergy analysis of combined cycle power plants," *Renewable and Sustainable Energy Reviews*, vol. 90, no. April, pp. 835–850, Jul. 2018, doi: 10.1016/j.rser.2018.03.072.
- [3] A. G. Memon, R. A. Memon, K. Harijan, and M. A. Uqaili, "Thermo-environmental analysis of an open cycle gas turbine power plant with regression modeling and optimization," *Journal of the Energy Institute*, vol. 87, no. 2, pp. 81–88, 2014, doi: 10.1016/j.joei.2014.03.023.
- [4] Ş. Balku, "Analysis of combined cycle efficiency by simulation and optimization," *Energy Conversion and Management*, vol. 148, pp. 174–183, Sep. 2017, doi: 10.1016/j.enconman.2017.05.032.
- [5] O. J. Khaleel, F. Basim Ismail, T. Khalil Ibrahim, and S. H. bin Abu Hassan, "Energy and exergy analysis of the steam power plants: A comprehensive review on the Classification, Development, Improvements, and configurations," *Ain Shams Engineering Journal*, vol. 13, no. 3, p. 101640, 2022, doi: 10.1016/j.asej.2021.11.009.
- [6] D. M. Mitrović, B. V. Stojanović, J. N. Janevski, M. G. Ignjatović, and G. D. Vučković, "Exergy and exergoeconomic analysis of a steam boiler," *Thermal Science*, vol. 22, pp. S1601–S1612, 2018, doi: 10.2298/TSCI18S5601M.
- [7] G. R. Ahmadi and D. Toghraie, "Energy and exergy analysis of Montazeri Steam Power Plant in Iran," *Renewable and Sustainable Energy Reviews*, vol. 56, pp. 454–463, 2016, doi: 10.1016/j.rser.2015.11.074.
- [8] O. K. Singh, "Assessment of thermodynamic irreversibility in different zones of a heavy fuel oil fired high pressure boiler," *Journal of Thermal Analysis and Calorimetry*, vol. 123, no. 1, pp. 829–840, 2016, doi: 10.1007/s10973-015-4959-4.
- [9] M. Hajzadeh aghdam, M. H. Khoshgoftar manesh, N. Khani, and M. Yazdi, "Energy, Exergy-Based and Emergy-Based Analysis of Integrated Solar PTC with a Combined Cycle Power Plant," *International Journal of Thermodynamics*, vol. 24, no. 4, pp. 17–30, Dec. 2021, doi: 10.5541/ijot.902374.

- [10] S. Zandi, K. G. Mofrad, A. Moradifaraj, and G. R. Salehi, "Energy, exergy, exergoeconomic, and exergoenvironmental analyses and multi-objective optimization of a CPC driven solar combined cooling and power cycle with different working fluids," *International Journal of Thermodynamics*, vol. 24, no. 2, pp. 151–170, May 2021, doi: 10.5541/ijot.873456.
- [11] M. R. Abedi, G. Salehi, M. T. Azad, M. H. K. Manesh, and H. Fallahsohi, "Exergetic and exergoeconomic analysis and optimization of gas turbine inlet air cooling systems with absorption or compression chilling," *International Journal of Thermodynamics*, vol. 24, no. 2, pp. 93–107, 2021, doi: 10.5541/ijot.785357.
- [12] R. Yildirim, A. Şencanşahin, and E. Dikmen, "Comparative Energetic, Exergetic, Environmental and Enviroeconomic Analysis of Vapour Compression Refrigeration Systems Using R515B as Substitute for R134a," *International Journal of Thermodynamics*, vol. 25, no. 1, pp. 125–133, Mar. 2022, doi: 10.5541/ijot.1011622.
- [13] A. K. Mahapatra and Sanjay, "Performance analysis of an air humidifier integrated gas turbine with film air cooling of turbine blade," *Journal of Energy in Southern Africa*, vol. 24, no. 4, pp. 71–81, 2013, doi: 10.17159/2413-3051/2013/v24i4a3148.
- [14] A. M. Alklaibi, M. N. Khan, and W. A. Khan, "Thermodynamic analysis of gas turbine with air bottoming cycle," *Energy*, vol. 107, no. x, pp. 603–611, 2016, doi: 10.1016/j.energy.2016.04.055.
- [15] F. Y. Ibrahim, T. K., Basrawi, F., Awad, O. I., Abdullah, A. N., Najafi, G., Mamat, R., & Hagos, "Thermal performance of a gas turbine based on an exergy analysis," *Applied Thermal Engineering journal*, vol. 128, p. 01027, Nov. 2019, doi: 10.1051/e3sconf/201912801027.
- [16] H. Kurt, Z. Recebli, and E. Gedik, "Performance analysis of open cycle gas turbines," *International Journal of Energy Research*, vol. 33, no. 3, pp. 285–294, Mar. 2009, doi: 10.1002/er.1472.
- [17] A. De Sa and S. Al Zubaidy, "Gas turbine performance at varying ambient temperature," *Applied Thermal Engineering*, vol. 31, no. 14–15, pp. 2735–2739, 2011, doi: 10.1016/j.applthermaleng.2011.04.045.
- [18] M. M. Abou Al-Sood, K. K. Matrawy, and Y. M. Abdel-Rahim, "Optimum Operating Parameters of an Irreversible Gas Turbine Cycle," *JES. Journal of Engineering Sciences*, vol. 40, no. 6, pp. 1695–1714, 2012, doi: 10.21608/jesaun.2012.114611.
- [19] H. Aydin, "Exergetic sustainability analysis of LM6000 gas turbine power plant with steam cycle," *Energy*, vol. 57, pp. 766–774, 2013, doi: 10.1016/j.energy.2013.05.018.
- [20] C. Carcasci, F. Costanzi, and B. Pacifici, "Performance Analysis in Off-Design Condition of Gas Turbine Air-Bottoming Combined System," *Energy Procedia*, vol. 45, pp. 1037–1046, 2014, doi: 10.1016/j.egypro.2014.01.109.
- [21] M. Ghazikhani, I. Khazaei, and E. Abdekhodaie, "Exergy analysis of gas turbine with air bottoming cycle," *Energy*, vol. 72, pp. 599–607, 2014, doi: 10.1016/j.energy.2014.05.085.
- [22] M. Ghazikhani, H. Takdehghan, and A. M. Shayegh, "Exergy Analysis of Gas Turbine Air- Bottoming Combined Cycle for Different Environment Air Temperature," *Proceedings of 3rd International Energy, Exergy and Environment Symposium*, no. November, pp. 1–8, 2007.
- [23] J. Rabovitser, S. Nester, S. Wohadlo, K. Smith, W. Nazeer, and D. White, "Development of a partial oxidation gas turbine (POGT) for innovative gas turbine systems," *Proceedings of the ASME Turbo Expo*, vol. 3, pp. 261–269, 2007, doi: 10.1115/GT2007-27539.
- [24] S. J. Zhang, J. L. Chi, and Y. H. Xiao, "Performance analysis of a partial oxidation steam injected gas turbine cycle," *Applied Thermal Engineering*, vol. 91, no. x, pp. 622–629, 2015, doi: 10.1016/j.applthermaleng.2015.08.062.
- [25] C. Diyoke, U. Ngwaka, and T. O. Onah, "Comparative assessment of a hybrid of gas turbine and biomass power system for sustainable multi-generation in Nigeria," *Scientific African*, vol. 13, 2021, doi: 10.1016/j.sciaf.2021.e00899.
- [26] Y. Fan, G., Lu, X., Chen, K., Zhang, Y., Han, Z., Yu, H., & Dai, "Comparative analysis on design and off-design performance of novel cascade CO₂ combined cycles for gas turbine waste heat utilization," *Energy*, vol. 254, 2022, doi: 10.1016/j.energy.2022.124222.
- [27] B. R. Ryu, P. A. Duong, and H. Kang, "Comparative analysis of the thermodynamic performances of solid oxide fuel cell–gas turbine integrated systems for marine vessels using ammonia and hydrogen as fuels," *International Journal of Naval Architecture and Ocean Engineering*, vol. 15, 2023, doi: 10.1016/j.ijnaoe.2023.100524.
- [28] J. Yi, "Design and optimization of gasoline direct injection engines using computational fluid dynamics," *Advanced Direct Injection Combustion Engine Technologies and Development: Gasoline and Gas Engines*, pp. 166–198, Oct. 2009, doi: 10.1533/9781845697327.166.
- [29] R. Kumar, "A critical review on energy, exergy, exergoeconomic and economic (4-E) analysis of thermal power plants," *Engineering Science and Technology, an International Journal*, vol. 20, no. 1, pp. 283–292, Feb. 2017, doi: 10.1016/j.jestch.2016.08.018.
- [30] E. Ersayin and L. Ozgener, "Performance analysis of combined cycle power plants: A case study," *Renewable and Sustainable Energy Reviews*, vol. 43, pp. 832–842, 2015, doi: 10.1016/j.rser.2014.11.082.
- [31] C. Michalakakis, J. Fouillou, R. C. Lupton, A. Gonzalez Hernandez, and J. M. Cullen, "Calculating the chemical exergy of materials," *Journal of Industrial Ecology*, vol. 25, no. 2, pp. 274–287, Apr. 2021, doi: 10.1111/jiec.13120.
- [32] M. Maheshwari and O. Singh, "Comparative evaluation of different combined cycle configurations having simple gas turbine, steam turbine and ammonia water turbine," *Energy*, vol. 168, pp. 1217–1236, Feb. 2019, doi:

10.1016/j.energy.2018.12.008.

- [33] M. Ghazikhani, I. Khazaei, and E. Abdekhodaie, "Exergy analysis of gas turbine with air bottoming cycle," *Energy*, vol. 72, pp. 599–607, 2014, doi: 10.1016/j.energy.2014.05.085.
- [34] D. Rabovitser, J., Wohadlo, S., Pratapas, J. M., Nester, S., Tartan, M., Palm, S., ... & White, "Experimental Study of a 200 kW Partial Oxidation Gas Turbine (POGT) for Co-Production of Power and Hydrogen-Enriched Fuel Gas," in *Volume 4: Cycle Innovations; Industrial and Cogeneration; Manufacturing Materials and Metallurgy; Marine*, Jan. 2009, vol. 4, pp. 133–145, doi: 10.1115/GT2009-59272.
- [35] M. A. Korobitsyn, P. W. Kers, and G. G. Hirs, "Analysis of a gas turbine cycle with partial oxidation," *Proceedings of the ASME Turbo Expo*, vol. 3, 1998, doi: 10.1115/98-GT-033.
- [36] Y. S. H. Najjar and M. S. Zaamout, "Performance analysis of gas turbine air-bottoming combined system," *Energy Conversion and Management*, vol. 37, no. 4, pp. 399–403, 1996, doi: 10.1016/0196-8904(95)00197-2.
- [37] M. N. Khan and I. Tlili, "New approach for enhancing the performance of gas turbine cycle: A comparative study," *Results in Engineering*, vol. 2, no. February, p. 100008, 2019, doi: 10.1016/j.rineng.2019.100008.
- [38] M. N. Khan, I. M. Alarifi, and I. Tlili, "Comparative energy and exergy analysis of proposed gas turbine cycle with simple gas turbine cycle at same operational cost," *ASME International Mechanical Engineering Congress and Exposition, Proceedings (IMECE)*, vol. 6, no. February 2022, 2019, doi: 10.1115/IMECE2019-10949.

Research Article

Economic, Enviroeconomic Analysis Of Active Solar Still Using Al₂O₃ Nanoparticles

^{1,2}D. Singh 

¹R. D. Engineering College Ghaziabad, U.P., India-201206

²Research Centre, Mata Rama Devi Trust, Modinagar, Ghaziabad, U.P., India-201201

E-mail: veerdharam76@gmail.com

Received 11 May 2023, Revised 3 June 2023, Accepted 14 Aug 2023

Abstract

The water scarcity is primary need of analysis. The current study analyses the Economic and Enviro-economic of an N-identical (N-PVTCPC) collector double slope solar desalination units (DS-DU) with a heat exchanger (HE) using water based Al₂O₃ nanoparticles. An analytical program fed into MATLAB, and the analysis was monitored on an annual basis New Delhi, India. The Indian Metrological Department in Pune, India provided the input data necessary for the mathematical procedure. Considering the energy production of the winter and summer, the average yearly energy production will be calculated. The system performance has been analyzed based on Economic and Enviro-economic. In an economic analysis was performed for 15 years has found for cost of water 1.25, 1.51, and 1.79₹/kg respectively, Enviro-economic analysis for life span of 15, 20, and 30 years have found CO₂ mitigation/ton 40.85, 57.46, and 90.67 kg/ton respectively and carbon credit earned 204.26, 287.30, and 453.36 (\$) respectively. The proposed system has found energy, yield, and productivity 7.31%, 8.5%, and 5.17% greater respectively. Therefore overall the proposed system found better to previous system.

Keywords: *Economic; CO₂ mitigation; carbon credit earned; environ-economic; nanoparticles.*

1. Aim and Scope

For various applications, such as heat exchangers, photovoltaic systems integrated into buildings, greenhouse dryers, space heaters, solar air collectors, solar water collectors, etc., renewable energy or photovoltaic thermal energy systems are a viable choice. A basic requirement for maintaining life on earth, along with access to clean food and air, is the availability of drinkable water. Lawrence and Tiwari [1] discussed the theoretical evaluation of a mathematical use it to analyze the influence of various parameters on the system's performance, such as the solar radiation, the cover plate's transmissivity, and the ambient temperature. Tiwari [2] provided a summary in the field of solar energy that was a useful for students and professionals in the subject overall, "Solar Energy: Fundamentals, Design, Modeling and Applications". Tiwari and Tiwari [3] provided a comprehensive understanding of the principles, design, and applications of solar distillation systems for water desalination. The book covers economics of solar stills and their applications in rural and remote areas, where access to potable water is limited. Otanicar and Golden [4] conducted a comparison of traditional solar hot water technology with nanofluid in terms of the environment and the economy. They discovered that although the inclusion of nanoparticles in the nanofluid technology results in improved thermal efficiency and heat transfer rates, it also necessitates a higher initial system cost and may have potential adverse environmental effects. Khullar and Tyagi [5] evaluated for several types of nanofluids, the potential environmental impact was assessed in terms of greenhouse

gas emissions and energy consumption, and it was compared to the traditional water-based system. Faizel et al. [6] conducted an analysis. It is discovered that CuO nanofluid's performance is best explained by its for different thermo-physical properties. Liu et al. [7] studied and found, using ETCs can greatly increase the solar desalination system's thermal performance, resulting in higher levels of freshwater output and reduced specific energy consumption. Sharon and Reddy [8] estimated environmental cost at \$6.29 per year. A saline water-filled active solar distiller's annual economic performance was examined. Dhivagar et al. [9] developed a mathematical model of the system and validate it using experimental data. The 4E analysis reveals that the system has a high exergy efficiency and low environmental impact, and its cost-effectiveness can be improved through optimization of the design parameters. Dharamveer and Samsher [10] compared the Energy matrices Enviroeconomic for active and passive solar desalination system. Performance of different solar still configurations have been discussed by the authors based on a variety of factors, including productivity ratio, thermal efficiency, exergy efficiency, and enviro-economic analysis. Shahsavaret al. [11] comparison made between the efficiency of hybrid, earth-air heat exchanger, and integrated photovoltaic/thermal systems utilized in buildings in terms of energy, the environment, economy, and finances. The analysis of energy matrices and the life cycle cost effectiveness of employing nanofluids for single and double slope flat plate collectors with a heat exchanger using water loaded

nanofluids have only been briefly studied. Shatar et al. [12] based on the examination of a solar still employing a partly coated condensing cover with thermoelectric cover cooling in terms of energy, efficiency, economics, and the environment. The system's productivity ratio, energy efficiency, energy destruction, leveled cost of water, and CO₂ emissions were all examined by the researchers.

The majority of research in the literature examined how flat plate collectors and heat exchangers function when solar energy is still being used. On the Nth partially covered solar thermal power hybrid desalination unit employing nanoparticles, no researchers have examined Energy matrices, Life cycle costs, or Energy payback times. Table 1 provides a summary of earlier research on solar distiller units that use water-loaded nanofluids. The current literature survey indicates that both passive and active solar stills have been the subject of several studies. The examination of active solar systems that are still filled with water-based nanofluids is, however, not well covered in the literature. Dharamveer et al. [23] were used CuO nanoparticles to study active double slope solar still. Exergoeconomic and Environmental ramifications based on Energy matrices have not been researched by any academic. Additionally, no studies have been conducted on water-based nanofluid-filled compound parabolic concentrator collectors or evacuated tube collectors for basin-style solar stills.

The proposed study would combine Active Solar Desalination unit that are filled with Water-based Nanofluids to better understand these impacts. In the current study, Productivity, Environmental Economics, are evaluated. The efficiency of the proposed strategy will also be assessed in light of the results of earlier research. (1) Nth partially covered (PVT) Solar Active Double Slope Desalination system (CPC) using a water based Nanoparticles with a helically coiled heat exchanger

(system-A). (2) An active double slope Nth partially covered PVT system with flat plate (FPC) collector using a heat exchanger of helically coiled (system-B). The suggested system examined the mass of base fluid and the optimal nanoparticle concentration. Table 1, below provides an overview of earlier research.

2. Material and Methods

2.1 System description

Figure 1, depicts the PVT module and focusing parabolic collector when solar energy is falling on them. As soon as the concentrating collector receives heat, it starts to raise the temperature of the nanofluid passing through the heat exchanger tube. How does the fluid gain energy as it travels from first PVT-CPC collector to the second PVT-CPC collector, given that the same fluid is travelling through both of them and a solar energy approx. 1367W/m². The fluid has gains some heat again through the other PVT-CPC collectors. After absorbing the most heat possible, fluid is poured into a high-quality copper helical coil heat exchanger. The open to the sun portion of this heat exchanger is situated inside a water tank. The temperature of the water in the water tank is raised to roughly 100°C during this process of water evaporation as solar radiation strikes and travels through the inside of the water tank. Sensible heating occurs when the fluid enters the heat exchanger and begins to lose heat as it comes into contact with the surrounding water in the tank. The difference between inner and outer glass cover, water vapor that has started to flow upward condenses. The glass cover is sloping on both sides. The working fluid is now removed from the heat exchanger's outlet and returned for the following cycle. To create a constant forced flow of working fluid, a DC motor is used. This DC motor's energy needs are met by solar panels, each of which has a capacity of 25 watts.

Table 1. Prior research on water based nanofluids solar distiller unit.

References	Adaptation in passive and active solar distiller	Conclusions
Kabeel et al. [14]	Providing single slope passive distiller, Al ₂ O ₃ NPs and external condenser	Al ₂ O ₃ with vacuum 116 %
Elango et al. [15]	Single slope basin type with Fe ₂ O ₃ , ZnO, Al ₂ O ₃ NPs	29.95% with Al ₂ O ₃ , 18.63% Fe ₂ O ₃ , ZnO with 12.67%
Sahota and Tiwari [16]	Investigated passive double slope desalination unit	45.23% Al ₂ O ₃ , 42.72% CuO, 39.74% TiO ₂
Shashir et al. [17]	Passive slope distiller CuO, and graphite with cooling rate over glass cover	47.8% with CuO, graphite 57.6%
Saleha et al. [18]	Solar distiller	Recommended ZnO
Chen et al. [19]	Solar distiller	Recommended SiC
Mahian et al. [20]	Heat exchanger operated using CuO, Al ₂ O ₃ , and TiO ₂ NPs	9.86% with CuO
Sahota et al. [21]	Helically coiled heat exchanger using flat plate collectors operated using CuO, Al ₂ O ₃ , and TiO ₂ NPs	With CuO with Al ₂ O ₃ than TiO ₂ system
Dharamveer et al. [22]	Active and passive operated Matrices, EPT, and LCCE.	CuO nanoparticles
Dharamveer et al. [23]	Performed active double slope desalination unit (N-PVT-HE-DS)	Using CuO nanoparticles
Dharamveer et al. [24]	Performed active single slope desalination unit (N-PVT-HE-DS)	Using CuO nanoparticles
Present study	Analyses of Enviro-economic to a helically coiled heat exchanger hybrid solar desalination unit Nth PVT-CPC-DS-HE.	Using Al₂O₃ nanoparticles

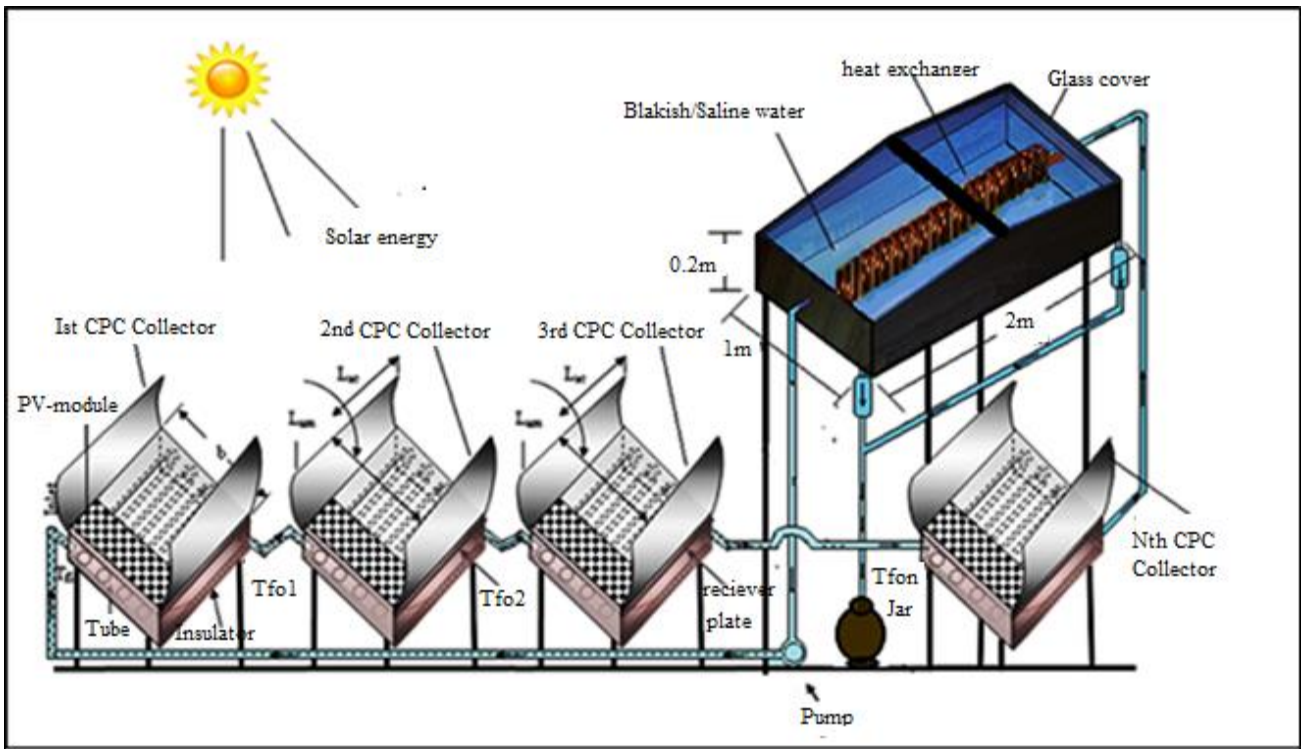


Figure 1. Representation of active double slope hybrid desalination unit.

2.2 Thermal modeling

2.2.1 Economic analysis

It is economically feasible for System-A and System-B total yearly cost, factor of shrinking fund, factor of recovery for both systems [10].

a. Capital cost

The capital investment of different components involve in system-A are given in Table 2, provide the system's fabrication cost.

b. System's lifespan

It is considered for 15 years.

c. Salvage value (S)

$$\text{Salvage value (s)} = 0.2 \times \text{Principal capital (PCC)} \quad (1)$$

PCC stands for principal capital cost

Cost of annual salvaging (ASC)

$$\text{Annually salvage} = S \times \text{shrinkage in fund (SFF)} \quad (2)$$

SFF is factor used for shrinkage

d. Yearly maintenance (YM)

$$\text{Yearly maintenance (YM)} = 0.15 \times \text{FYC}$$

FYC stands for first yearly cost.

e. Factor for capital recovered (CR).

At a fixed rate of interest, it shows the present cost as a constant annual cost across time.

$$\text{CR} = \frac{i(1+i)^n}{(1+i)^n - 1} \quad (4)$$

f. Factor of shrinking fund

$$\text{SFF} = \frac{i}{(1+i)^n - 1} \quad (5)$$

g. Cost of first annually gained

$$\text{FYC} = \text{PCC} \times \text{CR} \quad (6)$$

h. Total cost gained annually

$$\text{TAC} = \text{FYC} + \text{YM} - \text{ASC} \quad (7)$$

i. distillate cost/kg

$$\text{Cost/kg} = \frac{\text{TAC}}{\text{yield in life}} \quad (8)$$

2.2.2 Enviro-economic analysis

The following are examples of mathematical expressions for environmental costs like carbon credits and CO₂ mitigation annually [10]:

a. CO₂ Emission

$$(3) \quad \text{The mean CO}_2 \text{ intensity, which is about 0.98, and the electrical generation intensity are similar kg of CO}_2/\text{kWh}$$

$$\text{CO}_2 \text{ emission/year} = \frac{\text{Embodied energy} \times 0.98}{\text{life time}} \quad (9)$$

For Indian conditions

$$\text{CO}_2 \text{ emission/year} = \frac{\text{Embodied energy} \times 1.58}{\text{life time}} \quad (10)$$

b. CO₂ mitigation

Equation can be used to determine it per kWh

$$\text{CO}_2 \text{ mitigation/year} = (E_{\text{out}} \times n) \times 1.58 \quad (11)$$

Equation calculates total CO₂ mitigation

$$\text{Mitigation net over life} = (E_{\text{out}} \times n) \times 1.58 / 1000 \quad (12)$$

c. Earned carbon credit

$$\text{Carbon credit} = \text{Mitigation (during life span)} \times D \quad (13)$$

D is the shift from \$5 to \$20 per tones of CO₂ mitigation
Embodied energy of different component involve in fabrication of proposed system are given below in Table 3.

2.3 Methodology

The following steps are included in the approach used to study the suggested system:

Step-I

First, proposed systems for the annual are calculated using the Lui and Jordan equations.

Step-II

Calculate daily solar radiation by through number of days in a month by as clear, hazy, hazy, cloudy, and cloudy days.

Step-III

Maximize the collector output using all parameters. Environmental and energy economic characteristics have been assessed Economic and Environmental and energy economic characteristics have been assessed.

Step-IV

Proposed systems are contrasted with the prior system using numerically computed values.

Figure 2, represents the flow chart for the steps involve in computing the performance of proposed system on the basis of yield, economic, and enviro-economic.

Table 2. Capital investment previous and proposed system.

Parameters	System- B [21]		System-A	
	Cost ₹	\$	Cost ₹	\$
FRP body	10200	139.135	10200	139.135
Glass cover 2.05	1600	21.825	1600	21.825
MS stand	1000	13.641	1000	13.641
Nozzle (input/output)	200	2.728	200	2.728
MS clamp	250	3.410	250	3.410
Gaskets	200	2.728	200	2.728
Silicon gel	200	2.728	200	2.728
PVT-FPC (N=4) 8500	34000	463.784		0.000
PVT-CPC (N=4) 9000		0.000	36000	491.06
Pump & Motor	1200	16.369	1200	16.369
Heat exchanger (helical coiled)	466.25	6.360	466.25	6.360
Fabrication and other cost	6000	81.844	6000	81.844
100 gmsAl ₂ O ₃ nanoparticles	7425	101.282	7425	101.282
Total cost of	62741.25	855.83	64741.25	883.11

Table 3. Illustrates embodied energy of different components of previous and proposed system.

Name of component	Embodied energy (kWh)	
	System-B [10]	System-A
RFP body	755.61	755.61
MS angle	416.4	416.4
Cover (glass)	180.5	180.5
FPC (N=4)	2209.92	-
CPC (N=4)	-	3279.41
PV (glass-glass)	980	980
Copper heat exchanger	25.83	25.83
Nanoparticles (Al ₂ O ₃)	17.82	17.82
Others	20	20
Total EE of system	4606.08	5675.57

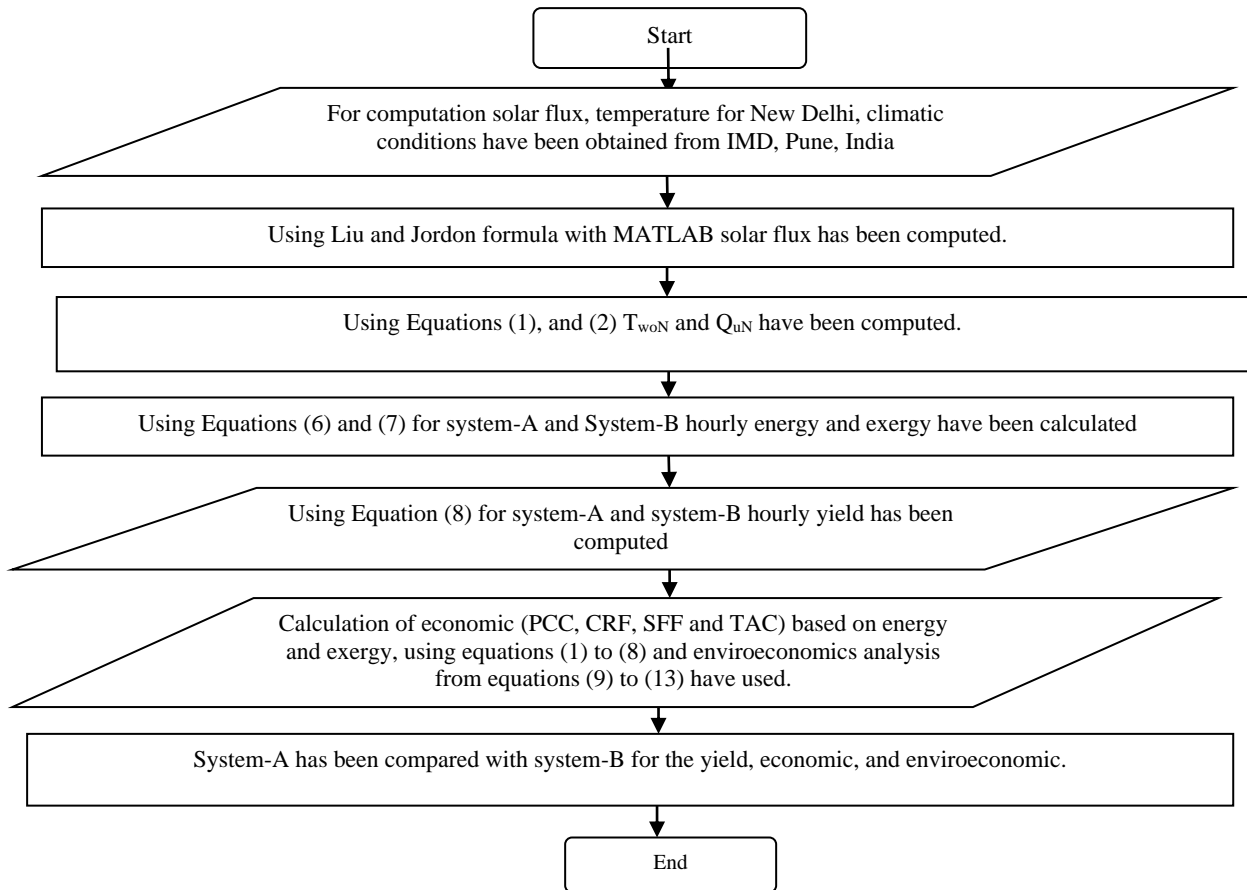


Figure 2. Flow chart of methodology adopted.

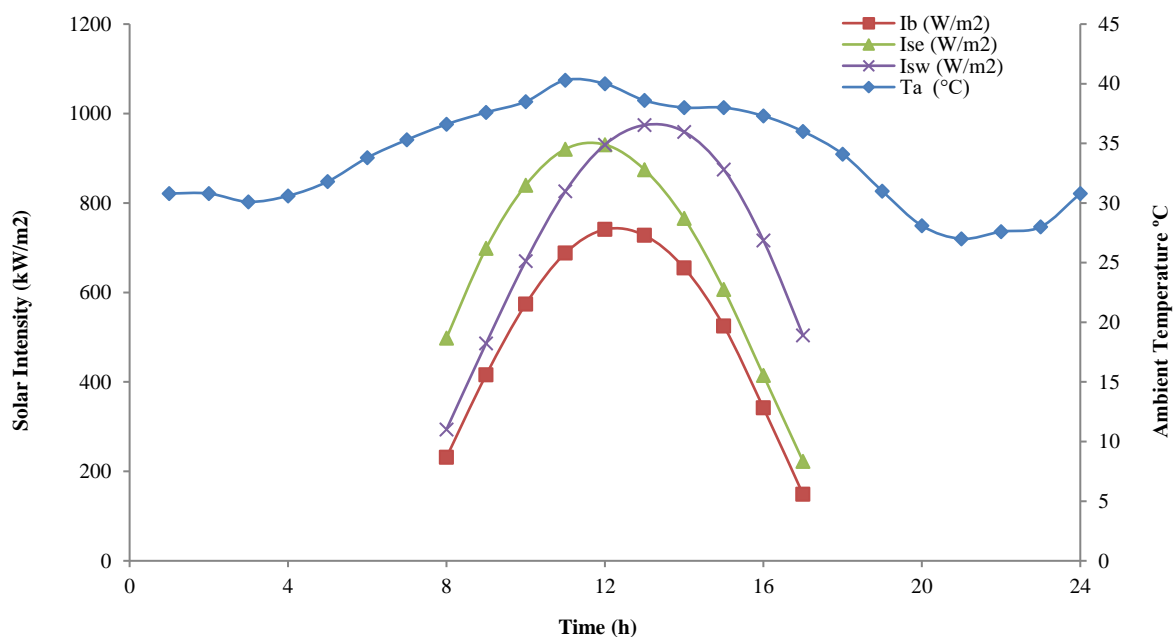


Figure 3. Shows per hour variation and the surrounding temperature in °C on May a-type days.

3. Result and Discussion

MATLAB has been used to calculate pertinent data and equations for the climate in New Delhi in terms of solar radiation and ambient temperature. The hourly changes of the beam radiation is shown in Figure 3. Using Lui Jordan Formula [23]

$$F = 1 - 0.0335 \sin 360^\circ(n_d - 94)/365 \quad (14)$$

Where n_d is the day of the year (on 1 January $n_d = 1$; on 31

December $n_d = 365$); the argument of the sine function is in degrees.

3.1 Analysis of the economics of employing Al_2O_3 nanoparticles in an active solar distiller with an NPVT-CPC collector and heat exchanger (helically coiled) -

For the system to be economically viable, economic analysis is required. Economic analysis of system-A and system-B are found that distillate cost (₹/kg) of system-A is less to system-B for interest rate of 1%, 3%, and 5%

respectively and total annual cost of system-A in (\$) for interest rate of 1%, 3%, and 5% is less for system-B as represent in Table 4. It is obvious the system-A better to system-B.

3.2 Enviro-economic analysis of active double slope still for proposed system-A using Al₂O₃ nanoparticles-

The environmental costs like carbon credits and CO₂ has reduced annually: The Enviro-economic analysis of the proposed and previous systems are illustrate in Figure 4. It is discovered that the proposed system's CO₂ energy-based mitigation/ton and carbon credit gains (\$) are 3.97% less than those of the previous approach for 15 years. The CO₂ mitigation per ton is 40.85kg, respectively.

The proposed and previous systems enviro-economic analysis is shown in Figure 5. It is observed that the proposed system-A PCC, is all 3.18 % higher than those of the preceding system. It is found that over a 15-year lifespan, are for embodied energy, yield, PCC all based on the suggested system's energy, which costs \$883.11 (\$). As the embodied energy is high while CO₂ mitigation and carbon credit earns in (\$) are better to previous system enviroeconomic analysis for 15, 20 and 30 years on the basis of CO₂ mitigation/ton, carbon credit earned in USD(\$) represents Table 5. It is obvious from data system-A is more economical to system-B.

4. Conclusion and Future Scope

4.1 Conclusions

Based on annual examination of the proposed system-A, energy, exergy, and yield with Al₂O₃ nanoparticles revealed the following final observations.

1. Based on distillate cost, System-A performs better than System-B. System-A for 15, 20, and 30 years at rate of interest 1%, 3%, and 5% the cost of distillate 1.25, 1.51,

and 1.79 ₹/ kg respectively and system-B, for 15, 20, and 30 years at rate of interest 1%, 3%, and 5% the cost of distillate 1.31, 1.59, and 1.89 ₹/ kg respectively.

2. Based on yield system-A is 8.5% greater, annual energy 3.9% greater to system-B.
3. System-A is more environmentally friendly than System-B, based on carbon credit earnings (\$) based on energy. System-A for 15, 20, and 30 years, \$204.26, \$287.30, and \$453.36 respectively and system-B, for 15, 20, and 30 years, \$212.71, \$295.75 and \$461.81 respectively.
4. Based on CO₂ mitigation/ton based on energy system-A for 15, 20, and 30 years, 40.85, 57.46, and 90.67 respectively and system-B, for 15, 20, and 30 years, 42.54, 59.15, and 461.81 respectively. it is obvious system-A is better to system-B.

The active solar still using Al₂O₃ nanoparticles is thought to be the best design overall because of its annual performance based on economic, environmental, and energy-related aspects.

4.2 Future scope

1. To operate the system at night extra supporting electrical appliances and partially covered FPC need to be increased over 25%. The mass water temperature could be raised even more by the CPC profile, which the PCM could also make use of at night. It may be another factor contributing to the improvement in system performance, and more study is required to determine its magnitude.
2. Use of various nanoparticles to study of energy matrices, environmental economics, and energy economics is conceivable. Investigations on the impact of size, shape, and mass flow rate are to be needed to examine.

Table 4. Economic analysis for proposed system (system-A) and previous system (system-B).

	Years (n)	I (%)	S (\$)	CRF	SFF	Cost of water (inkg)/annum (₹/kg)	TAC (\$)
System (A)		1	176.6	0.07	0.06	1.25	45.42
N-PVT-CPC-DS-HE (Proposed system)	15	3	176.6	0.08	0.05	1.51	97.97
		5	176.6	0.1	0.05	1.79	153.74
System (B)		1	171.1	0.07	0.06	1.31	41.11
N-PVT-FPC-DS-HE (Previous system)[21]	15	3	171.1	0.08	0.05	1.59	94.95
		5	171.1	0.1	0.05	1.89	148.99

Table 5. Enviroeconomic analysis of system-A and system-B for 15, 20, and 30 years.

		System-A NPVT-CPC-DS-HE	System-B [21] NPVT-FPC-DS-HE
15 Years	CO ₂ miti/ton	40.85	42.54
	Carbon credit earn(\$)	204.26	212.71
20 Years	CO ₂ miti/ton	57.46	59.15
	Carbon credit earn(\$)	287.30	295.75
30 Years	CO ₂ miti/ton energy	90.67	92.36
	Carbon credit earn(\$)	453.36	461.81

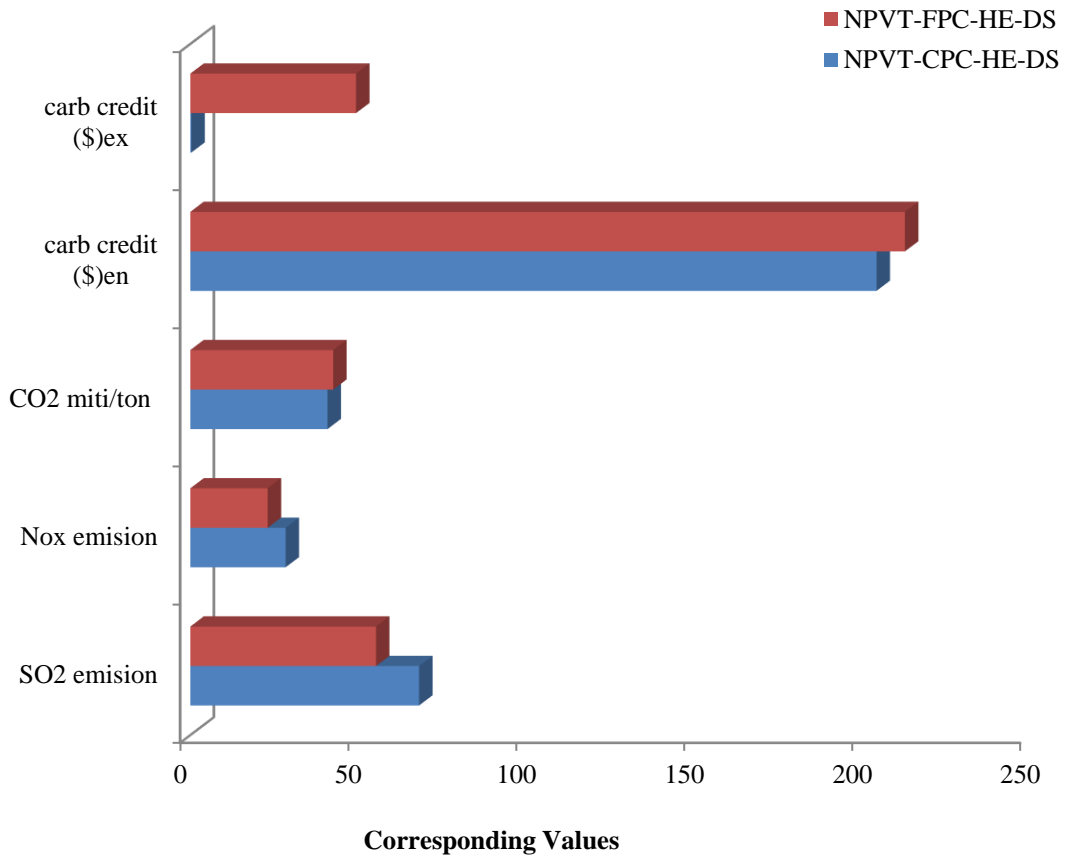


Figure 4. Enviro-economic analysis based on SO_2 , CO_2 and NO_x for 15 years.

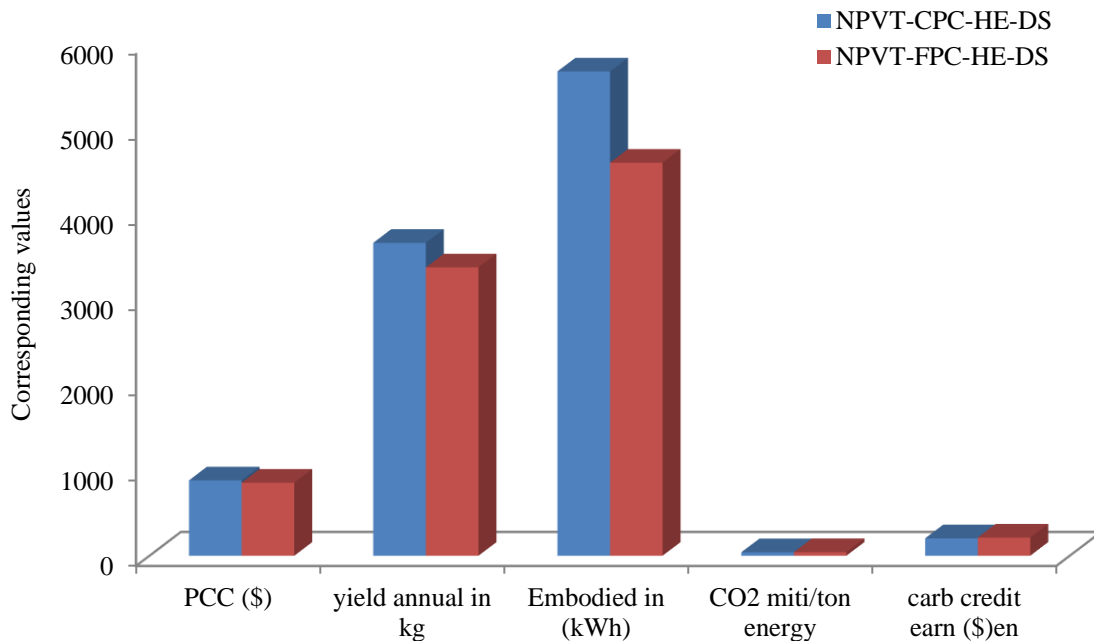


Figure 5. Enviro-economic analysis based on yield for 15 years.

Acknowledgements:

The authors gratefully acknowledge to Professor Samsher, Department of Mechanical Engineering, Delhi Technological University, Delhi, India-110042, for providing valuable suggestions.

Nomenclature

Symbol Variable

A_{ba} basin surface, in (m^2)
 A_{ca} flat plate collector area under glazing, in (m^2)

A_{gE} eastside glass cover area, in (m^2)
 A_{gW} westside glass cover area, in (m^2)
 A_m photovoltaic area in (m^2)
 D_i tube area under FPC, in (m^2)
 d_p Nps dia., in (nm)
 h_{HE} in heat exchanger convective heat transfer coefficient, in (W/m^2K)
 I_b on the collector solar irradiation, in (W/m^2)
 I_{SE} eastside over glass cover solar irradiation, in (W/m^2)

I_{SW}	westside over glass cover solar irradiation, in (W/m^2)
M_w	water mass, in kg
Q_{uN}	N identical 25% PVT-CPC linked in series, the rate of heat transfer, in (kWh)
T_a	surrounding temperature in ($^{\circ}C$)
T_{wi}	fluid inlet temperature in ($^{\circ}C$)
T_{bf}	in collector basefluid temperature, in ($^{\circ}C$)
T_{woN}	water temperature at the Nth collector outlet, in ($^{\circ}C$)
T_w	temperature of basin water in ($^{\circ}C$)
T_{wo}	temperature of water at $t=0$, in ($^{\circ}C$)
ΔT_{HE}	temperature between nanofluid to basefluid at heat exchanger, in ($^{\circ}C$)
ΔT	temperature between T_w and $\frac{T_{giE}}{T_{giW}}$ for time(t), in (h)

Subscripts

e_n	energy
e_x	exergy
E_{in}	input of embodied energy
E_{out}	output embodied energy
E_{sol}	annual solar energy
i	interest rate
n	life time period
p	particle

Abbreviation

YM	maintenance cost annually
ASC	salvage cost annually
CR	capital recovery factor
CM	carbon dioxide mitigation
FYC	fixed annual cost
FPC	flat plate, collector
HE	heat exchanger
PCC	primary capital cost
SFF	shrinking fund factor
S	value of future salvage
TAC	total annual cost
CPC	compound parabolic concentrator
N-PVT-DS-CPC-HE, incorporating PVT-CPC double slope with N^{th} collector using heat exchanger (helically coiled)	

References:

[1] S.A. Lawrence, and G.N. Tiwari, "Theoretical evaluation of solar distillation under natural circulation with heat exchanger", *Energy Convers. Manage.*, 30, pp. 205-213, 1990, [https://doi.org/10.1016/0196-8904\(90\)90001-F](https://doi.org/10.1016/0196-8904(90)90001-F).

[2] G.N. Tiwari, "Solar energy: fundamentals, design, modelling and applications", New Delhi/New York: CRC Publication/Narosa Publishing House, 2002.

[3] G.N. Tiwari, and A.K. Tiwari, "Solar distillation practice for water desalination systems", New Delhi: Anamaya Publishers, 2008.

[4] T.P. Otanicar, and J. Golden, "Comparative environmental and economic analysis of conventional and nanofluid solar hot water technologies", *Environ Sci. Technol.*, 43, pp. 6082-6087, 2009, <https://doi.org/10.1021/es900031j>.

[5] V. Khullar, and H. Tyagi, "A study on environmental impact of nanofluid based concentrating solar water heating system", *Int J. Environ. Studies.*, 69, pp. 220-232, 2012, <https://doi.org/10.1080/00207233.2012.663227>.

[6] M. Faizal, R. Saidur, S. Mekhilef, and M.A. Alim, "Energy, economic and environmental analysis of metal oxides nanofluid for flat-plate solar collector", *Energy Convers., Manage.*, 76, pp. 162-168, 2013, <https://doi.org/10.1016/j.enconman.2013.07.038>.

[7] X. Liu, W. Chen, M. Gu, S. Shen, G. Cao, "Thermal and economic analyses of solar desalination system with evacuated tubular collectors", *Solar Energy*, 93, pp.144-50, 2013, <https://doi.org/10.1016/j.solener.2013.03.009>.

[8] H. Sharon, and K.S. Reddy, "Performance investigation and enviro-economic analysis of active vertical solar distillation units", *Energy*, 84, pp. 794-807, 2015, <https://doi.org/10.1016/j.energy.2015.03.045>.

[9] R. Dhivagar, M. Mohanraj, K. Hindouri, and Y. Belyayev, "Energy, exergy, economic and enviroeconomic (4E) analysis of gravel coarse aggregate sensible heat storage assisted single slope solar still", *Journal of Thermal Analysis and Calorimetry*, 2020, <https://doi.org/10.1007/s10973-020-09766-w>.

[10] Dharamveer, and Samsher, "Comparative analyses energy matrices and enviro-economics for active and passive solar still", *materialstoday: proceedings*, 2020, <https://doi.org/10.1016/j.matpr.2020.10.001>.

[11] A. Shahsavari, P. Talebizadehsardari, and M. Arıcı, "Comparative energy, exergy, environmental, exergoeconomic, and enviroeconomic analysis of building integrated photovoltaic/thermal, earth-air heat exchanger, and hybrid systems", *Journal of cleaner production*, 362, 132510, 2022, <https://doi.org/10.1016/j.jclepro.2022.132510>.

[12] N.M. Shatar, M. F. M. Sabri, M. F. M. Salleh, and M. H. Ani, "Energy, exergy, economic, environmental analysis for solar still using partially coated condensing cover with thermoelectric cover cooling", *Journal of cleaner production*, 387, 135833, 2023, <https://doi.org/10.1016/j.jclepro.2022.135833>.

[13] D. Singh, A.K. Yadav, A. Kumar, and Samsher, "Energy matrices and life cycle conversion analysis of N-identical hybrid double slope solar distiller unit using Al_2O_3 nanoparticle", *Journal of Water and Environmental Nanotechnology*, 8, 3, pp. 267-284, 2023, <http://doi:10.22090/jwent.2023.03.006>.

[14] A.E. Kabeel, Z.M. Omara, and F.A. Essa, "Enhancement of modified solar still integrated with external condenser using nanofluids, an experimental approach", *Energy Convers. Manage.*, 78, pp. 493-498, 2014, <https://doi.org/10.1016/j.enconman.2013.11.013>.

[15] T. Elango, A. Kannan, and K.K. Murugavel, "Performance study on single basin single slope solar still with different water nanofluids", *Desalination*, 360, pp. 45-51, 2015, <https://doi.org/10.1016/j.desal.2015.01.004>.

- [16] L. Sahota, and G.N. Tiwari, "Effect of nanofluids on the performance of passive double slope solar still: A comparative study using characteristic curve", *Desalination*, 388, pp. 9-21, 2016, <https://doi.org/10.1016/j.desal.2016.02.039>.
- [17] S.W. Sharshir, G. Peng, L. Wu, N. Yang, F.A. Essa, and A. H. Elsheikh, "Enhancing the solar still performance using nanofluids and glass cover cooling: Experimental study", *Applied Thermal Engg.*, 113, pp. 684-693, 2017, <https://doi.org/10.1016/j.applthermaleng.2016.11.085>.
- [18] S.M. Saleha, A.M. Solimanb, M.A. Sharaf, V. Kaled, and B. Gadgile, "Influence of solvent in the synthesis of nano-structured ZnO by hydrothermal method and their application in solar-still", *J. Environ. Chem. Eng.*, 5, pp. 1219-1226, 2017, <https://doi.org/10.1016/j.jece.2017.02.004>.
- [19] W. Chen, C. Zou, X. Li, and L. Li, "Experimental investigation of SiC nanofluids for solar distillation system: Stability, optical properties and thermal conductivity with saline water based fluid", *International Journal of Heat Mass Transfer*, 107, pp. 264-270, 2017, <https://doi.org/10.1016/j.ijheatmasstransfer.2016.11.048>.
- [20] O. Mahian, A. Kianifar, S.Z. Heris, D. Wen, A.Z. Sahin, and S. Wongwises, "Nanofluids effects on the evaporation rate in a solar still equipped with a heat Exchanger", *Nano Energy*, 36, pp. 134-155, 2017, <http://doi.org/10.1016/j.nanoen.2017.04.025>.
- [21] L. Sahota, Shyam, and G.N. Tiwari, "Energy matrices, enviroeconomic and exergoeconomic analysis of passive double slope solar still with water based nanofluids", *Desalination*, 409, pp. 66-79, 2017, <https://doi.org/10.1016/j.desal.2017.01.012>.
- [22] Dharamveer, and Samsher, D.B. Singh, A.K. Singh, N. Kumar, "Solar Distiller Unit Loaded with Nanofluid- A Short Review", *Lecture Notes in Mechanical Engineering*, Springer, Singapore, pp. 241-247, 2019, https://doi.org/10.1007/978-981-13-6577-5_24.
- [23] Dharamveer, Samsher, and A. Kumar, "Analytical study of Nth identical photovoltaic thermal (PVT) compound parabolic concentrator (CPC) active double slope solar distiller with helical coiled heat exchanger using CuO Nanoparticles", *Desalination and Water Treatment*, 233, pp. 30-51, 2021, <https://doi.org/10.5004/dwt.2021.27526>.
- [24] Dharamveer, Samsher, and A. Kumar, "Performance analysis of N-identical PVT-CPC collectors an active single slope solar distiller with a helically coiled heat exchanger using CuO nanoparticles", *Water Supply*, 2021, <https://doi.org/10.2166/ws.2021.348>.
- [25] D. Singh, S. Singh, A.K. Yadav, O. Khan, A. Dewangan, M.Q. Alkahtani, and S. Islam, "From Theory to Practice: A Sustainable Solution to Water Scarcity by Using a Hybrid Solar Distiller with a Heat Exchanger and Aluminum Oxide Nanoparticles", *ACS Omega*, 2023, 8, (37) pp. 33543-33553 <https://doi.org/10.1021/acsomega.3c03283>.

Research Article

Calculation of Complex Chemical Equilibrium Using Optimization Package Ipopt

^{1*}G.V. Belov , ²N.M. Aristova 

^{1,2} Joint Institute for High Temperatures of Russian Academy of Sciences, Moscow, Russian Federation, 125412

¹ Bauman Moscow State Technical University, Moscow, Russian Federation, 105005

E-mail: ^{1*}gbelov@yandex.ru

Received 20 June 2023, Revised 3 September 2023, Accepted 8 October 2023

Abstract

An approach to the calculation of complex chemical equilibrium using the open-source optimization package Ipopt and the open-source package JuMP is proposed. The code of two procedures written in the open-source Julia programming language for calculating the equilibrium composition and properties of multicomponent heterogeneous thermodynamic systems is presented. The results of the test calculations showed a good performance of the code and a relatively high speed of calculations. Due to the compactness and simplicity of the code, it can be easily integrated into other applications, or used in combination with more complex models.

Keywords: *Chemical equilibrium; thermodynamics; Julia; JuMP; optimization package*

1. Introduction

One of the problems that many engineers and scientists facing in chemistry, chemical technology, plasma chemistry, combustion chemistry, gas dynamics, etc. is the need to calculate the equilibrium composition and properties of complex chemically reacting systems. In this article a complex system means a multicomponent heterogeneous thermodynamic system in which chemical and phase reactions are possible.

The calculation of equilibrium composition is a long-standing problem. Perhaps the first attempts to solve it in a general form were associated with the need to compute the characteristics of rocket fuels [1]. A detailed overview of the methods and algorithms used for this purpose is presented in the monograph [2]. Although the problem of calculating the equilibrium of complex thermodynamic systems is quite old [3-7], new developments appear in this area from time to time, see for example [8-11].

Two approaches can be distinguished that are applied to the calculation of the equilibrium composition - the analysis of the equilibrium of possible chemical reactions and the search for the coordinates of the constrained minimum of the thermodynamic potential. The second approach is more general, because it allows the use of well-developed algorithms for the optimization of functions with constraints.

Difficulties in solving the problem of calculating the equilibrium composition of a complex thermodynamic system are due to some of its features. The reliability of the calculation results essentially depends on the completeness of the thermodynamic database; in particular, the database must contain information on the largest possible number of substances in the condensed state. When creating a model of a thermodynamic system, information from the database is usually loaded automatically based on the list of reagents. However, not all phases that are automatically included in the composition of a model thermodynamic system can be

present in it in an equilibrium state, and it is not always known in advance which phases these are. Therefore, in the process of calculations, it is necessary to determine not only the chemical but also the phase composition, while the phase rule should not be violated. This means that the mathematical formulation of the problem may contain constraints in the form of inequalities. A model thermodynamic system can contain a large number of substances (about 1000), which means a large problem dimension, while the matrix of indices of chemical elements can be quite large and very sparse. In addition, the calculated values of the equilibrium concentrations of substances vary in a very wide range: from approximately 100 to values of the order of 10^{-100} moles, which is much less than the machine zero.

Perhaps that is why, despite its long history, the problem of calculating the equilibrium composition still attracts the attention of many researchers. To date, there are several large universal software systems equipped with databases on the thermodynamic properties of substances, see, for example, [12, 13]. It is possible to calculate the equilibrium using Microsoft Excel and Matlab [14, 15]. There is also a freely distributed library designed to calculate the equilibrium composition [16, 17].

However, until now, the ready-made packages for solving the constrained optimization problems were very rarely used to calculate the equilibrium composition. A possible reason for this was the inconvenience of using such packages. This paper presents a convenient method for determining the phase and chemical compositions of a complex thermodynamic system using the free Ipopt optimization package [18].

2. Calculation of the Equilibrium Composition by Minimization of the Thermodynamic Potential

From a computational point of view calculation of the equilibrium composition means determining the coordinates

of the conditional extremum of a function of several variables. The number of variables can vary from two to several hundred.

According to Duhem's theorem [19], in the absence of external fields, the equilibrium state of a thermodynamic system whose initial masses are known is uniquely characterized by the values of two thermodynamic parameters. The most common pairs of parameters are: temperature-pressure (T, p), temperature-volume (T, V), enthalpy-pressure (H, p) for the combustion in a flow type reactor, entropy-pressure (S, p) for the isentropic expansion to a given pressure, internal energy-volume (U, V) for the combustion at a constant volume, and entropy-volume (S, V) for the isentropic expansion to a given volume.

The formulation of the problem in temperature - pressure coordinates is equivalent to determining the coordinates of the conditional minimum of the Gibbs energy G

$$\begin{aligned} \min_{x \in R^n} G(T, p, x) \\ T = const, p = const, \\ \sum_{i=1}^N v_{ji} x_i = b_j, j = 1, \dots, m, \\ x_i \geq 0, i = 1, \dots, N \end{aligned} \quad (1)$$

where x is the unknown vector of composition, whose components are the numbers of moles of substances, the matrix v_{ji} defines the number of atoms of a chemical element j in the substance i (so-called formula matrix), N is the number of substances in the system, m is the number of chemical elements, and b_j is the amount of a chemical element j in the system.

One can express the Gibbs energy of a multicomponent heterogeneous system consisting of N_c single-component condensed phases and N_m mixtures as

$$G(T, p, x) = \sum_{i=1}^{N_c} G_i x_i + \sum_{j=1}^{N_m} \left[\sum_{i \in I_j} x_i (G_i + RT \ln a_i) \right] \quad (2)$$

where a_i is the activity of the substance i . In a dimensionless form, this relation can be represented as

$$g(T, p, x) = \sum_{i=1}^{N_c} g_i x_i + \sum_{j=1}^{N_m} \left[\sum_{i \in I_j} x_i (g_i + \ln a_i) \right] \quad (3)$$

where $g = G/RT$, $g_i = G_i/RT$.

The following relation is valid for the model «ideal gas, ideal solution, zero volume of condensed phases»

$$g(T, p, x) = \sum_{i=1}^{N_c} g_i x_i + \sum_{j=1}^{N_m} \left[\sum_{i \in I_j} x_i (g_i + \ln x_i) - y_j \ln y_j \right] \quad (4)$$

where $y_j = \sum_{i \in I_j} x_i$.

The reduced Gibbs energy for the condensed component i is given by

$$g_i = [H_i^\circ(T) - TS_i^\circ(T)]/RT \quad (5)$$

and for gaseous substances by

$$g_i = [H_i^\circ(T) - TS_i^\circ(T)]/RT + \ln(p/p^\circ) \quad (6)$$

where p° is the standard pressure, $H_i^\circ(T), S_i^\circ(T)$ are the values of enthalpy and entropy of the substance i in the standard state at temperature T .

The formulation of the equilibrium conditions in the temperature-volume coordinates is much less common. In this case, to calculate the equilibrium, it is necessary to determine the coordinates of the conditional minimum of the Helmholtz energy F

$$\begin{aligned} \min_{x \in R^n} F(T, V, x) \\ T = const, V = const, \\ \sum_{i=1}^N v_{ji} x_i = b_j, j = 1, \dots, m, \\ x_i \geq 0, i = 1, \dots, N \end{aligned} \quad (7)$$

One can express the Helmholtz energy of a multicomponent heterogeneous system consisting of N_c single-component condensed phases and N_m mixtures as

$$F(T, V, x) = \sum_{i=1}^{N_c} G_i x_i + \sum_{j=1}^{N_m} \sum_{i \in I_j} x_i (G_i + RT \ln a_i) - pV \quad (8)$$

Let us assume the mixture with $j = 1$ is in the gas phase. The set of indices of substances for this mixture can be denoted as I_g .

$$F(T, V, x) = \sum_{i=1}^{N_c} F_i^\circ x_i + \sum_{i \in I_g} x_i (F_i + RT \ln x_i) + \sum_{j=2}^{N_m} \left[\sum_{i \in I_j} x_i (F_i^\circ + RT \ln x_i) - RT y_j \ln y_j \right] \quad (9)$$

or in a dimensionless form

$$f(T, V, x) = \sum_{i=1}^{N_c} f_i^\circ x_i + \sum_{i \in I_g} x_i (f_i + \ln x_i) + \sum_{j=2}^{N_m} \left[\sum_{i \in I_j} x_i (f_i^\circ + \ln x_i) - y_j \ln y_j \right] \quad (10)$$

The Helmholtz energy for the condensed component i is

$$f_i^\circ = [H_i^\circ(T) - TS_i^\circ(T)]/RT \quad (11)$$

for the component i in a gas phase

$$f_i = [H_i^\circ(T) - TS_i^\circ(T)]/RT + \ln [RT/(p^\circ V)] - 1 \quad (12)$$

3. On the Packages JuMP and Ipopt

An open-source Julia programming language [20] was chosen to implement the above given calculation procedures. This language was designed for scientific and technical calculations. To find the equilibrium composition the packages JuMP and Ipopt were used.

To solve the problem of calculating the equilibrium composition an open-source optimization package Ipopt [21] was chosen. This package is designed to determine the coordinates of the conditional extremum of a non-linear function of many variables using the interior point method. The algorithm implemented in Ipopt is described in [18].

To provide access to a specialized optimization library, an algebraic modeling language is often used. Algebraic modeling languages (AMLs) are designed to describe optimization problems in a form convenient for the researcher. Modeling languages themselves do not solve

optimization problems; their purpose is to transfer the problem formulation to the optimization procedure and return the results of optimization in the most appropriate way. They are widely used in industry and science. Many of these languages are very effective for solving a wide range of problems, but they also have some disadvantages. In particular, using them the formulation of a problem can be very laborious, since in addition to the objective function and constraints, it is necessary to provide the gradient of the objective function, the Jacobian of the constraints, and the Hessian of the Lagrange function. Meanwhile, the most tedious part of this work (namely, calculating the gradient of the objective function, the Jacobian of the constraints, the Hessian of the Lagrange function) can be done by some of AMLs, and JuMP is one of them.

JuMP is an open-source modeling language [22, 23], which allows users to formulate a wide range of optimization problems using high-level algebraic syntax.

As it is mentioned in [23] JuMP is similar to such open-source modeling languages as YALMIP [24], CVX [25] and Pyomo [26]. These AMLs are built into general-purpose programming languages and are convenient to use. However, the low performance of languages such as MATLAB and Python does not allow taking full advantage of these AMLs. To solve this problem, JuMP was created, being integrated with the high-level programming language Julia.

When solving nonlinear optimization problems, AMLs generate procedures for the precise calculation of derivatives according to a given algebraic equation, which optimization packages can call directly. If necessary, automatic differentiation tools can be used to calculate derivatives instead of AML.

The technical tasks that AML must perform can be roughly divided into the following parts: load into memory the problem entered by the user, generate the input data, required by the optimization procedure according to the type of problem, transfer the problem into optimization library and get back the calculation results. All the tasks are solved by the JuMP package, which uses the automatic differentiation to evaluate the derivatives of the expressions entered by the user.

In addition to function gradients, optimization procedures often use matrices of second derivatives. Matrices of this kind can also be computed by the JuMP package using the automatic differentiation technique.

4. Implementation of the Equilibrium Calculation Algorithm in Julia for (T, p) and (T, V) Problems

The above equations (1)-(5) were used to create functions in the Julia language, designed to calculate the equilibrium composition. Gibbs and Helmholtz energies divided by RT are used as objective functions. The solution of the conditional minimization problem is implemented using the packages JuMP and Ipopt.

The input for the functions includes: the number of chemical elements (m), the number of substances (k), the number of solutions (ns), the number of pure condensed phases (nc), the array of dimensionless values of Gibbs (g) or Helmholtz (f) energies of substances, the array of indices of substances in phases-solutions (jx), the matrix (A), the amounts of chemical elements in the system (b). The substances in the list are ordered as follows. First, there are condensed substances that form pure phases, then gaseous substances, and then components of condensed solutions.

Each function returns the equilibrium concentrations of substances x_i (`equi_conc`), the numbers of moles of phases y_j (`phase_mols`) and the chemical potentials of elements λ_j (`lam`). In some cases, it is possible to determine the phase composition and equilibrium concentrations of substances present in the system in small amounts approximately only. The code of the functions is given in Figure 1.

```
function calc_Gibbs(m,k,ns,nc,g,jx,A,b)
model = Model(Ipopt.Optimizer)
@variable(model, x[1:k] >= 0, start = 1.e-3)
@variable(model, y[1:ns] >= 0, start = 1.e-3)
@NLOjective(model, Min, sum(x[i]*g[i] for i in 1:nc)+sum(sum(x[i]*(log(x[i]) + g[i]) for i in jx[1,j]:jx[2,j]) - y[j]*log(y[j]) for j in 1:ns))
for j in 1:ns
@constraint(model, sum(x[i] for i in jx[1,j]:jx[2,j]) == y[j])
end
@constraint(model, con, A'*x .== b)
JuMP.optimize!(model)
equi_conc=zeros(k)
for i in 1:k equi_conc[i]=value(x[i]) end
phase_mols=zeros(ns)
for i in 1:ns phase_mols[i]=value(y[i]) end
lam=zeros(m)
for i in 1:m lam[i]=shadow_price(con[i]) end
return equi_conc, phase_mols, lam
end

function calc_Helmholtz(m,k,ns,nc,f,jx,A,b)
model = Model(Ipopt.Optimizer)
@variable(model, x[1:k] >= 0, start = 1.e-3)
@variable(model, y[1:ns] >= 0, start = 1.e-3)
@NLOjective(model, Min, sum(x[i]*f[i] for i in 1:nc)+sum(x[i]*(log(x[i]) + f[i]) for i in jx[1,1]:jx[2,1])+sum(sum(x[i]*(log(x[i]) + f[i]) for i in jx[1,j]:jx[2,j]) - y[j]*log(y[j]) for j in 2:ns))
for j in 2:ns
@constraint(model, sum(x[i] for i in jx[1,j]:jx[2,j]) == y[j])
end
@constraint(model, con, A'*x .== b)
JuMP.optimize!(model)
@show objective_value(model)
equi_conc=zeros(k)
for i in 1:k equi_conc[i]=value(x[i]) end
phase_mols=zeros(ns)
for i in 1:ns phase_mols[i]=value(y[i]) end
lam=zeros(m)
for i in 1:m lam[i]=shadow_price(con[i]) end
return equi_conc, phase_mols, lam
end
```

Figure 1. The code of the functions `calc_Gibbs` and `calc_Helmholtz`.

The function `calc_Gibbs` can be called as it is shown in Figure 2.

```
equi_conc, phase_mols, lam =
calc_Gibbs(m, k, ns, nc, g, jx, A, b)
```

Figure 2. Example of the calling the `calc_Gibbs` function.

5. Implementation of the Algorithm When the Temperature is not Set

It is impossible to calculate the values of Gibbs and Helmholtz energies if the temperature is not assigned. In this case, it is necessary to find the temperature T as a root of a nonlinear equation

$$Z - \sum_{i=1}^N x_i(T)z_i(T) = 0 \quad (13)$$

where Z is the value of assigned parameter (e.g., enthalpy, entropy, internal energy), $x_i(T)$ is the equilibrium concentrations related to current value of the temperature, and $z_i(T)$ is the partial molar value of the parameter (enthalpy, entropy, internal energy respectively).

There are two approaches to solve the problem. The first of them involves the use of a special function to determine the root of the equation from the Roots.jl package [27]. As an example, we provide a function call to calculate the composition at given values of pressure and enthalpy, see Figure 3, where t_{\min} , t_{\max} are the upper and lower bounds of the interval for finding the root, eps is the maximum calculation error, find_S is a function that calculates the entropy of a thermodynamic system from the current values of temperature and chemical composition using information about the thermodynamic properties of substances.

```
T = findrootS(find_S, tmin, tmax,
eps)
```

Figure 3. Example of the calling the *findrootS* function.

The function *findrootS* is given in figure 4.

```
function findrootS(f, a, b, tol)
T=find_zero(f, [a, b], atol=tol,
Order1())
return T
end
```

Figure 4. The code of the functions *findrootS*.

The second approach is based on the direct use of the Newton's method, where the root of the equation is determined iteratively (i is the number of iteration)

$$x_{i+1} \approx x_i - f(x_i)/f'(x_i) \quad (14)$$

The temperature is determined by one of the following formulae (C_p and C_v are heat capacities):

$$T_{i+1} \approx T_i + [H - H(T_i)]/C_p(T_i) \quad (15)$$

if the pressure is known and the value of enthalpy H is given;

$$T_{i+1} \approx T_i [1 + (S - S(T_i))/C_p(T_i)] \quad (16)$$

if the pressure is known and the entropy value S is given;

$$T_{i+1} \approx T_i + [U - U(T_i)]/C_v(T_i) \quad (17)$$

if the volume is known and the value of the internal energy U is given;

$$T_{i+1} \approx T_i [1 + (S - S(T_i))/C_v(T_i)] \quad (18)$$

if the volume is known and the entropy value S is given.

In the case when the temperature is known and the value of entropy S is given, the pressure is determined by the formula

$$p_{i+1} \approx p_i + [S - S(p_i)]/[\partial S(p_i)/\partial p]_T = p_i - [S - S(p_i)]/[\partial v(p_i)/\partial T]_p \quad (19)$$

If the pressure is known, the composition is calculated using the function `calc_Gibbs`, if the volume is specified the procedure `calc_Helmholtz` is used.

6. On the Calculation of Thermodynamic Properties of Substances in the Standard State

To calculate the values of the Gibbs and Helmholtz energies of substances under standard conditions, it is necessary to know the corresponding values of enthalpy and entropy. The reference book [28] and the corresponding database IVTANTHERMO [29] contain information on the thermodynamic properties of pure substances in the form of tables and coefficients of the approximating polynomial a_i , which can be used to determine the values of entropy and enthalpy increment at a given temperature by the following formulas

$$S^\circ(T) = a_1 + a_2(\ln X + 1) - a_3/X^2 + 2a_5X + 3a_6X^2 + 4a_7X^3 \quad (20)$$

$$H^\circ(T) - H^\circ(0) = T(a_2 - 2a_3/X^2 - a_4/X + a_5X + 2a_6X^2 + 3a_7X^3) \quad (21)$$

here $X = T/10000$. The standard pressure p° in the reference book [28] equals 1 atm (101325 Pa).

The enthalpy value can be calculated as follows

$$H^\circ(T) = \Delta_f H^\circ(298.15) + H^\circ(T) - H^\circ(0) - [H^\circ(298.15) - H^\circ(0)] \quad (22)$$

where $\Delta_f H^\circ(298.15)$ is the enthalpy of formation of the substance at 298.15 K.

In the NIST Chemistry Webbook [30] the coefficients of similar relations are given for approximating the temperature dependence of thermodynamic functions in the form

$$S^\circ(T) = A \ln(t) + Bt + Ct^2/2 + Dt^3/3 - E/(2t^2) + G \quad (23)$$

$$H^\circ(T) = H^\circ(298.15) + At + Bt^2/2 + Ct^3/3 + Dt^4/4 - E/t + F - H \quad (24)$$

$t = T/1000$; A, B, C, D, E, F, G, H are the polynomial coefficients, J-mol-K. The standard pressure p° equals 1 bar.

When using NASA polynomials [31], the values of thermodynamic functions at a given temperature are calculated as follows (a_i, b_i are the coefficients)

$$S^\circ(T)/R = -a_1T^{-2}/2 - a_2T^{-1} + a_3 \ln T + a_4T + a_5T^2/2 + a_6T^3/3 + a_7T^4/4 + b_2 \quad (25)$$

$$H^\circ(T)/RT = -a_1T^{-2} + a_2(\ln T)/T + a_3 + a_4T/2 + a_5T^2/3 + a_6T^3/4 + a_7T^4/5 + b_1/T \quad (26)$$

7. Results and Discussion

The algorithm described above was implemented as a set of Julia routines available at the GitHub repository [36] under the open-source MIT license. The routines are presented along with their usage examples, which can be run from the command line. As Julia is a multi-platform programming language, the examples can be run on different operating systems. The present version of the code has no GUI interface, although it can easily be created using any of Julia GUI packages. Below in this section, we describe some of the test cases in more detail. In all cases, the information on thermodynamic properties of pure substances from the IVTANTHERMO database [29] has been used.

Calculations were performed for several hundred relatively simple and more complex thermodynamic systems, namely, for homogeneous gas-phase systems with and without ionization, for heterogeneous systems with a gas phase and single-component condensed phases, as well as for complex heterogeneous thermodynamic systems with a gas phase, condensed solutions, and single-component condensed phases. All the problems were solved correctly, although in some cases it was necessary to resort to scaling. For this, the content of chemical elements was recalculated to 1 kg. The most difficult problem included a list of substances formed by 22 chemical elements, while about 130 condensed substances and 135 gaseous substances were selected from the database and included in the system, from which two solutions and several dozen single-component phases were formed. The analysis of the calculation results includes the following checks: the mass balance equation, the Kuhn-Tucker condition, and the Gibbs phase rule. The results of all calculations that were performed with thermodynamic systems of varying complexity were compared with the results of our previous code for calculating the equilibrium composition [32], they were almost identical.

Besides, the calculations were performed at conditions, where the rank of the material balance constraint matrix is less than the number of chemical elements. Usually, it is a difficult task for the numerical algorithms. An example would be systems with a single reactant, such as H₂O or CO₂ at relatively low temperatures, when there is practically only one chemical compound in equilibrium, and the presence of other reaction products is negligible. The program coped with these tasks successfully.

Figure 5 shows the calculation results for the emergency state of a nuclear reactor. Equilibrium concentrations (in mol) are presented for dominant substances only. The initial composition for this calculation is given in [33]:
 $1014.5\text{UO}_2 + 0.096\text{Np} + 2.754\text{Pu} + 0.824\text{Ce} + 0.215\text{Y} + 0.138\%\text{Te} + 0.332\text{La} + 1.442\text{Zr} + 0.389\text{Ba} + 0.899\text{Ru} + 1.15\%\text{Mo} + 0.265\text{Pr} + 0.421\text{Sr} + 0.0385\text{I}_2 + 0.859\text{Nd} + 0.043\%\text{Nb} + 0.0064\text{Am} + 0.745\text{Cs} + 0.166\text{Rh} + 0.006\text{Sb} + 0.025\text{Eu} + 3725\text{H}_2\text{O} + 3725\text{H}_2$.

The calculation was carried out at a pressure of 1 bar and a temperature of 2000 K. A direct comparison of these results with the results of [33] is impossible as the thermodynamic database used in [33] is unavailable. Therefore, we present these simulation results as an illustration of studying a rather complex thermodynamic.

Table 1 shows the computed values of the performance characteristics of rocket fuel liquid oxygen-kerosene (O₂(L)+RP-1), combustion temperature T_{chamber} , specific impulse in vacuum I_{vac} , characteristic velocity C^* , obtained using the CEA code [34] and the ENGINE code, written in

Julia. The conditions are as follows: the pressure in the combustion chamber is 200 bar, nozzle exit pressure is 0.4 bar, oxidizer/fuel ratio is 3. Some discrepancy in the results can be explained by the fact that different thermodynamic databases were used in the calculations. To compute the characteristics of the propellant, it is necessary to calculate the equilibrium composition in the combustion chamber, in the throat, and at the exit of the nozzle. The calculation of the composition in the combustion chamber is carried out at given values of pressure and enthalpy, the other two calculations are carried out at given values of pressure and entropy [35].

The time for preparing the program for calculation is about several seconds. It includes the time required to load the packages and the database, as well as the time to compile the code. The actual calculation time depends on many factors, namely the number of phases and substances, the type of problem, the type of computer (memory, processor), etc. In our calculations the computation time ranged from several hundredths to tenths of a second if the temperature was given. If the temperature was not set, the calculation time could increase to several seconds. Further optimization of the code is possible.

Thermodynamic properties:		
p =	0.1	MPa
t =	2000	K
v =	1240.58	cub.m
s =	1972.06	kJ/K
h =	-1.38049e+06	kJ
u =	-1.50455e+06	kJ
Cp =	428.554	kJ/K
Cv =	366.525	kJ/K
Pure condensed phases		
Phase 1:	Ru (c)	0.898991
Phase 2:	Rh (c)	0.164611
Phase 3:	Mo (c)	0.310964
Phase 4:	Nb2O5 (c)	
	0.0166375	
Phase 5:	Y2O3 (c)	0.107237
Phase 6:	Ce2O3 (c)	0.411914
Phase 7:	Pr2O3 (c)	0.13243
Phase 8:	Nd2O3 (c)	0.429459
Phase 9:	Eu2O3 (c)	
	0.0123781	
Phase 10:	UO2 (c)	1006.11
Phase 11:	Np (c)	
	0.0831693	
Phase 12:	PuO2 (c)	2.75149
Phase 13:	BaZrO3 (c)	0.333271
Mixture 1, (gas phase):		
	H2 (g)	3741.23
	H2O (g)	3698.8
	H (g)	8.59741
	UO2OH (g)	8.00739
	OH (g)	0.843116
	CsOH (g)	0.593765
	Sr (OH) 2 (g)	0.405405
	LaO2 (g)	0.331998
	MoO3 (g)	0.301278
	MoO2 (OH) 2 (g)	0.281665
	MoOOH (g)	0.145607
	Cs (g)	0.134998
	Te (g)	0.1149
	U2O6 (g)	0.11274

Figure 5. Equilibrium composition and properties.

In our opinion, the use of an external optimization library may be appropriate in cases where high performance does not play a crucial role: for research purposes, for testing a thermodynamic model, and for educational purposes. The small size of the functions code makes them versatile,

readable, and ready to use after a short study. The presented functions can be easily integrated into a more complex algorithm that requires the calculation of the equilibrium composition.

Table 1. Computed performance characteristics of rocket fuel.

Program	T_{chamber} , K	I_{vac} , M/c	C^* , M/c
CEA	3867.2	3574.8	1781.1
ENGINE	3871.7	3575.3	1781.5

8. Conclusion

Two algorithms and their implementations in the Julia programming language are presented for calculating the equilibrium composition and properties of multicomponent heterogeneous thermodynamic systems.

An algorithm for calculating the equilibrium composition for situations with unknown temperature is proposed and implemented.

The test calculations showed a good performance of the functions and a relatively high speed of calculations.

The main advantages of the proposed code are its openness, compactness, versatility, and simplicity, which allows it to be easily integrated into other applications or used in combination with more complex models.

A few small examples illustrating the possibility of using the functions can be found at [36].

Acknowledgements:

This work was supported by the Ministry of Science and Higher Education of the Russian Federation (State Assignment No. 075-01129-23-00).

The authors are grateful to Dr. Igor Morozov for his help in preparing the manuscript.

Nomenclature:

AML - algebraic modeling language;
 C_p – heat capacity at constant pressure, J/(mol K);
 C_v – heat capacity at constant volume, J/(mol K);
 F – Helmholtz energy, J/mol;
 G – Gibbs energy, J/mol;
 H – enthalpy, J/mol;
 I_g – indices of substances in the gas phase;
 I_j – indices of substances in the mixture j ;
 N – number of substances;
 R – gas constant, J/(mol K);
 S – entropy, J/(mol K);
 T – temperature, K;
 V – volume, m³;
 a_i – activity of the substance i ;
 b_j – amount of a chemical element j in the system, mol;
 f – dimensionless value of Helmholtz energy;
 g – dimensionless value of Gibbs energy;
 m – number of chemical elements in the system;
 p – pressure, MPa;
 x_i – amount of substance i , mol;
 y_i – number of moles of phase i , mol;
 λ_j – chemical potential of the element j , J/mol;
 ν_{ji} – number of atoms of a chemical element j in the substance i .

References:

[1] D. S. Villars, "A method of successive approximations for computing combustion equilibria on a high speed

digital computer," *J. Phys. Chem.*, vol. 63, pp. 521-525, Apr. 1959, doi: 10.1021/j150574a016.

[2] W. R. Smith and R. W. Missen, *Chemical Reaction Equilibrium Analysis: Theory and Algorithms*, New York, NY, USA: Wiley, 1982.

[3] W. D. White, S. M. Johnson and G. B. Dantzig, "Chemical equilibrium in complex mixtures," *J. Chem. Phys.*, vol. 28, pp. 751-755, May 1958, doi: 10.1063/1.1744264.

[4] R. J. Duffin and C. Zener, "Geometric programming, chemical equilibrium, and the anti-entropy function," *Proc. Natl. Acad. Sci. U.S.A.*, vol. 63, pp. 629-636, Apr. 1969, doi: 10.1073/pnas.63.3.629.

[5] G. Eriksson, "Thermodynamic study of high temperature equilibria," *Acta. Chem. Scand.* vol. 25, pp. 2651-2658, Jul. 1971, doi: 10.3891/acta.chem.scand.25-2651.

[6] B. A. Murtagh and M. A. Saunders, "Large-scale linearly constrained optimization," *Math. Program.*, vol. 14, pp.41-72, Dec. 1978, doi: 10.1007/BF01588950.

[7] H. Greiner, "Computing complex chemical equilibria by generalized linear programming," *Math. Comput. Model.*, vol. 10, pp. 529-550, Jul. 1988, doi: 10.1016/0895-7177(88)90082-9.

[8] M. H. A. Piro and S. Simunovic, "Global optimization algorithms to compute thermodynamic equilibria in large complex systems with performance considerations," *Comput. Mater. Sci.*, vol. 118, pp. 87-96, Jun. 2016, doi: 10.1016/j.commatsci.2016.02.043.

[9] C. Tsanas, E. H. Stenby and W. Yan, "Calculation of multiphase chemical equilibrium by the modified RAND method," *Ind. Eng. Chem. Res.*, vol. 56, pp. 11983–11995, Oct. 2017, doi: 10.1021/acs.iecr.7b02714.

[10] B. Sundman, N. Dupin and B. Hallstedt, "Algorithms useful for calculating multi-component equilibria, phase diagrams and other kinds of diagrams," *Calphad*, vol. 75, p. 102330, Dec. 2021, doi: 10.1016/j.calphad.2021.102330.

[11] W. A. Roos and J. H. Zietsman, "Accelerating complex chemical equilibrium calculations - A review," *Calphad*, vol. 77, p. 102380, Jun. 2022, doi: 10.1016/j.calphad.2021.102380.

[12] Available: <https://www.factsage.com/> (accessed Aug. 27, 2023).

[13] "Thermo-Calc Software." Available: <https://thermocalc.com/> (accessed Aug. 27, 2023).

[14] Y. Lwin, "Chemical equilibrium by Gibbs energy minimization on spreadsheets," *Int. J. Eng. Educ.* vol. 16, pp.335-339, Apr. 2000.

[15] L. Eriksson, "CHEPP-a chemical equilibrium program package for Matlab," *SAE trans.*, vol. 113, pp. 730-741, 2004.

[16] M. H. A. Piro, S. Simunovic, T. M. Besmann, B. J. Lewis and W. T. Thompson, "The thermochemistry library Thermochemica," *Comput. Mater. Sci.*, vol. 67, pp.266-272, Feb. 2013, doi: 10.1016/j.commatsci.2012.09.011.

- [17] “ORNL-CEES / thermochemica.” Available: <https://github.com/ORNL-CEES/thermochemica> (accessed Aug. 27, 2023).
- [18] A. Wächter and L. T. Biegler, “On the implementation of an interior-point filter line-search algorithm for large-scale nonlinear programming,” *Math. Program.*, vol. 106, pp. 25–57, Mar. 2005. doi: 10.1007/s10107-004-0559-y.
- [19] I. Prigogine and R. Defay, *Treatise on thermodynamics: Based on the methods of Gibbs and De Donder*, London: Longmans, 1954.
- [20] J. Bezanson, A. Edelman, S. Karpinsky and V. B. Shah, “Julia: A fresh approach to numerical computing,” *SIAM Rev.*, vol. 59, pp. 65-98, Jan. 2017, doi: 10.1137/141000671.
- [21] Available: <https://coin-or.github.io/Ipopt/index.html> (accessed Aug. 27, 2023).
- [22] I. Dunning, J. Huchette and M. Lubin, “JuMP: A modeling language for mathematical optimization,” *SIAM Rev.*, vol. 59, pp. 295-320, Feb. 2017, doi: 10.1137/15M1020575.
- [23] B. Legat, O. Dowson, J. D. Garcia and M. Lubin, “MathOptInterface: a data structure for mathematical optimization problems,” *INFORMS J. Comput.*, vol. 34, pp. 672-689, Feb. 2022, doi: 10.1287/ijoc.2021.1067.
- [24] J. Lofberg, “YALMIP : a toolbox for modeling and optimization in MATLAB,” in *Proc. 2004 IEEE Int. Conf. on Robotics and Automation (IEEE Cat. No.04CH37508)*, Taipei, Taiwan, Sep. 2004, pp. 284-289, doi: 10.1109/CACSD.2004.1393890.
- [25] “CVX: Matlab Software for Disciplined Convex Programming.” Available: <http://cvxr.com/cvx/> (accessed Aug. 27, 2023).
- [26] W. E. Hart, C. D. Laird, J.-P. Watson, D. L. Woodruff, G. A. Hackebeil, B. L. Nicholson and J. D. Sirola, *Pyomo-optimization modeling in Python*. Berlin: Springer, 2017.
- [27] “JuliaMath / Roots.jl .” Available: <https://github.com/JuliaMath/Roots.jl> (accessed Aug. 27, 2023).
- [28] L. V. Gurvich and I. V. Veyts, *Thermodynamic Properties of Individual Substances*, New York: Hemisphere Publishing Corp., 1989.
- [29] G. V. Belov, S. A. Dyachkov, P. R. Levashov, I. V. Lomonosov, D. V. Minakov, I. V. Morozov, M. A. Sineva and V. N. Smirnov, “The IVTANTHERMO — online database for thermodynamic properties of individual substances with web interface,” *J. Phys.: Conf. Ser.*, vol. 946, p. 012120, 2018, doi: 10.1088/1742-6596/946/1/012120.
- [30] “NIST Chemistry WebBook, SRD 69.” Available: webbook.nist.gov (accessed Aug. 27, 2023).
- [31] B. J. McBride, “NASA Glenn coefficients for calculating thermodynamic properties of individual species,” NASA, Cleveland, Ohio, USA, Tech. Rep. NASA/TP-2002-211556, Sep. 2002. Available: <https://ntrs.nasa.gov/api/citations/20020085330/downloads/20020085330.pdf> (accessed Aug. 27, 2023).
- [32] G. Belov, “On linear programming approach for the calculation of chemical equilibrium in complex thermodynamic systems,” *J. Math. Chem.*, vol. 47, pp. 446-456, Jan. 2010, doi: 10.1007/s10910-009-9580-y.
- [33] A. D. Pelton, “Thermodynamic modeling and phase equilibrium calculations in nuclear materials,” *Pure Appl. Chem.*, vol. 69, pp. 2245-2252, Nov. 1997, doi: 10.1351/pac199769112245.
- [34] “CEARUN.” Available: <https://cearun.grc.nasa.gov/> (accessed Aug. 27, 2023).
- [35] G. P. Sutton and O. Biblartz, *Rocket Propulsion Elements*, New York, NY, USA: Wiley, 2017.
- [36] “gybelov / Heterogeneous-Equilibrium .” Available: <https://github.com/gybelov/Heterogeneous-Equilibrium> (accessed Aug. 27, 2023).